



Microstructural-Level Fuel-Performance Modeling of U-Mo Monolithic Fuel

September 2021

Benjamin Beeler^{a,f}, Larry Agesen^a, James Cole^a, Gerard Hofman^c, ATM Jahid Hasan^f, Shenyang Hu^b, Sourabh Kadambi^a, Curt Lavender^b, Linu Malakkal^a, Sean Masengale^g, Zhi-Gang Mei^c, Aaron Oaks^c, Maria Okuniewski^d, Gyuchul Park^d, Aashique Rezwan^g, Kelley Verner^c, Abdellatif Yacout^c, Bei Ye^c, and Yongfeng Zhang^a

^a Idaho National Laboratory

^b Pacific Northwest National Laboratory

^c Argonne National Laboratory

^d Purdue University

^e University of Idaho

^f North Carolina State University

^g University of Wisconsin, Madison



DISCLAIMER

This information was prepared as an account of work sponsored by an agency of the U.S. Government. Neither the U.S. Government nor any agency thereof, nor any of their employees, makes any warranty, expressed or implied, or assumes any legal liability or responsibility for the accuracy, completeness, or usefulness, of any information, apparatus, product, or process disclosed, or represents that its use would not infringe privately owned rights. References herein to any specific commercial product, process, or service by trade name, trade mark, manufacturer, or otherwise, does not necessarily constitute or imply its endorsement, recommendation, or favoring by the U.S. Government or any agency thereof. The views and opinions of authors expressed herein do not necessarily state or reflect those of the U.S. Government or any agency thereof.

Microstructural-Level Fuel-Performance Modeling of U-Mo Monolithic Fuel

Benjamin Beeler^{a,f}, Larry Aagesen^a, James Cole^a, Gerard Hofman^c, ATM Jahid Hasan^f, Shenyang Hu^b, Sourabh Kadambi^a, Curt Lavender^b, Linu Malakkal^a, Sean Masengale^g, Zhi-Gang Mei^c, Aaron Oaks^c, Maria Okuniewski^d, Gyuchul Park^d, Aashique Rezwani^g, Kelley Verner^e, Abdellatif Yacout^c, Bei Ye^c, and Yongfeng Zhang^a

^a Idaho National Laboratory

^b Pacific Northwest National Laboratory

^c Argonne National Laboratory

^d Purdue University

^e University of Idaho

^f North Carolina State University

^g University of Wisconsin, Madison

September 2021

Idaho National Laboratory
Idaho Falls, Idaho 83415
<http://www.inl.gov>

Prepared for the
U.S. Department of Energy
Under DOE Idaho Operations Office
Contract DE-AC07-05ID14517

Page intentionally left blank

EXECUTIVE SUMMARY

As the physics that governs the microstructural evolution of nuclear fuel span various time and spatial scales, to fully understand the fuel behavior inevitably involves atomic to mesoscale resolution that can be difficult to determine experimentally. Microstructural-level modeling and simulations can be used to develop physics-based materials models that can provide physical understanding to inform fabrication process control, as well as a valuable feedback mechanism between post-irradiation examination (PIE) results and fabrication parameters. In accordance with the program schedule, the primary goals of the microstructure modeling effort are to:

1. Address critical microstructural questions and provide practical guidance to the fabricator via the fuel product specification
2. Provide mechanistic inputs for the existing fuel-performance code to improve its descriptive and predictive capability at the macroscopic scale.

In fiscal year (FY)-21, the work scope consisted of six main facets: (1) the effect of carbides on fuel performance; (2) gas diffusivity in different phases; (3) integration of microstructural fuel-performance modeling; (4) property degradation; (5) irradiation creep; and (6) historical analysis of microstructure data. Brief summaries of each are included below.

DART Modeling Integrating Lower Length Scale Computational Data

The Dispersion Analysis Research Tool (DART) fuel-performance code has been updated to simulate U-10Mo monolithic fuel swelling behavior during irradiation. The parameters used in the rate-theory-based mechanistic model were either calibrated using measured fission-gas-bubble (FGB) characteristics or provided by lower length scale simulations. Additionally, phase-field-predicted U-10Mo grain-subdivision kinetics for various grain sizes were implemented to simulate fuel swelling behavior at high burnup. The effects of initial grain size on fuel swelling were investigated. The results show that the calculated swelling of initial grain sizes from $4.36\ \mu\text{m}$ to $17\ \mu\text{m}$ is in good agreement with the U-10Mo swelling correlation developed with experimental data, and larger grains have lower swelling rates. Higher fuel temperature or fission rate leads to greater swelling. Further examination by isolating the variation of fuel temperature from that of radiation-enhanced processes (gas diffusion and resolution) revealed that the increased fuel swelling induced by elevated fission rate is due to temperature effects but not the augmentations of gas-atom diffusivity and bubble resolution rate.

Model of Thermal Conductivity Degradation for U-Mo

The experimental determination of the thermal conductivity of irradiated fuels is difficult due to the time and cost involved. As such, there is limited experimental data on how the thermal conductivity varies as a function of burnup. Variation in thermal conductivity can lead to changes in temperature-dependent fuel properties and behaviors, including fission-gas swelling and creep. It is thus critically important to understand the degradation of thermal conductivity as a function of fission density to be able to predict fuel evolution in engineering-scale fuel-performance simulations. This work models the thermal conductivity degradation due to irradiation-induced microstructural changes in U-10Mo fuel. This model considers the effect of point defects (vacancy and fission products), grain boundaries, intergranular gas bubbles, and intragranular gas bubbles on the thermal conductivity in U-10Mo. This model separates each microstructural feature's effect on thermal conductivity by a parameter called the thermal conductivity degradation factor. The available experimental and simulated results were sources of the microstructural details required to model the thermal conductivity degradation. The details of the intergranular and intragranular porosity as a function of fission density were obtained from the DART simulations for microstructural changes in irradiated U-10Mo fuels. The thermal conductivity degradation model indicates that the effect of grain boundary on the thermal transport is negligible, and the point defect at a saturation concentration of $\sim 10^{-4}$ has a minimal impact ($\sim 1\%$) on the degradation of the thermal

conductivity at all fission densities. However, the intragranular bubble formation became significant only after 10% burnup (0.8×10^{21} fissions/cm³), and the maximum thermal conductivity degradation factor due to intragranular gas bubbles at high burnup is ~10%. At the same time, our model predicts that intergranular gas bubbles are the dominant factor responsible for the significant reduction in thermal conductivity in irradiated U-10Mo at higher burnup. At a burnup of 70% (5.5×10^{21} fissions/cm³), the intergranular gas bubbles alone reduce the thermal conductivity by a factor of 30%.

Degradation of Mechanical Properties in UMo

The evolution of microstructure in U-10Mo nuclear fuel critically influences the mechanical properties and, thereby, the fuel performance. The fuel microstructure undergoes significant changes during burnup, which involves the formation and evolution of intra- and intergranular voids and gas bubbles, in conjunction with grain growth and grain recrystallization. A multi-phase-field model combined with the asymptotic expansion homogenization technique is implemented using the mesoscale fuel-performance code MARMOT to calculate the degradation in the overall elastic properties of representative microstructures during fuel burnup. Molecular dynamics (MD) calculations were performed to inform the elastic constants of U-10Mo, and the Ronchi Xe equation of state was employed to inform the properties of the gas bubble. The calculations show a strong degradation in the elastic constants with pore volume and grain boundary coverage. The degradation is stronger for void microstructures due to the absence of gas pressure resisting compression, whereas the degradation in shear constants is identical for both void and bubble microstructures due to the inability of gas pressure to resist shear. For intergranular pores, the degradation occurs more rapidly with pore volume for larger grains. On the other hand, for saturated grain boundaries, the degradation is stronger for finer grains. A model is developed to assess the stress fields generated in the matrix of the fuel by highly pressurized nanometer-sized intragranular voids and bubbles. While underpressurized bubbles result in tensile stress fields due to the strong effect of surface tension, equilibrium Xe gas concentration in the bubbles provide the necessary equilibrium pressure to negate stresses in the matrix. A model for the degradation of mechanical properties based upon the microstructure and the underlying interaction with FGBs will be delivered to the engineering fuel-performance modeling team in FY-22.

Fracture Toughness in Monolithic U-10Mo Fuel

An interaction zone forms between U-10Mo and Zr, referred to as the UMo-Zr interaction zone, and grows during irradiation. At high burnups, fracture develops in the fuel plate, primarily in a region with high density of gas bubbles along the interface between the different sublayers in the interaction zone. This indicates potential degradation in fracture stress, either in the U-10Mo fuel or in the interaction zone, or both. The degradation in fracture properties induced by gas bubbles in U-10Mo fuel (21.8% in atomic percent) and in the UMo-Zr interaction zone have been studied. The change in fracture properties in bulk U-10Mo fuel is calculated using MD simulations. The change in fracture properties in the UMo-Zr interaction zone is simulated using the phase-field fracture method, with the model implemented in Idaho National Laboratory's (INL's) Multiphysics Object-Oriented Simulation Environment (MOOSE).

U-10Mo was found to be very ductile under uniaxial tension by MD simulations adopting the bicrystal model. No fracture propagation along GBs was observed with up to 50% engineering strain. Considering that the extremely high-loading rate in MD simulations usually facilitates fracture, the ductile nature of U-10Mo indicated by the MD simulations seems to be convincing. Three plastic deformation modes were identified depending on the loading orientation with the selection of deformation mode consistent with the Schmid law. The absence of fracture propagation in U-10Mo has some interesting implications on the fracture observed in the UMo-Zr interaction zone at high burnups. The appearance of fracture may be caused by three possible reasons: (1) extremely high gas-bubble coverage or gas bubble density, (2) creep damage at stress levels lower than the yield stress, and (3) phase separation in the UMo-Zr interaction zone. It should be noted the above three mechanisms are not mutually exclusive; they may

in fact operate together, and the failure of the UMo fuel matrix may be caused by their compounding effect. These three effects will be the subject of future research.

A phase field fracture model was designed and demonstrated for single-layer domain (e.g., bulk UMo) and for multiple-layer domain (e.g., UMo-Zr interaction zone) in MOOSE. The model is for brittle fracture without plastic deformation. The model is capable of modeling fracture initiation and propagation in domains with a distribution of gas bubbles in both 2D and 3D. In the future, the model will be further extended to include creep fracture, which is expected to be an important mechanism for failure of UMo fuel matrix. The model will be applied to study fracture in the interaction region with varying bubble size, density, and connectivity. A correlation between the fracture stress of the interaction zone and bubble morphology will be developed based on simulation results. The effects of phase separation, thickness of each layer, and fluctuation in layer thickness on fracture initiation and propagation will be studied as well.

The Effect of Carbides on Mechanical Properties and Swelling of U-Mo Fuel

Nonmetallic inclusions, such as carbides, are often found in the U-Mo alloy fuels, whether due to residual feedstock impurities or the formation during the manufacturing process. Carbide inclusions may affect the U-Mo fuel manufacturing process, the microstructure evolution, and fuel performance under irradiation. We investigated the effect of carbide inclusions on the mechanical properties of U-Mo fuel using different simulation approaches. Semi-empirical models and finite-element method modeling show that carbides have a minor impact on the mechanical properties of U-Mo fuel when the carbide inclusions have a typical volume fraction (0.5~1%) and average aspect ratio (1.5~2.5) as observed in experiments. Density functional theory calculations show that decreased Mo concentration of U-Mo alloy or increased hypo-stoichiometry in carbides can slightly decrease the mechanical strength of the UMo/ uranium carbide (UC) interface. Meanwhile, experiments show that the ^{235}U enrichment in carbides could be different from that in the U-Mo fuel matrix due to the incomplete mixing of depleted and highly enriched uranium feedstocks. Different enrichments in carbides and the fuel matrix present fission rate and temperature gradients in the fuel and potentially deleterious microstructural behavior during operation. By extending our previous work of fission rate effect on fuel swelling, we developed phase-field models to simulate the effect of variable ^{235}U enrichment in carbides on the gas bubble swelling in U-Mo fuel. Our simulation suggests that the ^{235}U enrichment and the volume fraction of UC inclusions have a minor impact on the gas bubble swelling if the targeted ^{235}U enrichment in the final U-Mo fuel can be achieved. Phase-field simulations also show that increased fission rate can result in accelerated gas bubble swelling enhanced by the increased ^{235}U enrichment in the U-Mo fuel.

Radiation-Enhanced Diffusion in UMo

Accurate prediction of fission-gas swelling requires accurate descriptions of the diffusion coefficients of relevant species in the fuel. Radiation-enhanced diffusion coefficients of U, Mo, and Xe in $\gamma\text{U-10Mo}$ were calculated using rate-theory models and MD simulations. In addition, intrinsic diffusion of Xe was calculated using MD simulations. Utilizing the intrinsic diffusion, radiation-enhanced diffusion, and radiation-driven diffusion, the total diffusion of U, Mo, and Xe under irradiation was also determined in the temperature range between 300 and 1400 K. It was found that radiation-enhanced diffusion of U and Mo were dominant in the intermediate temperature range (450 to 650 K) at the evaluated fission rates, whereas the radiation-enhanced diffusion of Xe did not significantly contribute to the total diffusion of Xe under irradiation at any temperature range. The total diffusion coefficients of U, Mo, and Xe calculated in this work will be utilized as important parameters in mesoscale and engineering-scale nuclear-fuel models.

Historical Characterization Data Analysis

The improvement and creation of predictive fuel microstructure modeling and simulation require accurate experimental data for computational inputs and validation. Predictions of the fuel behavior rely on the accuracy of the physics computations performed and the physical data used as inputs or for validation of said computations. Therefore, data collection of the microstructure characteristics of uranium molybdenum (U-Mo) alloy fuels was undertaken to understand the available data for computational scientists and provide a starting point for creating a library or collection of this data for use by computational researchers.

A major finding is the disconnect between data collection methods and data types, indicating a more standardized approach is required. Additionally, microstructural data from historical experiments was collected into one location. The following list highlights some significant improvements to the microstructure data needed to meet the computational data requirements:

1. Standardized or explicit determination of the fission density for each sample is required
2. Data on the internal pressure of FGB were not available and fall under the following tiers of data collection where ongoing work that provides this or brand-new tests must be performed to get the data
3. Need more volume fraction characterization and quantified for decomposed regions and precipitates from experiments.
4. As-fabricated data from all areas of the MM goals are necessary to characterize the general microstructure of the fuel prior to irradiation and connect that to the post-irradiation structure
5. Chemical homogenization data in the material and the inhomogeneity location are needed to understand the relation of other microstructure development to the chemical composition present.

Ongoing and planned fuel qualification projects have been identified that present opportunities for collaboration between computational scientists and experimentalists. The included project plans can meet some of the target microstructural modeling information. Collaboration between the two groups for data collection is an ongoing effort and will continue to fill in U-Mo data collection methods and use gaps.

Integrated Fission Gas Swelling Correlation for UMo Research Reactor Fuel

A mechanistic, microstructure-based approach has the potential to provide a more predictive fuel-performance capability than empirical fitting to limited experimental datasets. This is particularly the case when data is restricted to certain operating parameters, but the materials of interest may operate outside of that experimental phase space. By incorporating lower length scale information (e.g., experimental microstructures, atomistic diffusivities, and bubble evolution), a more general model can be developed that appropriately incorporates underlying physical phenomena into macroscale predictions. In this work, an updated fission-gas swelling model was generated that incorporates grain size, temperature, fission rate density, and fission density for UMo monolithic fuel. For the assumed nominal case, the swelling correlation presented here reasonably reproduces the experimentally based swelling correlations. This work has defined functional relationships relating the individual state variables of interest to the fission-gas swelling, allowing for exploration of operational phase spaces that are not able to be described by the existing experimental correlations. This work has highlighted the need to understand the initial microstructure of UMo monolithic fuel, as modifications in initial grain size can yield substantially different results in the fission-gas swelling behavior. This model has been delivered to the engineering fuel-performance modeling team and is currently undergoing evaluation.

Irradiation-Enhanced Creep

A mesoscale model of irradiation-enhanced creep in polycrystalline UMo with a Zr layer has been developed. The model integrates a spatial-dependent cluster-dynamics model of radiation defect evolution, a phase-field model of non-equilibrium gas bubble evolution, and elastic-plastic deformation under a crystal-plasticity framework. The radiation defects including U and Mo interstitials, U and Mo vacancies, vacancy and interstitial clusters, and Xe fission-gas atoms are considered. The lattice mismatch among host atoms (U and Mo) and defects (interstitial, vacancy, and Xe atom) is described by a stress-free strain tensor. It enables one to consider stress-driven diffusion of solutes and vacancies. It is assumed the irradiation and stress-enhanced diffusion is one of dominant creep mechanisms in UMo. In the phase-field model of non-equilibrium gas bubble evolution, the Xe concentration inside gas bubbles is determined by the absorption of vacancies and Xe atoms. Therefore, the model can describe the transition between over-pressurized gas bubbles and voids which is determined by the local flux of vacancies and Xe atoms to gas bubbles. The thermodynamic and kinetic properties of radiation defects are described in a function of order parameters which presents different phases including UMo, gas bubble, and Zr cladding. Therefore, the model captures the evolving thermodynamic and kinetic properties with gas-bubble evolution. Plastic strain rate-based crystal plasticity is employed to describe the elastic-plastic deformation. It enables the analysis of the effect of anisotropic mechanical properties, such as grain orientation and individual slip system, on elastic-plastic deformation and creep. In summary, this is a physics-based model with a multiphysics coupling of radiation damage, gas bubble swelling, stress-driven diffusion creep, and elastic-plastic deformation. The model has been used to study the effect of gas bubble structures on elastic-plastic deformation, the effect of radiation conditions and thermodynamic, and kinetic properties of radiation defects on defect accumulation and gas bubble evolution.

Atomistic modeling to support mesoscale creep models

Irradiation creep models rely on the fundamental behavior of point defects in a stress field. How that applied stress field affects diffusion or equilibrium concentrations of defects will in turn affect the time- and stress-dependent evolution of the material system. How point defect properties vary as a function of applied pressure is largely unknown for U-Mo systems. It has been shown in Fe that application of pressure can significantly affect both the formation energy of defects and their generation under irradiation. In this work, we study how the application of hydrostatic tension and compression affects the formation energy and diffusion coefficient of interstitials and vacancies in U-Mo as a function of pressure, temperature, and composition. On average, the maximum applied pressure of 10 kbar produces a 6% increase in the interstitial formation energy and a 3% decrease in the vacancy formation energy. Under reasonable applied bulk pressures below the yield point (<100 MPa), negligible deviations in the defect formations are observed. Also, applied pressures should yield negligible variation on point defect diffusion at relevant temperatures and pressures. There are impacts of the applied pressure on defect formation and diffusion, and clear trends can be observed, but these effects are sufficiently small; even at large pressures, they likely can be neglected for practical purposes. However, in circumstances where the pressures may be quite large (e.g., in the area surrounding a highly pressurized nanometer-sized bubble) statistically significant changes in the local defect formation energy and diffusion coefficient could be observed, potentially altering FGB evolution and creep behaviors.

Summary

This work has been conducted as a coordinated effort involving a team of modeling experts across INL, Argonne National Laboratory, Pacific Northwest National Laboratory, University of Idaho, University of Purdue, University of Wisconsin-Madison, and North Carolina State University. The multiscale modeling and simulation effort is generating knowledge and data that enhance the fundamental understanding of fuel behavior and can ultimately reduce risks and fuel cost.

Page intentionally left blank

CONTENTS

EXECUTIVE SUMMARY	iii
ACRONYMS	xix
1. INTRODUCTION.....	1
2. RESULTS.....	1
2.1 DART Modeling Integrating Lower Length Scale Computational Data	1
2.1.1 Introduction	1
2.1.2 DART Code Structure and Primary Models	2
2.1.3 Calibration of Fission-Gas-Behavior Parameters.....	8
2.1.4 U-Mo Swelling Behavior up to High-Fission Density for Various Grain Sizes	17
2.1.5 Fission-Rate and Fuel-Temperature Effects.....	18
2.1.6 Conclusions	19
2.2 Thermal Conductivity Degradation Model for U-10Mo	19
2.2.1 Introduction	19
2.2.2 Methodology	20
2.2.3 Results	22
2.2.4 Conclusion.....	26
2.3 Degradation of Mechanical Properties in Monolithic U-Mo Fuel	26
2.3.1 Atomistic Calculations	27
2.3.2 Mesoscale Calculations of Effective Elastic Constants and Stress Fields	31
2.4 Fracture Toughness in Monolithic U-10Mo Fuel	42
2.4.1 MD Simulations of Mechanical Deformation in U-10Mo Bicrystal.....	42
2.4.2 Phase Field Fracture	47
2.5 The Effect of Carbides on Mechanical Properties and Swelling of U-Mo Fuel	53
2.5.1 Analysis of Carbides in UMo Fuel from Image Processing.....	53
2.5.2 Effect of Carbides on the Mechanical Properties of U-Mo Alloy Fuel	57
2.5.3 Effect of ²³⁵ U Enrichment in Carbides on Gas Bubble Swelling of U-Mo Fuel.....	67
2.5.4 Conclusions	77
2.6 Radiation-Enhanced Diffusion in UMo	78
2.6.1 Computational Details.....	78
2.6.2 Results	80
2.6.3 Summary	87
2.7 Historical Characterization Data Analysis	87
2.7.1 Microstructure Data Library.....	90
2.7.2 M ³ Data Collection.....	91
2.7.3 Conclusions of the Data Collection.....	107
2.8 An Integrated Fission-Gas Swelling Correlation for UMo Research Reactor Fuel	108

2.8.1	Fitting Procedure	108
2.8.2	Results	110
2.8.3	Discussion	112
2.8.4	Conclusions	113
2.9	Irradiation-Enhanced Creep	113
2.9.1	An Integrated Model of Radiation Defect Evolution and Gas Bubble Swelling in Polycrystalline UMo	114
2.9.2	Material Properties of UMo	123
2.9.3	Model Parameters.....	123
2.9.4	Results	126
2.9.5	Conclusions and Remarks	135
2.10	Atomistic Modeling to Support Mesoscale Creep Models	136
2.10.1	Computational Details.....	136
2.10.2	Results	137
2.10.3	Conclusions	142
3.	REVIEW AND FUTURE STUDY	142
3.1	Fiscal Year 2021 Review	142
3.2	Publications	143
3.3	Conference Presentations	144
3.4	Fiscal Year 2022 Plan	144
4.	CONCLUSIONS	146
5.	REFERENCES	146

FIGURES

Figure 1. Flow chart of the DART computational code.....	3
Figure 2. Schematic of (a) the meshing grid of a monolithic fuel plate, (b) side view of the plate and (c) meshing inside an (x, z) node, and (d) division inside each k node to track the progression of recrystallization.....	7
Figure 3. Recrystallization kinetics calculated with the PF method for grain sizes 4.36 μm , 8.5 μm , and 17 μm , compared with the measurement data collected from U-10Mo dispersion fuel particles with an average grain size of $\sim 4.5 \mu\text{m}$	8
Figure 4. Comparisons of measured and calibrated intergranular-bubble-size distributions in plates (a) V6018G, (b) V6019G, and (c) V8005B.....	11
Figure 5. Comparison of measured and calibrated (a) bubble diameter, (b) visible porosity, and (c) U-Mo swelling.....	12
Figure 6. Sensitivity study results of the parameters related to the gas-atom diffusion process	14
Figure 7. Sensitivity study results of the parameters related to the bubble nucleation process	15
Figure 8. Sensitivity study results of the parameters related to radiation-induced resolution process.....	16
Figure 9. U-10Mo swelling as a function of fission density for three grain sizes, compared with the U-10Mo monolithic fuel-swelling correlation from [36].....	17
Figure 10. U-10Mo swelling as a function of fission density calculated with grain size = 8.5 μm for a variation of constant fission rates: $8.92 \times 10^{14} \text{ f}/(\text{cm}^3 \cdot \text{s})$, $5.94 \times 10^{14} \text{ f}/(\text{cm}^3 \cdot \text{s})$, and $2.97 \times 10^{14} \text{ f}/(\text{cm}^3 \cdot \text{s})$	18
Figure 11. U-10Mo swelling as a function of fission density calculated with grain size = 8.5 μm and constant FR = $5.94 \times 10^{14} \text{ f}/(\text{cm}^3 \cdot \text{s})$ to examine the effects of (a) the combination of D_0 and b_0 and (b) fuel temperature.	19
Figure 12. Thermal conductivity degradation factor due to intragranular gas bubble as a function of the FD compared with the work by Zhou et al. [42].	23
Figure 13. (a) Plot of degradation factor for intergranular bubbles as a function of the FD (b) Comparison of the thermal conductivity degradation factor due to intergranular and intergranular gas bubbles.	24
Figure 14. The point defect degradation factor considering the saturation concentration of 0.01% (10^{-4}).....	25
Figure 15. (a) Comparison of the degradation factor due to intragranular bubbles, intergranular bubbles, and the point defects (case3) considering the saturation concentration of 0.01% (1×10^{-4}); (b) Comparison of the thermal conductivity degradation as a function of FD at 150°C, considering the saturation concentration of point defects of 0.01% (1×10^{-4}).	26
Figure 16. The c/a ratio at various temperatures and Mo concentrations (c_{Mo} , molar fraction) calculated using a) (left) the original UMo ADP and b) (right) the newly constructed U-Mo-Xe ADP potentials.	28
Figure 17. Distribution of (left) interstitial and (right) vacancy formation energies in U-10Mo (21.8% atomic percent) at 300 K.	28

Figure 18. Bulk UMo containing 10% porosity with 142 (left) and 69 (right) bubbles.	29
Figure 19. Elastic moduli C_{11} , C_{12} and C_{44} of bcc U as functions of temperature and porosity.	29
Figure 20. Elastic moduli C_{11} , C_{12} and C_{44} of bcc U as functions of temperature and GVratio.	30
Figure 21. Fitted results for elastic moduli of U-10 Mo using Eqn. 2.3.1 versus MD results.	30
Figure 22. (Top panel) Schematic representations of the microstructure at different scales - multiscale (\mathbf{x}, \mathbf{y}) , representative volume element at microscale \mathbf{y} and homogenized macroscale \mathbf{x} . (Bottom panel) Typical displacement fields illustrated at the corresponding scales [62].	31
Figure 23. Xe gas bubble properties extracted from the Ronchi EOS at 500 K [30].	35
Figure 24. PF polycrystal microstructures for assessing effective elastic constants for (a) intergranular pores and (b) intragranular bubbles. (c) Heterogeneous elastic constants C_{44} for microstructure with intergranular voids.	37
Figure 25. Effective elastic constants for polycrystalline microstructure with 150 nm intergranular voids, calculated as a function of void volume percent for different grain sizes.	38
Figure 26. Stress distribution of the component σ_{xx} for a intragranular pore of 1 nm radius in a 2D system.	40
Figure 27. Radial, tangential, and hydrostatic stress fields across the pore-matrix interface for intragranular pore of 1 nm radius in the isotropic U-10Mo matrix.	41
Figure 28. Schematic of bicrystal model under uniaxial tension.	43
Figure 29. Stress-strain curves for simulations with $\langle 110 \rangle$ symmetrical tilt (ST) $\Sigma 3$, $\Sigma 9$, and $\Sigma 11$ GBs, showing ductile behavior via plastic deformation without fracture.	43
Figure 30. Snapshots of the atomic configurations showing dislocation emission from GBs in the simulation cell with $\langle 110 \rangle$ ST $\Sigma 3$ GBs with a GV ratio of 0.25.	44
Figure 31. Snapshots of the atomic configurations in the simulation cell with $\langle 110 \rangle$ ST $\Sigma 9$ GBs with a GV ratio of 0.25.	44
Figure 32. Snapshots of the atomic configurations in the simulation cell with $\langle 110 \rangle$ ST $\Sigma 11$ GBs with a GV ratio of 0.25.	45
Figure 33. Comparison of maximum Schmid factors for $\langle 111 \rangle / \{110\}$ slip system for dislocation and $\langle 111 \rangle / \{112\}$ slip system for twinning in the simulation cells with $\langle 110 \rangle$ ST $\Sigma 3$, $\Sigma 9$, and $\Sigma 11$ GBs.	46
Figure 34. Electron image and composition profile of sublayers across U-Mo/Zr interface and the planned simulation domain.	48
Figure 35. Bubble morphology from experiments and the proposed simulation cell design.	49
Figure 36. PF fracture simulation with a single bubble initiated as a pre-cracked surface.	50
Figure 37. PF fracture simulation of multiple bubbles align in the middle of the domain.	50
Figure 38. PF fracture simulation with multiple gas bubbles in the 3D domain.	51
Figure 39. Different configuration of material property application, fracture profile at the end of the simulation.	52

Figure 40. Stress-strain relationship for different configuration of material property application.	52
Figure 41. (a), (b), and (c) are BSE-SEM images of as-cast, homogenized, and hot-rolled U-10Mo alloy samples.....	55
Figure 42. Particle size distribution of uranium carbides in (a) as-cast, (b) homogenized, and (c) hot-rolled U-10Mo alloy samples.	55
Figure 43. The aspect ratio of uranium carbides in (a) as-cast, (b) homogenized, and (c) hot-rolled U-10Mo alloy samples.	56
Figure 44. Examples of synthetic microstructures with random particle distribution	56
Figure 45. Effective Young's modulus of U-10Mo alloy fuel a function of carbide volume fraction predicted by different models.	58
Figure 46. Effective shear modulus of U-10Mo alloy fuel a function of carbide volume fraction predicted by different models.	58
Figure 47. Effective Young's modulus of U-10Mo alloy fuel as a function of the aspect ratio of carbide inclusions with different volume fractions of UC.	60
Figure 48. Effective shear modulus U-10Mo alloy fuel as a function of the aspect ratio of carbide inclusions with different volume fractions of UC.	61
Figure 49. Atomic structures of UMo UC UMo interface models with a different number of UC layers of UC.	62
Figure 50. Tensile stress-strain curves of UMo/UC interface models with a different number of UC layers.	63
Figure 51. Atomic structures of UMo/UC interface models with different concentrations of Mo in $U_{1-x}Mo_x$ alloy	64
Figure 52. Young's modulus and ultimate tensile strength of UMo/UC interface models as a function of Mo concentration in $U_{1-x}Mo_x$ alloy.	65
Figure 53. Atomic structures of the UMo/UC interface models with different non-stoichiometries of C in UC_{1-x} : (a) $x=0$; (b) $x=0.0333$; (c) $x=0.1$; (d) $x=0.2$	66
Figure 54. Young's modulus and ultimate tensile strength of UMo/UC interface models as a function of non-stoichiometry x of C in UC_{1-x}	67
Figure 55. ^{235}U enrichment in U-Mo matrix as a function of carbon concentration for five different levels of enrichment in UC by assuming an effective ^{235}U enrichment of 19.75 wt.% in the final U-Mo fuel.	71
Figure 56. ^{235}U enrichment in U-Mo matrix as a function of the ^{235}U enrichment in UC for three different volume fractions of UC by assuming an effective ^{235}U enrichment of 19.75 wt.% in the final U-Mo fuel.	71
Figure 57. Effect of ^{235}U enrichment in UC (volume fraction of UC = 2%) on the gas bubble swelling of U-Mo fuel irradiated at a FR of 5.0×10^{20} f/m ³ ·s.	73
Figure 58. Effect of ^{235}U enrichment in UC (volume fraction of UC = 2%) on the gas bubble swelling of U-Mo fuel irradiated at a FR of 5.0×10^{20} f/m ³ ·s.	73
Figure 59. Effect of the volume fraction of UC (^{235}U enrichment of 25% in UC) on the gas bubble swelling of U-Mo fuel irradiated at a FR of 5.0×10^{20} f/m ³ ·s.	74

Figure 60. Effect of the volume fraction of UC (^{235}U enrichment of 25% in UC) on the gas bubble swelling of U-Mo fuel irradiated at a FR of $5.0 \times 10^{20} \text{ f/m}^3 \cdot \text{s}$.	75
Figure 61. Gas bubble swelling kinetics of U-Mo fuel without UC inclusion under different fission rates, compared with experimental data compiled by Kim [34].	76
Figure 62. Gas bubble swelling kinetics of U-Mo fuel with UC inclusion under different fission rates.	76
Figure 63. Gas bubble swelling of U-Mo fuel as a function of FR at the FD of $6.5 \times 10^{27} \text{ f/m}^3$ for three different cases of UC inclusion.	77
Figure 64. Evolution of defect concentration as a function of time at 1000 K.	80
Figure 65. (a) Formation energies of Xe-vacancy clusters as a function of temperature. (b) Binding energies of Xe-vacancy clusters at 1000 K.	82
Figure 66. Rate theory calculations of defect concentration evolution as a function of time at the FR of $5 \times 10^{20} \text{ fission/m}^3/\text{s}$ at 1000 K.	82
Figure 67. The steady-state defect concentration of (a) vacancies and interstitial (b) Xe-monovacancy as a function of temperature in $\gamma\text{U-10Mo}$ for three different FRs: 5×10^{19} , 5×10^{20} , and $5 \times 10^{21} \text{ fission/m}^3 \cdot \text{s}$.	83
Figure 68. Diffusion coefficient of (a) U, Mo, and Xe (b) Diffusion coefficient of Xe as a function of cluster size from 1000 to 1400 K.	84
Figure 69. Radiation-enhanced diffusion of (a) U/Mo (b) Xe at three different fission rates.	85
Figure 70. Intrinsic diffusion, radiation-driven diffusion, and radiation-enhanced diffusion of (a) U (b) Mo (c) Xe in $\gamma\text{U-10Mo}$ at three different fission rates.	86
Figure 71. The total diffusion of (a) U, Mo and (b) Xe at three different fission rates in $\gamma\text{U-10Mo}$. Xe1	87
Figure 72. Data overview of all collected microstructure data, each piece corresponds to the experiment the data is from, and the black and gray areas indicate the fuel type, monolithic or dispersion.	91
Figure 73. Box-and-whisker plot of the FD for available M^3 experimental data.	92
Figure 74. Box-and-whisker plot of the FR for the M^3 experiments.	93
Figure 75. Pore data types, including the experiments the data is from.	94
Figure 76. Porosity data collected from M^3 experiments showing the most data is from AFIP6-MKII and RERTR-7 experiments.	95
Figure 77. Boxplot of the M^3 experimental porosity values in which the variation in the values is noticeable and due to FD differences and fuel types.	95
Figure 78. Eccentricity data from the experiments where five of the experimental campaign present the shape of pores in this manner.	96
Figure 79. Boxplot of the pore eccentricity where the most elongated pores are in RERTR-7 and RERTR-8	96
Figure 80. FGB diameter versus the bubble density per cross section of fuel for RERTR-1,-3-, and -5 dispersion fuels.	97
Figure 81. Pore size area experiments where the majority is from RERTR-7.	97

Figure 82. Pore size area boxplot of the M^3 experiments.	98
Figure 83. Pore size diameter experiments.	98
Figure 84. Boxplot of the data spread of the pore size diameter in M^3 experiments	98
Figure 85. Grain size data breakdown shows that most grain size data come from the MP-1 as-fabricated characterization efforts.....	99
Figure 86. Boxplots of the grain number of the MP-1 characterization efforts	100
Figure 87. Grain size changes during irradiation of three available experiments.....	101
Figure 88. Compares the grain refinement and FD of various experiments showing the relationship between higher FD and the onset and completion of grain refinement.	103
Figure 89. Carbide volume fraction of MP-1 samples showing the highest amount of carbides are in the cold-rolled fabricated foils.....	104
Figure 90. Boxplot comparing the molybdenum weight percent in the MP-1 fuel samples for three differing fabrication methods.....	106
Figure 91. Power and temperature profiles for the planned RUSL transient tests to measure the elastic modulus of MP-1 samples.	107
Figure 92. Fuel swelling as a function of FD. Reproduced from [133].	109
Figure 93. Fission-gas swelling as a function of FD at three unique grain sizes.	111
Figure 94. Fission-gas swelling as a function of FD at three unique FR densities.	111
Figure 95. The fission-gas swelling as a function of FD at three unique temperatures.	112
Figure 96. The fission-gas swelling as a function of FD, comparing the previous gaseous swelling correlation to four grain sizes from the present work.	113
Figure 97. The flow chart of the integrated model of microstructure evolution in the UMo/Zr layer.....	114
Figure 98. Simulation cell with polycrystalline UMo and Zr layer.	115
Figure 99. Simulation cell of polycrystalline UMo with distributed gas bubbles to validate crystal-plasticity model.....	126
Figure 100. Pressure (P) and shear stress (σ_{13}) distributions on the plane S for gas bubbles with internal pressures of (a) 0.07 GPa and (b) 2.1 GPa.	128
The units of pressure and stress are GPa.....	128
Figure 101. Effect of gas bubble volume fraction and internal pressure on stress-strain curves.....	129
Results shown are for gas bubbles with a pressure of (a) $P_{gb} = 0.07GPa$, (b) $P_{gb} = 1.2GPa$. Both tensile and compressive stresses are applied.....	129
Figure 102. Distributions of plastic strain ϵ_{13p} on the plane S in polycrystalline structures with gas bubble volume fraction 9.7% at different applied strains ($\epsilon_{33} = 0.02, 0.054, \text{ and } 0.10$).	130
(a) gas bubbles with initial pressure $P_{gb} = 0.07GP$ and (b) gas bubbles with initial pressure $P_{gb} = 1.2GPa$	130
Figure 103. Distribution of shear stress σ_{13} at $\epsilon_{33} = 0.1$	131

(a) gas bubble with initial internal pressure $P_{gb} = 0.07GPa$, and (b) gas bubble with initial internal pressure $P_{gb} = 1.2GPa$	131
Figure 104. (a) the center plane of the simulation cell, (b) evolution of vacancy and interstitial concentrations, and (c) defect concentrations at $t=32s$ for different $Dratio = 1, 2, \text{ and } 20$	132
Figure 105. Evolution of vacancy and interstitial concentrations under a FR $f_0 = 3.05 \times 10^{21} \text{ fission}/m^3/s$ and $Dratio = 20$	133
Figure 106. (a) Polycrystalline structures with different volume fraction of gas bubbles, (b) pressure distribution at applied strain $\epsilon_{33} = -0.01$	134
Figure 107. Vacancy concentration distribution on the middle plane of the simulation cell after 30s radiation.....	135
(a) in the case without applied strain, and (b) in the case with applied strain $\epsilon_{33} = -0.01$	135
Figure 108. The interstitial and vacancy formation energy as a function of pressure for U-10Mo at 1200 K.....	138
Figure 109. The interstitial formation energy as a function of composition for five applied pressures at 1,200 K.....	139
Figure 110. The vacancy formation energy as a function of composition for five applied pressures at 1,200 K.....	139
Figure 111. Temperature and compositional dependence of interstitial and vacancy formation energies in U-Mo.	140
Figure 112. Diffusion coefficient of interstitials and vacancies as a function of temperature and composition.....	141
Figure 113. Diffusion coefficient of vacancies and interstitials as a function of pressure for U-10 Mo.....	141
Figure 114. Arrhenius plots of the interstitial diffusion coefficient as a function of inverse temperature for U-10Mo. Pressure in the legend is in units of kbar.....	142
Figure 115. Microstructural modeling working group roadmap.....	145

TABLES

Table 1. Characteristics of three miniature U-10Mo/Al dispersion fuel plates irradiated in the RERTR-5 test, used for fission-gas-parameter calibration [37].	9
Table 2. Optimized value set of calibrated key fission-gas-behavior parameters.....	9
Table 3. Formation energies (eV) of vacancy, interstitial, and Xe substitutional in U-10Mo at room temperature.	29
Table 4. Fitted coefficients for U-10Mo using Eqn. 2.3.1.	30
Table 5. Material properties and model parameters used for the PF model and effective elastic constant calculation.....	33
Table 6. Effective constants for polycrystal with equilibrium gas bubbles parameterized using the bulk modulus from Ronchi's EOS and compared against voids.	38

Table 7. Material properties used for the preliminary PF fracture analysis.....	49
Table 8. Summary of area fraction, number density, average size, and aspect ratio of carbide inclusion in as-cast, homogenized and hot-rolled U-Mo alloy samples.....	56
Table 9. Mechanical properties of UC and U-10Mo alloy.....	57
Table 10. Calculated Young's modulus, ultimate tensile strength, and work of adhesion of UMo/UC interface models with a different number of UC layers.....	62
Table 11. Calculated Young's modulus, ultimate tensile strength, and work of adhesion of UMo/UC interface models with different Mo concentrations in the $U_{1-x}Mo_x$ alloy.....	64
Table 12. Calculated Young's modulus, ultimate tensile strength, and work of adhesion of UMo/UC interface models with different non-stoichiometries of C in UC_{1-x}	66
Table 13. Material properties of U-Mo fuel used in the current PF simulations.....	69
Table 14. Recombination rate constants (K_{iv}) at different temperatures.....	81
Table 15. Microstructure modeling data collection targets and details.....	88
Table 16. Grain size and aspect ratio of as-fabricated fuel samples.....	100
Table 17. Grain size diameter of dispersion fuels using two measurement methods, four measurement average and the lineal intercept* methods.....	101
Table 18. Irradiated monolithic fuels grain size data.....	102
Table 19. Decomposed volume fraction of as-fabricated samples.....	103
Table 20. Carbides volume fraction in RERTR-12 and AFIP6-MkII experiments for fabricated and irradiated fuels.....	104
Table 21. Molybdenum homogeneity from RERTR-12 and AFIP6-MkII fabricated samples.....	105
Table 22. Fitting coefficients for the fission-gas swelling as a function of grain size and FD.....	110
Table 23. Model parameters of the crystal plasticity and the PF models of gas bubble evolution for U-Mo crystals [173].....	123
Table 24. The most probable isotopes of FPs from $^{235}_{92}U$ due to thermal neutrons, the independent fission product yield (iFPY), total kinetic energy (E_{tot}), electronic loss ($E_{electron}$), and $E_{damage} = E_{tot} - E_{electron}$ used in SRIM simulations to estimate the number of Frenkel pairs in γU with displacement threshold energy $E_d=35.6eV$ at 800K.....	124
Table 25. Model parameters in the cluster dynamics model [184].....	125

Page intentionally left blank

ACRONYMS

ADP	Angular dependent potential
AEH	Asymptotic expansion homogenization
AFIP	ATR full-size plate in center flux trap position
ANL	Argonne National Laboratory
APT	Atom probe tomography
ASTM	American Society for Testing and Materials
ATR	Advanced Test Reactor
B&A	Before and after
BSE	Backscattered electrons
DART	Dispersion Analysis Research Tool
DFT	Density functional theory
DU	Depleted uranium
EAM	Embedded-atom-method
EBSD	Electron backscatter diffraction
EOS	Equation of state
FD	Fission density
FEM	Finite-element method
FF	Fuel fabrication
FFT	Fast Fourier Transform
FFTW	Fast Fourier Transform in the West
FGB	Fission-gas-bubble
FP	Fission product
FQ	Fuel qualification
FR	Fission rate
FY	Fiscal year
GB	Grain boundaries
GRASS	Gas-release and swelling subroutine
GVratio	Gas to vacancy ratios
HEU	Highly enriched uranium
HS	Hashin and Shtrikman
INL	Idaho National Laboratory
KKS	Kim-Kim-Suzuki
LAMMPS	Large-scale Atomic/Molecular Massively Parallel Simulator

LEU	Low-enriched U
LLS	Lower length scale
MD	Molecular dynamics
MDMC	Molecular-dynamics Monte Carlo
ML	Monolayer
MM	Microstructure Modeling
MOOSE	Multiphysics Object-Oriented Simulation Environment
NCSU	North Caroline State University
NRT	Norgett, Robinson, and Torrens
OkMC	Object kinetic Monte Carlo
OM	Optical Microscopy
PF	Phase-field
PIE	Post-irradiation examination
PKA	Primary Knock-on Atom
PNNL	Pacific Northwest National Laboratory
RERTR	Reduced enrichment of research and test reactors
RUSL	Resonant ultrasonic spectroscopy laser
RVE	Representative volume element
SEM	Scanning electron micrographs
SRIM	Stopping and range of ions in matter
TEM	Transmission electron microscope
TREAT	Transient Reactor Test
UC	Uranium carbide
USHPRR	United States High-Performance Research Reactor

Page intentionally left blank

1. INTRODUCTION

The in-pile performance of nuclear fuel depends on the as-fabricated microstructure, as well as the evolution of the microstructure throughout irradiation. As the physics that governs the microstructural evolution spans various time and spatial scales, fully understanding the fuel behavior inevitably involves atomic to mesoscale resolution that can be difficult to determine experimentally. Microstructure level modeling is suitable for these kinds of studies and can be utilized to increase the physical understanding of materials behavior and inform experimental efforts and observations. Ideally, microstructural-level modeling and simulations can be used in conjunction with experimental results to develop science-based material models that can provide both physical understanding to inform fabrication process control, as well as provide a valuable feedback mechanism between post-irradiation examination (PIE) results and fabrication parameters. The primary goals of the microstructure modeling effort are to (1) address critical microstructural questions and provide practical guidance to the fabricator via the fuel product specification and (2) provide mechanistic inputs for the existing fuel-performance code to improve its descriptive and predictive capability at the macroscopic scale.

In fiscal year (FY)-17, a Microstructural-Level Modeling Working Group coordination meeting was held at Pacific Northwest National Laboratory (PNNL), with members from Idaho National Laboratory (INL), Argonne National Laboratory (ANL), and PNNL in attendance, representing both the fuel qualification (FQ) and fuel fabrication (FF) pillars. As part of this coordination meeting, a long-term roadmap describing the microstructural modeling effort for U-Mo monolithic fuel irradiation behavior was established. This roadmap defined the work scope for FY-18 through FY-25 and showed the connections between this working group and the FF, the FQ, and the reactor conversion pillars and, more specifically, with the experimental working group. The use of multiscale modeling and simulations, as defined in this plan, is expected to generate knowledge and data that reduces the risks of unexpected fuel failures, reduces the need for additional irradiation testing to address microstructural variations resulting from fabrication process optimization, and will ultimately reduce fuel costs by potentially relaxing fabrication specifications. By synergistically coupling modeling and experiments, the investment in microstructural modeling of fuel behavior leverages the planned FF and FQ campaigns, enhancing the fundamental understanding of fuel behavior and improving interpretation of PIE data in support of FQ.

In this report, a summary of the work performed by the microstructural modeling working group is presented. This report will cover the following various aspects of the FY-21 work scope: (1) the effect of carbides on fuel performance; (2) gas diffusivity in different phases; (3) integration of microstructural fuel-performance modeling; (4) property degradation; (5) irradiation creep; and (6) historical analysis of microstructure data. Summaries of each are included in this document.

2. RESULTS

2.1 DART Modeling Integrating Lower Length Scale Computational Data

2.1.1 Introduction

One of the requirements for U-10Mo monolithic fuel to be qualified is a stable and predictable swelling behavior during irradiation [1,2]. Hence, an integrated modeling approach was developed as an effective tool to evaluate the effects of various operational and microstructural parameters on the swelling behavior of U-10Mo. This modeling approach utilizes the DART computational code [3–5] as the nexus to connect an engineering-scale fuel-performance model for fuel-swelling simulation with lower-scale and meso-scale computational methods. The work performed this FY focuses on simulating the effect of initial grain size and fission rate (FR) on U-10Mo swelling using the DART code. The descriptions of other methods utilized within this integrated approach for simulating U-10Mo monolithic fuels can be found in the literature [6–10].

A computational route for U-10Mo monolithic fuel has been added to DART since 2018 to separate its calculations from those of dispersion fuel systems. In this monolithic branch, fission-gas-induced swelling is simulated using the gas-release and swelling subroutine (GRASS) module [11], which is a rate-theory-based mechanistic fission-gas behavior simulation module. GRASS tracks bubble nucleation, resolution, and growth processes both within the grain and on grain boundaries (GBs) by solving a series of nonlinear differential equations. Besides the GRASS module, the DART monolithic branch incorporates a set of models for describing assorted physical, thermal, and mechanical processes occurring during irradiation, such as heat transfer from the fuel plate center to the coolant, fuel thermal conductivity degradation, Al-cladding corrosion, etc. The modularized and parallelized framework allows the code to simulate irradiation behaviors of a large-sized fuel plate without compromising detailed descriptions of microstructural evolution.

Many of the fission-gas behavior parameters used in the GRASS module cannot be measured experimentally with currently available techniques. In this study, some of the parameters were calculated through atomic-scale simulation methods—the surface energy of U-10Mo calculated using the density functional theory (DFT) method [7], and the gas-atom diffusivity calculated using the molecular dynamics (MD) method [8]. The rest of the parameters were calibrated using the bubble-size distributions measured from irradiated U-10Mo fuels. As the irradiation data used for calibrations were obtained from fuels irradiated at relatively low-fission densities ($< 3 \times 10^{21}$ f/cm³) and the target burnup of U-10Mo monolithic fuel may be higher than 7×10^{21} f/cm³ in some reactors [2], it is of great interest to examine whether the parameters that were calibrated using low-burnup measurement data can be applied to a high-burnup regime. Therefore, testing the applicability of the fission-gas behavior parameters at high burnup is carried out in this study.

This study investigated the effect of initial grain size on U-Mo swelling. Initial grain size impacts fuel swelling from three aspects: (1) the number of intergranular gas bubble nucleation sites, (2) the travel distance for gas atoms from the grain interior to boundaries, and (3) the kinetics of grain subdivision [12] [13]—subdivided fuel volume fractions as a function of fission density. The first two aspects have been modeled with GRASS, while the third aspect needs additional inputs. Because as-fabricated U-10Mo fuel foils exhibit very heterogeneous grain morphology [14][15] with the grain-size range spanning from a few microns to over a hundred microns, grain-size-specific recrystallization kinetics are required to simulate fission gas behavior during the grain subdivision process. Nevertheless, it is almost impossible to obtain grain-size-specific recrystallization kinetics from experiments, as it is extremely difficult to produce samples that are composed of a single grain size. As an alternative solution, grain-size-specific recrystallization kinetics were predicted using the phase-field (PF) method [5] and implemented into DART.

The effects of operational parameters on fuel swelling are either too difficult or too expensive to be studied with experimental techniques because many of these parameters are intricately interconnected. For instance, fuel temperature is strongly dependent on FR. On the other hand, a well-designed and validated computational code is suitable for separately studying and testing individual mechanisms proposed to explain the complex irradiation behavior in fuels. Separate effects of FR and fuel temperature are explored in this study, using the DART code equipped with the recalibrated fission-gas-behavior parameters and PF-informed recrystallization kinetics.

2.1.2 DART Code Structure and Primary Models

This section describes the general code structure and primary models of the DART monolithic branch, as well as the meshing scheme and the recrystallization model in the GRASS module.

2.1.2.1 DART Code Structure

As shown in Figure 1, separate branches were implemented in the DART code to simulate the irradiation behavior of three types of fuels (U-Mo monolithic, U-Mo/Al dispersion, and U₃Si₂-Al

dispersion fuels). The dispersion and monolithic branches share the same peripheral models to simulate the heat transfer process from the centerline of the fueled zone to the coolant. The two branches diverge from each other starting from the point at which the fueled zone calculations are performed. Detailed models for the fuel swelling calculation in the monolithic branch are described in Sections 2.1.2.2–2.1.2.4.

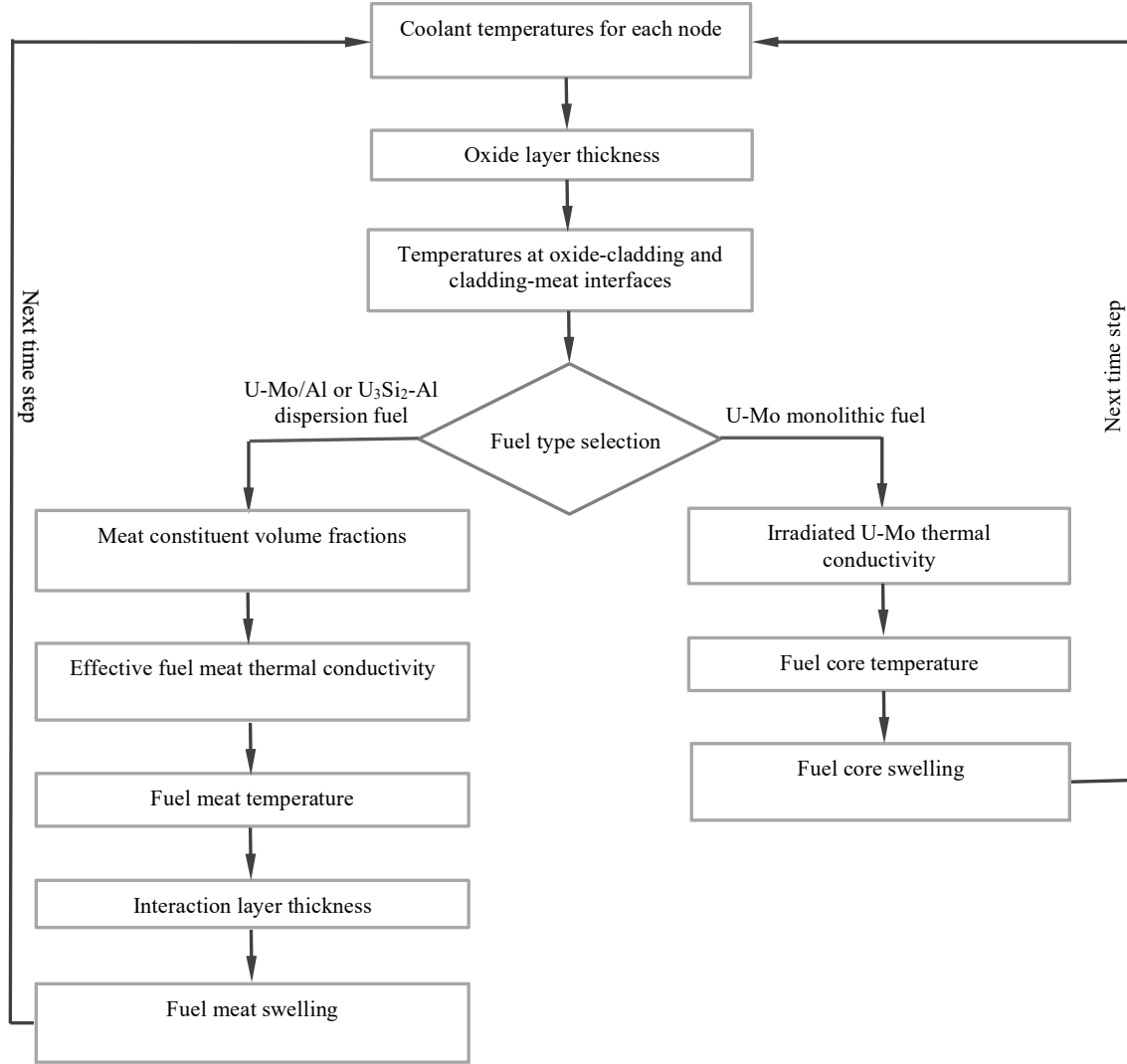


Figure 1. Flow chart of the DART computational code.

2.1.2.2 Fission-Gas-Behavior Models in the GRASS Module

GRASS includes models for intra- and intergranular fission-gas-bubble (FGB) behavior as well as a mechanistic description of the role of grain-edge interlinked porosity on releasing fission gases to triple points (grain corners) [11]. The primary physics models are described in [11] and summarized below:

1. Gas bubble nucleation

For intragranular gas, the rate of bubble nucleation is

$$N_{R-intra} = 16\pi \cdot f_N \cdot D_{Xe} \cdot r_{Xe} \cdot C_{Xe}^2 \quad (1)$$

where $N_{R-intra}$ is the intragranular bubble nucleation rate in $\text{cm}^{-3}\text{s}^{-1}$; f_N is the nucleation factor, describing the probability that two gas atoms come together to form a dimer; D_{Xe} is the diffusivity of a Xe

atom in U-Mo in cm^2/s ; $r_{Xe} = 2.16 \times 10^{-8}$ cm is the Xe atomic radius; C_{Xe} is the Xe atom concentration in U-Mo in cm^{-3} . This nucleation model assumes a dimer as the nucleus of gas bubbles, which is a reasonable practical treatment for handling the mathematical complexity in the simulation [16]. Values of f_N ranging from 10^{-7} to 10^{-2} were proposed for UO_2 in the literature [16]. This parameter is treated as an adjustable variable to be determined by fitting to measurement data in this study. D_{Xe} is the total gas-atom diffusivity, composed of intrinsic (thermal), and radiation-driven components [8]:

$$D_{Xe} = (1.28 \times 10^{-5}) \times \exp\left(-\frac{1.76}{kT}\right) + 5.07 \times 10^{-31} \times \dot{f} \quad (2)$$

where $k = 8.617 \times 10^{-5}$ is the Boltzmann constant in eV/K, T is the fuel temperature in K, and \dot{f} is the FR in $\text{cm}^{-3}\text{s}^{-1}$. Description of radiation-enhanced diffusion is still under development and will be included once it becomes available. Gas atoms have faster transport on GBs than in the lattice [17]. Hence, gas-atom diffusivity on GBs is approximated with D_{Xe} multiplied with an enhancement factor z . The z value for UO_2 is in the range of $10^2 - 10^7$, according to the estimation in [17].

For intergranular gas, the bubble nucleation rate is assumed to be proportional to that of intragranular gas:

$$N_{R-inter} = N_{R-intra} \cdot f_{N-GB} \quad (3)$$

where $N_{R-inter}$ is the intergranular-bubble nucleation rate in $\text{cm}^{-3}\text{s}^{-1}$; f_{N-GB} is the proportional factor. Bubble nucleation on GBs is much more rapid at the beginning of irradiation, but it reaches saturation much earlier than that in the lattice [18]. Therefore, f_{N-GB} can be much smaller than 1.

2. Radiation-induced bubble resolution

The radiation-induced bubble resolution model adopted in DART is

$$b = b_0 \cdot \dot{f} \cdot R \quad (4)$$

where b_0 is the bubble destruction probability, \dot{f} is the FR, and R is a piecewise function, representing different resolution modes for small and large gas bubbles. Eqn. 4 assumes gas-atom resolution from a bubble is isotropic, and single gas atoms are ejected [18]. This formula is applied to both intra- and intergranular gas bubbles in DART calculations.

The b_0 parameter can be estimated with the interaction volume of a thermal spike with bubbles [16,19]:

$$b_0 = Z_0^2 \cdot \mu_{ff} \quad (5)$$

where Z_0 is the radius of a thermal spike and μ_{ff} is the recoil length of fission fragments. Eqn. 5 was proposed to model the dynamic bubble resolution process in UO_2 [16][20], presuming that a bubble is either partially or totally “chipped away” when it is traversed by a fission fragment, and the efficiency of this sputtering mechanism is related to the interaction distance between the fission fragment path and the bubble [21,22]. For UO_2 , Z_0 is on the order of 1–7 nm [16], and μ_{ff} on the order of 6 μm [23]. Since the electrical resistance of U-Mo is much smaller than UO_2 [24], the radius of a thermal spike in U-Mo is expected to be smaller than that in UO_2 [19]. Therefore, although the dimension of a thermal spike was estimated to be ~ 13 nm in U-Mo in [24], the value of 1–7 nm is applied in this study as an estimation of Z_0 . The recoil length of μ_{ff} is ~ 5 μm , as determined by the stopping range of 80 MeV Xe in U-10Mo calculated using the stopping and range of ions in matter (SRIM) software [25]. Consequently, b_0 is on the order of 10^{-18} cm^3 .

The piecewise function R is a simplified version of the model proposed in [18]:

$$R = \begin{cases} 1 & r_b \leq \lambda \\ 1 - \left(\frac{r_b - r_{resol}}{r_b}\right)^3 & r_b > \lambda \end{cases} \quad (6)$$

where r_b in nm is the bubble radius, λ in nm is the gas-atom knock-out distance, and r_{resol} in nm is the thickness of the annulus within which all gas atoms are knocked out. The order of magnitude of λ (~10 nm) is borrowed from the value for UO₂ [20,26]. As suggested in Eqn. 6, when a gas bubble is struck by a fission fragment, all gas atoms are ejected if the bubble size is smaller than λ , and only the gas atoms in the outer shell of the bubble are ejected for a large bubble. Gover's MD study [20] on Xe-bubble resolution in UO₂ also suggests that (1) gas atoms are more likely to be knocked out in smaller bubbles, and (2) the probability for knocked-out atoms to be trapped back to bubbles increases with bubble size. Therefore, r_{resol} can be much smaller than λ , because of the trapping effect of large bubbles. Both λ and r_{resol} are handled as adjustable variables, and their values are determined by fitting to experimental data in this study using the order of magnitude described above. Eqn. 6 also indicates that the relative resolution effect of intergranular bubbles is much smaller than that of intragranular bubbles, given the larger size of intergranular bubbles. This inference is reasonable because GBs have strong trapping effects. A steep gas-atom concentration gradient is expected to exist next to GBs. Ejected gas atoms within the concentration gradient can be sucked back to the GBs immediately [27].

3. Gas bubble growth

The GRASS module consists of a set of coupled nonlinear differential equations for calculating the concentrations of gas atoms and bubbles in different sizes at various locations (bulk, grain face, grain edge, and grain corner). These equations take the form of [11,28]

$$\frac{dC_i}{dt} = -a_i C_i C_i - b_i C_i + c_i \quad (i = 1, \dots, N) \quad (7)$$

where C_i is the number of bubbles in the i -th size class per unit volume. $a_i = a_i(C_i)$ represents the rate at which bubbles grow out of the i -th size class because of coalescence with bubbles in the same class; $b_i = b_i(C_1, \dots, C_{i-1}, C_{i+1}, \dots, C_N)$ represents the rate at which bubbles are lost from the i -th size class because of coalescence with bubbles in other size classes and resolution, and $c_i = c_i(C_1, \dots, C_{i-1}, C_{i+1}, \dots, C_N)$ represents the rate at which bubbles are being added to the i -th size class because of fission-gas generation and gas atom release due to resolution (for $i = 1$), bubble nucleation (for $i = 2$), bubble growth resulting from bubble coalescence and diffusion of gas atoms into bubbles (for $i > 2$), and bubble shrinkage due to irradiation-induced resolution (for $i > 2$). Size distributions of intra- and inter-granular bubbles are obtained by solving the equations in Eqn. 7 for each type of bubble.

Bubble growth is generally achieved through the mechanism of bubble coalescence. The process of gas-atom diffusion into bubbles can also be understood as the coalescence between bubbles and gas atoms. The probability of an i bubble coalescing with a j bubble is [11]:

$$P_{ij} = 4\pi(r_i + r_j)(D_i + D_j) + \pi(r_i + r_j)^2 |v_j - v_i| \quad (8)$$

where P_{ij} is the coalescence probability in cm³/s; r_i and r_j in cm are the average radius of the bubbles in i -th and j -th size classes, respectively; D_i and D_j in cm²/s are the average diffusivity for the bubbles in i -th and j -th size classes, respectively; and v_i and v_j in cm/s are the velocity of the i bubble and j bubble moving in a temperature gradient, respectively. The first and second terms on the right-hand side of Eqn. 8 are the probability of bubble interaction due to random motion [29] and the biased migration (induced by a temperature gradient), respectively [11].

The size of the bubbles in i -th size class is calculated in GRASS at each time step using the current fuel temperature and stresses (including both hydrostatic stress and U-Mo surface energy) according to the hard-sphere equation of state (EOS) developed by Ronchi [30], which was strictly fitted to experimental data for argon, xenon, and krypton at high pressure.

4. Gas-atom migration path from the grain interior to boundaries

The model in GRASS assumes gas-atom generation occurs within grains as fission products. Gas atoms and bubbles migrate to GBs through diffusion induced by a concentration gradient and a

temperature gradient. The gas-atom migration process from the grain interior to boundaries consists of a series of intragranular trapping and irradiation-induced resolution. The flux of gas-atom diffusion arriving at GBs is solved using Speight's model in [31]. The derivation details are presented in [11], and the result is listed here:

$$R_I^g = 3(C_I - C_g) \cdot \left\{ \left[\frac{D_{Xe} b}{a^2(b+g)(t-t_0)} \right]^{0.5} - \frac{D_{Xe} b}{a^2(b+g)} \right\} \quad (9)$$

where R_I^g is the rate of fission-gas-atom diffusion to the GBs; C_I is the gas-atom concentration in grain at the beginning of this time step t_0 ; C_g is the gas-atom concentration at the grain boundary location; a is grain radius; D_{Xe} is gas-atom diffusivity in Eqn. 2; g is the probability of a gas atom in solution being captured by a bubble per second; and b is the resolution probability, defined in Eqn. 4.

When the grain-face coverage by intergranular bubbles reaches saturation, gas atoms diffuse from grain faces to grain edges. The saturation criterion (*FaceCovMax*) is set based on an ideal situation, in which the grain faces are occupied by equal-sized, close-packed, round, and touching bubbles, which gives the maximum areal coverage per unit area of grain boundary to be 0.907 [11]. In reality, intergranular bubbles are in lenticular shape and have a size distribution. Hence, the value of *FaceCovMax* can be less than 0.907.

The GRASS calculation for the gas-atom diffusion from grain faces to grain edges is based on the model developed in [32]. The rate of gas-atom diffusion to the edges is a function of both gas-atom diffusivities in the lattice and on GBs and grain morphology. In this study, the grains of the same size are approximated with identical tetrakaidecahedrons. Based on this geometry, the effective distance which gas atoms must travel before encountering an edge can be estimated.

Gas atoms on edges stay trapped at the edges until a gas release tunnel forms to allow gas atoms to be dumped into triple points (grain corners). Porosity tunnels along the grain edges were observed in UO₂ fuels. The probability of pore interlinkage is estimated using percolation theory [33] and is a function of grain size and edge bubble size distribution [11]. The criterion of pore tunnel formation is established using fuel swelling due to edge bubbles. The threshold value of fuel swelling due to edge bubbles (*LinkSwell*) is ~ 0.07 for UO₂ [11] and is treated as an adjustable variable in this study.

2.1.2.3 Meshing Scheme and Parallelization

A three-level meshing scheme is implemented in DART. Level-1 meshing ($[x, z]$ node), shown in Figure 2a and b, is defined for thermal and power calculations and is usually adapted from the settings in neutronics calculations. This level of calculations is executed outside of the GRASS module. Level-2 (k node) and level-3 (p zone) meshing are set up inside each (x, z) node to facilitate GRASS calculations. Each (x, z) node is divided into k regions (Figure 2 [c]), representing different grain types defined with grain size and aspect ratio. The volume of each k node is defined as

$$V_{(x,z,k)} = \Delta x \cdot \Delta z \cdot f_k \cdot y \quad (10)$$

where Δx and Δz are the dimensions of the (x, z) node in the x - and z -directions, respectively; f_k is the volume fraction of the k^{th} type of grain, and y is the thickness of the fuel foil.

Each k node is further divided into multiple segments (denoted as p zones) with equal volume ($V_{(x,y,k,p)}$) to track the progression of grain subdivision, as shown in Figure 2 (d). The equations described in Section 2.1.2.2 are solved for each p zone. In this study, the number of p zones is set to 50. The amount of p zones is selected to enable the code to satisfactorily replicate the PF-calculated recrystallization kinetics described in Section 2.1.2.3 without consuming excessive computational resources.

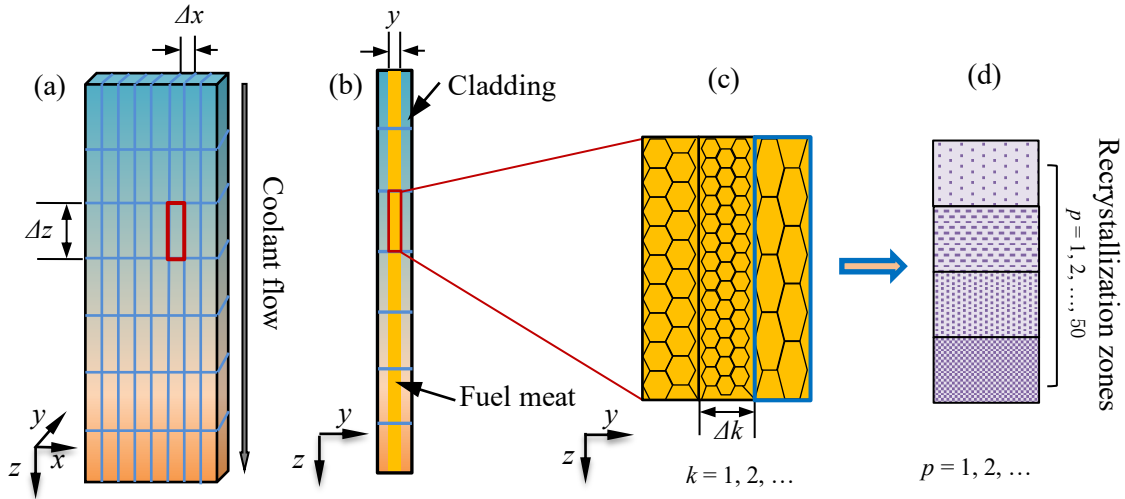


Figure 2. Schematic of (a) the meshing grid of a monolithic fuel plate, (b) side view of the plate and (c) meshing inside an (x, z) node, and (d) division inside each k node to track the progression of recrystallization.

In order to ease the computational burden of solving multiple sets of differential equations simultaneously for each of the thousands of nodes, the DART code was extended with message-passing interface-based data communication subroutines, so that data could be passed between nodes consistently as needed. A load-balancing subroutine was added to determine the number of processes allocated to a computational run and distribute the parallel load as evenly as possible. Currently, the GRASS module which performs the swelling calculations over the level-1 mesh elements was modified to run the calculations for each time step in parallel and redistribute the results when complete. Further development in the parallelization calculation scheme to extend the parallel computation to level-2 and level-3 mesh elements is undergoing.

2.1.2.4 Grain Subdivision Process

In this study, recrystallization kinetics for three grain sizes ($4.36 \mu\text{m}$, $8.5 \mu\text{m}$, and $17 \mu\text{m}$) were calculated using a set of two-dimensional (2D) polycrystalline structures in a PF model, which gives a more realistic representation of the material than a one-dimensional structure. A detailed description of the PF model can be found in [5]. The predicted recrystallization kinetics are displayed in Figure 3, showing apparent grain-size dependency. Larger size grains have lower volume fractions of recrystallized fuel at a given fission density. The effects of aspect ratio and FR on recrystallization are not studied explicitly in these simulations. Compared with the experimental data collected from irradiated U-10Mo dispersion fuel particles (average grain size: $\sim 4.5 \mu\text{m}$) [34], the calculated recrystallization kinetics are within the uncertainty range of the measurement data. An interfacing module was added into the DART code to read the tabulated recrystallization kinetics. The input and DART-calculated recrystallization kinetics are identical for all grain sizes, demonstrating the recrystallization kinetics were correctly implemented.

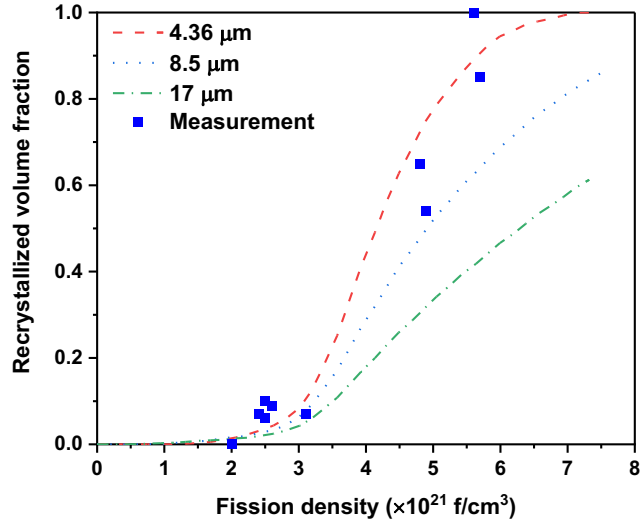


Figure 3. Recrystallization kinetics calculated with the PF method for grain sizes 4.36 μm , 8.5 μm , and 17 μm , compared with the measurement data collected from U-10Mo dispersion fuel particles with an average grain size of $\sim 4.5 \mu\text{m}$. The “measurement” data is from [33]

2.1.3 Calibration of Fission-Gas-Behavior Parameters

Calibration of fission-gas-behavior parameters in DART was performed by fitting to the intergranular-bubble-size distributions measured from samples irradiated to low-fission densities, prior to the onset of recrystallization. The reasons for using this specific type of data are explained as follow:

1. Bubble size distribution carries more information indicating the underlying mechanisms of fission gas behavior than averaged values and total porosity [35]
2. Data obtained prior to recrystallization record the information closer to the early stage of bubble formation and evolution without the influence of grain refinement.

The applicability of the fission-gas-behavior parameters calibrated with low-burnup data to the systems irradiated to high burnup is verified in Section 2.1.4 by comparing calculation results to the U-10Mo monolithic fuel-swelling correlation developed based on measured data [36].

2.1.3.1 Calculation Setup and Input Parameters

The data measured from three miniature-sized U-10Mo/Al dispersion fuel plates (mini plates) irradiated in the reduced enrichment of research and test reactors (RERTR)-5 test in the Advanced Test Reactor (ATR) were used for the calibration [37]. These plates were irradiated to relatively low-fission densities, and no recrystallization was observed in these plates. Moreover, although these plates are dispersion fuels, in which the fuel phase exists as particles embedded in an Al matrix, the fuel phase material is U-10Mo and is the same as that in monolithic plates. Therefore, there is no difference in material properties related to fission-gas behaviors, which ensures the validity of applying this set of data for calibration. The irradiation parameters of these three plates are listed in Table 1, and they are the input parameters for the calibration calculations. Three k nodes were defined within each (x, z) node, and each of them has the initial grain size of 4.36 μm , 8.5 μm , and 17 μm , respectively.

Table 1. Characteristics of three miniature U-10Mo/Al dispersion fuel plates irradiated in the RERTR-5 test, used for fission-gas-parameter calibration [37].

Plate ID	FD (f/cm^3)	Avg. FR ($f/cm^3 \cdot s$)	Temperature ($^{\circ}C$)	If recrystallized?	Initial grain size (μm)	Avg. bubble diameter (μm)
V6018G	2.31×10^{21}	2.3×10^{14}	121	No	4.9 ± 2.0	0.14
V6019G	2.91×10^{21}	2.9×10^{14}	142	No	8.5 ± 3.6	0.16
V8005B	2.41×10^{21}	2.4×10^{14}	170	No	8.1 ± 4.5	0.16

2.1.3.2 Calibration Results

The optimized value set of fission-gas-behavior parameters are listed in Table 2. Some of the data were obtained through atomic-scale simulation, and other parameter values were selected by fitting the calculated intergranular-bubble-size distributions with measurement data. The bounding limits of each fitted parameter were taken from the literature and described in Section 2.1.2.2.

Table 2. Optimized value set of calibrated key fission-gas-behavior parameters.

Parameter	Description	Unit	Best value obtained	Ref.	Bounding limits	Ref.
D_0	Linear coefficient of radiation-driven gas-atom diffusivity	cm^5	5×10^{-31}	[8]	N/A	
Q	Activation energy for intrinsic gas-atom diffusion	cal	40559	[8]	N/A	
z	GB diffusion enhancement factor	N/A	3×10^4	This work	$10^2 - 10^7$	[17]
f_n	The probability for two gas atoms to come together and become a bubble in lattice	N/A	2×10^{-7}	This work	$10^{-7} - 10^{-2}$	[16]
f_{n-GB}	Adjustment factor for	N/A	6×10^{-10}	This work	can be $\ll 1$	[18]

Parameter	Description	Unit	Best value obtained	Ref.	Bounding limits	Ref.
	Bubble nucleation probability on GB					
γ_{U10Mo}	Surface energy of U-10Mo	dyne/cm	1850	[7]	N/A	
b_0	The probability for a bubble interacting with fission fragments	cm ³	2×10^{-18}	This work	on the order of 10^{-18}	Refs. of Eqn. 5
λ	The gas-atom knock-out distance from bubbles	cm	5×10^{-7}	This work	~ 10 nm	[20,26]
r_{resol}	The destructed outer-shell thickness of bubbles	cm	3×10^{-9}	This work	< 10 nm	Refs. of Eqn. 6

The comparisons between the fitted and measured intergranular-bubble-size distributions are presented in Figure 4 for all three plates, in which the calibrated and measured peak bubble sizes reasonably agree with each other. Calculation results of both 4.36 μm and 8.5 μm grains were employed, as they are close to the observed fuel grain sizes. Only the calculated bubble size distributions on grain faces are plotted in Figure 4, although calculated intergranular bubbles include bubbles at grain edges and triple points as well. This approximation is reasonable because the bubbles that form at other locations are much fewer and smaller than those on grain faces at the irradiation conditions of the three plates.

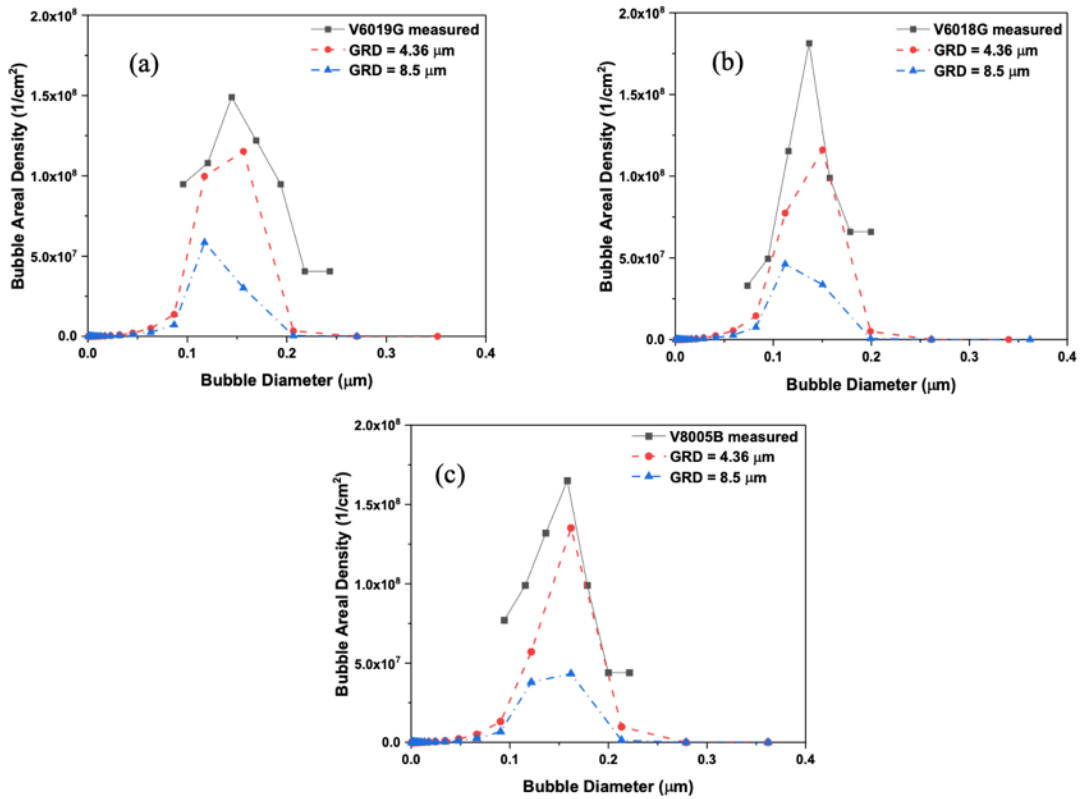


Figure 4. Comparisons of measured and calibrated intergranular-bubble-size distributions in plates (a) V6018G, (b) V6019G, and (c) V8005B.

The primary criterion of the calibration is to obtain the best match between the peak positions of calibrated and measured intergranular-bubble-size distributions for both grain sizes in all three plates. The differences in bubble densities are less important in comparison with the peak bubble size because the experimental limitations, such as undulating sample surface and limited number of images to obtain good counting statistics, can lead to large uncertainties in bubble density. For instance, the uncertainties for the measured data in Figure 4 are $\pm 10\%$ near peak position and $\pm 50\%$ at both ends of the distributions [37]. Besides the measurement uncertainties, many other sources can contribute to the peak bubble density differences. An apparent one is related to the density conversion process. The experimental data was initially measured as linear bubble density (number of bubbles per unit grain boundary length), while the calculation results were expressed as volume densities. For the comparison purpose, both experimental and calculated quantities were converted to areal density. To achieve the best accuracy of density conversion, it is required that the bubbles are homogeneously distributed in the material [38]. Such an ideal condition does not exist in the fuel plates for calibration. Moreover, other assumptions that were applied for the conversions, such as the shape of grains and packing patterns of bubbles, may not reflect reality well. All these uncertainty factors together may make the converted density deviate from real data. The results in Figure 4 show that the calculated peak bubble densities are two to three times lower than the measured data. Considering the uncertainties described above, this discrepancy is deemed acceptable.

Besides the bubble size distributions, the calibrated parameter set was also verified by comparing calculated and measured average bubble diameters, visible porosities, and swelling, as shown in Figure 5. A cutoff diameter of 100 nm was applied when estimating the average bubble diameters and visible

porosities using calculated bubble size distributions, which is consistent with the resolution limit of the scanning electron micrographs (SEM) used for bubble measurement [37].

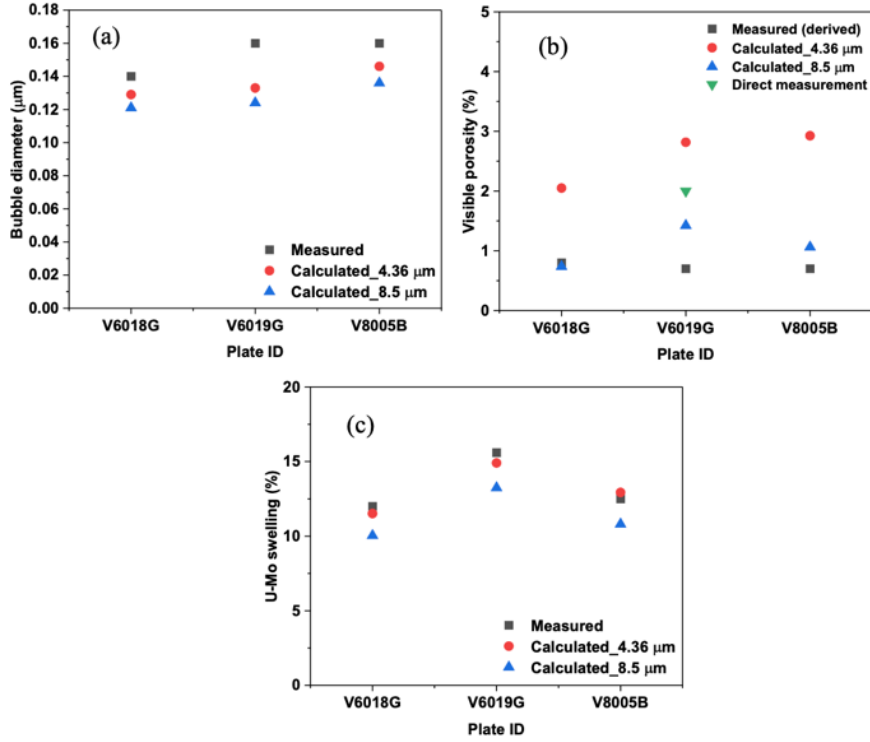


Figure 5. Comparison of measured and calibrated (a) bubble diameter, (b) visible porosity, and (c) U-Mo swelling. The measured data are from [37].

The average bubble size and visible porosity were therefore calculated according to the equations below

$$\bar{d} = \frac{\sum 2C_i r_i}{\sum C_i} \quad (r_i > 50 \text{ nm}) \quad (11)$$

$$p_{\text{visible}} = 100 \times \sum \frac{4\pi}{3} C_i r_i^3 \quad (r_i > 50 \text{ nm}) \quad (12)$$

where \bar{d} is the average bubble diameter in cm, p_{visible} is the visible porosity in percentage, and C_i in $1/\text{cm}^3$ and r_i in cm are the number density and average radius of the bubbles in the size classes whose bubble radii are larger than 50 nm, respectively.

Fuel swelling includes the contributions from both gaseous and solid fission products. The swelling by fission gases is calculated through the summation of all bubble volumes, and solid-fission-product swelling is proportional to fission density and expressed as [39]:

$$\left(\frac{\Delta V}{V_0}\right)_{\text{solid}} = 4.0 \times FD \quad (13)$$

where $\left(\frac{\Delta V}{V_0}\right)_{\text{solid}}$ is the swelling by solid fission products in percentage, and FD is the fission density in 10^{21} f/cm^3 .

As shown in Figure 5 (a), the calculated bubble sizes are slightly smaller than the measured data for these plates (differences $\leq 25\%$), which is consistent with the differences in bubble size distributions shown in Figure 4 and can be explained with the uncertainties associated with measurements. Figure 5 (b)

shows that although the calculated visible porosities are generally higher than the measured quantities, the difference between calculated and direct measurement data is small. Directly measured porosity is only available for plate V6019G, and the other measurement data were derived based on the conversion from the bubble density per unit length of GBs to volumetric density [37]. As explained earlier, such conversion may introduce notable errors in the resultant porosity. This can be demonstrated with the difference between derived and direct measured values of plate V6019G. Considering the uncertainties associated with derived data, the agreement between calculated and measured data in Figure 5(b) is satisfactory. For the comparison of total swelling shown in Figure 5(c), the calculated values are close to the measured data (differences $\leq 15\%$). The overall agreements exhibited in Figure 5 confirm the parameter value set in Table 2 which, when applied to the models detailed in Section 2.1.2, can be used to describe fission-gas behavior in U-10Mo irradiated at the conditions similar to those listed in Table 1.

It is also revealed in Figure 4 and Figure 5 that the bubbles in 8.5- μm -grain fuel have a larger size and correspondingly lower bubble density than those in the 4.36- μm -grain fuel. These differences in bubble characteristics are due to lower grain boundary area per unit fuel volume in the larger grain case (i.e., reduced number of intergranular-bubble nucleation sites).

2.1.3.3 Sensitivity Study of the Calibrated Value Set

As many of the parameter values in Table 2 are not directly measurable, the uncertainties of the fitted values are unknown, as well as their combined effects on the calculated bubble characteristics. Therefore, it is necessary to perform sensitivity studies on the calibrated parameter set to examine how the uncertainties in individual parameters can quantitatively impact outputs. The one-at-time approach was taken in this work because it is practical and easy to detect whether a gas-behavior mechanism functions as expected. The intergranular-bubble-size distributions for 4.36- μm grains using the data from plate V6018G were calculated and compared when varying the values of each parameter.

Figure 6 shows the sensitivity study results of two diffusion-related parameters: linear coefficient of radiation-driven gas-atom diffusivity (D_0) and grain boundary diffusion enhancement factor (z). D_0 universally impacts the diffusivities of all gas atoms in the system, while the z factor only changes gas-atom diffusivity on GBs. Although the value of D_0 was computed through MD simulations, the sensitivity study was performed to investigate the potential uncertainty of missing the component of radiation-enhanced diffusion in Eqn. 2. The comparison in Figure 6(a) clearly shows that the peaks of the intergranular-bubble-size distribution move towards the right while the profiles become flattened with the increased D_0 , indicating more gas atoms diffused to GBs, which is confirmed with the gas-atom distribution profile in the inset of Figure 6(a). The greater bubble coalescence probability (Eqn. 8) due to a higher D_0 also assists these changes. Similar changes were observed in Figure 6(b) when the z factor increases.

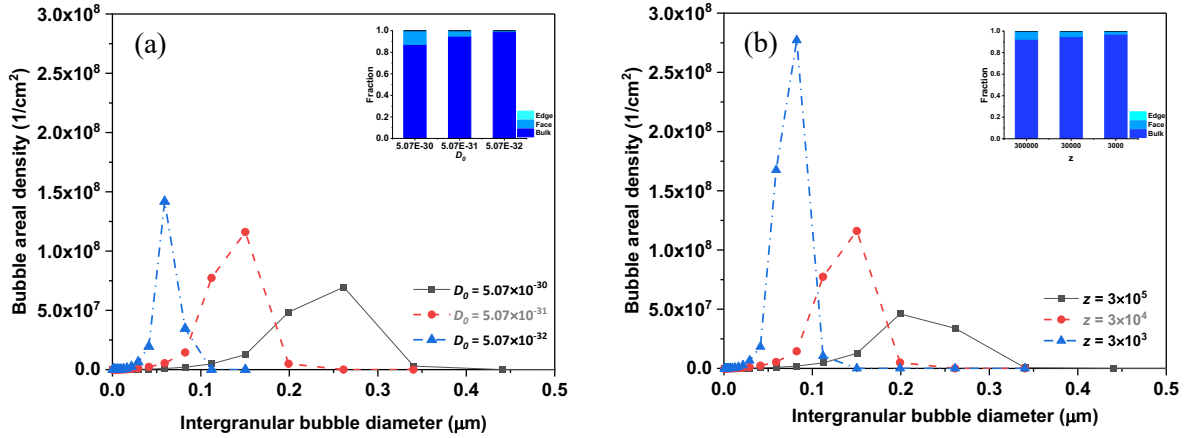


Figure 6. Sensitivity study results of the parameters related to the gas-atom diffusion process: (a) D_0 and (b) z . The insets show the breakdown of gas atoms located in bulk, on grain faces, and on grain edges. The calculations were performed using the input parameters of V6018G and grain size of 4.36 μm. The results calculated using the optimized values in Table 2 are presented in both figures: “ $D_0 = 5.07 \times 10^{-31}$ ” in (a) and “ $z = 3 \times 10^4$ ” in (b), respectively.

Both the general bubble nucleation probability (f_n) and the adjustment factor for nucleation probability on grain boundaries (f_{n-GB}) were investigated for their effects on intergranular-bubble behaviors. The results in Figure 7 show that increasing either f_n or f_{n-GB} shifts the bubble size distribution profiles toward the left (i.e., reducing the peak intergranular-bubble-size). Although increasing f_n inflates the gas-bubble nucleation probabilities both in the lattice and on GBs, the extent of the increase is relatively higher for gas atoms in the lattice according to Eqn. 3. Consequently, more gas atoms are trapped in intragranular bubbles, and fewer gas atoms arrive at GBs, as illustrated in the inset of Figure 7(a). The effect of this weakened gas-atom flux from the lattice to GBs is compounded by the increased nucleation rate at GBs. Both effects make it difficult for intergranular bubbles to grow. The opposite trend can be observed when f_n is reduced. The results in Figure 7(b) show that when f_{n-GB} is increased, intergranular-bubble density increases significantly with shrunken bubble size. The inset in Figure 7(b) manifests that the fraction of the gas atoms arriving GBs reduces with the increase of f_{n-GB} , indicating the weakened sink strength of GBs at this condition.

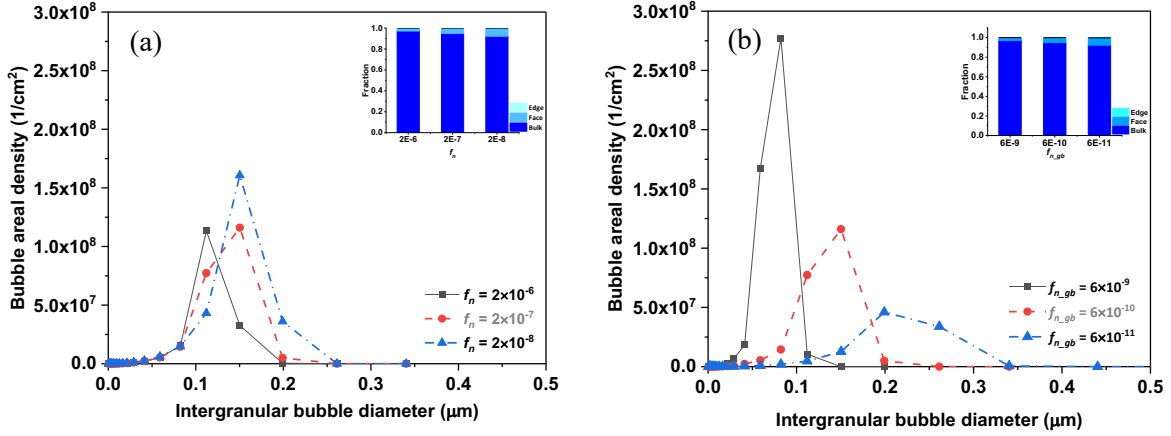


Figure 7. Sensitivity study results of the parameters related to the bubble nucleation process: (a) f_n and (b) f_{n-GB} . The insets show the breakdown of gas atoms located in bulk, on grain faces, and on grain edges. The calculations were performed using the input parameters of V6018G and grain size of 4.36 μm. The results calculated using the optimized values in Table 2 are presented in both figures: “ $f_n = 2 \times 10^{-6}$ ” in (a) and “ $f_{n-GB} = 6 \times 10^{-10}$ ” in (b), respectively.

The other important parameters investigated are b_0 , λ , and r_{resol} , all of which are related to the bubble resolution process. b_0 is the probability for a bubble interacting with fission fragments, impacting all gas bubbles in the system. A larger b_0 means gas atoms are more likely to be knocked out from existing bubbles by a transverse fission fragment, and more gas atoms become available during a short period (before the system achieves a new equilibrium state) for nucleating new bubbles. In this case, more bubbles can nucleate but are difficult to grow, as presented in Figure 8(a). A reversed trend can be observed with a reduced b_0 . Two competing mechanisms are involved in the change of b_0 . For instance, when b_0 is reduced: (1) the sink strength of GBs is enhanced by large bubble formation and growth, and (2) lattice gas atoms are more likely to be trapped within intragranular bubbles. The result shown in the inset of Figure 8(a) indicates that between the two, the former effect prevails over the latter one.

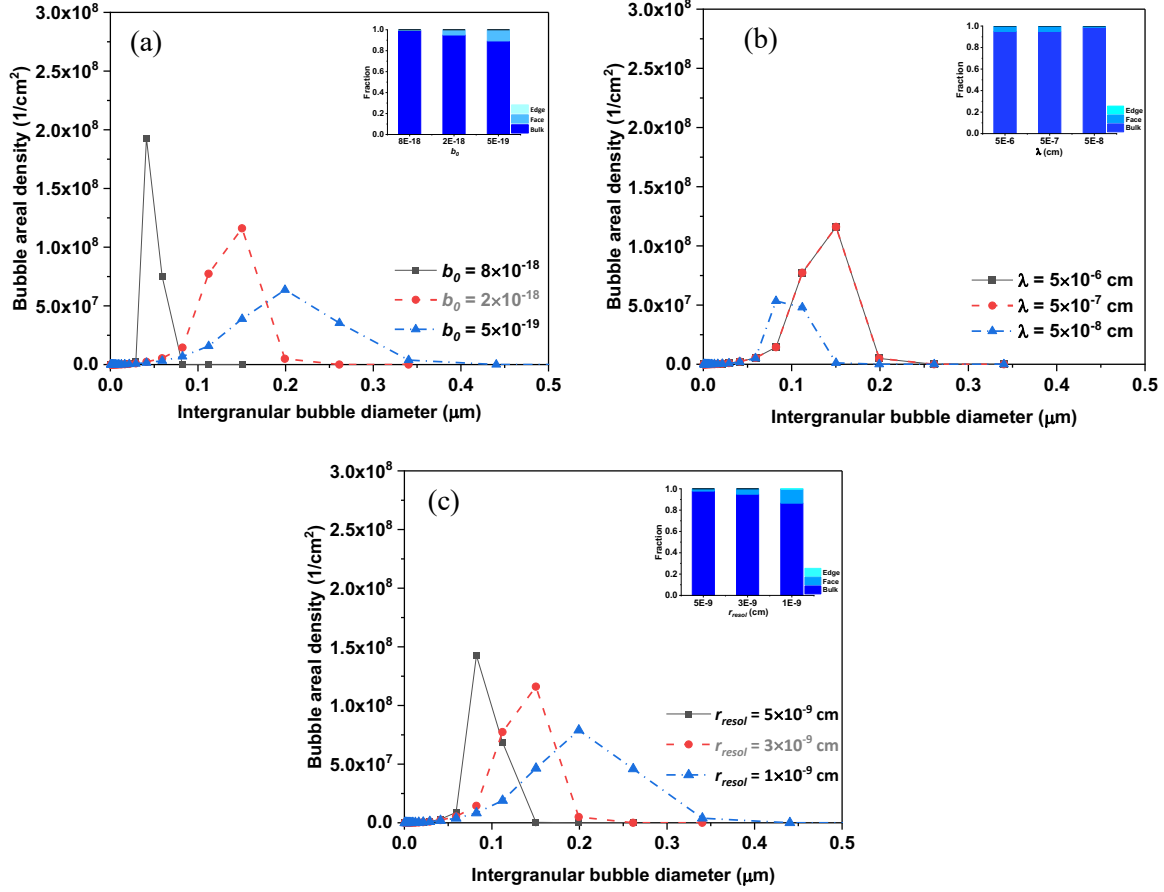


Figure 8. Sensitivity study results of the parameters related to radiation-induced resolution process: (a) b_0 , (b) λ , and (c) r_{resol} . The insets show the breakdown of gas atoms located in bulk, on grain faces, and on grain edges. The calculations were performed using the input parameters of V6018G and grain size of 4.36 μm. The results calculated using the optimized values in Table 2 are presented in all figures: “ $b_0 = 2 \times 10^{-18}$ ” in (a), “ $\lambda = 5 \times 10^{-7}$ cm” in (b), and “ $r_{resol} = 3 \times 10^{-9}$ cm” in (c), respectively.

The gas-atom knock-out distance from bubbles λ is applied as an approximate cutoff threshold for separating different bubble destruction modes as a function of bubble size in Eqn. 6. Figure 8(b) shows that the results do not change when λ varies from 5×10^{-7} cm to 5×10^{-6} cm. This is because of two facts: (1) the bubble destruction mode remains the same for all intragranular bubbles, as they are smaller than 5×10^{-7} cm; and (2) the increase of λ only slightly promoted the resolution of small intergranular bubbles ($\sim 0.1\%$ of total gas atoms in bubbles), whose influence on results was negligible. However, reducing this variable to 5×10^{-8} cm significantly lowered the size and density of intergranular bubbles because the destruction efficiency of intragranular bubbles was greatly reduced, leading to much fewer gas atoms arriving at GBs.

r_{resol} is the thickness of the destroyed bubble annulus when the bubble is larger than λ according to Eqn. 6. Its variation only impacts intergranular bubbles, as the majority of the intragranular bubbles are smaller than λ (peak intragranular bubble radius: ~ 1 nm). Figure 8(c) shows that intergranular-bubble characteristics are sensitive to r_{resol} . A thicker r_{resol} (5×10^{-9} cm vs. 3×10^{-9} cm) makes it difficult for bubbles to grow and reduces the number of gas atoms at GBs.

For a complex computational code like DART, the sensitivity study performed here only investigates a subset of the assumptions and parameter values applied in the code. These results help to test whether the models function as expected and provide information on the primary parameters that most impact the results. However, a complete understanding of the uncertainties of the model inputs has not yet been obtained. For example, as discussed in a previous study [4], the calibrated fission-gas-parameter values like the set listed in Table 2 are not unique. Other combinations of the values may also yield satisfactory calibration results because some of the underlying mechanisms impacting the processes of FGB formation and growth counteract each other, yet the interval of parameter values within which equivalent results can be achieved is not quantified. Moreover, the sensitivity study performed in this study assumes independence between the tested variables, which may not be the case for some variables. It is also possible that the perturbation of two or more parameters simultaneously can cause variation in the results greater than that of varying individual parameters alone, due to interactions between models. These uncertainties will be further investigated with a global sensitivity study in the future to explore the space of the parameter values.

2.1.4 U-Mo Swelling Behavior up to High-Fission Density for Various Grain Sizes

U-Mo swelling behavior up to high-fission density was calculated using a constant FR of 5.94×10^{14} f/(cm³·s) for three grain sizes: 4.36 μm, 8.5 μm, and 17 μm. The average fuel centerline temperatures were maintained at about 150°C for all cases by slightly altering coolant inlet temperatures. Fuel swelling as a function of fission density is illustrated in Figure 9. Generally, the fuels with larger grains have less swelling. The curves exhibit a clear transition in swelling rate at around 3×10^{21} f/cm³— 3.5×10^{21} f/cm³—becoming steeper after passing the transition fission densities due to the inception of grain subdivision. Calculated fuel swelling is compared with the swelling correlation developed with in-pile irradiation data of monolithic U-Mo fuels [36] in Figure 9. All calculated swelling curves stay within the vicinity of the swelling correlation, indicating that the calculation results are reasonable, provided that current calculations were performed with simplifying assumptions such as constant FR and limited representation of grain morphology (no consideration of grain shape effect), etc.

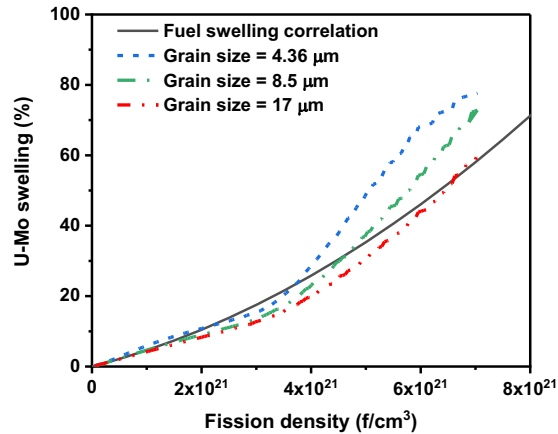


Figure 9. U-10Mo swelling as a function of fission density for three grain sizes, compared with the U-10Mo monolithic fuel-swelling correlation from [36].

2.1.5 Fission-Rate and Fuel-Temperature Effects

In order to examine the FR effect on U-Mo fuel swelling, calculations were performed for three constant fission rates: $8.92 \times 10^{14} \text{ f}/(\text{cm}^3 \cdot \text{s})$, $5.94 \times 10^{14} \text{ f}/(\text{cm}^3 \cdot \text{s})$, and $2.97 \times 10^{14} \text{ f}/(\text{cm}^3 \cdot \text{s})$, representing the high, medium, and low FRs in the RERTR-12 plates, respectively [40,41]. A grain size of $8.5 \mu\text{m}$ was used in all calculations. All other operating conditions were kept the same. The comparison of the calculated fuel swelling, presented in Figure 10, shows that the swelling behaviors of these three cases were very similar at low-fission densities and the deviations started at $\sim 3 \times 10^{21} \text{ f}/\text{cm}^3$ when the recrystallization process began. The discrepancies between the three curves become larger with the increase of fission density. For instance, when the FR increases from $2.97 \times 10^{14} \text{ f}/(\text{cm}^3 \cdot \text{s})$ to $8.92 \times 10^{14} \text{ f}/(\text{cm}^3 \cdot \text{s})$, the swelling increases from 38.54% to 54.91% at the fission density of $6 \times 10^{21} \text{ f}/\text{cm}^3$.

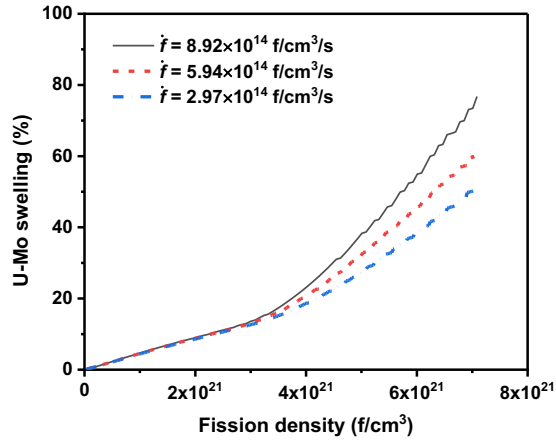


Figure 10. U-10Mo swelling as a function of fission density calculated with grain size = $8.5 \mu\text{m}$ for a variation of constant fission rates: $8.92 \times 10^{14} \text{ f}/(\text{cm}^3 \cdot \text{s})$, $5.94 \times 10^{14} \text{ f}/(\text{cm}^3 \cdot \text{s})$, and $2.97 \times 10^{14} \text{ f}/(\text{cm}^3 \cdot \text{s})$.

In order to understand the trends observed in Figure 10, it is important to track down the parameters and operating conditions that are related to FR. Both gas-atom diffusion and bubble resolution are enhanced for a similar order of magnitude when FR increases. These two fission-gas-behavior processes have competing effects on bubble formation and growth. Hence, the increase of gas-atom diffusivity and the increase in bubble resolution rate due to the FR increase does not necessarily change fuel swelling behavior. The simulation results shown in Figure 11(a) demonstrate that when FR and fuel temperature were kept the same, increasing either D_0 or b_0 one order of magnitude barely changed fuel swelling. On the other hand, fuel temperature is also elevated when the FR increases. Calculations were performed by varying fuel temperature only while keeping all other parameters unchanged. The results in Figure 11(b) show that a difference of 34°C can result in a change of fuel swelling from 45.7% to 54.5% at $6 \times 10^{21} \text{ f}/\text{cm}^3$. Therefore, based on the results in Figure 11, it is concluded that the apparent FR effect shown in Figure 10 was mainly caused by the changes in fuel temperature, not the variation of gas-atom diffusivity and bubble resolution rate. Note that the fuel-temperature effect presented in Figure 11(b) is not due to increased thermal diffusion of gas atoms, which is negligible comparing to radiation-driven diffusion. Instead, it is induced by the correlation between bubble volume and temperature, described in the EOS.

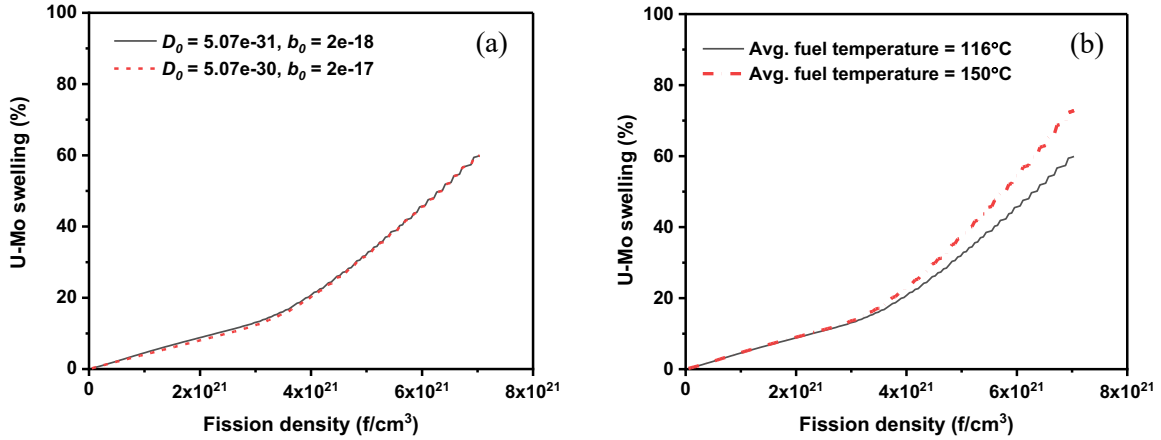


Figure 11. U-10Mo swelling as a function of fission density calculated with grain size = 8.5 μm and constant FR = 5.94×10^{14} f/($\text{cm}^3 \cdot \text{s}$) to examine the effects of (a) the combination of D_0 and b_0 and (b) fuel temperature.

2.1.6 Conclusions

The DART fuel-performance code has been updated to simulate U-10Mo monolithic fuel-swelling behavior during irradiation. The parameters used in the rate-theory-based mechanistic model were either calibrated using measured FGB characteristics or provided by lower length scale simulations. Additionally, PF-predicted U-10Mo grain-subdivision kinetics for various grain sizes were implemented to simulate fuel-swelling behavior at high burnup. The effects of initial grain size on fuel swelling were investigated. The results show that the calculated swelling of initial grain sizes from 4.36 μm to 17 μm is in good agreement with the U-10Mo swelling correlation developed with experimental data, and larger grains have lower swelling rates. Higher fuel temperature or FR leads to greater swelling. Further examination by isolating the variation of fuel temperature from that of radiation-enhanced processes (gas diffusion and resolution) revealed that the increased fuel swelling induced by elevated FR is due to temperature effect but not the augmentations of gas-atom diffusivity and bubble resolution rate.

2.2 Thermal Conductivity Degradation Model for U-10Mo

2.2.1 Introduction

Thermal conductivity is a critical nuclear fuel property that governs both the performance and safety of a nuclear reactor. Also, it is a well-known fact that irradiation in nuclear fuel can cause several microstructural changes, and these changes can cause a significant reduction in the thermal conductivity of the irradiated nuclear fuel. Hence, it is essential to fully understand the thermal conductivity of the U-10Mo fuels as a function of burnup and temperature before their utilization in high-performance research reactors. However, the experimental determination of the thermal conductivity of the irradiated fuels is difficult due to the time and cost involved. Moreover, it is not easy to separate phenomena in experimental measurements. Therefore, in this work, we model the thermal conductivity of the irradiated U-10Mo fuel as a function of burnup considering the effects of point defects (vacancies and interstitials), intergranular bubbles, intragranular bubbles, and the GBs on the thermal conductivity of the U-10Mo fuels.

Recently, a general thermal conductivity degradation model for the metallic alloy systems has been developed by Zhou et al. [42] considering the microstructural changes due to irradiation such as the point defects, intragranular gas bubbles, intergranular gas bubbles, and GBs. They have also modeled the thermal conductivity degradation in U-10Mo as a case study. However, one of the main shortcomings of that work has been the lack of reliable microstructural information for the intragranular and intergranular gas bubbles. The polynomial fits for various parameters to predict the thermal conductivity degradation factors were based on few experimental data points. The experimental studies have revealed that the intergranular gas bubbles presence at higher fission densities is significantly higher than intragranular gas bubbles. Therefore, the intergranular bubbles should be a dominant factor adversely affecting the thermal transport of irradiated U-10Mo fuel. Whereas, the Zhou et al. [42] model predicted intragranular bubbles to be the dominant factor in the thermal conductivity degradation at higher fission densities. Moreover, the saturation concentration of the point defects was significantly higher than observed experimentally. Therefore, in this work, we predict the thermal conductivity of irradiated U-10Mo by applying the model developed by Zhou et al. [42], using the microstructural data for the intergranular and intragranular porosity from the DART thermal dispersion fuel-performance code.

2.2.2 Methodology

This section provides a detailed description of the methodology followed to model the thermal degradation in U-10Mo fuel. The total thermal conductivity in a metallic material is the sum of contributions due to phonons (k_{ph}) and electrons (k_e). The phonon contribution to the thermal conductivity in alpha-uranium for a temperature range of 400–933 K is shown to be ~ 2%-9% [43]. Hence, in this work, we only consider the effect of irradiation-induced defects on the electronic thermal conductivity. It is worth noting that the assumption of neglecting the phonon contribution will break down at lower temperatures. The electronic contribution of thermal conductivity (k_e) is related to the electrical resistivity by the Wiedemann-Franz law as given below.

$$K_e = L_o \times T \times \sigma(T) \quad (14)$$

where L_o is the Lorentz factor ($2.44 \times 10^{-8} W\Omega K^{-2}$), T is temperature, and $\sigma(T)$ is the electrical conductivity as a function of temperature. The electrical conductivity is nothing but the reciprocal of the electrical resistivity (ρ).

2.2.2.1 Total Thermal Conductivity Degradation Factor

Following Lucuta et al. [44] and Zhou et al. [42], a pragmatic approach is proposed to model the thermal conductivity of the irradiated U-10Mo fuel. The total thermal conductivity degradation factor (f_{total}) is the product of the degradation factor due to the intragranular bubbles (f_{intra}), intergranular bubbles (f_{inter}), grain boundary (f_{gb}), and point defects (f_{pd}) as shown in Eqn. 15

$$f_{total} = f_{intra} \times f_{inter+gb} \times f_{pd} \quad (15)$$

The effective thermal conductivity (k_{eff}) of the irradiated U-10Mo as a function of fission density/burnup is obtained by multiplying the thermal conductivity of the unirradiated U-10Mo (k_o) with the total thermal conductivity degradation factor corresponding to the given temperature and fission density.

$$k_{eff} = f_{total} k_o \quad (16)$$

It must be noted that this degradation is targeted at U-10Mo, and currently, the degradation behavior is assumed to vary negligibly over the relevant compositional range in UMo fuels.

2.2.2.2 Intragranular Bubble Degradation Factor as a Function of Fission Density

Irradiation of U-10Mo produces fission products such as xenon (Xe), and these fission products form bubbles at high burnup, resulting in intragranular and intergranular bubbles [45][39][46]. The thermal conductivity of the gas bubbles is orders of magnitude lower than the fuel elements and thus can reduce the thermal conductivity significantly. Several analytical and empirical expressions have been proposed to model the thermal conductivity degradation due to uniformly distributed intragranular bubbles. These analytical expressions include the Maxwell-Eucken [46], Bruggeman model [47], Cunningham and Peddicord [48], and Bauer model [49]. Zhou et al. [42] has shown that the Bauer model captures the effect of intragranular bubbles on the thermal conductivity of uranium-based alloys. Therefore, we model the thermal conductivity degradation factor f_{intra} due to intragranular bubbles using Bauer's model [49]. According to this model, the f_{intra} as a function of the intragranular porosity (p_{intra}) is given as follows,

$$f_{intra} = (1 - p_{intra})^{2.58} \quad (17)$$

2.2.2.3 Grain Boundary and Intergranular-Bubble Degradation Factor as a Function of Fission Density

GBs in a polycrystalline material can act as scattering sites during thermal transport and hinder heat conduction. During the irradiation of material, the FGBs are formed at the GBs. For example, in U-10Mo, Kim et al. [37] have demonstrated the intergranular bubble of diameter $\sim 0.15 \mu m$ at a separation of $\sim 0.4 \mu m$. The coupled effect of the grain boundary and the intergranular bubbles can significantly reduce the thermal transport in U-10Mo fuel. However, Zhou et al. [42] has shown that the thermal conductivity degradation due to the grain boundary alone is $<1\%$. Therefore, in this work, we neglect the effect of the GBs and model the thermal conductivity degradation due to intergranular gas bubbles only. The thermal conductivity degradation due to intergranular bubbles (f_{inter}) as a function of the porosity of intergranular bubbles (p_{inter}) is given by connecting the Bauer model [49] (Eqn. 17) and the analytical model of electrical resistors developed for UO_2 by Tonks [50].

$$f_{inter} = \left(\frac{1}{1+3.20p_{inter}} \right) \quad (18)$$

2.2.2.4 Point Defect Thermal Conductivity Degradation Factor

The point defects are ubiquitous and can scatter the phonons and electrons, causing a significant reduction in the thermal conductivity of irradiated materials, especially at low temperatures or at high-defect concentrations. Four different types of point defects considered in this study, including vacancies and fission products xenon, krypton, and helium. Four different case studies with a varying population of the point defects for a saturation concentration of 1×10^{-4} were considered. The varying populations are grouped into case1, case2, case3, and case4. In case1, the concentration of each type of point defect is considered the same amount. Whereas, in other cases, the concentrations of point defects are 50% of Vac and 50% of Xe (case2); 25% of Vac and 75% of Xe (case3); and 30% of Vac, 60% of Xe, and 10% of Kr (case4). The thermal conductivity degradation factor due to point defects, (f_{pd}), is a function of the concentration of the defects and the temperature and is given as:

$$f_{pd}(c, T) \approx \frac{k(c, T)}{k(0, T)} \approx \frac{\rho(0, T)}{\rho(c, T)} \quad (19)$$

where c is the concentration of each type of point defect, $k(0, T)$, also written as $k_o(T)$, and $\rho(0, T)$,, are the thermal conductivity and the resistivity of unirradiated U-10Mo fuel as a function of temperature, and $k(c, T)$ and $\rho(c, T)$ are the thermal conductivity and resistivity for the U-10Mo fuel with the point defects with concentration c . In this work, the resistivity of a single-phase metal is taken from the previously published work by Zhou et al. [42] and is given by the expressions shown below.

$$\rho(T) = \frac{\rho_{int}(T) + \rho_{res}}{1 + \frac{\rho_{int}(T)}{\rho_{sat}}} \quad (20)$$

where, $\rho_{int}(T)$ is the intrinsic resistivity due to the electron scattering with other electrons and phonons, ρ_{res} is the residual resistivity at 0 K, which is due to defects including alloying, impurities, and irradiation-induced defects, and ρ_{sat} is the saturation resistivity. It is worth noting that the ρ_{res} and ρ_{sat} are approximately independent of temperature. For an unirradiated concentrated alloy, the ρ_{res} is primarily due to alloying, and the ρ_{res} in Eqn. 20 can be replaced by $\rho_{alloying}$. The $\rho(0, T)$ can then be written as

$$\rho_o(T) = \rho(0, T) = \frac{\rho_{int}(T) + \rho_{alloying}}{1 + \left(\frac{\rho_{int}(T)}{\rho_{sat}}\right)} \quad (21)$$

For U-10Mo with point defects, the ρ_{res} is produced by both alloying and point defects and, in this work, we assume the point defect to be dilute, which means the residual resistivity arising due to point defects are independent of each other. Hence, the ρ_{res} in Eqn. 21 can be replaced by

$$\rho_{res} = \rho_{alloying} + \sum_{i=1}^n \rho_{pd,i}(c_i) \quad (22)$$

Here, the $\rho_{alloying}$ is the same as the unirradiated U-10Mo fuel, and the $\rho_{pd,i}(c_i)$ is the residual resistivity due to different type of point defects (“i” here is the various type of point defect considered) with a concentration of c_i . The $\rho_{pd,i}(c_i)$ is obtained by combining the density functional theory Boltzmann transport equation (DFT-BTE) model with semiclassical theory as shown in Eqn. 23:

$$\rho_{pd,i}(c_i) = \frac{c_i A_i v_F}{S_0(T) V_{atom}} \quad (23)$$

where c_i is the concentration of point defect i , A_i is the electron point defect scattering cross section, V_{atom} is the volume per atom, $S_0(T)$ is the ratio of electrical conductivity (ρ) and electronic relaxation time (τ) calculated for no point defect case and is obtained from the DFT-BTE approach, and v_F is the Fermi velocity. The residual resistivity of metal under the fast neutron irradiation is a function of time, as proposed by Horak and Blewitt [51].

$$\rho_{res} = \rho_{max} (1 - e^{-\beta t}) \quad (24)$$

where ρ_{max} is the saturation value of residual resistivity, and β is a constant. If the burnup rate is assumed constant, the burnup is proportional to irradiation time. As ρ_{res} is proportional to the point defect concentration, the effective point defect concentration (C_{eff}) as a function of burnup is calculated using

$$C_{eff} = C_{max} \left(1 - e^{-\frac{x}{x_0}}\right) \quad (25)$$

where C_{max} is the effective total defect concentration at saturation, x is burnup percent, and x_0 is 0.15, a constant. The x_0 was set to 0.15 to attain the saturation concentration of 1×10^{-4} at 40% burnup.

2.2.3 Results

2.2.3.1 Thermal Conductivity Degradation Factor Due to Intragranular Gas Bubbles as a Function of Fission Density

The intragranular gas bubble porosity (p_{intra}) data as a function of fission density (FD) needed to model the thermal conductivity degradation factor (f_{intra}) is obtained from the simulated microstructural changes in an irradiated U-10Mo, performed using the DART fuel-performance code [52]. Analyzing the intragranular gas bubble porosity data at 150°C, we observed that the intragranular porosity is negligible up to the FD of $1 \times 10^{21} \frac{fissions}{cm^3}$, and for a FD greater than $1 \times 10^{21} \frac{fissions}{cm^3}$, the intragranular porosity increased. Based on these data a polynomial fit is proposed, as shown below

$$p_{intra} = 0 \text{ for } x < 1 \times 10^{21} \frac{fissions}{cm^3} \quad (26)$$

$$p_{intra} = -0.0015x^2 - 0.0178x - 0.0126 \text{ for } x > 1 \times 10^{21} \frac{\text{fissions}}{\text{cm}^3}$$

Using the p_{intra} values and the Bauer's model (Eqn. 17), the f_{intra} as a function of the FD is provided in Figure 12.

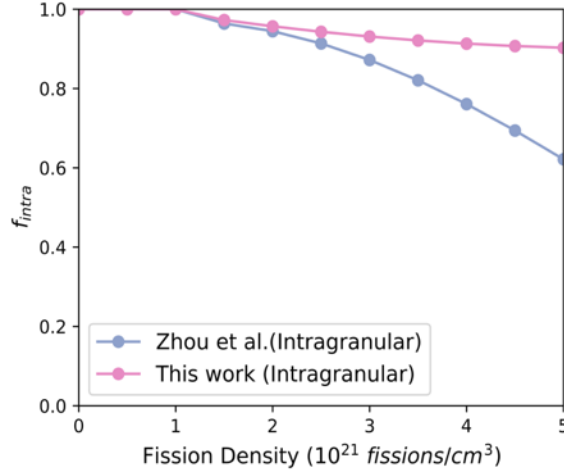


Figure 12. Thermal conductivity degradation factor due to intragranular gas bubble as a function of the FD compared with the work by Zhou et al. [42].

As expected, the f_{intra} as a function of FD decreased with increasing intragranular porosity, with a maximum thermal conductivity degradation of 10%. The f_{intra} reported by Zhou et al. [42] is significantly higher at fission densities greater than $3 \times 10^{21} \frac{\text{fissions}}{\text{cm}^3}$ and predicted the maximum thermal conductivity degradation value of more than 60%. The stark contrast between the two works is primarily due to differences in the intragranular porosity data. The polynomial fit for intragranular porosity as a function of burnup proposed by Zhou et al. [42] considered only a few data points and hence overestimated the intragranular porosity value at higher burnup.

2.2.3.2 Thermal Conductivity Degradation Factor Due to Intergranular Gas Bubbles as a Function of Fission Density

The average intergranular porosity as a function of FD at 150°C is also obtained from simulated microstructural changes in an irradiated U-10Mo, performed using the DART fuel-performance code [52]. For FDs less than $1 \times 10^{21} \frac{\text{fissions}}{\text{cm}^3}$, the presence of intergranular gas bubble is negligible. For FDs greater than $1 \times 10^{21} \frac{\text{fissions}}{\text{cm}^3}$, the intergranular porosity starts to increase and becomes significantly higher at FDs greater than $3 \times 10^{21} \frac{\text{fissions}}{\text{cm}^3}$. Based on the data, a second-order polynomial fit is derived for the intergranular porosity as a function of FD, as shown below

$$p_{inter} = 0 \text{ for } x < 1 \times 10^{21} \frac{1}{\text{cm}^3} \tag{27}$$

$$p_{inter} = 0.0114x^2 - 0.038x + 0.0365 \text{ for } x > 1 \times 10^{21} \frac{1}{\text{cm}^3}$$

Figure 13(a) illustrates that the f_{inter} becomes predominant at a FD greater than $3 \times 10^{21} \frac{\text{fissions}}{\text{cm}^3}$, and the thermal conductivity degrades by a maximum of 30% at a FD of $5 \times 10^{21} \frac{\text{fissions}}{\text{cm}^3}$. Whereas, the maximum thermal conductivity degradation due to intergranular gas bubbles reported by Zhou et al. [42] is ~20%. The difference in the predicted thermal conductivity degradation due to intergranular gas bubbles is because Zhou et al. [42] relied on one data point to model the intergranular gas bubbles

population. Figure 13(b) compares the thermal conductivity degradation factor due to intragranular and intergranular gas bubbles predicted in this work with that of Zhou et al. [42]. The comparison of the f_{inter} and f_{intra} clearly indicate that at higher FDs the intergranular bubbles have the dominant effect on thermal conductivity degradation compared to intragranular bubbles.

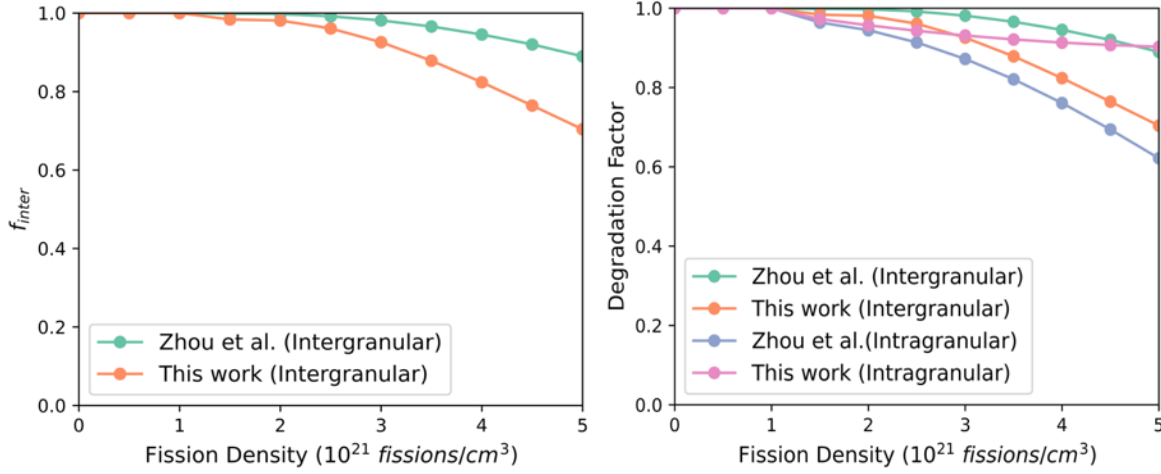


Figure 13. (a) Plot of degradation factor for intergranular bubbles as a function of the FD (b) Comparison of the thermal conductivity degradation factor due to intergranular and intragranular gas bubbles.

2.2.3.3 Point Defect Degradation Factor as a Function of Fission Density

The effect of point defects on the thermal conductivity of U-10Mo fuel is evaluated using the equation described in Section 2.2.2.3. The values of $\rho_o(T)$, $\rho_{int}(T)$, $\rho_{alloying}$, ρ_{sat} , $V_{atom} = 9.4 \text{ \AA}^3$, $v_F = 1.62 \times 10^6 \text{ m/s}$, $s_o(T) = 2.1 \times 10^{20} (\Omega ms)^{-1}$ and the total electron scattering cross-section area for the vacancy (7 \AA^2), Xe (39 \AA^2), Kr (25 \AA^2), and He (4 \AA^2) to evaluate the f_{pd} were all taken from a previous work [43]. To evaluate the effective total electron scattering cross-section area; we have adopted the weighted average of the electron cross-section area due to each point defect. The previous work [42] considered only the effect of point defects in equal concentration and the effective total electron scattering cross-section area was calculated by taking the mean value of electron cross-section area of each point defect. The f_{pd} as a function of FD for various cases of point defect populations maintaining a saturation concentration of 1×10^{-4} is presented in Figure 14. The results suggest that point defects at lower concentrations (1×10^{-4}) had a negligible effect on the thermal conductivity degradation. For all the cases of the varying populations of the point defects considered in this study, the maximum thermal conductivity degradation due to point defects is predicted to be $\sim 1\%$. Among the different cases considering the varying population of point defects, case3 (75% Xe and 25% vacancy) will be relatively more detrimental to the thermal transport due to the large electron scattering cross section of Xe.

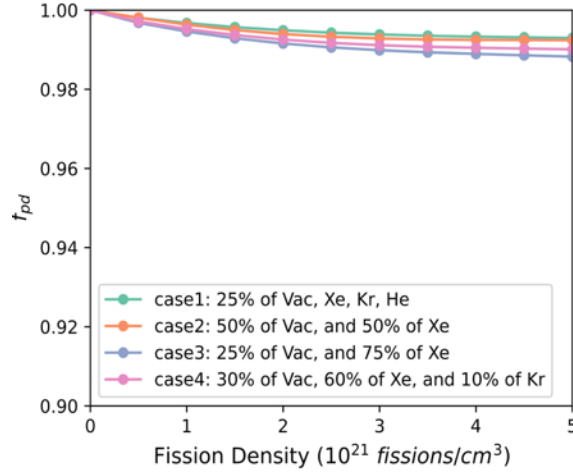


Figure 14. The point defect degradation factor considering the saturation concentration of 0.01% (10^{-4}).

2.2.3.4 Total Thermal Conductivity Degradation and Effective Thermal Conductivity of Irradiated U-10Mo

From the calculated values of the thermal conductivity degradation factors due to point defects, intragranular gas bubbles, and intergranular gas bubbles, the total thermal conductivity degradation is calculated using Eqn. 15. The effective thermal conductivity of irradiated U-10Mo alloys is calculated by multiplying the total thermal conductivity degradation factor with the thermal conductivity of the unirradiated U-10Mo for the given temperature (Eqn. 16). Figure 15(a) shows the thermal conductivity degradation factor due to individual defects and the total thermal conductivity degradation factor as a function of FD. At all considered FDs, the effect of point defects on the thermal transport in U-10Mo is negligible. Whereas up to a FD of $\sim 3 \times 10^{21} \frac{\text{fissions}}{\text{cm}^3}$, the intragranular gas bubbles dominate the thermal conductivity degradation, and for a FD greater than $\sim 3 \times 10^{21} \frac{\text{fissions}}{\text{cm}^3}$, the intergranular porosity becomes sufficient to dominate the degradation process. Figure 15(b) shows the comparison of the thermal conductivity degradation as a function of FD at 150°C, considering all cases of point defects with a saturation concentration of 0.01% (1×10^{-4}). At 150°C, the thermal conductivity of the U-10Mo is 14.69 W/mK and is multiplied with f_{total} to obtain the thermal conductivity degradation of U-10Mo as a function of FD.

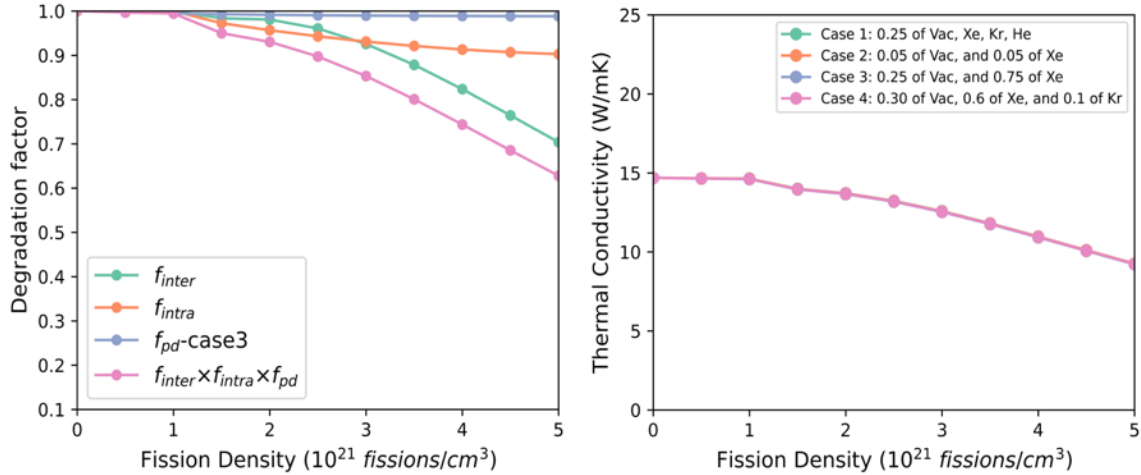


Figure 15. (a) Comparison of the degradation factor due to intragranular bubbles, intergranular bubbles, and the point defects (case3) considering the saturation concentration of 0.01% 1×10^{-4}); (b) Comparison of the thermal conductivity degradation as a function of FD at 150°C, considering the saturation concentration of point defects of 0.01% (1×10^{-4}).

2.2.4 Conclusion

A thermal conductivity degradation model for the irradiated U-10Mo fuel is presented. Our models combine the microstructural information from simulations and experiments to model the thermal conductivity degradation due to various defects observed in the irradiated material. This model incorporates the effect of point defects, GBs, intragranular gas bubbles, and intergranular gas bubbles. The thermal conductivity degradation due to each defect type is calculated separately, and the overall thermal conductivity degradation is obtained by multiplying the degradation due to each defect type. Our model predicts that the effect of GBs and point defects at low concentration on thermal transport in U-10Mo is negligible. Also, we found that at a FD less than $\sim 3 \times 10^{21} \frac{\text{fissions}}{\text{cm}^3}$ the intragranular gas bubble were the dominant factor in the thermal conductivity degradation. However, at higher FDs (greater than $\sim 3 \times 10^{21} \frac{\text{fissions}}{\text{cm}^3}$), the intergranular bubbles become significant and affect the thermal transport in U-10Mo fuels. Finally, the total thermal conductivity degradation of irradiated U-10Mo at 150°C as a function of FD is determined and can be implemented into engineering-scale fuel-performance simulations.

2.3 Degradation of Mechanical Properties in Monolithic U-Mo Fuel

The formation and evolution of voids and FGBs in irradiated U-10Mo nuclear fuel are known to impact the thermo-mechanical properties and, thereby, the fuel performance. The transmission electron microscope (TEM) and SEM investigations have revealed the sequence of microstructural evolution as a function of fuel burnup and FD [27,34,39]. Intragranular FGBs are typically fine and dense with a radius of 1 nm and spacing of few nanometers. Intergranular gas bubbles are formed at FD exceeding 4×10^{21} f/m³ and are coarser in size with a radius exceeding 100 nm. On the other hand, the initial grain morphology is determined by prior thermo-mechanical processing conditions, and the GBs act as preferential nucleation sites for the gas bubbles. At high FDs, recrystallization of the grains occurs where the initial grains become finer, which is accompanied by the disappearance of intragranular gas bubbles. Similarly, voids without fission gas are formed via accumulation of excess vacancies generated during the irradiation damage cascade and subsequent diffusion. The distribution of voids, gas bubbles, and grains therefore determine the elastic response of the microstructure. Voids can be considered to offer negligible elastic resistance under tensile, compressive, and shear loading conditions. On the other hand, gas atoms pressurize the pores and are known to resist compressive loads and possess a finite bulk modulus that can

range from a very small value to tens of GPa depending on the gas pressure. Since voids and gas bubbles can cause structural degradation of the fuel over time, it is important to develop a modeling and computational methodology to assess the overall effective elastic properties of the microstructure given the distribution and morphologies of voids, gas bubbles, and grains. In this work, MD and PF methods are utilized to explore the degradation of elastic properties of UMo as a function of burnup.

2.3.1 Atomistic Calculations

2.3.1.1 Method

The calculations were performed with the LAMMPS [53] simulation package. Both the embedded-atom-method (EAM) potential [54] and the angular dependent potential (ADP) [55] have been assessed. In their original forms, the EAM potential for U-Mo has included Xe, and the ADP potential has not. During the study, it was found that the EAM potential did not capture the phase stability of solid solution U-10Mo at high temperatures, at which Mo was found to precipitate out from the bcc UMo matrix in hybrid MD Monte Carlo (MDMC) simulations. To make up for this deficiency, an ADP potential for U-Mo-Xe was created by Beeler et al. by merging the ADP U-Mo potential with the Mo-Xe, U-Xe, and Xe-Xe interactions from the EAM potential [56]. This newly created ADP U-Mo-Xe potential was used in most simulations unless otherwise stated. Due to the different types of MD simulations that have been performed, the detailed simulation setup will be described before presenting the corresponding results.

2.3.1.2 Results

Phase Stability and Defect Formation Energies

To assess the newly created ADP U-Mo-Xe interatomic potential, the phase stability of U-Mo with respect to temperature and composition was computed using MD simulations, and the results are compared with the original ADP U-Mo potential. The simulations used $10 \times 10 \times 10 a_0$ cubic supercells with different U-Mo compositions, where a_0 is the lattice constant of bcc U-Mo. A periodic, zero-pressure boundary condition was applied along all three directions. Starting from 0 K, the system temperature was incrementally increased to 1200 K. For each step, the temperature was raised by 50 K, followed by a 100 ps relaxation for the system to evolve into the lowest energy phase at the corresponding temperature. The c/a ratio obtained after relaxation is plotted in Figure 16 as a function of temperature and composition to indicate the phase selection. With both ADP potentials, at low temperatures and low Mo concentrations, a tetragonal structure was seen, with the c/a ratio smaller than 1. With increasing temperature or Mo concentration, the bcc phase became stable, with a c/a ratio of 1.0, as shown in Figure 16. Theoretically, these two ADP potentials should give identical results when no Xe is included in the simulations. Minor differences were noticed in terms of the exact temperature and Mo concentration boundaries for the bcc phase to be stable. The c/a ratio obtained for the tetragonal phase was slightly different as well. These differences may be caused by the spatial discretization used in the potential tabulation and possible stochastic effects in MD simulations. However, these minor discrepancies are not expected to affect the results in the high-temperature, high-Mo content region where the bcc phase is stable.

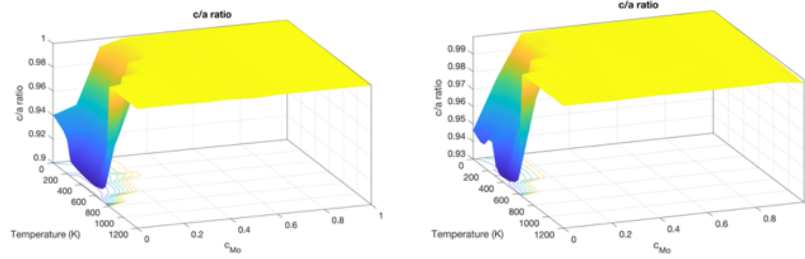


Figure 16. The c/a ratio at various temperatures and Mo concentrations (c_{Mo} , molar fraction) calculated using a) (left) the original UMo ADP and b) (right) the newly constructed U-Mo-Xe ADP potentials.

The point defect formation energies for a vacancy, an interstitial, and a Xe substitutional in U-10Mo have also been calculated using the U-Mo-Xe ADP potential following a recently developed statistical approach [57]. In concentrated alloys, the point defect formation energies are dependent on the local atomic environment and are expected to exhibit distributions. An example of such a distribution is shown in Figure 17 for the interstitial and vacancy formation energies in U-10Mo (atomic percent) at 300 K. The interstitial formation energy may be negative at this temperature because it is at the edge of phase stability for the bcc phase, as shown in Figure 16. For random alloys, it has been found that the Gaussian distribution accurately describes the distribution in defect formation energies. Therefore, for each type of defect, a mean value and a standard deviation are needed to fully describe the distribution of its formation energy, assuming a Gaussian distribution. The corresponding results for a vacancy, an interstitial, and a Xe substitutional in U-10Mo at room temperature are shown in Table 3. The mean vacancy formation energy obtained in this work, 1.15 eV, is within the range from the literature for U vacancy, 1.08–1.38 eV; the mean interstitial formation energy obtained, 0.71 eV, is higher than the 0.5 eV and 0.55 eV for $\langle 100 \rangle$ and $\langle 110 \rangle$ U dumbbell reported; the mean Xe substitute formation energy, 6.57 eV, is also higher than the 5.549 eV reported in the literature [58]. It should be noted that the previous calculations were mostly done at 0 K and have not included the distribution ranges of these formation energies. Direct comparison is difficult without knowing the exact atomic environment used in previous calculations. However, the results in the literature are all within the distribution ranges obtained here, indicating reasonable agreement. Results for other temperatures have been obtained as well.

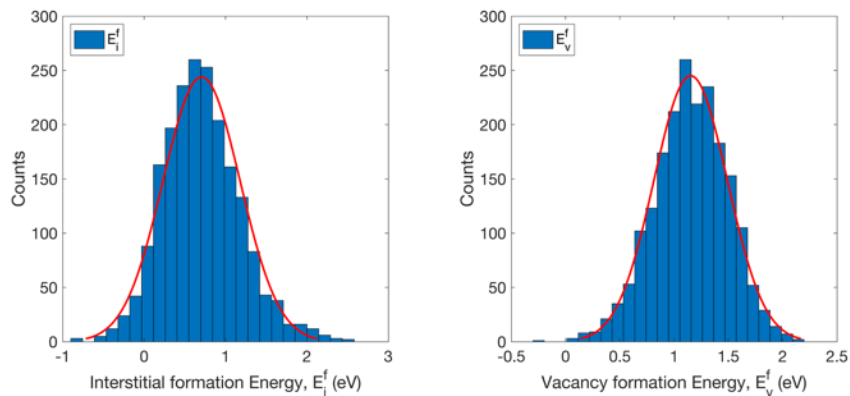


Figure 17. Distribution of (left) interstitial and (right) vacancy formation energies in U-10Mo (21.8% atomic percent) at 300 K. The red curve is fitted to normal distribution.

Table 3. Formation energies (eV) of vacancy, interstitial, and Xe substitutional in U-10Mo at room temperature.

Defect	Vacancy	Interstitial	Xe substitutional
Mean formation energy	1.151985	0.705297	6.570478
Standard deviation	0.338552	0.474126	0.298592

Elastic Moduli

The elastic moduli in bcc U and U-10Mo were calculated with different porosities, pore sizes, gas to vacancy ratios (GVratio), and temperatures to show the effect of gas bubbles on elasticity degradation. To represent realistic gas bubble morphology, kinetic MC simulations were carried out to prepare randomly distributed bubbles with different bubble sizes in a periodic simulation cell, as shown in Figure 18. Six different porosities (0, 2.5, 5.0, 7.5, 10.0, and 15.0 volumetric percent) were used in the calculations with three different GVratios (0.0, 0.1, and 0.25). The temperature was varied from 200 K to 1000 K, with one data point every 200 K. The elastic moduli C_{11} , C_{12} and C_{44} were calculated using the same approach described in our previous report [59] and used to derive bulk modulus K and Poisson's ratio ν .

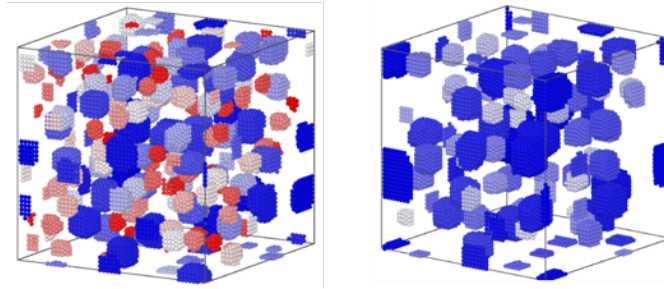


Figure 18. Bulk UMo containing 10% porosity with 142 (left) and 69 (right) bubbles. The bubbles are colored from red to blue showing increasing bubble size.

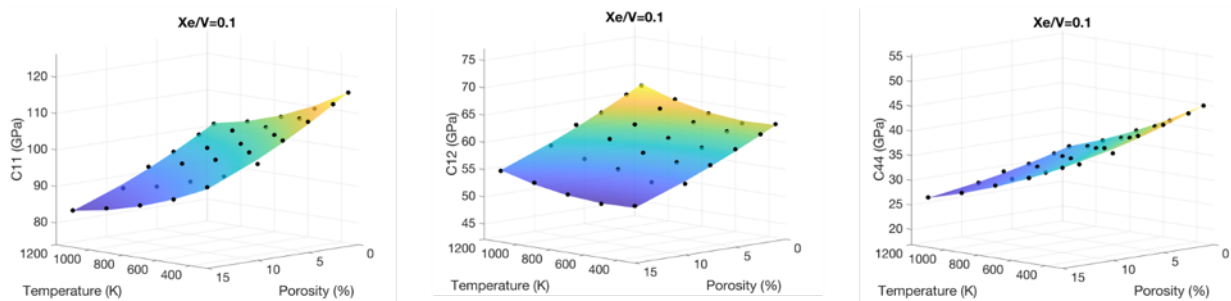


Figure 19. Elastic moduli C_{11} , C_{12} and C_{44} of bcc U as functions of temperature and porosity. The dots are from MD simulations and the surface is fitted using the polynomials in Eqn. 28.

For both U and U-10Mo, the elastic moduli were found to be insensitive to the average bubble size. Therefore, we will focus on the effects of temperature, porosity, and GVratio while presenting the results. As shown in Figure 19, elastic moduli C_{11} and C_{44} of bcc U decrease with temperature and porosity, while C_{12} decreases with porosity but increases with temperature. In comparison, these elastic moduli increase very slightly with gas bubble internal pressure, which is represented by GVratio, as shown in Figure 20. The bulk modulus of bcc U decreases with temperature and porosity, while the Poisson's ratio increases with temperature and porosity. The same trends have been observed for U-10Mo as well.

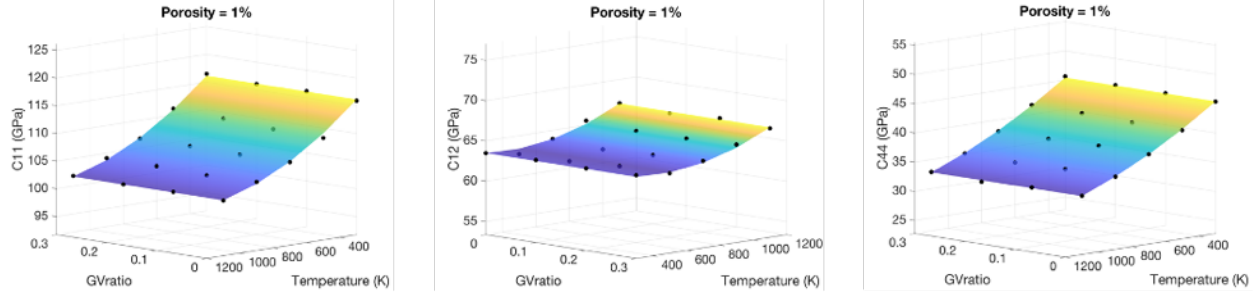


Figure 20. Elastic moduli C_{11} , C_{12} and C_{44} of bcc U as functions of temperature and GVratio. Higher GVratio means higher bubble internal pressure. These elastic moduli increase slightly with increasing GVratio. The dots are from MD simul.

The results from MD simulations suggest that the effects of different factors are not strongly coupled with each other. Inspired by this observation, we have further fitted the elastic moduli using the below equation using the least square error fitting algorithm

$$y = y_0 f(T) * g(p) * h(c_g) \quad (28)$$

In Eqn. 28, y is one of the elastic moduli, C_{11} , C_{12} , C_{44} , bulk modulus K , or Poisson's ratio ν . y_0 is a fitting constant, representing a reference elastic modulus. $f(T)$ is a 2nd order polynomial function of temperature T (e.g., $f = a_1 x^2 + a_2 x + a_3$), $g(p)$ a 2nd order polynomial of porosity p , and $h(c_g)$ a 2nd order polynomial of GVratio (i.e., c_g). The fitted coefficients for U-10Mo are listed in Table 4. As shown in Figure 21, the fitted equation reproduces the results from MD for U-10Mo very well.

Table 4. Fitted coefficients for U-10Mo using Eqn. 28.

	y_0	a_1	a_2	a_3	b_1	b_2	b_3	c_1	c_2	c_3
c_{11}	154.56 1197	8.70E- 08	0.0002 276	0.9992 89	0.0002 475	0.0170 17	1.0068 7	0.0821 37	0.0334 926	0.9999 83
c_{12}	98.732 990	-2.10E- 08	3.9582 E-05	1.0001 4	0.0002 4314	0.0172 434	1.0078 2	0.1066 02	0.0447 629	0.9997 24
c_{44}	42.685 797	-8.26E- 08	3.5043 E-05	0.9999 85	0.0001 7092	0.0146 669	1.0043 6	0.0622 485	0.0520 73	0.9997 83
B	117.34 2392	2.65E- 08	7.802E -05	0.9997 63	0.0002 4449	0.0171 402	1.0074 4	0.0964 667	0.0400 48	0.9998 33
ν	0.3897 96	-5.98E- 08	0.0001 6707	1.0004 5	4.063E -06	0.0001 436	1.0005 7	0.0140 712	0.0065 3702	0.9998 49

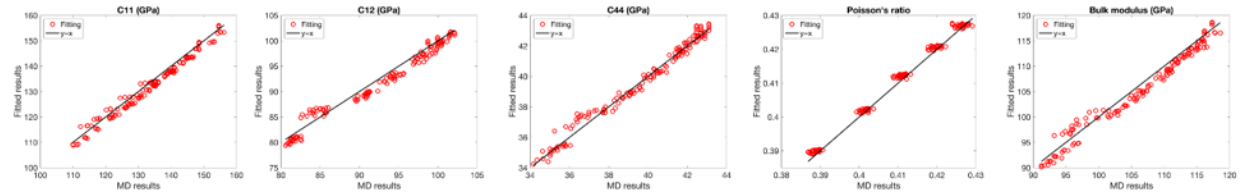


Figure 21. Fitted results for elastic moduli of U-10 Mo using Eqn. 28 versus MD results.

2.3.1.3 Summary

In summary, MD simulations were carried out to compute the elastic moduli of U-10Mo. The existing interatomic potentials in the literature were assessed in terms of phase stability, and a new version of ADP U-Mo-Xe potential developed by Beeler et al. at NCSU was used in most simulations. The elastic moduli of U-10 Mo depend critically on temperature and porosity, and insignificantly on bubble internal pressure and average bubble size. Slight hardening (i.e., increase in moduli) was observed in the simulations due to increasing bubble internal pressure. The effects of temperature, porosity, and bubble pressure seemed not to be correlated strongly with each other, allowing for the development of a reduced-order model. Specifically, a polynomial-based model which is the product of three 2nd order polynomials describing the separated effects of temperature, porosity, and bubble pressure has been fitted using the data from MD calculations. This model is convenient to use in engineering-scale modeling.

2.3.2 Mesoscale Calculations of Effective Elastic Constants and Stress Fields

2.3.2.1 Asymptotic Expansion Homogenization

Asymptotic expansion homogenization (AEH) is a computational technique to determine the homogenized physical properties of heterogeneous microstructures with underlying periodicity. It has been successfully utilized to determine the effective thermal, mechanical, and diffusive behaviors of structural materials with composite microstructures [60,61]. The effective material properties can be determined from the properties of chosen microscale representative volume elements with periodic boundary conditions. In other words, the AEH technique prescribes a system of equations to compute homogenized material constants of the mesoscale for use at the engineering scale. A detailed derivation of the strong form of the governing partial differential equations of AEH for linear elasticity problems has been reviewed and developed elsewhere in [62,63]. The discretized weak-form of the equations were implemented using the finite-element method within INL's Multiphysics Object-Oriented Simulation Environment (MOOSE) framework [64].

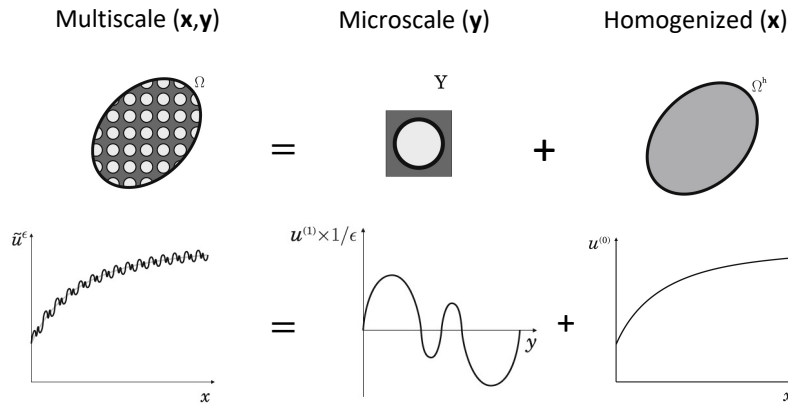


Figure 22. (Top panel) Schematic representations of the microstructure at different scales - multiscale (\mathbf{x}, \mathbf{y}) , representative volume element at microscale (\mathbf{y}) and homogenized macroscale (\mathbf{x}) . (Bottom panel) Typical displacement fields illustrated at the corresponding scales [62].

The microstructure of a linear elastic body Ω is assumed to be made of a spatially periodic distribution of a representative volume element (RVE) region Y containing the heterogeneity. Two systems of coordinates can be identified as shown by the schematic in Figure 22: macroscale \mathbf{x} , microscale \mathbf{y} . The relation between the two scales of coordinates is given by $\mathbf{y} = \mathbf{x}/\epsilon$ ($\epsilon \ll 1$). The elastic stiffness tensor can be expressed independently of the macroscale \mathbf{x} as $C_{ijkl}^\epsilon(\mathbf{x}) = C_{ijkl}(\mathbf{x}/\epsilon) = C_{ijkl}(\mathbf{y})$; the superscript ϵ denotes the Y -periodicity of \mathbf{C} .

For the multiscale problem, the mechanical equilibrium condition, linear strain-displacement relation, and the linear stress-strain constitutive law are given by

$$\frac{\partial \sigma_{ij}^\epsilon}{\partial x_i^\epsilon} + f_i = 0, \quad \sigma_{ij}^\epsilon = C_{ijkl}^\epsilon \epsilon_{kl}^\epsilon, \quad \epsilon_{ij}^\epsilon = \frac{1}{2} \left(\frac{\partial u_i^\epsilon}{\partial x_j^\epsilon} + \frac{\partial u_j^\epsilon}{\partial x_i^\epsilon} \right). \quad (29)$$

Assuming the two distinct scales of spatial microstructure and its properties, the displacement field can be approximated using an asymptotic expansion ($u_i^\epsilon(\mathbf{x}) = u_i^{(0)}(\mathbf{x}) + \epsilon u_i^{(1)}(\mathbf{x}, \mathbf{y}) + \dots$). This expression can be substituted in the multiscale equations to obtain expressions for the strain and stress tensors in terms of powers of ϵ . It can be shown that $\sigma_{ij}^{(0)} = 0$, $\epsilon_{ij}^{(0)} = 0$, and $\sigma_{ij}^\epsilon = 0$, and algebraic manipulation of these expressions under the assumption $\epsilon \rightarrow 0$, together with the application of appropriate boundary conditions, yields the microscale fields for displacements, strains, and stresses. The first-order displacement field is obtained as $u_i^{(1)}(\mathbf{x}, \mathbf{y}) = \chi_i^{kl}(\mathbf{y}) \frac{\partial u_k^{(0)}}{\partial x_l}(\mathbf{x})$; here, $u^{(0)}$ is independent of the microscale \mathbf{y} , and therefore, it is the global displacement field of the macroscale homogenized material. χ is the first-order characteristic displacement field tensor whose solutions are to be determined from the microscale stress divergence equation

$$\frac{\partial \sigma_{ij}^{(1)}}{\partial y_i} = 0, \quad \sigma_{ij}^{(1)} = \left[C_{ijkl}(\mathbf{y}) \left(\mathbf{I} + \frac{\partial \chi_k^{mn}}{\partial y_l} \right) \right] \frac{\partial u_m^{(0)}}{\partial x_n}. \quad (30)$$

The above microscale equations are homogenized by applying the averaging operator $\langle \cdot \rangle_Y$. This yields the homogenized macroscale versions of equilibrium differential equation and constitutive law as

$$\frac{\partial \sigma_{ij}^H}{\partial x_i} = 0, \quad \sigma_{ij}^H = C_{ijkl}^H(\mathbf{y}) \frac{\partial u_m^{(0)}}{\partial x_n} \quad (31)$$

where $\sigma_{ij}^H = \langle \sigma_{ij}^{(1)} \rangle_Y$ and $C_{ijkl}^H(\mathbf{y}) = \frac{1}{|Y|} \int_Y \left[C_{ijkl}(\mathbf{y}) \left(\mathbf{I} + \frac{\partial \chi_k^{mn}}{\partial y_l} \right) \right] d\mathbf{y}$ are the components of the homogenized stress and elastic stiffness tensors. $C_{ijkl}^H(\mathbf{y})$ is evaluated in the present work using periodic RVEs characteristic of the microscale U-10Mo fuel microstructures.

The AEH approach implemented in MOOSE has been validated for standard benchmark problems for linear elasticity and against other homogenization techniques [64]. It was shown to yield good results without requiring overly fine computational meshes.

2.3.2.2 Multi-phase-field Model

The total grand potential Ψ of the heterogeneous microstructure of polycrystalline grains and secondary phase pores can be formulated as [65–67][68]

$$\Psi = \int_V \left\{ w \left[\left(\frac{\eta_{b0}^4}{4} - \frac{\eta_{b0}^2}{2} \right) + \sum_{i=0}^{p-1} \left(\left(\frac{\eta_{mi}^4}{4} - \frac{\eta_{mi}^2}{2} \right) + \frac{\gamma_{mib0}}{2} \eta_{mi}^2 \eta_{b0}^2 + \sum_{j=0, j \neq i}^{p-1} \frac{\gamma_{mimj}}{2} \eta_{mi}^2 \eta_{mj}^2 \right) \right] + \frac{\kappa}{2} |\nabla \eta_{b0}|^2 + \frac{\kappa}{2} \sum_{i=0}^{p-1} |\nabla \eta_{mi}|^2 \right\} dV, \quad (32)$$

where $b0$ denotes either the bubble or void phase and mi denotes a matrix grain of index i ranging from 0 to $p - 1$. A $b0$ phase is represented by $\eta_{b0}(\mathbf{x}) = 1$ and all $\eta_{mi}(\mathbf{x}) = 0$. Similarly, the mi grain is represented in the region where $\eta_{mi}(\mathbf{x}) = 1$, $\eta_{b0}(\mathbf{x}) = 0$, and $\eta_{mj(j \neq i)}(\mathbf{x}) = 0$. Diffuse interfaces between two adjacent phases αi and βj are described by $0 < \eta_{\alpha i}, \eta_{\beta j} < 1$. The microstructure evolves following the Allen-Cahn equation $\frac{\partial \eta_{\alpha i}}{\partial t} = -L \frac{\delta \Omega}{\delta \eta_{\alpha i}}$. For the present work, starting microstructures are used to evaluate homogenized properties using AEH using a single time step in computation. Therefore, concentrations and their dependence on properties are not explicitly treated but accounted implicitly for simplicity.

The interfacial energies σ_{mimj} of the grain boundary and the pore surface σ_{mib0} are defined via the energetic model parameters: barrier energy coefficient w , gradient energy coefficient κ , and interface-specific adjustment parameter $\gamma_{\alpha\beta j}$ ($\alpha\beta j$ is $mib0$ or $mimj$). For convenience of parameterization, the bubble/void interfaces $mib0$ are chosen to be symmetric (i.e., $\eta_{b0} = 1 - \eta_{mi}$). The limitation to the degrees of freedom available in the model parameters will determine the grain-grain interfaces $mimj$ to be asymmetric with $\eta_{mj(j\neq i)} \neq 1 - \eta_{mi}$. Thereby, the interfacial energies ($\sigma_{mb} = \sigma_{mib0}$, $\sigma_{mm} = \sigma_{mimj}$) are given by the following relationships

$$\sigma_{mib0} = g(\gamma_{mib0} = 1.5)\sqrt{\kappa w} = \frac{\sqrt{2}}{3}\sqrt{\kappa w}, \quad \sigma_{mimj} = g(\gamma_{mimj})\sqrt{\kappa w}, \quad (33)$$

where $\kappa = \frac{3}{4}\sigma_{mb}l_{mb}$, $w = \frac{6\sigma_{mb}}{l_{mb}}$, σ_{mb} , and σ_{mm} are known from experiments/atomistic calculations, while the interfacial width l_{mb} is chosen to easily resolve the computational domain. These relations uniquely determine the model parameters κ and w and the function value $g(\gamma_{mimj}) = \frac{\sqrt{2}}{3} \frac{\sigma_{mib0}}{\sigma_{mimj}}$. Using

$g(\gamma_{mimj})$, the remaining unknown model parameter γ_{mimj} can be determined via the expression $\gamma_{mimj} = (-5.288g^8 - 0.09364g^6 + 9.965g^4 - 8,813g^2 + 2.007)^{-1}$.

The phase-specific properties, viz. elastic constants, are interpolated across the diffuse interface via the phase switching functions, $h_{mi} = \frac{\eta_{mi}^2}{\eta_{b0}^2 + \sum_{i=1}^p \eta_{mi}^2}$ and $h_{b0} = \frac{\eta_{b0}^2}{\eta_{b0}^2 + \sum_{i=1}^p \eta_{mi}^2}$. Therefore, the stiffness tensor $\mathbf{C}(\mathbf{y})$ at any point in the domain is described by interpolating the components of bubble/void \mathbf{C}_{b0} and grain \mathbf{C}_{mi} as

$$\mathbf{C}(\mathbf{y}) = h_{b0}\mathbf{C}_{b0} + \sum_{i=1}^p h_{mi}\mathbf{C}_{mi}. \quad (34)$$

Using the above multiphase model, it has been demonstrated [69] that intergranular phases like bubbles or voids satisfy the dihedral contact angle θ_{mb} that balances the interfacial energies of the intersecting interfaces via Young's equation, $\cos\left(\frac{\theta_{mb}}{2}\right) = \frac{\sigma_{mm}}{2\sigma_{mb}}$. Material properties and model parameters used in the model are listed in Table 5.

Table 5. Material properties and model parameters used for the PF model and effective elastic constant calculation. (t_c, l_c, E_c) are the characteristic time, length, and energy scales used to non-dimensionalize the model parameters and scale them for improved numerical performance.

	Parameters	Intragranular	Intergranular	Reference
Pore radius	R	1 nm	150 nm	
Grain boundary energy	σ_{mm}	0.5 J/m ²		[70]
Surface energy	σ_{mb}	1.5 J/m ²		[70]
Contact angle	θ_{mb}	160°		This work
Characteristic time	t_c	0.1 s		This work
Characteristic length	l_c	1 nm		
Characteristic energy	E_c	10 GPa	64 GPa	
Temperature	T	500 K		
Barrier energy	w	180×10^8 J/m ³	1.5×10^8 J/m ³	This work
Gradient energy	κ	5.62×10^{-10} J/m	6.75×10^{-8} J/m	
Adjustment factors	γ_{mimj}	0.5522		
	γ_{mib0}	1.5		
Grain boundary width	l_{mm}	0.78 nm	93.4 nm	
Surface width	l_{mb}	0.5 nm	60 nm	
Lattice molar volume	Ω_m	14×10^{-6} m ³ /mol		

	Parameters	Intragranular	Intergranular	Reference
Kinetic mobility	L	$1.5 \times 10^{-11} \text{ m}^3/(\text{J}\cdot\text{s})$		This work
Elastic constants of cubic U-10Mo crystal	C_{11}^m	140.2 GPa		Sec. 2.3.1
	C_{12}^m	89.6 GPa		
	C_{44}^m	38.7 GPa		
Elastic constants of gas bubble	C_{11}^b	13 GPa	0.01 GPa	Calculated from [30]
	C_{12}^b	13 GPa	0.01 GPa	
	C_{44}^b	10^{-3} GPa	10^{-3} GPa	

2.3.2.3 Elastic Constants of Grains, Voids, and Gas Bubbles

Elastic constants for single crystal γ -U-10Mo grain are parameterized from MD calculations. At 500 K, the three independent components of the cubic crystal structure are $(C_{11}, C_{12}, C_{44}) = (140.2, 89.6, 38.7)$ GPa. The full elastic stiffness tensor \mathbf{C}_{m0} for this single crystal is given by

$$\mathbf{C}_{m0} = \begin{bmatrix} C_{11} & C_{12} & C_{12} & 0 & 0 & 0 \\ C_{12} & C_{11} & C_{12} & 0 & 0 & 0 \\ C_{12} & C_{12} & C_{11} & 0 & 0 & 0 \\ 0 & 0 & 0 & C_{44} & 0 & 0 \\ 0 & 0 & 0 & 0 & C_{44} & 0 \\ 0 & 0 & 0 & 0 & 0 & C_{44} \end{bmatrix}. \quad (35)$$

The grain orientation-dependence in a U-10Mo polycrystal is modeled by randomly rotating the stiffness tensor of \mathbf{C}_{m0} and generating $\mathbf{C}_{mi(i \neq 0)}$ for the remaining grains in the microstructure

$$\mathbf{C}_{mi} = \mathbf{R}_i \cdot \mathbf{R}_i \cdot \mathbf{C}_{m0} \cdot \mathbf{R}_i^T \cdot \mathbf{R}_i^T, \quad (36)$$

where \mathbf{R} is the rotation matrix defined in terms of (ψ, θ, ϕ) , which are the Euler angles for the sequence of axis-rotations, with ψ being the first rotation about the z-axis, θ being the rotation performed about the new y-axis, and ϕ being the final rotation performed about the new z-axis. For a two-dimensional microstructure, only the first rotation via ψ is performed.

The void phase (zero-fission-gas concentration) is considered to offer negligible elastic resistance. For the sake of numerical stability and convergence of the computation, the elastic constants are set a negligible but non-zero value of $C_{11} = C_{12} = C_{44} = 10^{-3}$.

The Xe gas bubble phase is considered to offer finite elastic resistance under compressive load, but a negligible resistance under shear and all other loading conditions. This description assumes that Xe is present in the pores in the gaseous phase, which is expected, except at very large gas pressures. The bulk modulus K is the only relevant elastic constant and is anticipated to have a non-trivial dependence with gas pressure P_g . To obtain quantitative estimates for K over a wide range of pressures, Ronchi's EOS [30] is employed. This EOS is was found to be valid over a wider range of pressures (especially higher) compared to the Van der Waals EOS and was shown to be well-suited for PF simulations [71,72]. From the data provided by Ronchi for Xe at 500 K, $P_g v_m = Z(P_g)RT$, where $Z(P_g)$ is the compressibility function that can be fit with the data of P_g . The $Z - P_g$ data for $P_g < 5$ GPa and $P_g > 5$ GPa were fit to two third-order polynomials to obtain good fits over the entire data range; the agreement with original data is shown in Figure 23a. The obtained polynomial fits are $Z(5 < P_g < 50 \text{ GPa}) = 6.001 + 5.183P_g - 0.02726P_g^2 + 0.00025P_g^3$ and $Z(0.01 < P_g < 5 \text{ GPa}) = 0.6959 + 9.007P_g - 1.194P_g^2 + 0.1313P_g^3$. Analytic expressions for $v_m(P_g)$ were obtained for the fits, which were subsequently used to generate numerical data for $K(P_g)$ using

$$K(P_g) = -v_m(P_g) \left[\frac{dv_m(P_g)}{dP_g} \right]^{-1}. \quad (37)$$

The gas concentration in the bubble is defined as the ratio of the gas molar volume v_m and the molar volume of the lattice site vacancy or atom Ω_m , and is obtained as $c_g(P_g) = \frac{\Omega_m}{v_m} = \frac{\Omega_m P_g}{Z(P_g)RT}$. Furthermore, for simplicity, the gas bubbles are treated to be at mechanical equilibrium with the surrounding matrix. This condition is satisfied when the outward force exerted by gas pressure on the pore surface exactly balances the inward force exerted by the surface tension of a given pore radius. From the Young-Laplace equation, the equilibrium radius-gas pressure relationship $R_{eq} - P_g$ is obtained as $R(P_g) = \frac{2\sigma_{mb}}{P_g}$.

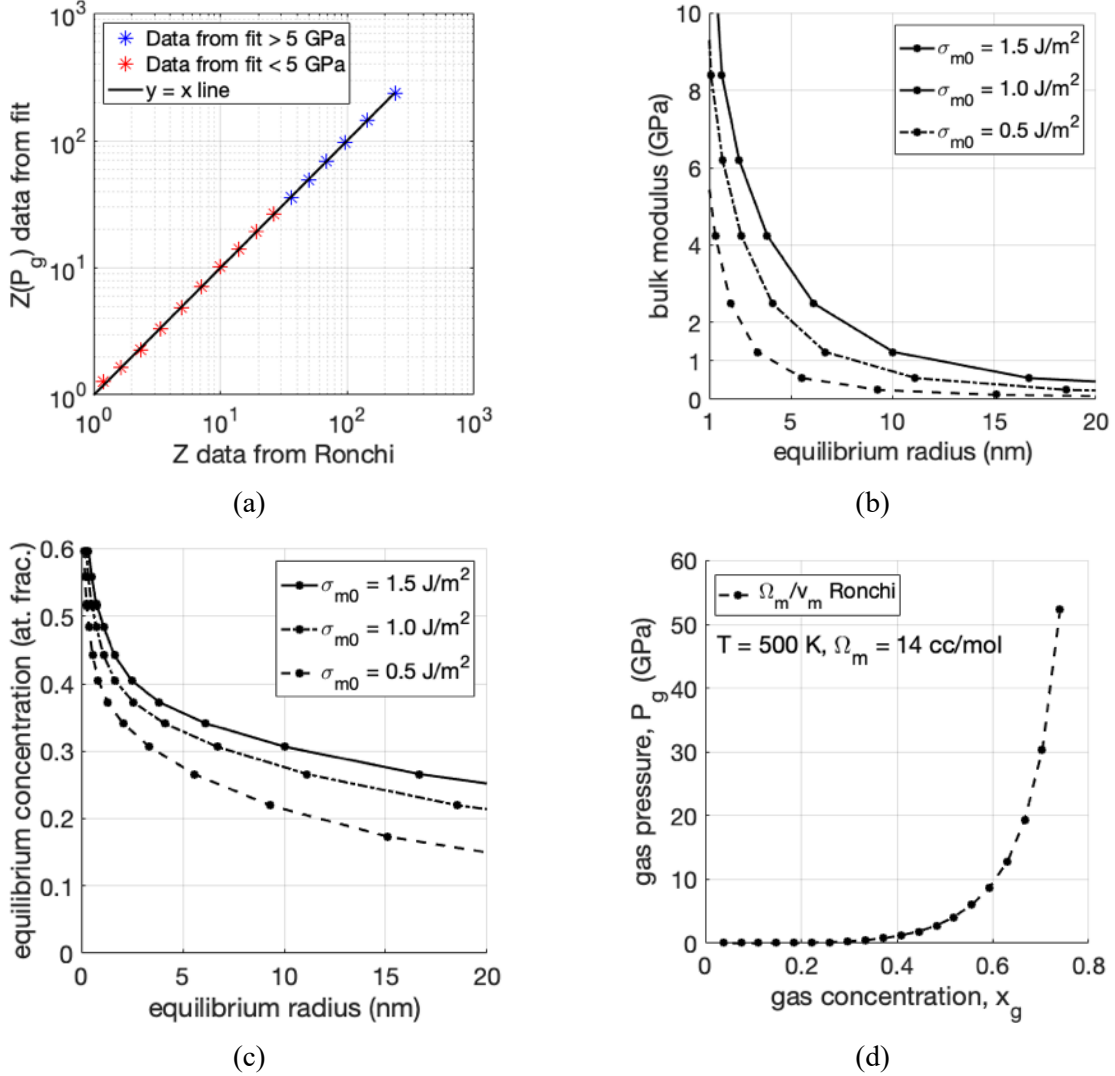


Figure 23. Xe gas bubble properties extracted from the Ronchi EOS at 500 K [30]. (a) The compressibility function $Z(P_g)$ is fit to two polynomials for $P_g < 5$ GPa and $P_g > 5$ GPa. The data from the fit is plotted (in a log-log scale) against that from Ronchi; (b) bulk modulus as determined from the fit as a function of equilibrium gas bubble size; (c) equilibrium gas concentration for various bubbles sizes; (d) gas pressure as a function of gas bubble concentration in U-10Mo. Calculations of equilibrium radius is shown for different values surface energies σ_{mb} .

Using Figure 23, K for a given equilibrium gas bubble radius is determined for the model. In order to parameterize the components of the gas bubble's elastic stiffness tensor \mathbf{C}_{b0} , the stress-strain constitutive relation for an isotropic material is first invoked as $\boldsymbol{\sigma} = \lambda \text{tr}(\boldsymbol{\varepsilon})\mathbf{I} + 2G\boldsymbol{\varepsilon}$, where $K = \lambda + \frac{2}{3}G$. Setting $G \approx 0$ and the diagonal components of the stress as $-(P - P_o)$, yields $-(P - P_o)\mathbf{I} = 3\lambda\varepsilon_{kk}\mathbf{I}$, which is equivalent to the defining expression for bulk modulus given by $(P - P_o) = -K\Theta$; where $\Theta = \frac{\Delta V}{V_o} = 3\varepsilon_{kk}$ is the volumetric strain and P_o is the reference pressure. Therefore, the above constitutive equation is used to set the components of \mathbf{C}_{b0} as

$$\mathbf{C}_{b0} = \begin{bmatrix} K & K & K & 0 & 0 & 0 \\ K & K & K & 0 & 0 & 0 \\ K & K & K & 0 & 0 & 0 \\ 0 & 0 & 0 & 10^{-3} & 0 & 0 \\ 0 & 0 & 0 & 0 & 10^{-3} & 0 \\ 0 & 0 & 0 & 0 & 0 & 10^{-3} \end{bmatrix} \quad (38)$$

2.3.2.4 Effective Elastic Constants Calculations

The multi-PF model was used to describe the elastically heterogeneous microstructure, and the AEH model was employed to evaluate the effective stiffness tensor \mathbf{C}^H . Validation of the model was performed on polycrystal α -U by comparing the AEH calculation obtained from the present PF-AEH integrated model with that performed on a microstructure defined over a conventional (non-PF) finite-element domain. Elastic constants of the orthorhombic single crystal $(C_{11}, C_{12}, C_{22}, C_{44}) = (299, 132, 231, 59)$ GPa were used. The effective constants for the polycrystal were obtained as $(C_{11}^H, C_{12}^H, C_{22}^H, C_{44}^H) = (292.6, 127, 272, 72.2)$ GPa, which agrees with the values reported from finite-element microstructures reported in [59].

For the evaluation of effective constants for γ -U-10Mo, a polycrystal microstructure (as shown in Figure 24) was generated using a random Voronoi tessellation algorithm. AEH calculations were performed for a different number of grains in the periodic representative volume cell and with different randomly generated rotation angles for the crystal/stiffness tensor orientations. A cell with 36 grain orientations was found to yield effective elastic constants that satisfied the isotropic elasticity criteria $C_{11}^H - C_{12}^H - 2C_{44}^H \approx 0$, which is expected from a non-textured polycrystal microstructure. Cells with a lower number of grains were found to yield $C_{11}^H - C_{12}^H - 2C_{44}^H > 0.5$ GPa and therefore not considered. The computational cost with the larger number of grains was optimized by employing only 10 non-overlapping grain order parameters in the PF model. Using the single crystal reference orientation constants $(C_{11}, C_{12}, C_{44}) = (140.2, 89.6, 38.7)$ GPa, the effective constants for the polycrystal are $(C_{11}^H, C_{12}^H, C_{44}^H) = (146.4, 83.3, 31.2)$ GPa. The single-crystal elastic constants were obtained from MD calculations and are reported in Section 2.3.1. The computational interface width was varied up to $1/10^{\text{th}}$ of the average grain size—compared to a very sharp interface; this resulted in a minor and negligible decrease (by less than 1.5%) in the effective constants.

In order to efficiently perform AEH calculations using a single timestep computation, the representative PF domain needs to be initialized to the required microstructure of pore-grain morphology and distribution. For this purpose, subroutines were developed in a MOOSE-based application to generate the PF microstructures for intergranular and intragranular pores. The intergranular pore distribution (Figure 24a) is generated by specifying the pore size, number density, and the contact angle of the lenticular pore. The intragranular pore distribution (Figure 24b) is generated by specifying the size, number density, and denuded zone width across the grain boundary. The cubic elastic constants for the void phase are set to a negligible finite value ($C_{11} = C_{12} = C_{44} = 10^{-3}$) while those for gas bubble phase are set to $C_{11} = C_{12} = K, C_{44} = 10^{-3}$. Figure 24c shows the heterogeneous variation in the elastic constants C_{44} for the void.

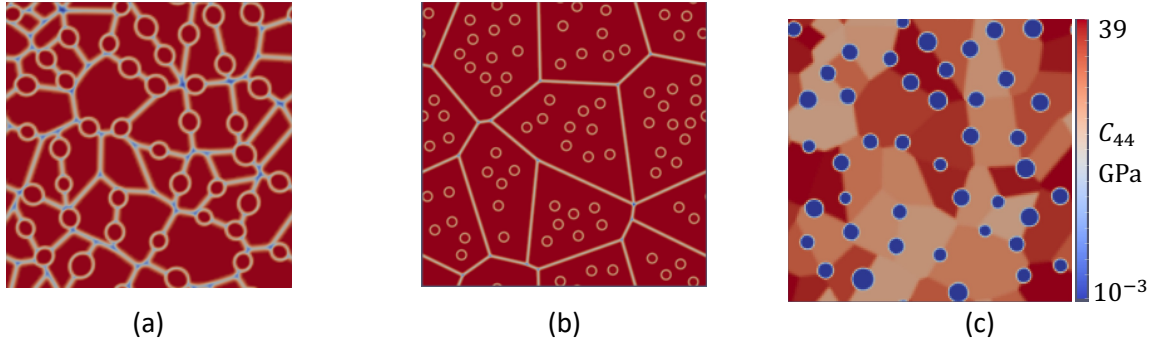


Figure 24. PF polycrystal microstructures for assessing effective elastic constants for (a) intergranular pores and (b) intragranular bubbles. (c) Heterogeneous elastic constants C_{44} for microstructure with intergranular voids.

AEH calculations were performed for intergranular voids of 150 nm radius distributed in microstructures with an average grain size of 1, 2.5, and 5 μm . Such microstructures are observed experimentally at higher burnups and post recrystallization of grains [27,39]. Figure 25 shows the degradation in the effective constants as a function of void volume fraction (relative to the void-free polycrystal) and for a given average grain size. The following trends are observed: (i) for a given pore volume fraction, larger grains exhibit greater GB coverage fraction, and therefore, show greater degradation in the effective constants; (ii) for smaller grains, GB saturation is reached at a larger pore volume fraction; however, the corresponding degradation is significantly lower compared to the saturated larger grains. These results indicate that both volume fraction and GB coverage are important parameters to quantify elastic property degradation. A case study was performed to look at the importance of GB coverage of the lenticular morphology of intergranular pores. Lenticular pores with the same number density and volume as that of equivalent circular pores exhibited up to 4% lower effective constants. Therefore, the accuracy/uncertainty of the AEH calculations will depend on the accurate representation of grain-pore morphology, in addition to the accuracy of grain and pore phase elastic constants.

AEH calculations for the Xe gas bubble distribution in the polycrystal were performed, with the bulk modulus values obtained from the fit to the Ronchi EOS. Since the gas bubbles have finite $C_{11} = C_{12} = K$, in contrast to the vanishing value for voids, the degradation in these constants is expected to be lower for higher gas concentration. The effective constants obtained for 1 nm and 150 nm pore sizes are contrasted for a void (zero gas concentration) and an equilibrium gas bubble in Table 6. The number densities and volume fractions used for the current calculations were taken from a similar study [73] focused on assessing the effective thermal conductivity degradation in U-10Mo.

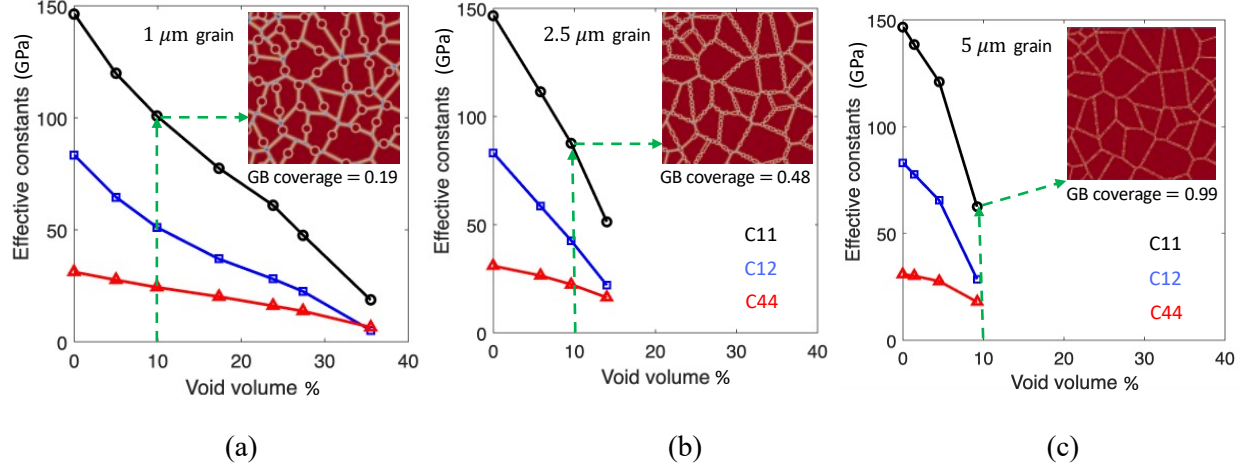


Figure 25. Effective elastic constants for polycrystalline microstructure with 150 nm intergranular voids, calculated as a function of void volume percent for different grain sizes.

Table 6. Effective constants for polycrystal with equilibrium gas bubbles parameterized using the bulk modulus from Ronchi's EOS and compared against voids.

	Radius (nm)	Number density	Volume %	Equilibrium Xe concentration	Phase elastic constants		Effective elastic constants		
					C_{11}, C_{12}	C_{44}	C_{11}^H	C_{12}^H	C_{44}^H
Void	1	$3 \times 10^{-3}/\text{nm}^3$	4.0	0	10^{-3}	10^{-3}	125.9	68.2	28.5
Bubble				0.49	13	10^{-3}	132.5	74.7	28.5
Void	150	$3.4 \times 10^{-7}/\text{nm}^2$	2.5	0	10^{-3}	10^{-3}	132.9	73.4	29.5
Bubble				0.08	0.01	10^{-3}	132.9	73.4	29.5

2.3.2.5 Effect of Interfacial Stress and Gas Pressure

In addition to the bulk elastic stresses defined via linear elasticity, $\sigma_m = \mathbf{C}_m : \boldsymbol{\varepsilon}_m$, additional stress contributions generated by the pore-matrix interface σ_{mb}^{st} and gas pressure σ_b^p need to be incorporated to model the stress state across microstructure. For this purpose, the Voigt-Taylor scheme is utilized to define the phase stress tensors and their interpolation across the diffuse interface [74]. The mechanical equilibrium condition is given by

$$\nabla \cdot \boldsymbol{\sigma} = \nabla \cdot [h_m \boldsymbol{\sigma}_m + h_b \boldsymbol{\sigma}_b + \boldsymbol{\sigma}_{mb}^{st}] = 0 \quad (39)$$

Assuming that the surface tension is of the same magnitude as the surface energy, the surface tension for the multi-order parameter (η_{m0}, η_{b0}) interface can be derived as [75]

$$\boldsymbol{\sigma}_{mb}^{st} = \left(w \psi(\gamma_{mb}) + \frac{\kappa}{2} |\nabla \eta_{m0}|^2 + \frac{\kappa}{2} |\nabla \eta_{b0}|^2 \right) \mathbf{I} - (\kappa \nabla \eta_{m0} \otimes \nabla \eta_{m0} + \kappa \nabla \eta_{b0} \otimes \nabla \eta_{b0}) \quad (40)$$

where $\psi(\gamma_{mb})$ is the non-gradient contribution to the potential energy defined in the integrand of the functional Ψ in Eqn. 29. At steady state, the above expression reduces to the interfacial energy σ_{mb} and acts tangentially along the interface. The surface tension exerts a force $\nabla \cdot \boldsymbol{\sigma}_{mb}^{st}$ that is proportional to σ_{mb} and the curvature of the interface and acting in the direction normal to the interface. In the presence of gas within the pore, an outward dilatational stress should be exerted by the gas atoms. This contribution $\sigma_b^p = -P_g^{EOS}(c_g) \mathbf{I}$ is defined using the pressure-concentration relationship $P_g^{EOS}(c_g)$ derived from the Ronchi EOS. Therefore,

$$\boldsymbol{\sigma}_b = \mathbf{C}_b : \boldsymbol{\varepsilon}_b - P_g^{EOS}(c_g) \mathbf{I} \quad (41)$$

where the elastic constants in \mathbf{C}_b are assumed to be negligible for simplicity, with a very small non-zero value to ensure continuity of the displacement fields. The negative sign in the second term corresponds to the compressive stress that the bubble pressure exerts on the surrounding matrix. If the outward force exerted by the gas pressure on the bubble interface is sufficiently high, it can balance the inward force due to the surface tension.

The model is demonstrated via 2D ($d = 2$) simulation in Figure 26 for a void and an equilibrium gas bubble of 1 nm radius in polycrystalline, isotropic U-10Mo matrix. Natural boundary conditions are employed for the simulation. The void is seen to exert a tensile stress component σ_{xx} in the surrounding matrix radially along the x direction. On the other hand, for the equilibrium gas bubble, the gas pressure exactly balances the surface tension $P_g^{eq} = \frac{(d-1)\sigma_{mb}}{R}$, and therefore, no tensile or compressive stress component σ_{xx} is observed within the matrix. The stress fields are better demonstrated by solving the problem in spherical coordinates, which are also representative of three-dimensions ($d = 3$). The solutions of radial σ_{rr} , tangential $\{\sigma_{\theta\theta}, \sigma_{\phi\phi}\}$ and hydrostatic $\sigma_h = \frac{1}{3}(\sigma_{rr} + \sigma_{\theta\theta} + \sigma_{\phi\phi})$ stress fields are plotted in Figure 27 for the various scenarios of a 1 nm intragranular pore: (a) void, (b) equilibrium Xe gas bubble, (c) underpressurized Xe gas bubble, and (d) over-pressurized Xe gas bubble. To validate the implementation, the simulated solutions are compared with analytic solutions, which are represented by σ^{an} and plotted as dashed lines. Assuming isotropic elasticity and a sharp pore-matrix interface, the analytic stress fields within the bulk regions are derived following the general procedure outlined in [76,77].

$$\text{For } r < R, \sigma_{rr} = \sigma_{\theta\theta} = \sigma_{\phi\phi} = -\frac{3K_b}{4G_m+3K_b} \left(\frac{2\sigma_{mb}}{R} - P_g \right) - P_g. \quad (42)$$

$$\begin{aligned} \text{For } r > R, \sigma_{rr} &= \frac{4G_m}{4G_m+3K_b} \left(\frac{2\sigma_{mb}}{R} - P_g \right) \frac{R^3}{r^3}, \\ \sigma_{\theta\theta} = \sigma_{\phi\phi} &= -\frac{2G_m}{4G_m+3K_b} \left(\frac{2\sigma_{mb}}{R} - P_g \right) \frac{R^3}{r^3}. \end{aligned} \quad (43)$$

In the above equations, G_m and K_b are the shear modulus of the matrix and the bulk modulus of the pore, respectively. We assume $K_b = 0$ to obtain simplified solutions. Within the bulk regions beyond the diffuse interface width l_{mb} , i.e., $r > R + \frac{l_{mb}}{2}$ and $r < R - \frac{l_{mb}}{2}$, the stress fields from the PF simulations match exactly with that from the analytic solutions. Furthermore, from the solutions to the equilibrium gas bubble, we numerically evaluate the difference between the tangential and radial stress distribution as $\int_0^{+\infty} (\sigma_{\theta\theta} - \sigma_{rr}) = \sigma_{mb}$ and confirm that the magnitude of the interfacial energy σ_{mb} is recovered exactly. From the results in Figure 27, we can draw the following observations:

1. A void generates tensile radial stress field $\sigma_{rr} = \frac{2\sigma_{mb}R^2}{r^3}$ within the matrix. The pressure difference between the matrix and void phase is zero, $\Delta P_h \approx 0$.
2. A Xe gas bubble with equilibrium concentration (≈ 0.49 for 1 nm radius) provides the pressure necessary to exactly balance the surface tension, $P_g^{eq} = \frac{2\sigma_{mb}}{R}$ ($= 3$ GPa) and therefore $\sigma_{rr} = 0$ within the matrix phase. The pressure difference between the phases is $\Delta P_h = P_g^{eq}$.
3. An underpressurized gas bubble with concentration less than the equilibrium value results in a tensile radial stress $\sigma_{rr} = \left(\frac{2\sigma_{mb}}{R} - P_g \right) \frac{R^3}{r^3} > 0$ since $P_g < P_g^{eq}$.
4. An over-pressurized gas bubble with concentration greater than the equilibrium value generates a compressive radial stress $\sigma_{rr} < 0$ within the matrix since $P_g > P_g^{eq}$.

5. In all of the above cases (irrespective of the surface tension and the pressure within the pore), the hydrostatic pressure within the matrix vanishes (i.e., $P_h = -\sigma_h = 0$), which is consistent with the analytic solution obtained using Eq. 43. A slight shift in the stress fields of the over-pressurized and underpressurized bubbles is expected if the assumption $C_b = 0$ and $K_b = 0$ is relaxed to realistic gas bubble values.

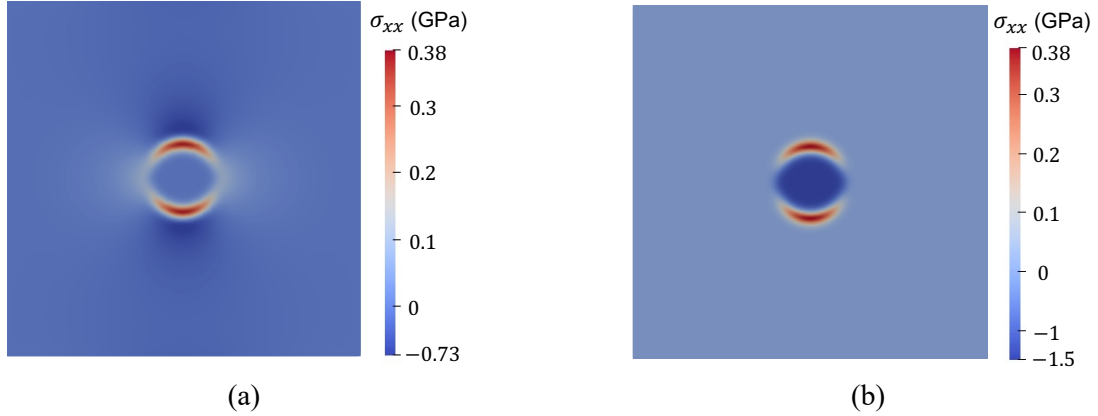


Figure 26. Stress distribution of the component σ_{xx} for a intragranular pore of 1 nm radius in a 2D system. (a) Void (zero gas pressure). (b) Equilibrium Xe gas bubble.

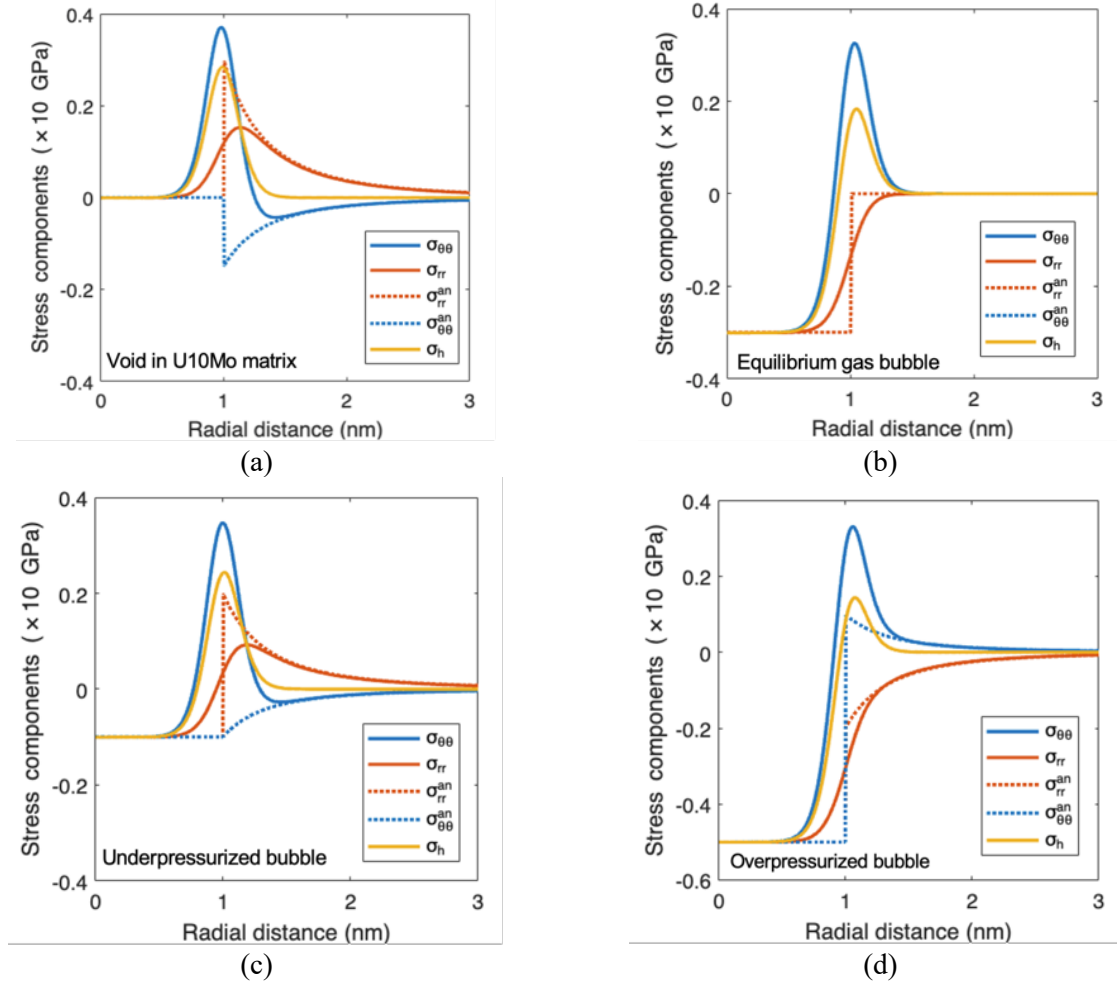


Figure 27. Radial, tangential, and hydrostatic stress fields across the pore-matrix interface for intragranular pore of 1 nm radius in the isotropic U-10Mo matrix. Dashed lines are the analytic solutions of the stress fields within the bulk derived under the sharp-interface assumption. (a) Void with zero gas pressure, $P_g = 0$. (b) Xe gas bubble with equilibrium pressure, $P_g = 3$ GPa. (c) Underpressurized bubble with $P_g = 1$ GPa. (d) Over-pressurized bubble with $P_g = 5$ GPa.

2.3.2.6 Summary

The AEH method for linear elasticity theory was employed in this study to allow evaluations of effective elastic constants for U-10Mo fuel microstructures representative of different FDs during fuel burnup. The interfacial energies and the elastic heterogeneity of the polycrystalline U-10Mo with inter- and intragranular voids and gas bubbles were modeled using a multi-PF grand potential model combined with linear, small-strain mechanics. The cubic elastic constants for single crystal U-10Mo were informed from atomistic calculations. The properties of Xe gas were extracted from the data and EOS by Ronchi [30,72]. This EOS was used to derive the bulk modulus data required for quantitative AEH calculations. Furthermore, the EOS was used along with the Young-Laplace equation to derive properties of the equilibrium bubble phase, viz. gas pressure, concentration, and bubble size. To enable efficient AEH calculations, subroutines were developed to generate representative microstructures with intragranular and lens-shaped intergranular voids. The results of AEH calculations showed a strong degradation in elastic constants with an increase in void and gas bubble volume fraction and grain boundary coverage. The effective constants in shear C_{44} were found to be identical for both void and bubble microstructures, whereas the effective C_{11} and C_{22} were significantly lower for microstructures with void (as compared to

equilibrium bubbles) due to the absence of gas pressure resisting compression. In order to model the effect of gas more physically, we developed a model accounting for the surface tension and the additional gas pressure in the bubble. The results show that surface tension effects can be strong for the nanometer-sized intragranular voids, and large equilibrium gas concentrations can provide the necessary pressure in a bubble to balance the surface tension effects.

The present study demonstrated the utility of the AEH-PF modeling technique to obtain crucial insight into the degradation of the overall properties of the fuel. For simplicity, we neglected the explicit concentration-dependence, generation of fission products and their reactions, and diffusive evolution of the microstructure. However, the model can be extended further to enable more accurate representations of the fuel microstructure during burnup. For instance, chemical potential dependence can be added to the grand potential model to study the effect of gas concentration on stress fields (and vice-versa). In addition to providing mechanistic insight, the developed AEH-PF modeling technique provides homogenized material property information that can be used by larger-scale engineering models.

2.4 Fracture Toughness in Monolithic U-10Mo Fuel

To minimize the interaction between the U-10Mo fuel and the Al-alloy matrix, in the monolithic fuel design, a Zr diffusion barrier is added between the fuel and the matrix. Consequently, an interaction zone forms between U-10Mo and Zr, referred to as the UMo-Zr interaction zone [78], and grows during irradiation. At high burnups, fracture develops in the fuel plate, primarily in a region with high density of gas bubbles along the interface between the different sublayers in the interaction zone [1]. This indicates potential degradation in fracture stress either in the U-10Mo fuel or in the interaction zone, or both. This section focuses on the degradation in fracture properties induced by gas bubbles in U-10Mo fuel (21.8% in atomic percent) and in the UMo-Zr interaction zone. The change in fracture properties in bulk U-10Mo fuel is calculated using MD simulations. The change in fracture properties in the UMo-Zr interaction zone is simulated using the PF fracture method [79][80], with the model implemented in MOOSE [81]. The objective of this work is to elucidate the effect of gas bubbles, in terms of gas bubble size, density, and connectivity on fracture initiation and propagation in U-10Mo fuel and the interaction zone.

2.4.1 MD Simulations of Mechanical Deformation in U-10Mo Bicrystal

The possible fracture propagation along GBs in U-10 Mo was studied using MD simulations with the ADP U-Mo-Xe potential discussed in Section 2.3.1. Here, Mo atoms with 21.8 atomic percent were randomly mixed with U atoms to create bcc U-10Mo in solid solution. A bicrystal model as shown in Figure 28 was adopted, with an oval through-void/bubble (referred to as bubble) in the middle. Periodic boundary conditions were applied along all three directions, meaning that there was another GB at the top/bottom of the simulation cell in Figure 28. Three different types of GBs, $\langle 110 \rangle$ symmetric tilt (ST) $\Sigma 3$, $\Sigma 9$, and $\Sigma 11$ were simulated to investigate the effects of GB character and loading geometry. Three different GVratios (0.0, 0.1, and 0.25) were simulated by introducing different amount of gas atoms into the notch (a through bubble) to represent different bubble internal pressure. After relaxing the simulation cells using zero-stress boundary conditions, uniaxial tension was applied along the GB normal direction, with a strain rate of $10^8/s$, which is extremely high compared to experimental tensile conditions but typical in MD simulations. Zero-stress boundary conditions were kept for the other two directions during loading. Up to 50% engineering strain was reached in the simulations. The temperatures were kept at 300 K, 600 K, and 900 K during the loading period. For postprocessing, the stress-strain curves were obtained by averaging the virial atomic stress. The deformation mechanisms were extracted using the dislocation extraction algorithm implemented in Ovito [82].

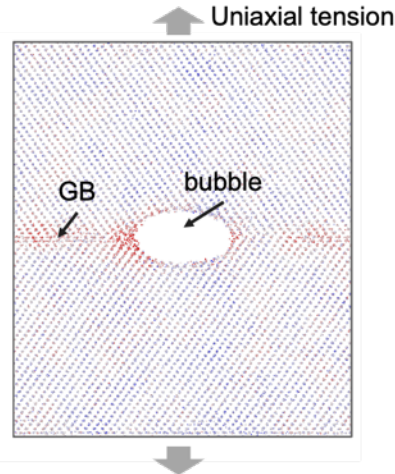


Figure 28. Schematic of bicrystal model under uniaxial tension. An oval through notch (the bubble) is created on the GB in the middle. The atoms are colored by atomic stress showing that without gas atoms introduced in the bubble, stress concentration develops at the intersection of bubble and grain boundary.

As shown in Figure 29, under uniaxial tension, U-10 Mo was deformed by plastic deformation without fracture propagation, as indicated by the sawtooth shaped stress-strain curves. Following the initial elastic deformation, significant stress drop was induced by initiation of plastic events such as dislocation emission or twinning, which will be described later. Recovery of stress took place once the dislocations or twinning has reached the other GB. The same process repeated with up to 50% engineering strain without fracture propagation, suggesting that bulk U-10Mo is very ductile.

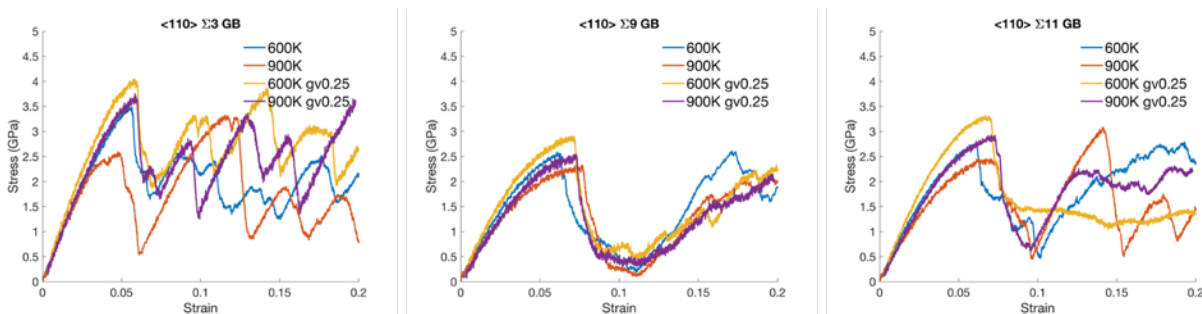


Figure 29. Stress-strain curves for simulations with $\langle 110 \rangle$ symmetrical tilt (ST) $\Sigma 3$, $\Sigma 9$, and $\Sigma 11$ GBs, showing ductile behavior via plastic deformation without fracture.

It can be seen that an increasing temperature softens U-10Mo by comparing the stress-strain curves at 600 K and 900 K. The elastic modulus, represented by the slope of the stress-strain curve in the elastic range, decreased with increasing temperature for all three cases. This is consistent with the temperature dependence obtained in bulk U-10Mo in the previous section. The yield strength, which is the first peak in stress following the elastic range, also decreased with increasing temperature. It is also interesting to see that increasing bubble pressure hardens U-10Mo by increasing both the elastic modulus and the yield strength without reducing the ductility. Very similar stress-strain curves were obtained with (GV=0.25) and without (GV=0.0) Xe gas atoms.

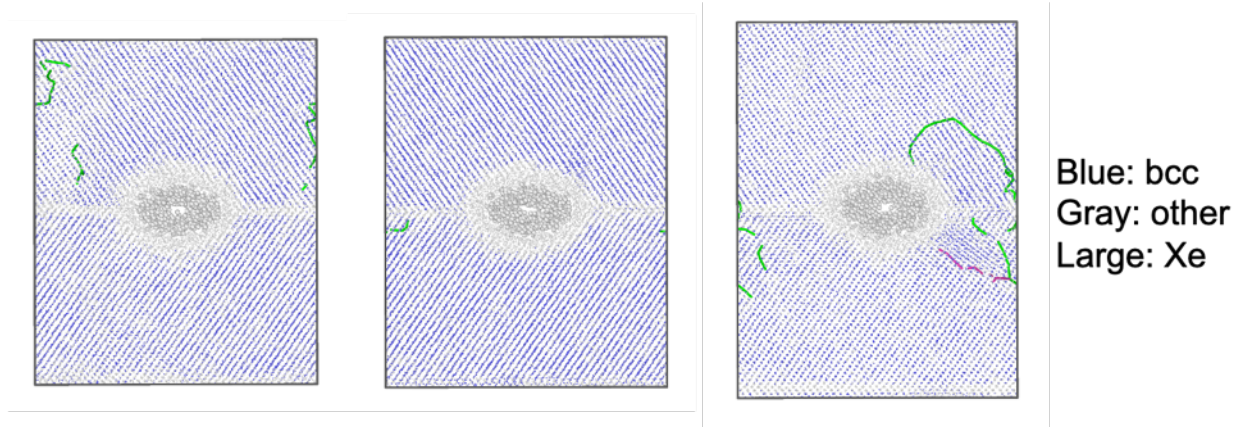


Figure 30. Snapshots of the atomic configurations showing dislocation emission from GBs in the simulation cell with $\langle 110 \rangle$ ST $\Sigma 3$ GBs with a GV ratio of 0.25. The green lines are $1/2 \langle 111 \rangle$ dislocations and the purple lines are $\langle 100 \rangle$ dislocations.

The deformation process of the $\langle 110 \rangle$ $\Sigma 3$ simulation cell is described in Figure 30. The plastic deformation was mainly mediated by $1/2 \langle 111 \rangle / \{110\}$ slip. Laterally, junctions of dislocations with the $\langle 100 \rangle$ Burgers vector have also been identified. Interestingly, most dislocations are not emitted from the intersection of the bubble and the GB, which is supposedly a location for stress concentration and preferential dislocation emission. The region around the bubble surface, about 1 nm in thickness, was found to become disordered due to bubble pressure. Different relaxation procedures have been attempted during preparing the simulation cells, and such a disordered region occurred in all cases. Another surprising observation is that the Xe gas atoms developed a shelled configuration, with a center hole in the notch. As Xe gas atoms are expected to repel each other and occupy open space whenever possible; the formation of a center hole requests some further assessment of the potential.

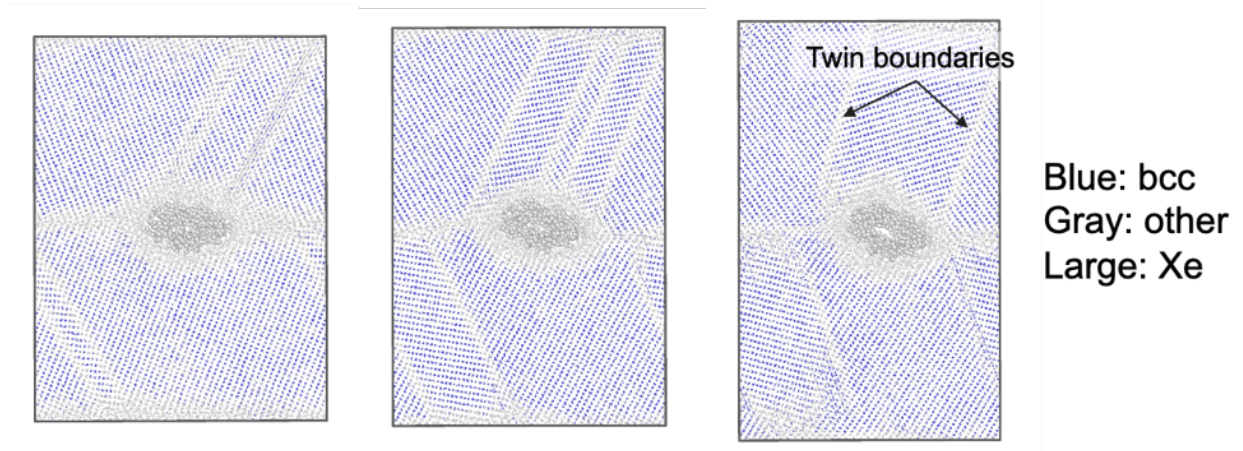


Figure 31. Snapshots of the atomic configurations in the simulation cell with $\langle 110 \rangle$ ST $\Sigma 9$ GBs with a GV ratio of 0.25. The deformation is dominated by twinning.

The deformation process of the $\langle 110 \rangle \Sigma 9$ simulation cell is described in Figure 31. Different than that for the case of $\langle 110 \rangle \Sigma 3$ bicrystal, the plastic deformation for the $\langle 110 \rangle \Sigma 9$ bicrystal was dominated by deformation twinning. In bcc crystals, deformation twinning takes place by $\frac{1}{6}\langle 111 \rangle$ slip on adjacent $\{112\}$ planes [83] with the twin boundaries on the $\{112\}$ plane. Twinning was found to initiate from both bubble surfaces and GB regions away from the bubble, again showing no preferential nucleation at the bubble and GB intersection.

The deformation process of the $\langle 110 \rangle \Sigma 11$ simulation cell is described in Figure 32. In this case, both deformation twinning and dislocation emission were identified with the former being dominant. Again, twinning and dislocations could be emitted from both the bubble surface and the GB, with no preferential nucleation at the bubble and GB interaction. Similar to the cases of $\langle 110 \rangle \Sigma 3$ and $\Sigma 9$ bicrystals, the Xe-bubble surface became disordered, with a center hole free of gas atoms that formed in the middle of the bubble.

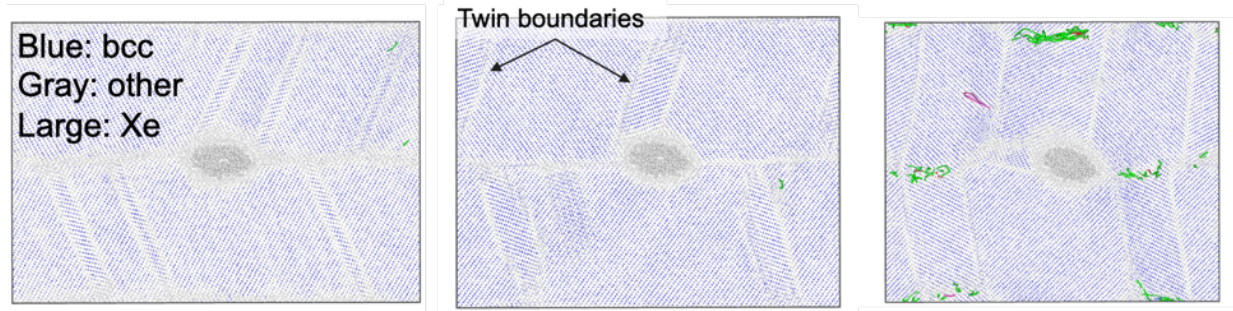


Figure 32. Snapshots of the atomic configurations in the simulation cell with $\langle 110 \rangle \Sigma 11$ GBs with a GV ratio of 0.25. The deformation is mediated by both twinning and dislocation slip.

The different deformation modes characterized in the above simulations can be understood by calculating the maximum Schmid factor for the $\langle 111 \rangle / \{110\}$ and the $\langle 111 \rangle / \{112\}$ slip systems, which are responsible for dislocation slip and twinning, respectively. The Schmid factor is defined as

$$S = \cos \phi \cos \lambda \quad (44),$$

where ϕ is the angle between the loading direction and the slip plane normal, and λ is the angle between the loading direction and the Burgers vector; it is essentially the ratio of the resolved shear stress over the applied stress. Due to the periodic boundary condition, not all slip systems are available. Specifically, only slip planes that are parallel to the tilt axis of the bicrystal, $\langle 110 \rangle$ here, are compatible with the periodic boundary condition and can be activated. Here, the maximum Schmid factors were calculated for the available slip systems only and compared in Figure 33.

For the $\Sigma 3$ bicrystal, the $\langle 111 \rangle / \{110\}$ slip system has a higher maximum Schmid factor, indicating dislocation slip is favored over twinning, consistent with the results shown in Figure 30. While for the $\Sigma 9$ bicrystal, the maximum Schmid factor for the $\langle 111 \rangle / \{112\}$ slip system is much higher than that for $\langle 111 \rangle / \{110\}$, indicating twinning is favored, consistent with the results shown in Figure 31. The $\langle 111 \rangle / \{112\}$ slip system also has a much higher maximum Schmid factor than $\langle 111 \rangle / \{110\}$, although the difference is not as large as for the $\Sigma 9$ bicrystal. Accordingly, the plastic deformation for the $\Sigma 11$ bicrystal was still primarily via deformation twinning, with limited dislocation slips, as shown in Figure 32. These results indicate that the deformation modes in U-10Mo are consistent with the Schmid law overall, although it has been well known that the Schmid law may be violated in bcc crystals.

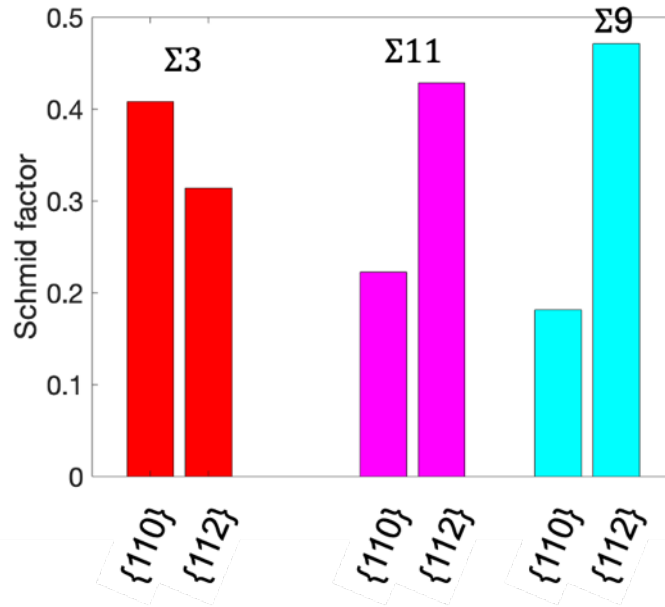


Figure 33. Comparison of maximum Schmid factors for $\langle 111 \rangle / \{110\}$ slip system for dislocation and $\langle 111 \rangle / \{112\}$ slip system for twinning in the simulation cells with $\langle 110 \rangle$ ST $\Sigma 3$, $\Sigma 9$, and $\Sigma 11$ GBs. Slip systems that are not compatible with the periodic boundary conditions are ignored.

2.4.1.1 Summary

U-10Mo was found to be very ductile under uniaxial tension by MD simulations adopting the bicrystal model. No fracture propagation along GBs was observed with up to 50% engineering strain. Considering that the extremely high-loading rate in MD simulations usually facilitates fracture, the ductile nature of U-10Mo indicated by the MD simulations seems to be convincing. To the author's knowledge, there has been no experimental observations of fracture in U-10Mo. Three plastic deformation modes were identified depending on the loading orientation: (i) $\langle 111 \rangle / \{110\}$ dislocation slip, (ii) $\langle 111 \rangle / \{112\}$ deformation twin, and (iii) their combinations, respectively. Overall, the selection of deformation mode was found to be consistent with the Schmid law. Increasing temperature softens U-10Mo, decreasing both the elastic moduli and yield strength. Increasing bubble pressure hardens U-10Mo, increasing both the elastic moduli and yield strength.

Further assessment of the interatomic potential is suggested by two specific observations. First, the bubble surface became disordered after relaxation at finite temperatures. This led to release of the stress concentration at crack tips, which was partially responsible for the absence of fracture propagation. The second is the formation of a center hole in gas bubbles, likely caused by attractive instead of repulsive interaction between metal atoms (U and Mo) with Xe. Attention is needed to identify possible deficiencies in current interatomic potentials and to improve the accuracy of MD to maximize the usefulness of atomistic data in engineering-scale modeling.

The absence of fracture propagation in U-10Mo has some interesting implications on the fracture observed in the UMo-Zr interaction zone at high burnups [84]. The appearance of fracture may be caused by three possible reasons:

1. Extremely high gas bubble coverage or gas bubble density. At extremely high bubble density, bubbles are very close to each other, so that the stress in regions between bubbles are substantially higher than in other regions, leading a necking effect. The bubbles may grow by emission and propagation of

dislocations until they coalesce with each other, causing the failure of the fuel matrix. This effect will be further studied by MD simulations.

2. Creep damage at stress levels lower than the yield stress. Instead of having cleavage fracture, creep damage may occur and manifest itself as bubble growth. Such creep damage is expected to occur in regions with high bubble densities due to the higher stress in regions between bubbles. Creep damage will grow until complete failure takes places. This will be further evaluated using PF fracture.
3. Phase separation in the UMo-Zr interaction zone. As has been shown in the literature [84], different phases develop in the interaction zone, with a U enriched zone, likely in the alpha-U phase. This zone also features the highest bubble density, probably because of the higher FD caused by the locally higher U concentration. Therefore, fracture is actually in the alpha-U phase or along the phase interfaces, which are usually weak point in materials, instead of in the U-10Mo matrix. This will also be studied further using both MD and PF fracture.

It should be noted that the above three mechanisms are not mutually exclusive, they may in fact operate together and the failure of the UMo fuel matrix may be caused by their compounding effect.

2.4.2 Phase Field Fracture

2.4.2.1 Methodology

The PF brittle fracture model is adopted from [79,80]. The damage parameter in the PF model is non-smooth and is described by an exponential function

$$c(x) = \exp\left(-\frac{|x|}{l}\right) \text{ for } -\infty < x < \infty \quad (45)$$

where the diffuse crack profile is governed by the diffuse crack width l .

The damage variable, c , evolves to minimize the total free energy in the system. During crack initiation and propagation, elastic energy is released in the form of fracture energy, and the total free energy can be described by

$$\Psi_{total} = \Psi_{elastic} + \Psi_{fracture} \quad (46)$$

The elastic energy release is defined as

$$\Psi_{elastic} = \int_{\Omega} \psi d\Omega \quad (47)$$

where ψ is the elastic energy density of the material. The elastic energy density ψ is generally split into the tensile, ψ^+ , and compressive, ψ^- , parts as

$$\psi = g(c)\psi^+ + \psi^- \quad (48)$$

where ψ^+ is the portion of the energy density that contributes to the crack propagation while ψ^- does not. In the present study, due to the nature of the loading condition considered, the decomposition of elastic energy density is turned off. Therefore, both the compressive and tensile stress relief due to fracture propagation is considered. $g(c)$ is a degradation function that removes ψ within a crack and is defined by

$$g(c) = (1 - c)^2(1 - b) + b \quad (49)$$

where $b \ll 1$ is a numerical parameter that ensures positive definiteness of the system when $c = 1$.

The surface energy of the crack can be described as

$$\Psi_{fracture} = \int_{\Omega} G_c \gamma d\Omega \quad (50)$$

where G_c is the crack surface energy, and γ is the crack surface density function per unit volume

$$\gamma(c, \nabla c) = \frac{1}{2l} c^2 + \frac{l}{2} |\nabla c|^2 \quad (51)$$

The total free energy can be rewritten as

$$\Psi_{total} = \Psi_{elastic} + \Psi_{fracture} \quad (52)$$

$$\Psi_{total} = \int_{\Omega} \psi d\Omega + \int_{\Omega} G_c \gamma d\Omega \quad (53)$$

$$\Psi_{total} = \int_{\Omega} g(c) \psi d\Omega + G_c \int_{\Omega} \left(\frac{1}{2l} c^2 + \frac{l}{2} |\nabla c|^2 \right) \quad (54)$$

Taking the variations of the total energy, the governing equation can be written as

$$\frac{dc}{dt} - \frac{1}{\eta} \left(\frac{dg(c)}{dc} \psi + \frac{G_c}{l} c - \nabla \cdot (G_c l \nabla c) \right) = 0 \quad (55)$$

$$\nabla \cdot (g(c) \sigma) = 0 \quad (56)$$

Due to the irreversibility of the damage (i.e., that crack do not heal once initiated), the maximum value that ψ experienced at a given location, $[\psi]_{max}$, is used throughout the simulation.

Assuming the evolution of c to be quasistatic

$$\frac{dg(c)}{dc} [\psi]_{max} + \frac{G_c}{l} c - \nabla \cdot (G_c l \nabla c) = 0 \quad (57)$$

$$\nabla \cdot (g(c) \sigma) = 0 \quad (58)$$

2.4.2.2 Simulation Set Up

The geometry for the simulation is designed to capture the correlation between critical fracture stress with bubble size, density, alignment, and gas pressure. According to previous experimental data [78], the interaction between U-Mo/Zr forms several sublayers with varying U compositions (Figure 34). These sublayers have different mechanical properties, and the SEM image of the irradiated sample showed variable bubble density across the interface [84]. The varying size and density of the bubbles may correlate to the U contents within the layers. Thus, a simulation domain has been designed (Figure 35) with three sublayers (UZr₂, U-Mo with U enriched, and U-Mo with low U) that have different mechanical properties and bubble distributions.

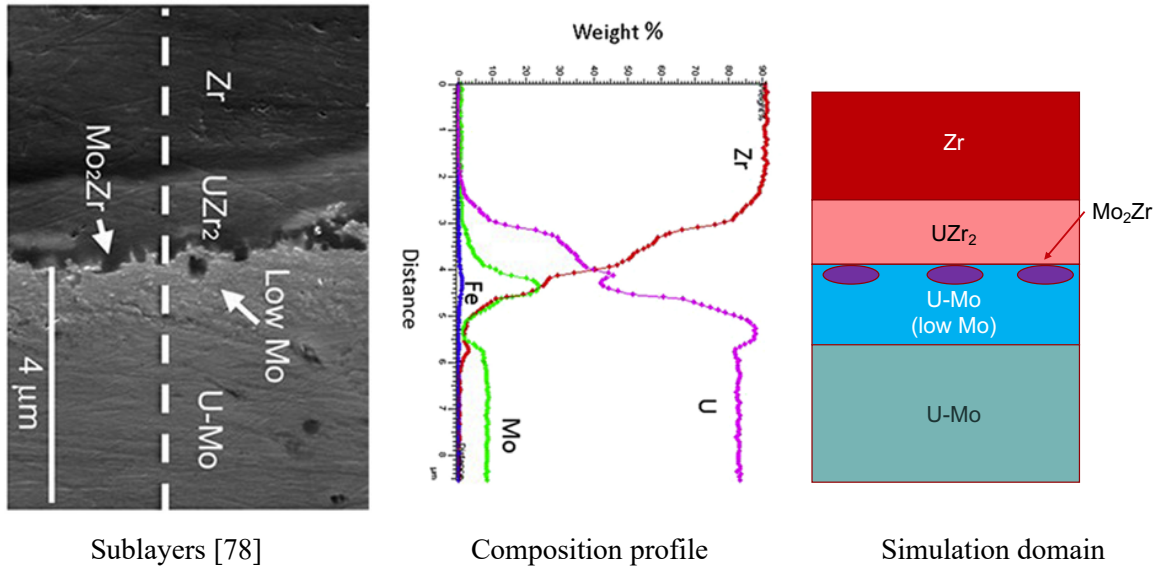


Figure 34. Electron image and composition profile of sublayers across U-Mo/Zr interface and the planned simulation domain.

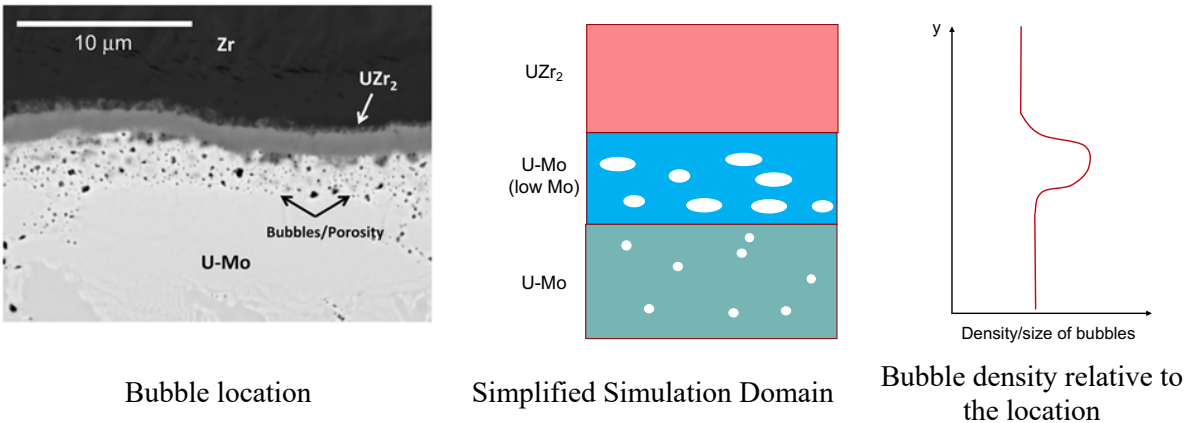


Figure 35. Bubble morphology from experiments and the proposed simulation cell design.

2.4.2.3 Preliminary Results

The model adopted for the analysis was tested with a simple geometry and with a single preinitialized bubble. For testing the model, several conditions have been simulated which are depicted in Figure 36–Figure 38 to demonstrate the capability. The 2D fracture initiation from a single gas bubble is shown Figure 36, and that from a random distribution of gas bubbles is shown in Figure 37. In Figure 38, 3D fracture initiation and propagation is shown. The bubbles are considered lenticular in shape as those formed on GBs or phase boundaries. In all these simulations, the domain is considered to be a single uniform crystal aligned to the laboratory axis direction. The bottom boundary was set to the Roller condition (i.e., no displacement in the y-direction), and uniform outward displacement with time from the top boundary was applied. For the material property, uniform UMo (U-rich) is considered (Table 7). The simulation shows the expected fracture propagation path and stress distribution at the end of the simulation. Stress initially increased near the gas bubbles, and once it reached the critical value, the fracture started propagating. While the crack propagated, the stress was relaxed near the fracture plane while increasing on the fracture tip. Once the fracture divided the domain in half, the stresses were fully relaxed, and no more fracture was initiated.

Table 7. Material properties used for the preliminary PF fracture analysis.

Material	Elastic Constant (MPa)	Poisson Ratio	Critical fracture surface energy (MPa-mm)	Crack Width (μm)
UZr ₂	126.7	0.3	0.214	0.25
UMo (U-rich)	169	0.3	0.214	0.25
UMo	100	0.3	0.214	0.25

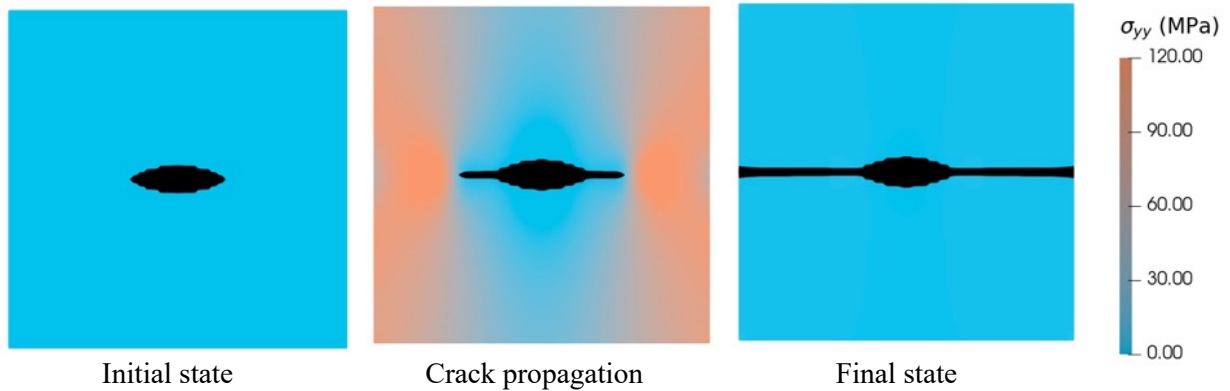


Figure 36. PF fracture simulation with a single bubble initiated as a pre-cracked surface. Roller constraint was applied on the bottom of the domain, and uniform displacement with time was applied outward from the top boundary.

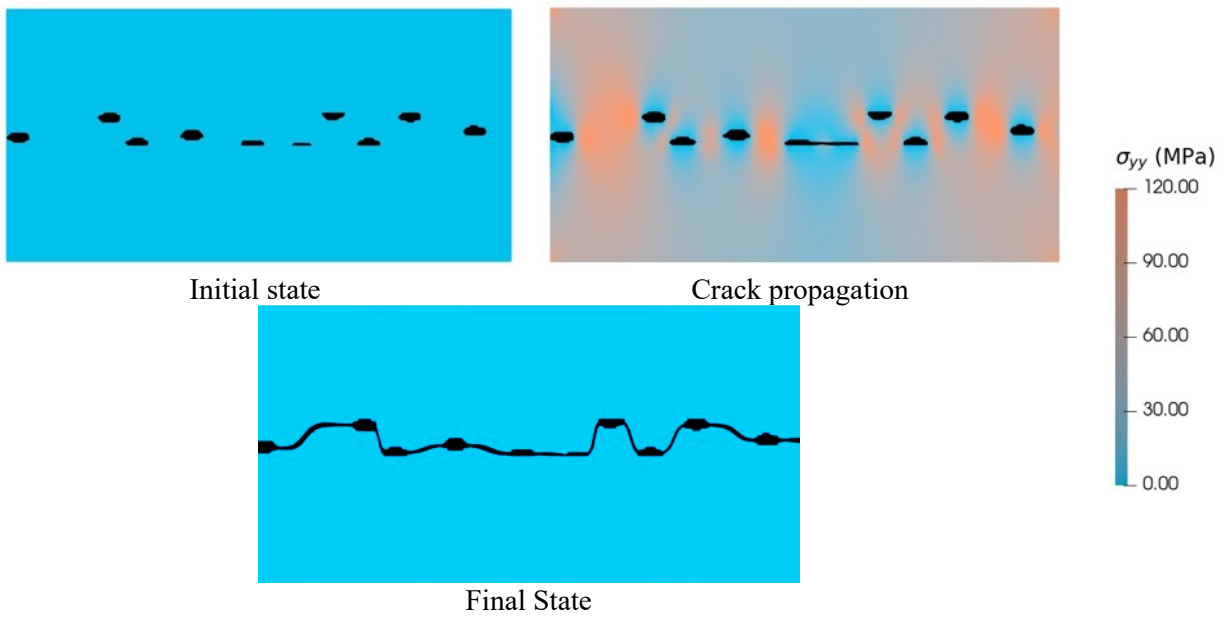


Figure 37. PF fracture simulation of multiple bubbles align in the middle of the domain. The boundary conditions are similar to that of Figure 36.

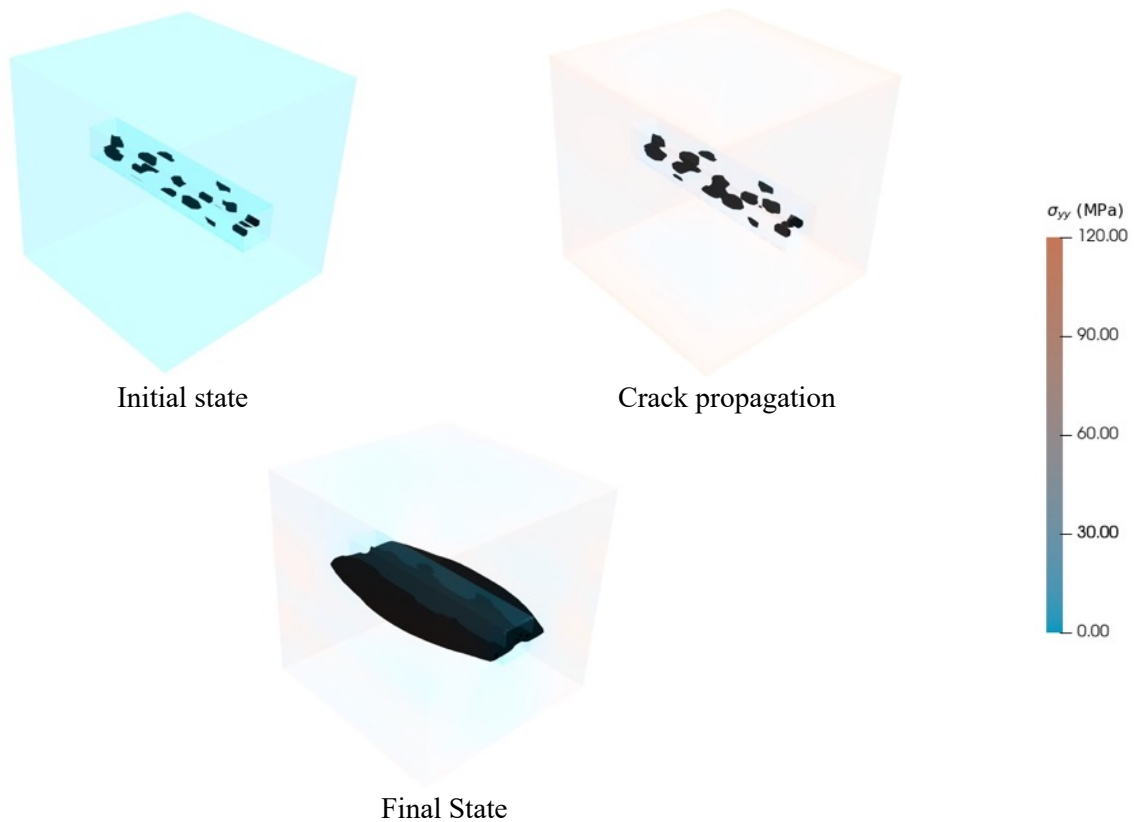


Figure 38. PF fracture simulation with multiple gas bubbles in the 3D domain. Boundary conditions are similar to Figure 36.

The model is further tested with multiple layers with different material properties. The project's goal is to introduce three different layers with properties of UZr_2 , UMo (U-rich), and UMo , respectively. To test the effect of spatially varying material properties, three different configurations are compared at first. One with uniform material properties as a reference, second by dividing the domain into three subdomains, each with varying material properties, and third as a smooth function to define three different layers. For the second case, the interface between the sublayer is considered to be rigidly bonded together. This design of the domain could help us in modeling interface effect for the varying mechanical properties of the three layers. The third case is designed to focus on the calculation of strength reduction due to fracture on varying density of gas bubble. Similar boundary condition was used as described above, and the material property used for this analysis is shown in Table 7. Due to the unavailability of fracture data, only elastic constant was varied between three layers while same fracture property is used for the analysis. Further analysis will be done to test the effectiveness of either of the configurations to model realistic behavior. Figure 39 shows fracture propagation in different configurations of material property applications at the end of the simulation. In all these cases, the bubble size is applied as a function of height to correspond to the experimental bubble size. Figure 40 shows the stress-strain diagram for each of these cases. The first crack initiated at the same stress level for all of the cases but at different amount of displacement due to the different distribution of material properties. While the stress-strain profile for diffuse property and subdomain block both shows the similar profile, the diffuse property configuration failed to converge after certain displacement value. The fracture profile shows that this happened when the fracture path propagated towards the interface of a material. This issue will be resolved in the future. Both subdomain block and diffuse property cases shows the fracture tends to propagate towards the interface of the material, which is not present in the uniform case. Thus, the

interface of the layers plays a role in the fracture propagation path and may affect the fracture toughness of the UMo sublayers. As the three subdomain block shows more robustness in simulation convergence as well as the usefulness of applying contact mechanics between layers due to its contact interface modeling capability between different layers, this configuration may be more useful for the present study.

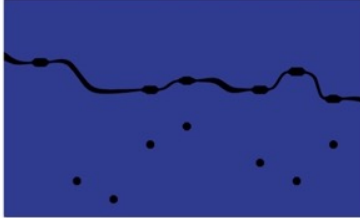
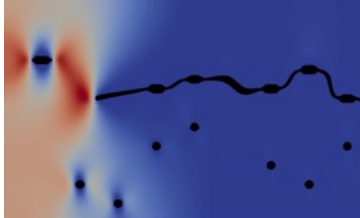
Uniform Properties	Subdomain Block	Diffuse Properties	
<ul style="list-style-type: none"> Single material properties have been applied throughout the domain 	<ul style="list-style-type: none"> Three subdomains defined with three different material properties The interface of the layers is assumed to be rigidly bonded together 	<ul style="list-style-type: none"> An order parameter with three distinct values sets the three different regions of materials Properties across the interface are smooth No mechanical interface modeled 	
			

Figure 39. Different configuration of material property application, fracture profile at the end of the simulation. Note that, the diffuse property case failed to converge after certain displacement and is shown here the latest configuration before the simulation timestep reaches a minimum value.

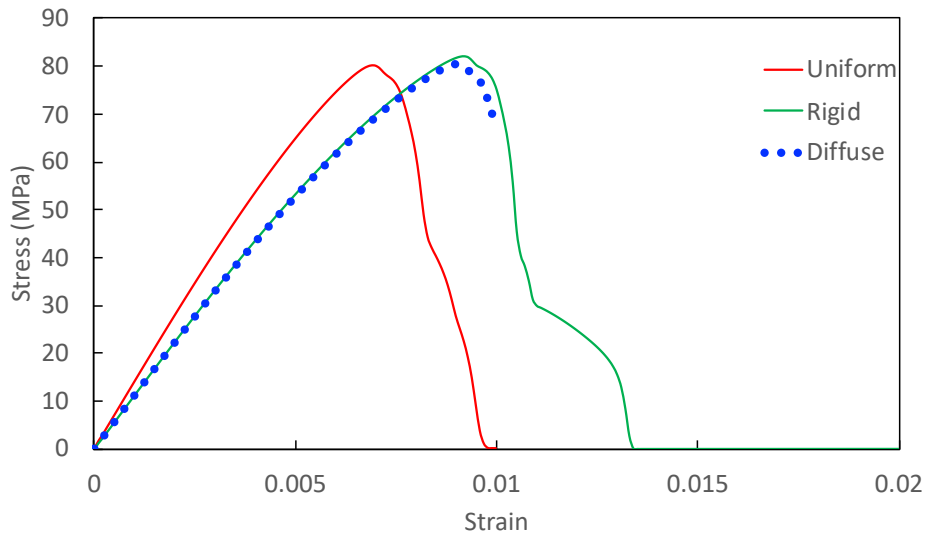


Figure 40. Stress-strain relationship for different configuration of material property application.

2.4.2.4 Summary and Future Work

A PF fracture model has been designed and demonstrated for single-layer domain (e.g., bulk UMo) and for multiple-layer domain (e.g., UMo-Zr interaction zone) in MOOSE. The model is for brittle fracture without plastic deformation. The model is capable of modeling fracture initiation and propagation in domains with a distribution of gas bubbles in both 2D and 3D.

In the future, the model will be further extended to include creep fracture, which is expected to be an important mechanism for failure of UMo fuel matrix. The model will be applied to study fracture in the interaction region with varying bubble size, density, and connectivity. A correlation between the fracture stress of the interaction zone and bubble morphology will be developed based on simulation results. The effects of phase separation, thickness of each layer, and fluctuation in layer thickness on fracture initiation and propagation will be studied as well.

2.5 The Effect of Carbides on Mechanical Properties and Swelling of U-Mo Fuel

Nonmetallic inclusions are often found in U-Mo alloy fuels, whether due to residual feedstock impurities or the formation during the manufacturing process. To elucidate the origin and formation mechanisms, Kautz et al. [85,86] characterized the nonmetallic inclusions in U-10Mo fuel from sub-nanometer to millimeter scale. The main inclusions were determined to be either uranium carbides or oxides, and they were observed at both grain interiors and GBs. Analysis of inclusions via atom probe tomography (APT) revealed that carbide inclusions were hypo-stoichiometric. Meanwhile, APT also revealed that the elemental compositions vary significantly between matrix and inclusion phases [85]. Although U enrichments within the fuel plate determined via APT agreed with the targeted enrichment for the low-enriched U (LEU) fuel, differences in U isotope abundance between phases and positions in the U-Mo casting were observed. Due to the incomplete mixing of depleted uranium (DU) and highly enriched uranium (HEU) feedstocks, it is possible that the enrichment of the carbides that are present within the fuel do not exactly correspond to the enrichment of the fuel matrix. This was initially expected to result in higher enriched carbides due to the nature of the feedstock. However, more recent evidence seems to suggest the possibility of carbides exhibiting a lower enrichment than the fuel matrix.

Due to the different chemical natures of materials (i.e., ceramic vs. alloy), carbide inclusions may affect the U-Mo fuel manufacturing process, the microstructure evolution, and fuel performance under irradiation. It has been shown that carbides can act as bubble nucleation sites and are expected to additionally act as stress concentration sites that can potentially accelerate grain refinement under irradiation. In this chapter, we investigated the effect of carbide inclusions on the mechanical properties of U-Mo fuel using different simulation approaches, including semi-empirical models, finite-element method (FEM) modeling, and DFT simulations. Different ^{235}U enrichment in carbides and U-Mo fuel matrix present FR gradients in the fuel, temperature gradients, and potentially deleterious microstructural behavior during operation. Recent in-pile experiments of U-Mo dispersion fuel show that a high FR may lead to an enhanced fuel swelling at high FDs [87]. By extending our previous work of FR effect on fuel swelling, we developed PF models to simulate the effect of variable ^{235}U enrichment in carbides on the gas bubble swelling in U-Mo fuel.

2.5.1 Analysis of Carbides in UMo Fuel from Image Processing

To model the effect of carbide inclusion on the mechanical properties of U-Mo alloy fuel, it is important to obtain the detailed carbide distribution inside U-Mo fuel (e.g., volume fraction, particle size distribution, and morphology). The microstructures of U-Mo alloy fuels have been extensively studied using different characterization techniques [88], in which SEM and TEM are two of the most popular ones. Among the two, SEM with backscattered electrons (BSE) is often used to characterize the nonmetallic inclusions and FGBs in U-Mo alloy fuels [85,86,89,90]. Due to the mass differences, carbide inclusions can be distinguished from the U-Mo matrix in the BSE-SEM micrographs based on pixel intensities.

The formation of carbides in U-Mo alloy fuel has been reported in several studies [85,86,89,90,91]. For example, Nyberg et al. [89] studied the effect of casting conditions and homogenization on the microstructures of the as-cast U-10Mo alloys, while Joshi et al. [91] investigated the effect of hot-rolling on the microstructure evolution in the as-cast and homogenized U-10Mo samples. The carbide distribution in U-Mo fuel has been investigated using the threshold-based image segmentation method (i.e., Otsu's method) [85,89]. However, due to the global threshold nature of Otsu's method, the volume fraction of carbides might be underestimated due to the uneven illumination and artifacts formed during sample preparation. In contrast, adaptive local threshold algorithms, such as the Sauvola [92] and Pansalkar [93] methods, can overcome these image problems caused by noise, illumination, and other source type-related degradations and determine a local threshold for each pixel. In this work, ImageJ software [94] was used to measure the carbide-particle-size distribution in U-Mo alloy fuel from previously reported SEM micrographs. The area fraction of carbides was used as a proxy for the estimation of volume fraction. A typical image processing workflow used in this work includes the following steps: (1) set scale; (2) crop image; (3) adjust brightness and contrast; (4) apply bilateral filter to remove image noise; (5) apply local threshold algorithm to segment carbide from fuel matrix; (6) measure particle size and morphology.

To investigate the effect of homogenization and hot-rolling on the as-cast U-Mo alloy samples, we used SEM images from as-cast, homogenized, and hot-rolled samples [89,91]—examples are shown in Figure 41(a), (b), and (c). The carbides identified by the local threshold method are shown in white color in Figure 41(d), (e), and (f) with the U-Mo fuel matrix in black. For easy visual inspection of the accuracy of image segmentation results, the contours of the identified carbides are overlaid on top of the original SEM images in yellow, shown in Figure 41(g), (h), and (i). From the binary images generated by the auto local threshold algorithm, the particle size and morphology of carbides can be measured using the “Analyze Particles” function implemented in ImageJ. Figure 42 and Figure 43 show the particle size and aspect ratio distributions of carbides in the as-cast, homogenized, and hot-rolled U-Mo alloy samples. Table 8 summarizes the area fraction, number density, average particle size, and aspect ratio for carbide inclusions in three types of U-Mo fuel samples. It can be seen that the homogenization process reduces the aspect ratio of carbides while increasing the average particle size and volume fraction compared to the as-cast samples. Meanwhile, the hot-rolling process significantly increases the aspect ratio of carbides and the average particle size of carbides. The currently obtained particle size and aspect ratio distributions of carbides were adopted to generate synthetic microstructures of U-Mo alloy fuel with different distributions of carbides. Figure 44 shows the examples of synthetic microstructures of U-Mo fuel with a random distribution of carbides, which will be used for the following simulations of the effect of carbide inclusions on the mechanical properties of U-Mo fuel.

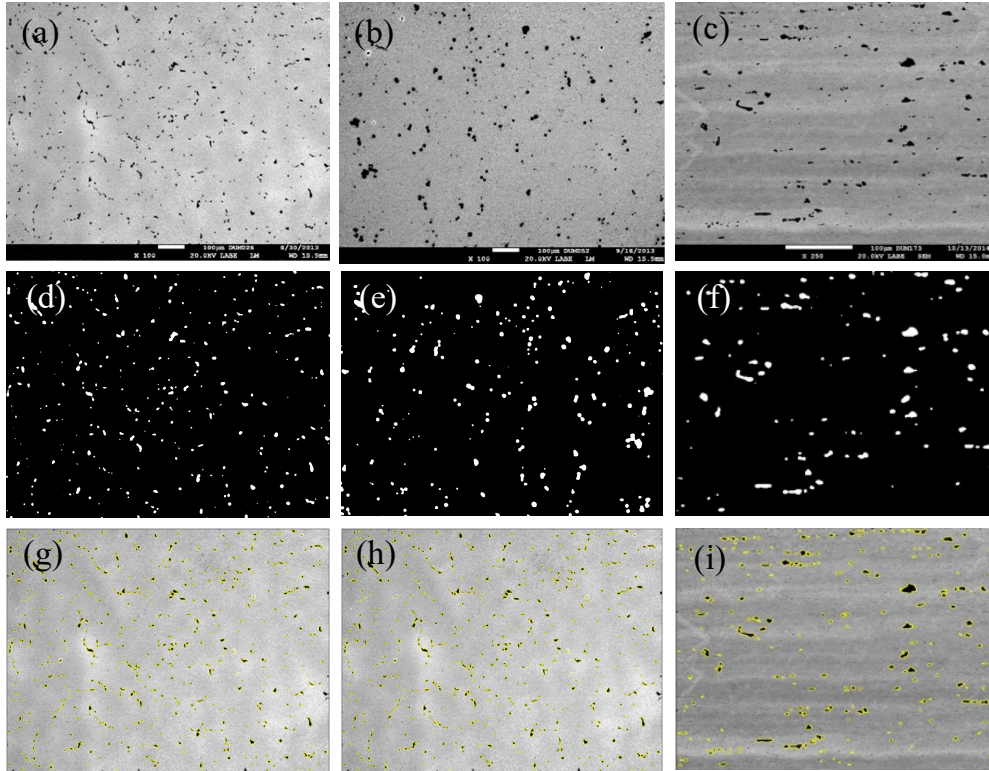


Figure 41. (a), (b), and (c) are BSE-SEM images of as-cast, homogenized, and hot-rolled U-10Mo alloy samples, respectively; (d), (e), (f) are binary images with carbides segmented by adaptive local threshold algorithm in white color; (g), (h) and (i) are images with carbides contours overlaid on top of the original BSE-SEM images [89,91].

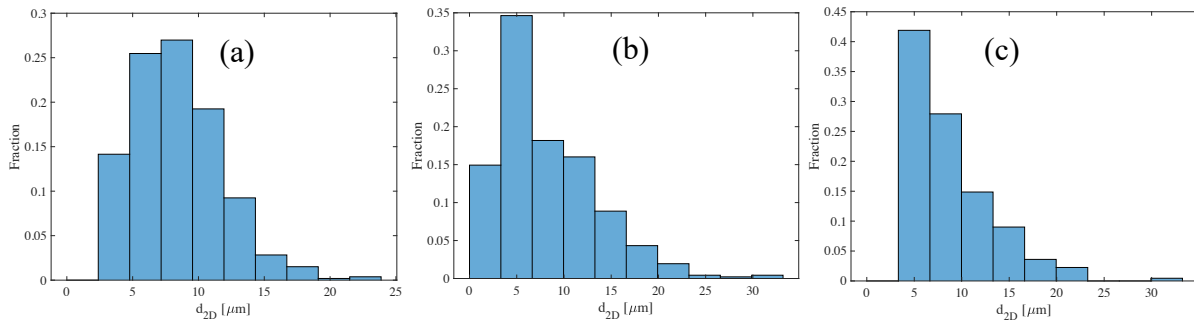


Figure 42. Particle size distribution of uranium carbides in (a) as-cast, (b) homogenized, and (c) hot-rolled U-10Mo alloy samples.

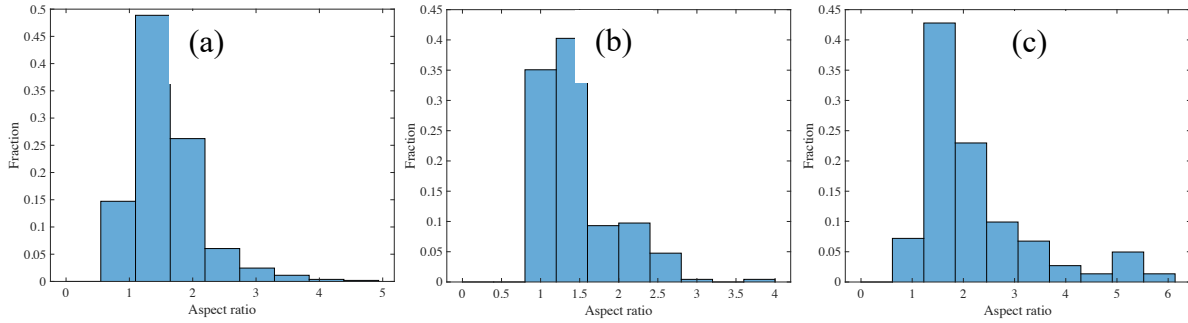


Figure 43. The aspect ratio of uranium carbides in (a) as-cast, (b) homogenized, and (c) hot-rolled U-10Mo alloy samples.

Table 8. Summary of area fraction, number density, average size, and aspect ratio of carbide inclusion in as-cast, homogenized and hot-rolled U-Mo alloy samples.

	Area fraction	Number density (mm^{-2})	Average size (μm)	Aspect ratio
As-cast	2.2%	410	8.34	1.58
Homogenized	2.9%	358	8.46	1.45
Hot-rolled	2.5%	327	8.70	2.22

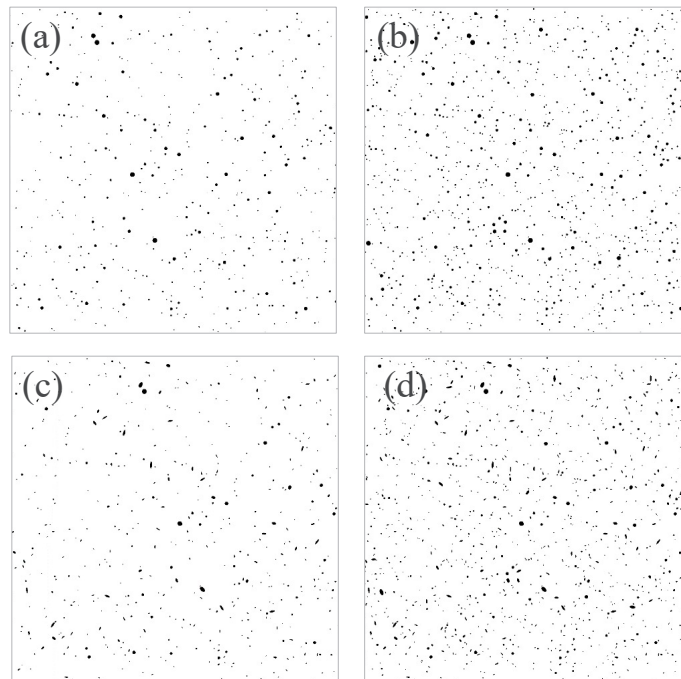


Figure 44. Examples of synthetic microstructures with random particle distribution: (a) and (b) are circular carbides with volume fractions of 1% and 2%, respectively, and (c) and (d) are elliptical particles (average aspect ratio of 2) with volume fraction of 1% and 2%, respectively.

2.5.2 Effect of Carbides on the Mechanical Properties of U-Mo Alloy Fuel

2.5.2.1 Analytical Models

The U-Mo fuel with carbide inclusions can be treated as a composite material with carbides dispersed in the U-Mo alloy matrix. The main goal of this study is to evaluate the effect of carbide inclusion on the mechanical properties of U-Mo fuel. Analytical models have been widely used to estimate the effective material properties of composite materials. Among the first well-known analytical models for estimating the effective properties are those of Reuss and Voigt [95]. They are a consequence of solving the boundary value problem of random media while assuming a homogeneous material. In order to invoke heterogeneity, Voigt assumed a constant strain inside the domain. Analogously, Reuss assumed a constant stress, hence resulting in the upper (Voigt) and lower (Reuss) bounds for estimating the effective properties of any composite (i.e., the so-called rule of mixtures), such that

$$E_{\text{Voigt}}^* = \phi_M E_M + \phi_{\text{UC}} E_{\text{UC}}, \quad (59)$$

$$E_{\text{Reuss}}^* = \left(\frac{\phi_M}{E_M} + \frac{\phi_{\text{UC}}}{E_{\text{UC}}} \right)^{-1}, \quad (60)$$

where ϕ_M is the volume fraction of the U-10Mo matrix, ϕ_{UC} is the volume fraction of UC inclusion, and E_M and E_{UC} are the elastic property (Young's or bulk modulus) of the U-10Mo alloy matrix and uranium carbide (UC), respectively. However, it is well known that the rule of mixtures is not very accurate. A better model has been proposed by Hashin and Shtrikman (HS) [96], which is more accurate and has tighter bounds than those from the rule of mixtures. These bounds are given as follows for isotropic elastic (uniaxial and bulk) modulus

$$E_{\text{HS}^-}^* = -E_M + \left(\frac{\phi_M}{2E_M} + \frac{\phi_{\text{UC}}}{E_{\text{UC}} + E_M} \right)^{-1}, \quad (61)$$

$$E_{\text{HS}^+}^* = -E_{\text{UC}} + \left(\frac{\phi_M}{E_M + E_{\text{UC}}} + \frac{\phi_{\text{UC}}}{2E_{\text{UC}}} \right)^{-1}, \quad (62)$$

$$G_{\text{HS}^-}^* = G_M + \frac{\phi_M}{\frac{1}{G_{\text{UC}} - G_M} + \frac{6(K_M + 2G_M)\phi_M}{5G_M(3K_M + 4G_M)}}, \quad (63)$$

$$G_{\text{HS}^+}^* = G_{\text{UC}} + \frac{\phi_{\text{UC}}}{\frac{1}{G_M - G_{\text{UC}}} + \frac{6(K_{\text{UC}} + 2G_{\text{UC}})\phi_{\text{UC}}}{5G_{\text{UC}}(3K_{\text{UC}} + 4G_{\text{UC}})}}, \quad (64)$$

where E^* is the effective Young's modulus, and G^* is the effective shear modulus. The subscripts HS^+ and HS^- stand for the upper and lower HS bounds, respectively.

To estimate the bounds for the mechanical properties of UC dispersed U-Mo alloy using the rule of mixtures and the HS model, the properties of the constituent materials (i.e., U-Mo alloy and UC phase) should be known and are listed in Table 9.

Table 9. Mechanical properties of UC and U-10Mo alloy.

Properties	UC	U-10Mo alloy
Density (g/cm^3)	13.63 [97]	13.37 [97]
Young's modulus (GPa)	225 [98]	67 [99]
Bulk modulus (GPa)	177 [98]	143 [100]
Poisson's ratio	0.288 [98]	0.35 [99]
Shear modulus (GPa)	87 [98]	36 [100]

Using the rule of mixture and the HS model, the predicted upper and lower bounds for the effective Young's and shear modulus of U-Mo alloy fuel with UC volume fraction up to 8% are shown in Figure 45 and Figure 46. Clearly, the upper and lower bounds predicted by the HS model are much tighter than those predicted by the rule of mixtures. It should be noted that the analytical models used in this study only take into account the volume fraction of carbides, while the shape and distribution of carbides are not considered. To validate the results from analytical models, FEM simulations will be performed to examine the effect of volume fraction and aspect ratio of carbides on the mechanical properties of U-Mo alloy fuel in the next section.

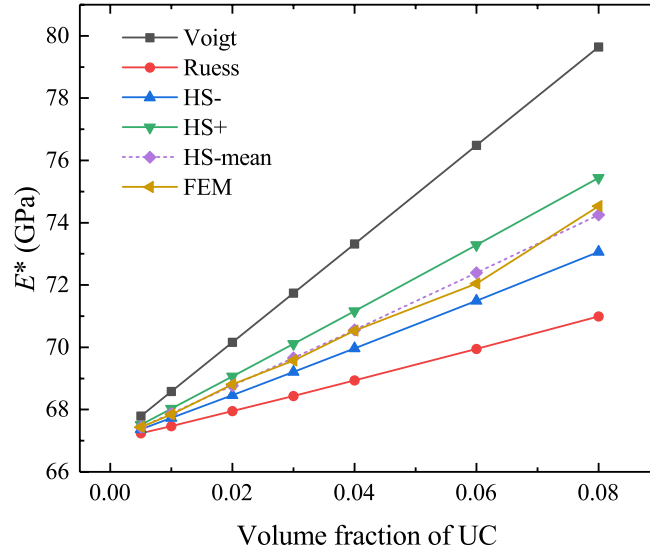


Figure 45. Effective Young's modulus of U-10Mo alloy fuel a function of carbide volume fraction predicted by different models.

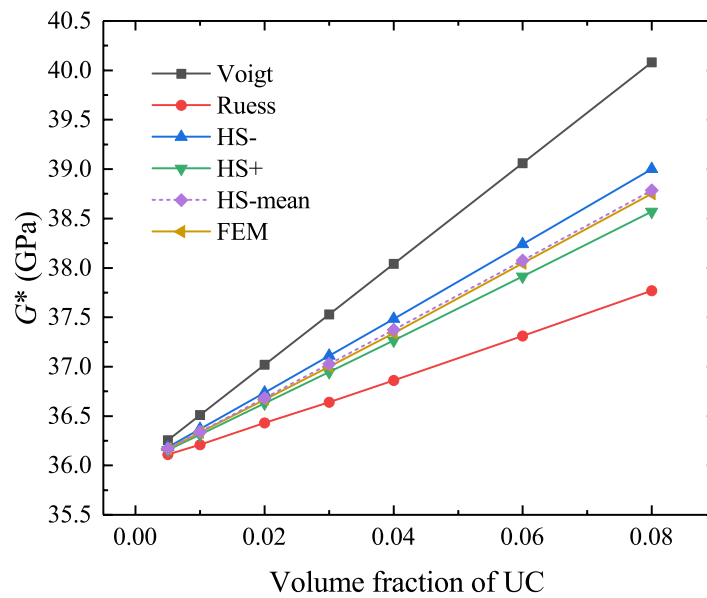


Figure 46. Effective shear modulus of U-10Mo alloy fuel a function of carbide volume fraction predicted by different models.

2.5.2.2 Finite-Element Modeling

To simulate the effect of carbide inclusion on the mechanical properties of U-Mo fuel, synthetic microstructures of U-Mo fuel with different microstructural features of carbides were generated using the carbide information obtained in Section 2.5.1 (i.e., seven volume fractions of carbide [$\phi_{UC} = 0.5, 1, 2, 3, 4, 6, \text{ and } 8\%$] with circular carbides and seven aspect ratios of elliptical carbides [$AR_{UC} = 1, 1.5, 2, 2.5, 3, 3.5 \text{ and } 4$]). A total of 28 microstructural features were generated based on the variation of volume fraction and aspect ratio of carbides. Some examples of the generated synthetic microstructures with different microstructural features (i.e., carbide volume fraction and aspect ratio) are shown in Figure 44. The size of all the microstructures is $800 \mu\text{m} \times 800 \mu\text{m}$. All the generated microstructures were converted to FEM model input using a python script. The 2D FEM models were created using a fine mesh with a $1 \mu\text{m} \times 1 \mu\text{m}$ element size. This RVE contains a total of 640,000 elements. Each element was assigned mechanical properties based on the pixel location in the image. A commercial finite-element code COMSOL Multiphysics was used to conduct the simulations using explicit formulation. The “solid mechanics” module implemented in COMSOL was used to determine the elastic properties.

In this work, the UC inclusion and U-Mo matrix were considered as isotropic and homogenous. The properties of the constituent phases (i.e., UC and U-10Mo alloy) used for the FEM simulations are shown in Table 9. The apparent stress (average stress) can be obtained using the following homogenization expressions:

$$\bar{\sigma} = \frac{1}{V} \int_V \sigma dV \quad (65)$$

where $\bar{\sigma}$ is the effective stress of the composite, and V is the element volume.

The effective uniaxial (Young's) modulus, E^* , can be obtained from

$$\bar{\sigma} = E^* \bar{\varepsilon}. \quad (66)$$

where $\bar{\varepsilon} \approx \varepsilon^0 = u^0/L$. The effective bulk modulus, K^* , is obtained using

$$\bar{p} = K^* \bar{e} \quad (67)$$

where $\bar{p} = (\bar{\sigma}_{11} + \bar{\sigma}_{22} + \bar{\sigma}_{33})/3$ is the mean effective stress and $\bar{e} = (\bar{\varepsilon}_{11} + \varepsilon_{22} + \varepsilon_{33})/3$ is the volumetric strain. The effective shear modulus, G^* , is obtained by

$$\bar{\sigma}_{ij} = G^* \bar{\gamma}_{ij} \text{ for } i \neq j, \quad (68)$$

where $\bar{\gamma}_{ij} = 2\bar{\varepsilon}_{ij} = 2\varepsilon^0$ with ε^0 being the applied strain.

By applying Eqn. 66, the effective Young's modulus (E^*) of UC dispersed U-Mo fuel was calculated and compared with the results predicted by analytical models in Figure 45. As expected, E^* increases with an increase in the volume fraction of carbides due to the more rigid nature of carbides. The FEM predicted Young's modulus falls between the upper and lower bounds predicted by both the rule of mixtures and the HS model. However, the HS model provides a much tighter bound, and the mean value of the upper and lower bounds predicted by the HS model is in very good agreement with the FEM prediction. Meanwhile, the effective shear modulus (G^*) of the U-Mo alloy with UC inclusions is also predicted to increase with an increase in the carbide volume fraction as shown in Figure 46. Similar to the Young's modulus, the mean value of the upper and lower bounds predicted by the HS model provides a very good estimation of G^* compared to the results predicted by FEM. For a typical carbide volume fraction of 1%, the current simulations show that the effect of carbide inclusions on the mechanical

properties of U-Mo fuel is very small, about a 1% increase for both Young's and Shear modulus compared to the case without UC inclusion.

To evaluate the effect of carbide shape on the mechanical properties of U-Mo fuel, the effective Young's and shear modulus for U-Mo fuel were predicted for carbide inclusions with different aspect ratios ranging from 1 to 4. As shown in Figure 47 and Figure 48, both E^* and G^* are predicted to increase with an increased aspect ratio of carbide inclusions. At the typical carbide volume fraction of 1%, it was predicted that the Young's and shear modulus of U-Mo fuel increases by less than 1% when the aspect ratio of carbides increases from 1.5 (average aspect ratio of carbides in as-cast U-Mo alloy sample) to 2.5 (average aspect ratio of carbides in hot-rolled U-Mo alloy samples). However, with a high carbide volume fraction (e.g., 4%), the E^* and G^* U-Mo fuel will become more sensitive to the increased aspect ratio of carbides (see Figure 47 and Figure 48 for more details).

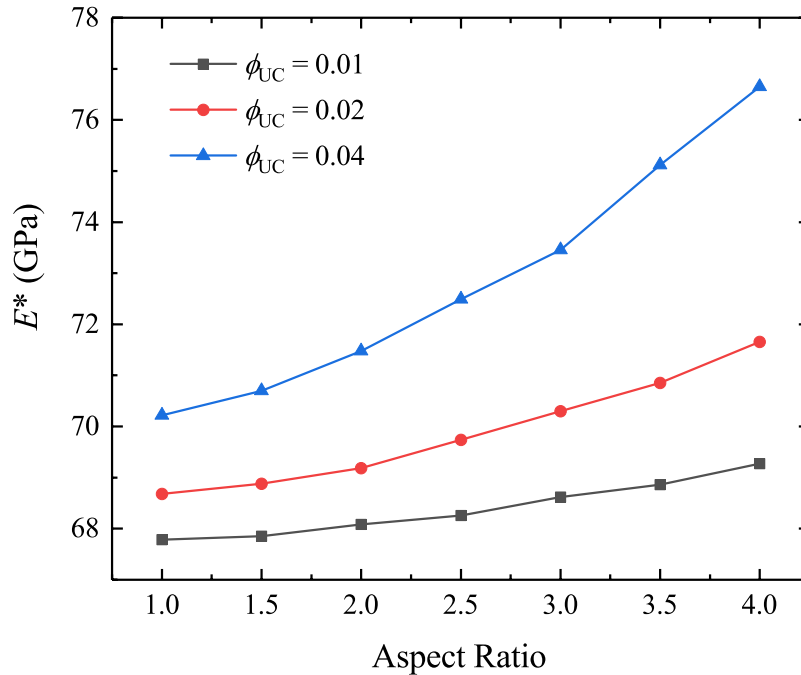


Figure 47. Effective Young's modulus of U-10Mo alloy fuel as a function of the aspect ratio of carbide inclusions with different volume fractions of UC.

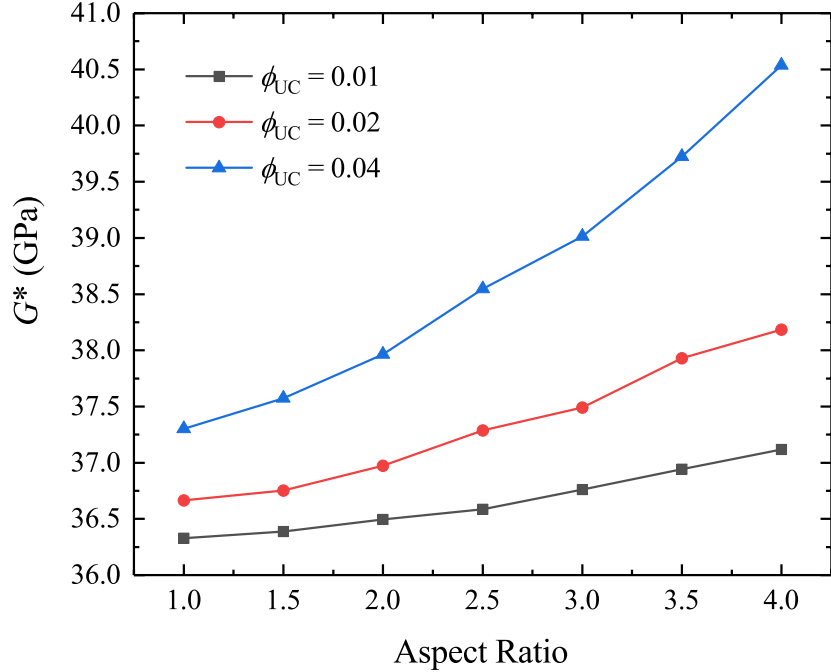


Figure 48. Effective shear modulus U-10Mo alloy fuel as a function of the aspect ratio of carbide inclusions with different volume fractions of UC.

2.5.2.3 Effect of Carbides on the Mechanical Properties of UMo by DFT

In this section, we investigated the effect of UC on the mechanical properties of U-Mo fuel using DFT calculations. The UC in U-Mo alloy was simulated using the slab model with UC sandwiched between UMo layers (i.e., UMo|UC|UMo). The mechanical properties, including ultimate tensile stress and Young's modulus, were obtained from the calculated tensile stress-strain curves. Due to the inhomogeneous distribution of Mo along the UMo/UC interface, the effect of Mo concentration on the mechanical properties of U-Mo fuel was simulated. Meanwhile, the effect of non-stoichiometry of UC on the mechanical properties of U-Mo fuel was also investigated because of the non-stoichiometric nature of carbide observed in the fuel.

Methodology and Computation Details

In this work, all DFT calculations were performed using the Vienna ab initio simulation package (VASP) [101,102] based on the projector augmented wave method (PAW) [103]. The exchange-correlation functional is described by the Perdew-Burke-Ernzerhof generalized gradient approximation (GGA) [104]. The $6s^2 6p^6 5f^3 6d^1 7s^2$ and $2s^2 2p^3$ electrons are treated as valence electrons of U and C, respectively. A cutoff energy of 500 eV was adopted for the plane wave basis sets. To account for the strong on-site Coulomb interactions of f electrons in uranium, the rotationally invariant form of the DFT+ U approach [105] was adopted, in which U_{eff} is set as 2.5 eV. To model the non-stoichiometric UC and U-Mo alloy phases, the special quasirandom structures method implemented in Alloy Theoretic Automated Toolkit (ATAT) [106] was used to simulate the random distribution of C vacancies in hypo-stoichiometric UC_{1-x} and Mo distribution in U-Mo alloy. Based on our previous study, one of the most stable interfaces between UMo and UC (i.e., UMo(110)/UC(001) interface [denoted as UMo/UC for simplicity]) was studied in this work.

To simulate the tensile deformation applied to the interface, the calculations were conducted by extending the lattice parameter of the interface models along the z-direction, which is perpendicular to the interface. All ions in the interface model were relaxed, and the volume and the shape of the interface unit

cell were also optimized during the stress tensor calculation process. The ultimate tensile strength and Young's modulus were determined from the calculated stress-strain curve. In addition to the ultimate tensile strength, another important quantity determining the strength of interfaces is the ideal work of adhesion (W_{ad}). The ideal work of adhesion of the UMo/UC interface was determined by

$$W_{ad} = (E_{UC} + E_{UMo} - E_{UMo/UC})/A, \quad (69)$$

where E_{UC} and E_{UMo} are the total energies of isolated UC and UMo slabs, $E_{UMo/UC}$ is the total energy of the interface system including UC and UMo, and A is the total interface area.

Mechanical Properties of UMo/UC Interface

Before investigating the mechanical properties of the UMo/UC interface, we first studied the effect of UC layer thickness on the work of adhesion of the interface. Figure 49 shows the atomic structures of the UMo/UC interface with a different number of UC monolayers (MLs). The effect of UC layer thickness was tested up to 5 MLs. As shown in Table 10, W_{ad} of UMo/UC interface decreases from 3.85 J/m² to 3.31 J/m² as the number of UC MLs increases from 1 to 5. With 5 MLs for the UC layers, the W_{ad} is converged with an error less than 0.02 J/m². Therefore, 5 MLs for the UC layer is thick enough to simulate the bulk behavior of UC in U-Mo fuel. Therefore, 5 MLs of the UC layer were adopted in the following simulation of UMo/UC interfaces.

To calculate the mechanical properties, the tensile stress-strain curves of UMo/UC interfaces with a different number of UC layers were simulated. As shown in Figure 50, the ultimate tensile strength of the interface decreases as the number of UC MLs increases. The layer thickness dependence is consistent with the predicted work of adhesion (i.e., a thin UC layer interface model has higher tensile strength and work of adhesion). In comparison, the Young's modulus of the interface increases as the number of UC layers increases. Table 10 provides a complete summary of calculated Young's modulus, ultimate tensile strength, and work of adhesion of the studied interfaces.

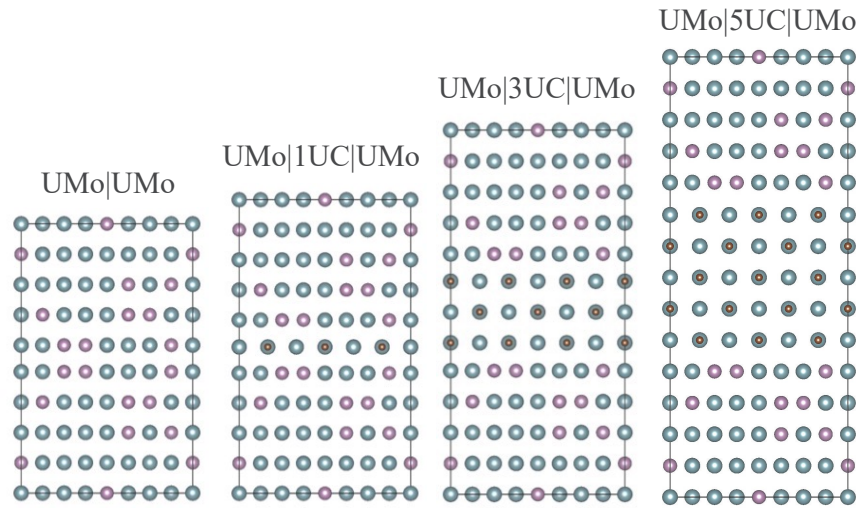


Figure 49. Atomic structures of UMo|UC|UMo interface models with a different number of UC layers of UC. Green, purple, and brown spheres represent U, Mo, and C atoms, respectively.

Table 10. Calculated Young's modulus, ultimate tensile strength, and work of adhesion of UMo/UC interface models with a different number of UC layers.

	Young's modulus (GPa)	Ultimate tensile strength (GPa)	W_{ad} (J/m ²)
UMo UMo	85.1	11.2	3.70

UMo 1-UC UMo	98.6	12.1	3.85
UMo 3-UC UMo	102.5	9.1	3.34
UMo 5-UC UMo	105.5	9.0	3.31

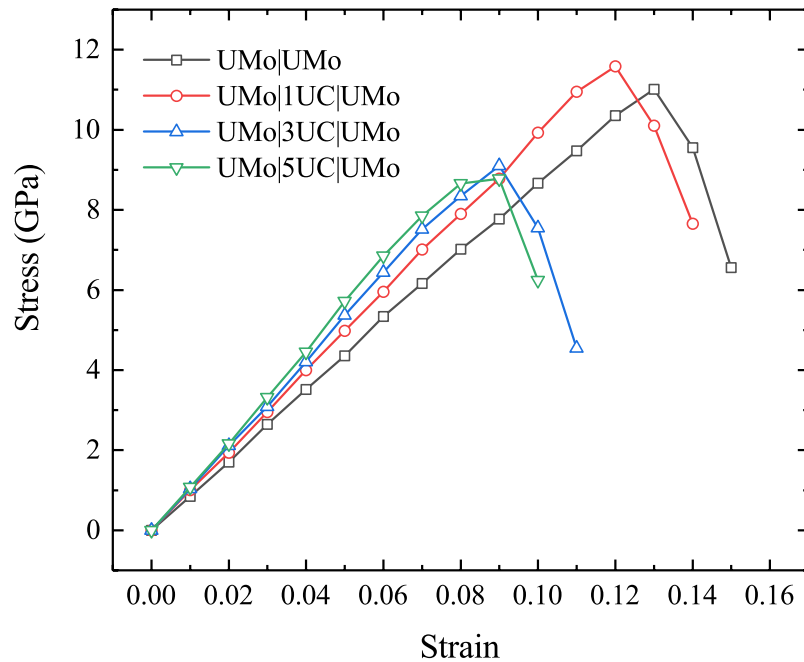


Figure 50. Tensile stress-strain curves of UMo/UC interface models with a different number of UC layers.

Effect of Mo Concentration on Mechanical Properties of the UMo/UC Interface

To investigate the effect of Mo concentration on the mechanical properties of the UMo/UC interface, we simulated the U-Mo alloys with three different Mo concentrations (i.e., 12.5% [4.2 wt.%], 25% [9.2 wt.%], and 37.5% [15.4 wt.%]), which can be achieved by replacing 10, 20, and 30 U atoms by Mo in the 80-atom U layers, respectively. Figure 51 shows the atomic structures of the UMo/UC interface models with different concentrations of Mo in the U-Mo alloy. As shown in Table 11, the W_{ad} of the UMo/UC interface increases with increasing Mo concentration in the U-Mo alloy. The increased work of adhesion between the UC and U-Mo alloy can be ascribed to the enhanced bonding strength between the UC and U-Mo alloy compared to the UC/U interface. Figure 52 shows the calculated Young's modulus and ultimate tensile strength of UMo/UC interfaces as a function of Mo concentration. Consistent with the calculated W_{ad} , the Young's modulus and ultimate tensile strength of the interface increases with the increasing Mo concentration (see Table 11 for a summary of the calculated mechanical properties of the interface with different Mo concentrations for U-Mo alloy). Recent experimental studies suggest that carbide inclusions often locate in the Mo-lean areas of the U-Mo fuel, which has a lower Mo concentration compared to the nominal Mo concentration of the U-Mo fuel [85,86]. Our simulation shows that the Young's modulus and ultimate tensile strength of the UMo/UC interface decrease by 3.5% and 3.0%, respectively, when the Mo concentration in the U-Mo alloy decreases from 25% (9.2 wt.%) to 12.5% (4.2 wt.%).

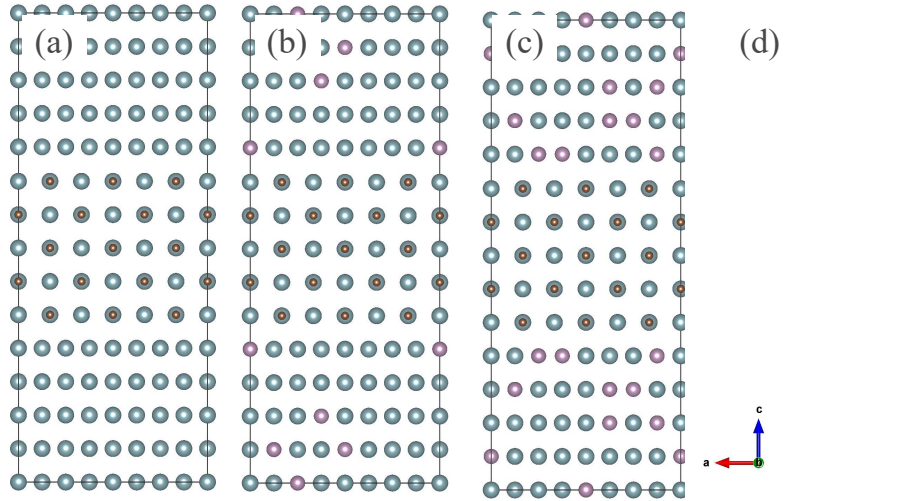


Figure 51. Atomic structures of UMo/UC interface models with different concentrations of Mo in $U_{1-x}Mo_x$ alloy: (a) $x = 0$, (b) $x = 0.125$, (c) $x = 0.25$, and (d) $x = 0.375$. Green, purple, and brown spheres represent U, Mo, and C atoms, respectively.

Table 11. Calculated Young's modulus, ultimate tensile strength, and work of adhesion of UMo/UC interface models with different Mo concentrations in the $U_{1-x}Mo_x$ alloy.

Mo concentration x	Young's modulus (GPa)	Ultimate tensile strength (GPa)	W_{ad} (J/m ²)
0	99.5	8.4	3.20
0.125	101.8	8.7	3.24
0.25	105.5	9.0	3.31
0.375	114.3	9.6	3.41

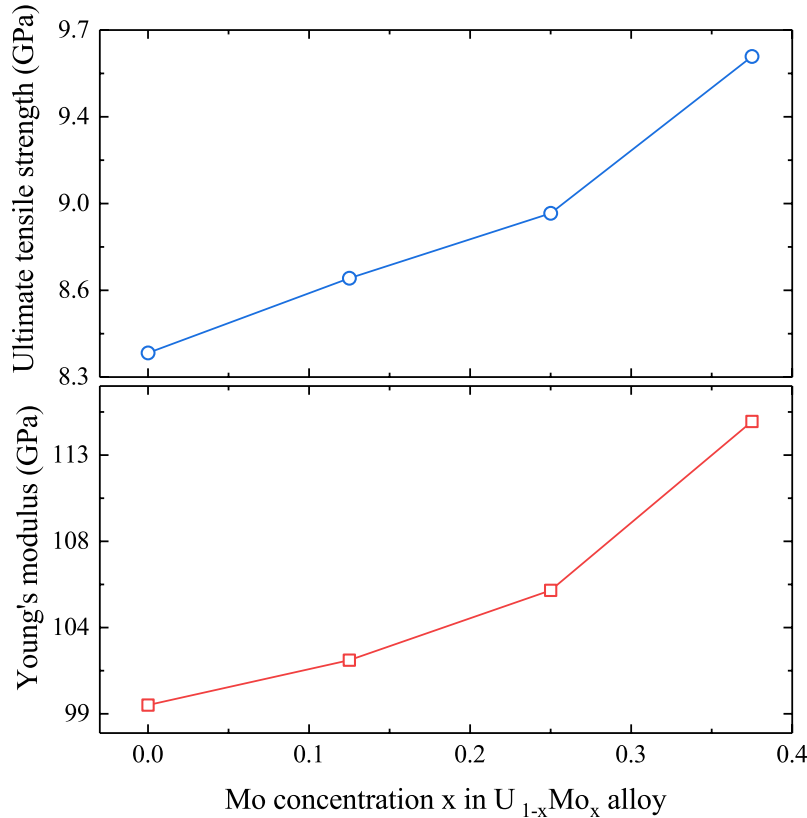


Figure 52. Young's modulus and ultimate tensile strength of UMo/UC interface models as a function of Mo concentration in $U_{1-x}Mo_x$ alloy.

Effect of Non-stoichiometry in UC on Mechanical Properties of UMo/UC Interface

To evaluate the effect of non-stoichiometry in UC on the mechanical properties of U-Mo fuel, we studied the UMo/UC interface with a hypo-stoichiometric (UC_{1-x}) composition. Three hypo-stoichiometries for UC_{1-x} (i.e., 0.0333, 0.1, and 0.2) were simulated by removing 1, 3, and 6 C atoms from the 30-C atoms UC layers in the interface, respectively (see Figure 53 for the atomic structures of the interface models). The predicted work of adhesion of UMo/UC interfaces with hypo-stoichiometric UC is shown in Table 12. Our study shows that the adhesion strength of the interface decreases with increased non-stoichiometry in UC. At a hypo-stoichiometry of 0.2 for UC, the adhesion strength of the UMo/UC interface decreases by 8.2% compared to the case with stoichiometric UC. Figure 54 shows the calculated Young's modulus and ultimate tensile strength of the UMo/UC interface models as a function of non-stoichiometry in UC. In agreement with our previous study of the non-stoichiometric UC phase, the Young's modulus and ultimate tensile strength of the interface decrease with the increase of non-stoichiometry of UC. Compared to the interface with stoichiometric UC, the Young's modulus and ultimate tensile strength of the interface with hypo-stoichiometric $UC_{0.8}$ decrease by 18.8% and 17.4%, respectively.

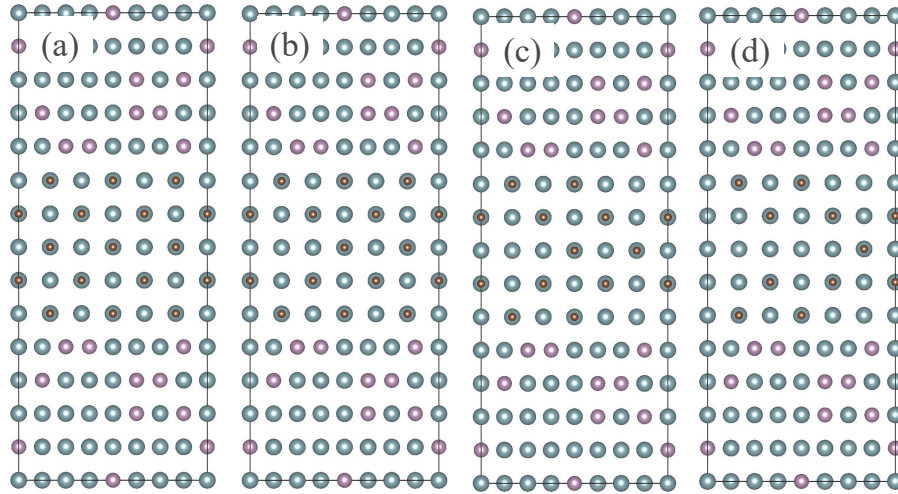


Figure 53. Atomic structures of the UMo/UC interface models with different non-stoichiometries of C in UC_{1-x} : (a) $x=0$; (b) $x=0.0333$; (c) $x=0.1$; (d) $x=0.2$. Green, purple, and brown spheres represent U, Mo, and C atoms, respectively.

Table 12. Calculated Young's modulus, ultimate tensile strength, and work of adhesion of UMo/UC interface models with different non-stoichiometries of C in UC_{1-x} .

Non-stoichiometry of C in UC_{1-x}	Young's modulus (GPa)	Ultimate tensile strength (GPa)	W_{ad} (J/m^2)
0	105.5	9.0	3.31
0.0333	99.6	8.5	3.23
0.1	92.5	8.1	3.15
0.2	85.6	7.4	3.04

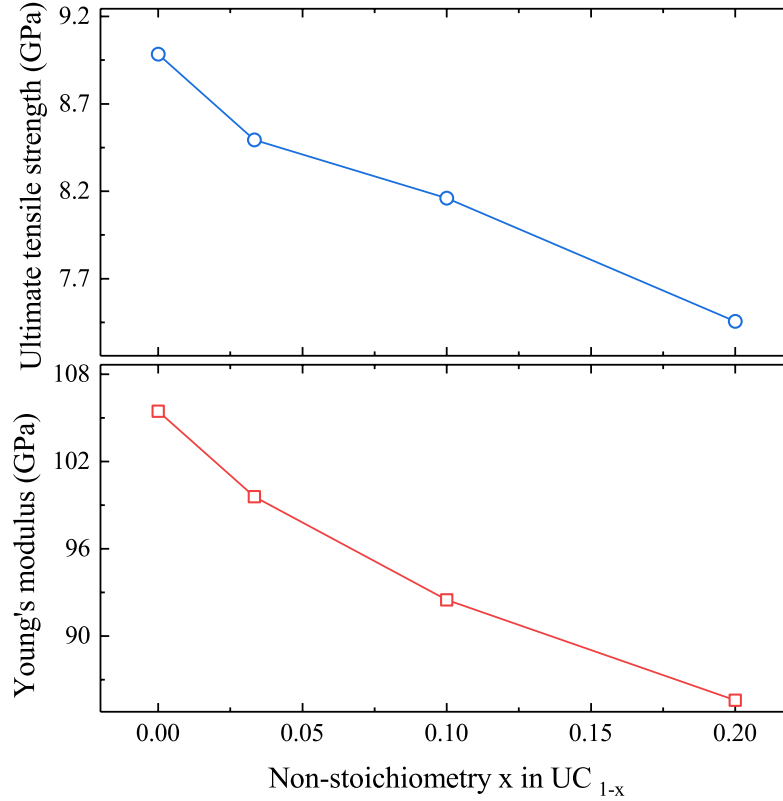


Figure 54. Young's modulus and ultimate tensile strength of UMo/UC interface models as a function of non-stoichiometry x of C in UC_{1-x}.

2.5.3 Effect of ²³⁵U Enrichment in Carbides on Gas Bubble Swelling of U-Mo Fuel

2.5.3.1 Phase-field Model Description

The formation of intergranular gas bubbles coupled with grain recrystallization in U-Mo fuel is modeled by a multi-phase PF model. In the PF model, the grain parameter $\eta_i(r, t)$ ($i=1, 2, \dots, p$) is chosen to describe the polycrystalline structure, the phase parameter $\eta_j(r, t)$ ($j=p+1, p+2, \dots, q$) is chosen to describe the gas bubble, and c_g is chosen to describe the concentration of fission gas Xe. The total free energy of the system is described by [107]

$$F(c_g, \eta_i) = \int \left[f_{bulk}(c_g, \eta_i) + \sum_{i=1}^p \frac{\kappa_\eta}{2} |\nabla \eta_i|^2 + \frac{\kappa_c}{2} |\nabla c_g|^2 + f_{stored}(\eta_i) \right] dV, \quad (70)$$

where f_{bulk} is the bulk free energy density describing the composition and volume fraction of the equilibrium phases; κ_η and κ_c are the gradient energy coefficients for the phase parameter and composition, respectively; p represents the total number of grain orientations in a grain structure; q represents the total number of gas bubbles; and f_{stored} is the stored elastic energy density due to the introduction of dislocations [107][108].

The spatial and temporal evolution of grain parameters and Xe concentration follows the Allen-Cahn and Cahn-Hilliard equations [109]

$$\frac{\partial \eta_i}{\partial t} = -L_\eta \frac{\delta F}{\delta \eta_i}, \quad i = 1, 2, \dots, q, \quad (71)$$

$$\frac{\partial c_g}{\partial t} = \nabla M(\eta) \nabla \frac{\delta F}{\delta c_g} + \dot{G} - \dot{R}, \quad (72)$$

where L_η is the kinetic coefficient of grain boundary movement, M is the gas-atom mobility, \dot{G} is the fission production of the gas atoms, and \dot{R} is the fission-induced gas-atom resolution. The production rate of the Xe gases is described by $\dot{G} = \varpi Ran$, where ϖ is related to the FR and Ran is a random number having uniform distribution between 0 and 1. The generation rate in the fuel can be related to the FR according to $\varpi = \delta \dot{f} \Omega$, where δ is a constant, and Ω is the volume of a lattice site in U-Mo.

The mobilities of fission-gas atoms are related to the diffusivities through Einstein's relation, $M_{b,g} = D_{b,g}/k_B T$. According to Rest's derivation, the diffusivities of gas atoms can be related to the FR as $D_{b,g} = D_{b,g}^0 \dot{f}$, where $D_{b,g}^0$ is the diffusivity of gas atoms in the grain interior or along GBs without irradiation [110].

During the nucleation process, Xe gas bubbles have a higher probability to nucleate on GBs because of the higher concentration and diffusivity on GBs than inside grains. In the simulations, the nucleation probability in a discretized area is calculated as a function of the local nucleation probability [111]

$$J(t) = Z \beta N_0 \exp(-\Delta G^*/k_B T) \exp(-\tau/t), \quad (73)$$

where ΔG^* is the nucleation activation energy, Z is the Zeldvoich factor, N_0 are the lattice sites per unit volume of the crystal, k_B is the Boltzmann's constant, τ is the incubation time, and β is the atomic impingement rate. The impingement rate is the number of atoms that hit a surface per second and unit area at a constant pressure. We assume the impingement rate is linearly dependent on the FR, $\beta = \beta_0 \dot{f}$, where β_0 is the impingement rate without irradiation. Following Simmons et al.'s derivation [111], Eqn. 73 can be simplified to

$$J(t) = k_1 \dot{f} \exp(-k_2/\Delta c), \quad (74)$$

where $k_1 = Z \beta_0 N_0$. The phase transition driving force ΔG_a is proportional to local supersaturation $\Delta c = c_g - c_m^e$. For a 2D model, we have $\Delta G^* = \pi \gamma^2 / \Delta G_a = \pi \gamma^2 / (\alpha \Delta c)$ and thus $k_2 = \pi \gamma^2 / (\alpha k_B T)$, where γ is the surface energy of gas bubble, and α is a constant. The nucleation probability in a discretized area is calculated by

$$P(t) = 1 - \exp(-J \Delta t), \quad (75)$$

where Δt is the time interval over which the nucleation probability is calculated.

The model described above aims to consider the effect of FR on the nucleation of gas bubbles, generation of fission gases, dislocations accumulation, and diffusivities of gas atoms. A detailed description of the model can be found in our previous work [107,108]. The modified PF model can be used to study the effect of FR on the nucleation and growth of intergranular gas bubbles as well as the recrystallization process in irradiated U-Mo fuels.

To study the effect of ^{235}U enrichment on the swelling of U-Mo fuel, FR is assumed to be proportional to the concentration of ^{235}U based on $\dot{f} = N_{235} \bar{\Phi}_{th}$, where N_{235} is the atom density of ^{235}U , and $\bar{\Phi}_{th}$ is a ratio constant. Variations of ^{235}U enrichment in UC and U-Mo matrix can lead to the varied FR inside U-Mo fuel, which will result in different nucleation and growth behaviors of gas bubbles under irradiation. Due to the lack of the material properties required for the explicit simulation of fission-gas behaviors in UC, UC inclusions were treated as U-Mo grains but with different ^{235}U enrichment (i.e., using the material properties of U-Mo for UC in this work). We performed PF simulations on a simple square domain. The PF model was implemented in an in-house simulation code, and the semi-implicit FFTW numerical method was employed to solve the coupled Equations 71 and 71 [112]. Periodic boundary conditions were imposed on the simulation domain.

2.5.3.2 Materials Properties

Table 13 lists the parameters used to simulate the microstructural evolution in U-Mo fuel using a PF model. The Xe production rate due to fission, described by the constant δ , is set as $4.0 \times 10^{-5} \text{ s}^{-1}$. The Xe equilibrium concentration in U-Mo is assumed to be 1.0×10^{-7} considering its very low solubility. The Xe equilibrium concentration in the bubble is 1.0. A model size of $25.6 \mu\text{m} \times 25.6 \mu\text{m}$ and the grid size $\Delta x = \Delta y = 0.05 \mu\text{m}$ were used in all the simulations. The initial grain size is set as $5.0 \mu\text{m}$. Three different FRs (i.e., 3.0×10^{20} , 5.0×10^{20} , and $9.0 \times 10^{20} \text{ fission/m}^3\text{s}$) were used to study the FR effect on the swelling in U-Mo fuel [34].

Table 13. Material properties of U-Mo fuel used in the current PF simulations.

Quantity	Symbol	Value	Reference
Lattice constant of U-Mo	a	$3.42 \times 10^{-10} \text{ m}$	[113]
Atomic volume	Ω	$a^3/2$	[114]
Surface energy	γ	1.64 J/m^2	[107,108]
Grain boundary energy	σ_{gb}	0.50 J/m^2	[100]
Kinetic coefficient	L_η	$1.82 \times 10^{-14} \text{ m}^3 \text{ s}^{-1} \text{ J}^{-1}$	[107]
Gas-atom mobility	M_b	$2.5 \times 10^{-25} \text{ m}^5 \text{ s}^{-1} \text{ J}^{-1}$	[28]
Free energy coefficient	A	$3.0 \times 10^7 \text{ Jm}^{-3}$	[107]
Free energy coefficient	C_p	1.5	[65]
Free energy coefficient	C_q	1.8	This work
Shear modulus	G	36.0 GP	[100]
Burgers vector	b_v	$3.42 \times 10^{-10} \text{ m}$	[114]
Gradient coefficient	κ_c	$2.74 \times 10^{-7} \text{ Jm}^{-1}$	This work
Gradient coefficient	κ_η	$3.75 \times 10^{-8} \text{ Jm}^{-1}$	This work
Xe equilibrium concentration in matrix	c_m^e	1.0×10^{-7}	This work
Xe equilibrium concentration in bubble	c_b^e	1.0	This work
Parameter for nucleation	k_1	5.0×10^{-3}	This work
Parameter for nucleation	k_2	1.0×10^{-6}	This work
Nucleation time interval	Δt	0.05	This work

2.5.3.3 Results and Discussion

Before examining the effect of ^{235}U enrichment in carbides on the gas bubble swelling, we first evaluated the potential volume fraction of carbides and ^{235}U enrichment in U-10Mo fuel based on the carbon concentration and the targeted enrichment of 19.75 wt.% for the LEU fuel. With that information, we conducted a series of simulations to investigate the effects of carbide volume fraction, ^{235}U enrichment, and FR on gas bubble swelling in U-Mo fuel.

Evaluation of Volume Fraction of Carbides and ^{235}U Enrichment in U-10Mo Fuel

Depending on the manufacturing conditions, varied carbide volume fraction and ^{235}U enrichment are expected in the final U-Mo alloy fuels. To investigate these variables on the fuel performance, the potential ranges of these factors should be evaluated. Following a previous study by Devaraj et al. [97], we estimated the carbide volume fraction based on the typical carbon concentration in the final U-Mo alloy fuel, and the ^{235}U enrichment in carbides and fuel matrix. Based on the microstructure characterization [85], the bcc-structured $\gamma\text{-UMo}$ phase and UC phase are the two dominant phases in the as-cast and homogenized U-10Mo alloy. Assuming that (1) $\gamma\text{-UMo}$ and UC are the only two phases in the final U-10Mo alloy, (2) the final alloy composition of $\text{U}_{90-x}\text{Mo}_{10}\text{C}_x$ with 19.75 wt.% of total U weight as ^{235}U , and (3) zero solubility of C in U-Mo matrix, the volume fraction of UC phase as a function of carbon concentration is predicted as

$$\text{Volume fraction of UC (\%)} = 2.622 \times 10^{-3} \times \text{Concentration of C (wt. ppm)}. \quad (76)$$

For a typical carbon concentration of 200~1200 weight ppm, the volume fraction of carbides is predicted to be 0.5~3.0%. Based on BSE scanning electron microscopy (BSE-SEM) images, the volume fraction of UC can also be estimated using threshold-based image processing techniques. Recent works by Nyberg et al. have shown that UC volume fraction in as-cast depleted U-Mo ranges from 1~2% [89]. The currently calculated carbide volume fraction based on carbon concentration is in good agreement with the measurement from SEM images.

Since the fabricated U-10Mo LEU fuel is made from the mixing and melting of the DU and HEU feedstocks, the ^{235}U is expected to come mainly from the HEU feedstock. The UC phase in the final U-Mo fuel can come preexisting from the HEU which stays undissolved during the fuel manufacturing stages, or it can be formed during the melting and casting processes. Therefore, the final ^{235}U enrichment in the UC phase will depend on when the UC phase was formed. To satisfy the LEU specification of a 19.75 wt.% enrichment in the fabricated U-Mo fuel, the final enrichment in the U-Mo matrix is affected by the volume fraction of UC in the final fuel, which depends on the carbon concentration. For this reason, we estimated the effective enrichment of ^{235}U in the U-Mo matrix by considering the following five enrichment levels of UC phases:

1. 0% enrichment, corresponding to pure ^{238}UC
2. 19.75% enrichment, corresponding to LEU UC
3. 50% enrichment, corresponding to medium-enriched (MEU) UC
4. 90% enrichment, corresponding to high-enriched (HEU) UC
5. 100% enrichment, corresponding to pure ^{235}UC .

Figure 55 shows the calculated ^{235}U enrichment in the U-Mo fuel matrix as a function of carbon concentration. Clearly, the pure ^{238}UC and ^{235}UC cases represent the upper and lower bounds for the ^{235}U enrichment in the U-Mo matrix.

We also plotted the ^{235}U enrichment in the U-Mo matrix as a function of ^{235}U enrichment in UC for three different volume fractions of UC (i.e., 1%, 2%, and 4%) in Figure 56. With an increased volume fraction of carbides, the ^{235}U enrichment in the U-Mo matrix decreases faster as the ^{235}U enrichment in UC increases. The currently obtained ^{235}U enrichment in U-Mo fuel due to different ^{235}U enrichment and volume fractions of UC will be used to investigate their impact on the gas bubble swelling in U-Mo fuel in the following sections.

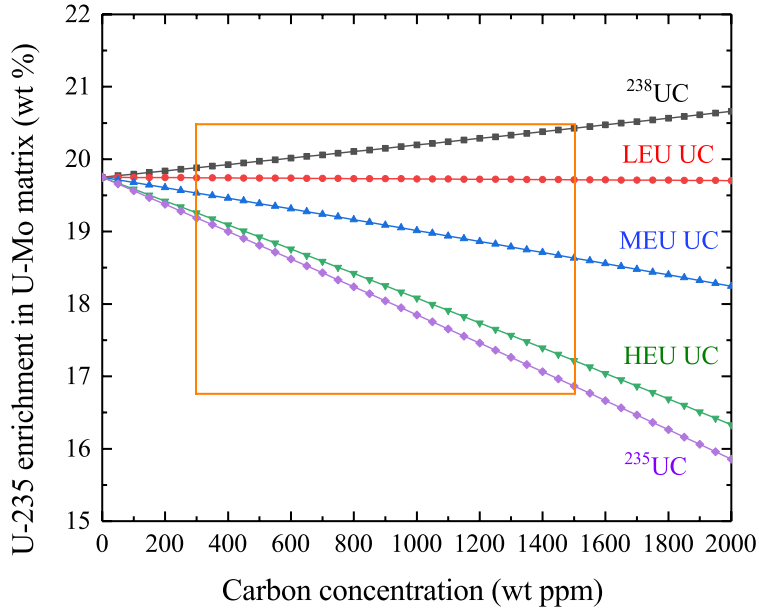


Figure 55. ^{235}U enrichment in U-Mo matrix as a function of carbon concentration for five different levels of enrichment in UC by assuming an effective ^{235}U enrichment of 19.75 wt.% in the final U-Mo fuel.

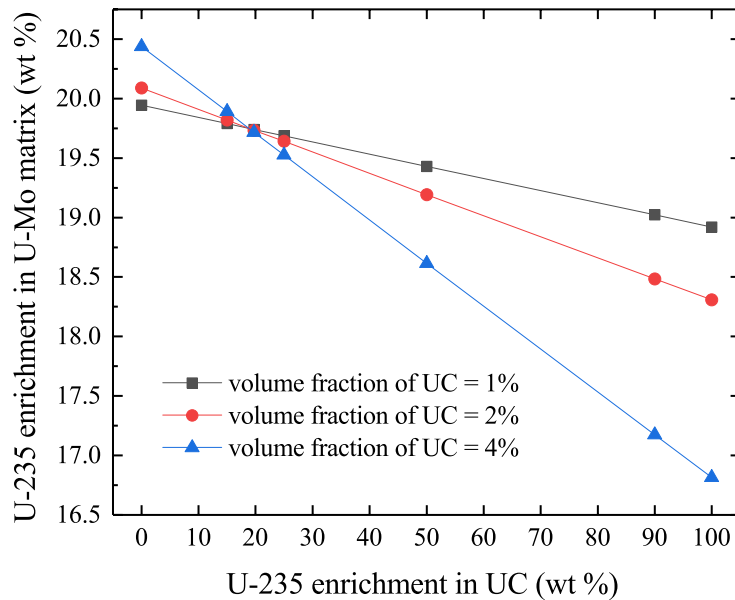


Figure 56. ^{235}U enrichment in U-Mo matrix as a function of the ^{235}U enrichment in UC for three different volume fractions of UC by assuming an effective ^{235}U enrichment of 19.75 wt.% in the final U-Mo fuel.

Effect of ^{235}U Enrichment in Carbides on Gas Bubble Swelling

To simulate the effect of ^{235}U enrichment in UC on the gas bubble swelling of U-Mo fuel, we considered four different ^{235}U enrichments for the UC phase, (i.e., 15%, 19.75%, 25%, and 50%), in which 19.75% is the targeted enrichment for the final U-Mo fuel. The following two scenarios regarding the potential ^{235}U enrichment in the U-Mo fuel matrix were investigated,

1. Uniform ^{235}U enrichment in U-Mo fuel matrix balanced by an effective ^{235}U enrichment of 19.75 wt.% in the final U-Mo fuel. The corresponding ^{235}U enrichment in the U-Mo fuel matrix can be obtained from Figure 56.
2. Uniform ^{235}U enrichment in U-Mo fuel matrix fixed at 19.75 wt.%. The effective ^{235}U enrichment in the final U-Mo fuel could be either higher or lower than the targeted enrichment of 19.75 wt.%, depending on the enrichment in UC.

To exclude the additional variable of carbide volume fraction, we fixed the volume fraction of UC at 2% in this section, which represents an upper bound for the carbide volume fraction measured from the SEM images of the U-10Mo fuel [85,89]. The microstructure of carbide distribution in the U-Mo fuel matrix was generated based on the previous study of the morphology and size distribution of carbides in U-10Mo alloy fuel. In this work, we assumed that carbides are dispersed inside the fuel grain. The effect of intergranular carbides on fuel swelling will be studied in the next FY. As we pointed out early, due to the lack of the material properties required for the explicit simulation of fission-gas behaviors in UC, UC inclusions were treated as U-Mo grains but with different ^{235}U enrichment. Therefore, the simulation of ^{235}U enrichment in UC on fuel swelling is effectively modeling the inhomogeneous distribution of ^{235}U in U-Mo fuel.

The simulated gas bubble swelling kinetics due to different ^{235}U enrichment in UC for case1 is shown in Figure 57. It can be seen that the effect of ^{235}U enrichment in UC on the swelling is minor due to the fixed effective ^{235}U enrichment in the final fuel. Even with a very high ^{235}U enrichment of 50% in UC, the gas bubble swelling in U-Mo changes slightly compared to the case with homogeneously distributed ^{235}U of 19.75 wt.% in both the UC and the U-Mo matrix. In comparison, the effect of ^{235}U enrichment in UC on gas bubble swelling is more notable in case2, (i.e., with a fixed ^{235}U enrichment in the U-Mo fuel matrix). As shown in Figure 58, at a FD of 7.0×10^{27} f/m³, the gas bubble swelling in U-Mo fuel increases by 7.9% as the ^{235}U enrichment in UC increases from 15 to 50%.

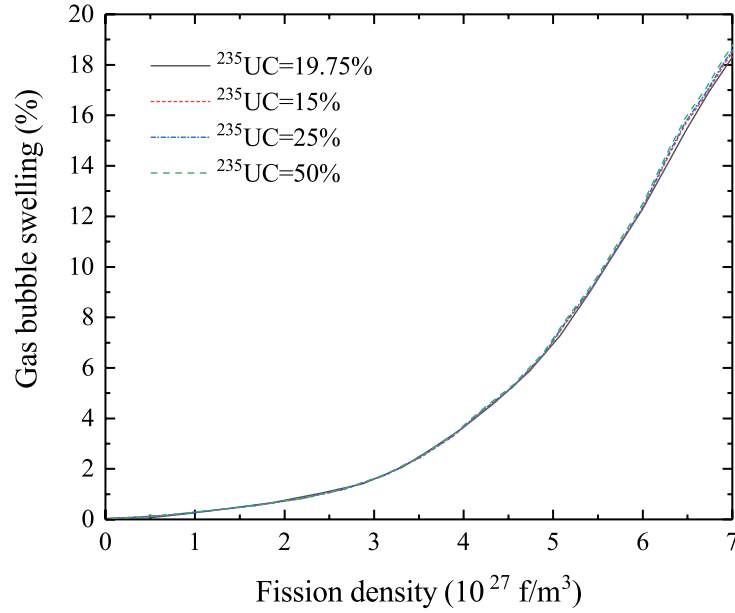


Figure 57. Effect of ^{235}U enrichment in UC (volume fraction of UC = 2%) on the gas bubble swelling of U-Mo fuel irradiated at a FR of $5.0 \times 10^{20} \text{ f/m}^3 \cdot \text{s}$. The effective ^{235}U enrichment in the final fuel was fixed at 19.75 wt.%.

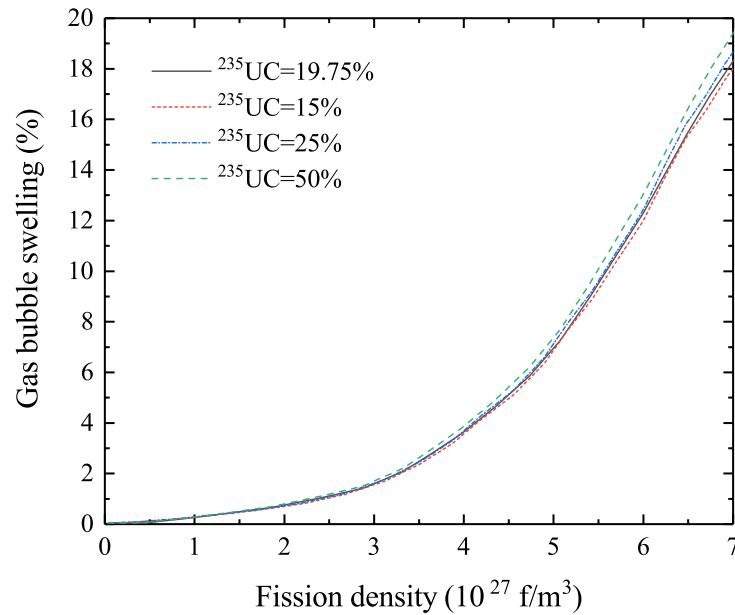


Figure 58. Effect of ^{235}U enrichment in UC (volume fraction of UC = 2%) on the gas bubble swelling of U-Mo fuel irradiated at a FR of $5.0 \times 10^{20} \text{ f/m}^3 \cdot \text{s}$. The ^{235}U enrichment in the U-Mo matrix was fixed at 19.75 wt.%.

Effect of Volume Fraction of Carbides on Gas Bubble Swelling

To simulate the effect of the volume fraction of UC on the gas bubble swelling, we considered four different UC volume fractions (i.e., 0%, 1%, 2%, and 4%). To isolate the effect of ^{235}U enrichment in UC on fuel swelling, the enrichment of UC was fixed at 25%, which is about 5% higher than the targeted enrichment for the final U-Mo fuel. Two scenarios regarding the potential ^{235}U enrichment in the U-Mo fuel matrix were examined:

1. Uniform ^{235}U enrichment in U-Mo fuel matrix balanced by an effective ^{235}U enrichment of 19.75 wt.% in the final U-Mo fuel
2. Uniform ^{235}U enrichment in U-Mo fuel matrix fixed at 19.75 wt.%.

The simulated gas bubble swelling kinetics in U-Mo fuel with different volume fractions of carbides for case1 are shown in Figure 59. We can see that the carbide inclusion has a very small impact on the gas bubble swelling if the effective ^{235}U enrichment in the final U-Mo fuel can be controlled at the targeted value of 19.75 wt.%. Even for the extreme case of a 4% volume fraction of UC inclusion, the gas bubble swelling only slightly increases by 1.2% compared to the case without any UC inclusion.

For case2, since the ^{235}U enrichment in the U-Mo fuel matrix is fixed at 19.75 wt.%, the effective enrichment in the final U-Mo fuel will be slightly higher than the targeted value of 19.75 wt.%. As expected, the gas bubble swelling increases as the volume fraction of UC increases. For example, at a FD of $7.0 \times 10^{27} \text{ f/m}^3$, the gas bubble swelling in U-Mo fuel increases by 3.6% when the volume fraction of UC inclusions increases from 0% to 4%.

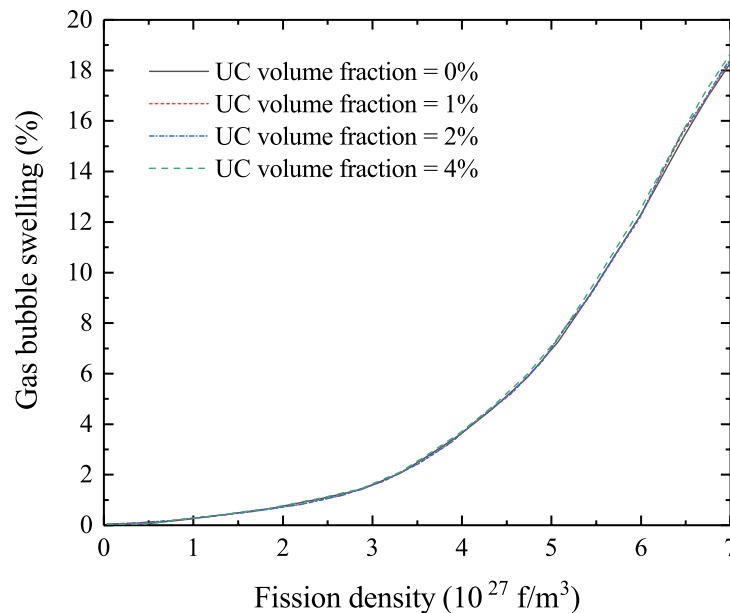


Figure 59. Effect of the volume fraction of UC (^{235}U enrichment of 25% in UC) on the gas bubble swelling of U-Mo fuel irradiated at a FR of $5.0 \times 10^{20} \text{ f/m}^3 \cdot \text{s}$. The effective ^{235}U enrichment in the final fuel was fixed at 19.75 wt%.

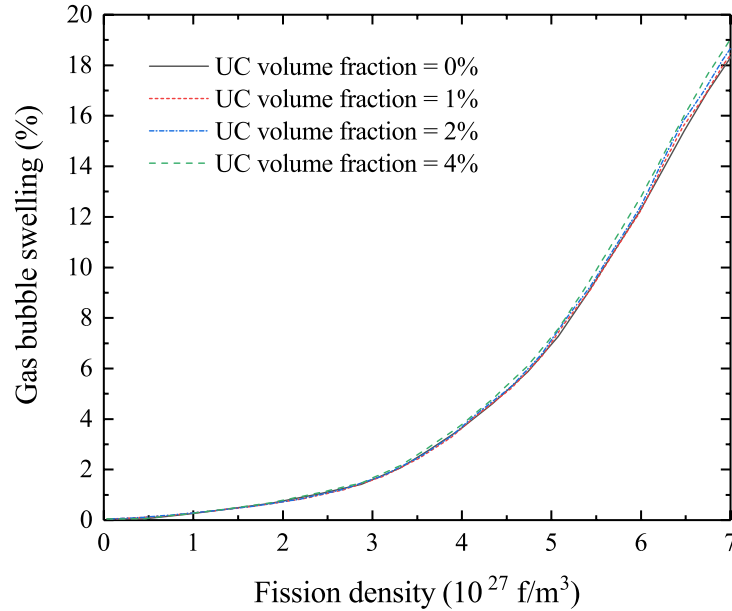


Figure 60. Effect of the volume fraction of UC (^{235}U enrichment of 25% in UC) on the gas bubble swelling of U-Mo fuel irradiated at a FR of $5.0 \times 10^{20} \text{ f/m}^3 \cdot \text{s}$. The ^{235}U enrichment in the U-Mo matrix was fixed at 19.75 wt.%.

Effect of Fission Rate on Gas Bubble Swelling

The effect of FR on the gas bubble swelling in U-Mo fuel has been simulated in our previous work, in which the effects of FR on the nucleation of gas bubbles, generation of fission gases, dislocation accumulation, and diffusivities of gas atoms were considered. To understand the effect of FR on the fuel swelling in U-Mo with UC inclusions, we simulated the gas bubble swelling in the U-Mo alloy fuel using three different FRs (i.e., 3.0×10^{20} , 5.0×10^{20} , and $9.0 \times 10^{20} \text{ f/m}^3 \cdot \text{s}$). In terms of the volume fraction and ^{235}U enrichment in the UC phase, the following three cases were investigated in this work:

Case 1: There is no UC inclusion, and the ^{235}U enrichment in U-Mo fuel matrix fixed at 19.75 wt.%.

Case 2: There is 4% volume fraction of UC with ^{235}U enrichment of 25%, and effective ^{235}U enrichment in the final U-Mo fuel is fixed at 19.75 wt.%.

Case 3: There is 4% volume fraction of UC with ^{235}U enrichment of 25%, and ^{235}U enrichment in U-Mo matrix is fixed at 19.75 wt.%. The effective ^{235}U enrichment in the final U-Mo fuel will be slightly higher than the targeted value of 19.75 wt.%.

It should be noted that the volume fraction and ^{235}U enrichment simulated for Cases 2 and 3 are much higher than the typical volume fraction (0.5 ~ 2%) and ^{235}U enrichment (19~21%) for UC inclusion observed from experiments.

The effect of FR on the gas bubble swelling of U-Mo fuel without any UC inclusion is shown in Figure 61. The predicted swelling kinetics at a FR of $5.0 \times 10^{20} \text{ f/m}^3 \cdot \text{s}$ is consistent with the experimental data compiled by Kim [34]. At FDs below $3 \times 10^{27} \text{ f/m}^3$, the effect of FR on gas bubble swelling is negligible. At higher FDs, the gas bubble swelling was enhanced with an increasing FR. For example, at a FD of $6.5 \times 10^{27} \text{ f/m}^3$, the gas bubble swelling in U-Mo fuel was predicted to increase by 13.1% when the FR increases from 5.0×10^{20} to $9.0 \times 10^{20} \text{ f/m}^3 \cdot \text{s}$.

Figure 62 shows the gas bubble swelling kinetics of U-Mo fuel with a volume fraction of 4% UC inclusion under different FRs, corresponding to Cases 2 and 3, respectively. For better visualization of the

effect of UC inclusion and enrichment on fuel swelling, the calculated gas bubble swelling at a FD of $6.5 \times 10^{27} \text{ f/m}^3$ are plotted in Figure 63 as a function of FR. Due to the same effective ^{235}U enrichment in the final U-Mo fuel, the gas bubble swelling calculated for Case 2 are very close to Case 1 without any UC inclusion. In comparison, the gas bubble swelling for Case 3 is notably higher compared to Case 1, which can be attributed to the higher effective ^{235}U enrichment for case 3.

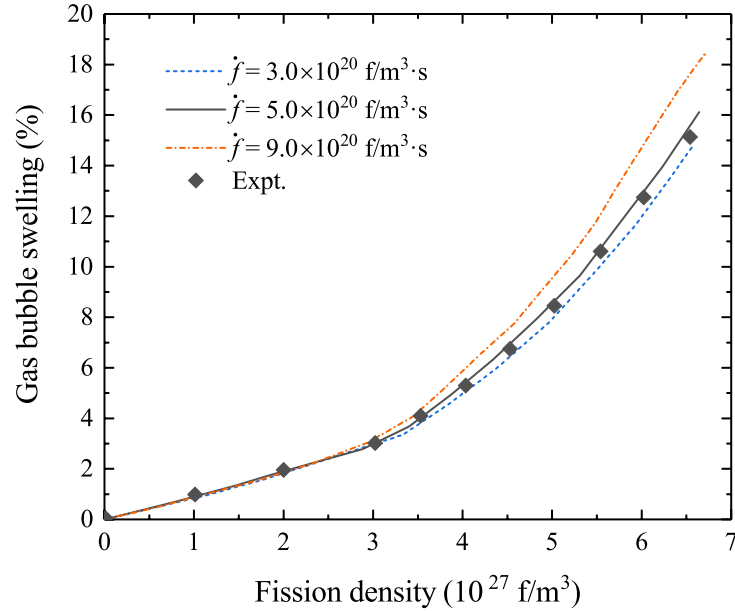


Figure 61. Gas bubble swelling kinetics of U-Mo fuel without UC inclusion under different fission rates, compared with experimental data compiled by Kim [34].

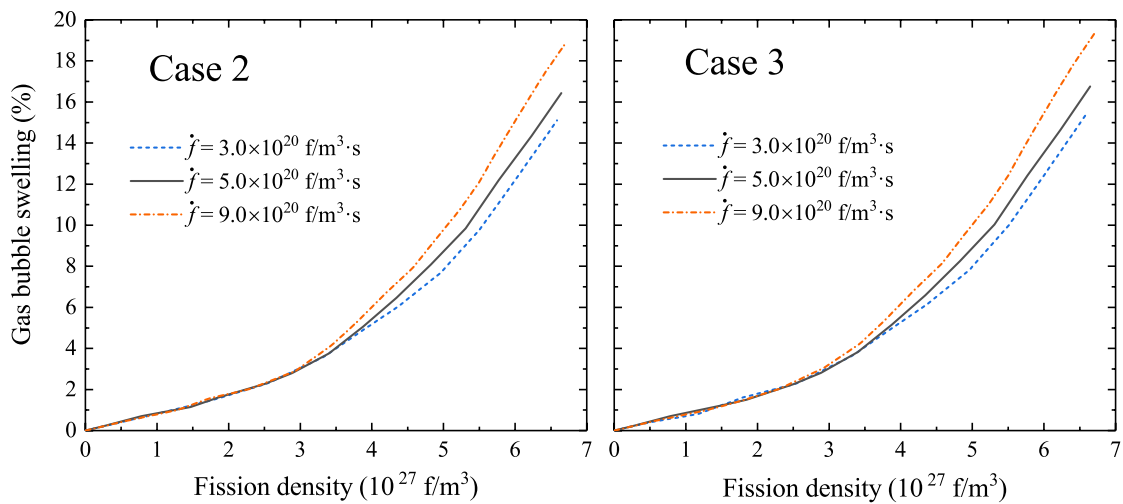


Figure 62. Gas bubble swelling kinetics of U-Mo fuel with UC inclusion under different fission rates.

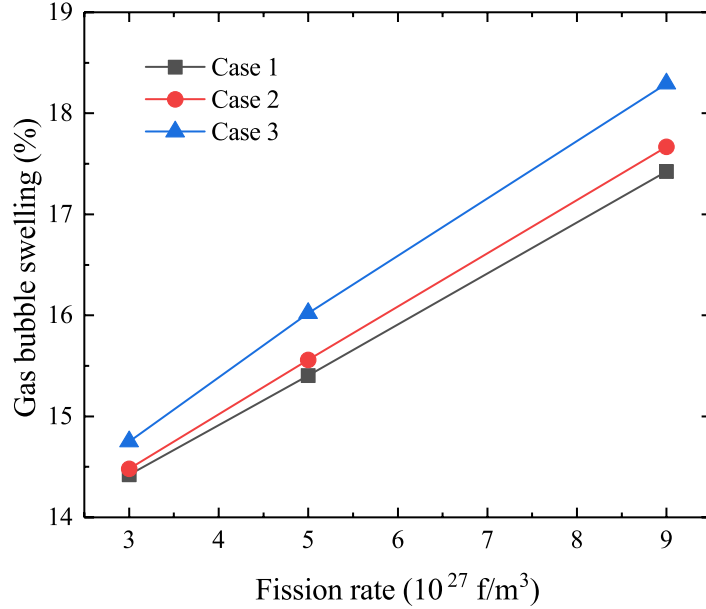


Figure 63. Gas bubble swelling of U-Mo fuel as a function of FR at the FD of $6.5 \times 10^{27} \text{ f/m}^3$ for three different cases of UC inclusion.

2.5.4 Conclusions

To summarize, we investigated the effect of UC inclusions on the mechanical properties of U-Mo alloy fuel using different simulation approaches (i.e., analytical models, FEM, and DFT simulations). From the analysis of the BSE-SEM images of the as-cast, homogenized, and hot-rolled U-Mo alloy samples, the particle size distribution, volume fraction, and shape of carbide inclusions were obtained using image processing techniques. The obtained information regarding the carbide volume fraction, size distribution, and aspect ratio was used to generate synthetic microstructures for the evaluation of carbides on the mechanical properties of U-Mo fuel using both analytical models and FEM simulations. Calculations show that carbides have a minor impact on the Young's and shear modulus of U-Mo fuel when the carbide inclusions show a typical volume fraction of 0.5~1% and average aspect ratio of 1.5~2.5 as observed in experiments. Meanwhile, DFT simulations were performed to investigate the effects of Mo concentration of U-Mo alloy and non-stoichiometry of UC on the mechanical properties of U-Mo with carbides. DFT calculations show that decreased Mo concentration of U-Mo alloy will slightly decrease the mechanical strength of the UMo/UC interface, while increased hypo-stoichiometry of C in carbides will also decrease the mechanical strength of the interface, especially for highly non-stoichiometric UC. We also performed PF simulations to study the effect of the ^{235}U enrichment in UC inclusions on the gas bubble swelling in U-Mo fuel. The potential ranges of the volume fraction of UC inclusions and the ^{235}U enrichment in UC and the U-Mo fuel matrix were obtained based on the carbon concentration in U-Mo alloy fuel and the targeted ^{235}U enrichment of 19.75 wt.% in the final U-Mo fuel. Our simulation suggests that the ^{235}U enrichment and the volume fraction of UC inclusions have a minor impact on the gas bubble swelling if the targeted ^{235}U enrichment of 19.75% in the final U-Mo fuel can be achieved. However, for cases with the enrichment in U-Mo fuel matrix fixed at the targeted value, highly enriched UC inclusions can lead to an increased gas bubble swelling compared to the case without any UC inclusions due to the increased effective ^{235}U enrichment in the final U-Mo fuel. Finally, we studied the effect of FR on the gas bubble swelling in U-Mo fuel with and without UC inclusions. Calculations show that increased FR can result in higher gas bubble swelling, and the changing rate of gas bubble swelling due to FR will be enhanced by the increased effective ^{235}U enrichment in the final U-Mo fuel. Since the currently studied ^{235}U enrichment (15~50%) and volume fraction of UC (1~4%) are considerably higher than those

observed in experiments (19~21% for ^{235}U enrichment, and 0.5~1% for volume fraction), the current simulations should provide the lower and upper bounds for the potential impact of UC inclusions on the gas bubble swelling in U-Mo alloy fuel.

2.6 Radiation-Enhanced Diffusion in UMo

The evolution of the microstructure in nuclear fuel under irradiation is a complicated process with numerous phenomena involved from the atomic to the micro scale. The behavior of FGBs in U-Mo fuel under irradiation includes noble gases such as Xe and Kr, with low solubility, precipitating and forming FGBs both inside the grains (intragranular FGBs) and along the GBs (intergranular FGBs). The intergranular FGBs grow with increasing temperature and FR since the created gases diffuse into the GBs. This rate of diffusion plays a significant role in the fission-gas swelling behavior but is generally unknown as a function of temperature and FR. In this work, the radiation-enhanced diffusion is determined for U, Mo, and Xe as a function of composition and temperature in UMo alloys. This work serves to complement the previous studies on radiation-driven diffusion in prior FYs.

2.6.1 Computational Details

2.6.1.1 Interatomic Potential

MD simulations were performed with the LAMMPS software package [53]. The accuracy of MD simulations greatly depends on the accuracy of the interatomic potential used. The success of EAM potentials to describe metallic systems is derived from its formalism in describing many-body interactions, which pair-wise potentials are unable to do. A general form of the EAM potential is described as follows [115,116]

$$E_{total} = \sum_{i<j} \phi_{ij}(r_{ij}) + \sum_{i<j} F\left(\sum_{j\neq i} \rho_j(r_{ij})\right) \quad (77)$$

where E_{total} is the total energy of the system, and ϕ_{ij} is the pair-wise energy term, which depends on the distance (r_{ij}) between two given atoms i and j . The term $F(\sum_{j\neq i} \rho_j(r_{ij}))$ is the embedding energy of atom i , which describes the many-body interatomic interactions, depending on the background electron density (ρ_i) at the location of atom i . In this study, the EAM potential for the ternary U-Mo-Xe system, developed by Smirnova et al. [54], was utilized.

2.6.1.2 Evolution of Defect Concentration under Irradiation

It is assumed that apart from vacancies and interstitials, Xe, the most present fission product, is continuously produced, and thus, Xe interstitial atoms and Xe-vacancy clusters exist in the system. The rate of change of defect concentrations including Xe and Xe-vacancy clusters with time can be described by Eqns. 78-84 as shown below.

$$\frac{dC_v}{dt} = \epsilon\dot{F} - K_{iv}C_iC_v - k_{vs}^2D_vC_v + \sum_{k=1}^n \alpha_{k+1}C_{Xe-kv} - \sum_{k=1}^{n-1} \beta_k C_vC_{Xe-(k-1)v} + \sum_{k=1}^{n-1} kR C_{Xe-kv} \quad (78)$$

$$\frac{dC_i}{dt} = \epsilon\dot{F} - K_{iv}C_iC_v - k_{vs}^2D_iC_i \quad (79)$$

$$\frac{dC_{Xe}}{dt} = \tau\dot{F} - \beta_1C_vC_{Xe} + \alpha_2C_{Xe-1v} + \sum_{k=1}^n R C_{Xe-kv} \quad (80)$$

$$\frac{dC_{Xe-1v}}{dt} = \beta_1C_vC_{Xe} - \beta_2C_vC_{Xe-1v} - \alpha_2C_{Xe-1v} + \alpha_3C_{Xe-2v} - RC_{Xe-1v} \quad (81)$$

$$\frac{dC_{Xe-2v}}{dt} = \beta_2C_vC_{Xe-1v} - \beta_3C_vC_{Xe-2v} - \alpha_3C_{Xe-2v} + \alpha_4C_{Xe-3v} - RC_{Xe-2v} \quad (82)$$

$$\frac{dC_{Xe-3v}}{dt} = \beta_3C_vC_{Xe-2v} - \beta_4C_vC_{Xe-3v} - \alpha_4C_{Xe-3v} + \alpha_5C_{Xe-4v} - RC_{Xe-3v} \quad (83)$$

$$\frac{dC_{Xe-nv}}{dt} = \beta_n C_v C_{Xe-(n-1)v} - \alpha_{n+1} C_{Xe-nv} - R C_{Xe-nv} \quad (84)$$

where \dot{F} is the FR; ϵ is the defect production rate per fission event; K is the recombination constant of vacancies and interstitials; k^2 is the sink strength of GBs; D is the diffusion coefficient; C_{Xe} is the Xe concentration; C_{Xe-nv} is the concentration of Xe cluster containing n vacancies; τ is the yield of Xe from fission reaction (0.06); β_n is the absorption coefficient; α_n is the emission coefficient; and R is the resolution rate of a Xe-vacancy cluster. Initial concentration of vacancies and interstitials were set to 5.5×10^{-9} . The subscripts i, v, and s denote interstitial, vacancy, and sink, respectively. Thus, the subscripts iv, is, and vs indicate the interaction between interstitials and vacancies/interstitials and sinks/vacancies and sinks. In this case, sinks are restricted to GBs. The defect production is calculated from the arc-dpa model, which is a modification of the Norgett, Robinson, and Torrens (NRT) model for calculating displacements that also includes recombination. The number of defects generated (N_d) is described by the arc-dpa model as

$$N_d = \frac{0.8T_d}{2E_d} \xi \quad (85)$$

where T_d is the damage energy, E_d is the displacement energy, and ξ is the arc-dpa efficiency function. The magnitude of E_d and for γ U-Mo is not well known but can be potentially determined from MD or from experiments. Given that such studies are beyond the scope of this work, reasonable approximations are made for the displacement energy (60 eV) [117], based upon MD simulations in γ U, and for the arc-dpa efficiency (0.25), which is approximately the same as bcc Fe. The damage energy is taken as the kinetic energy of the fission fragments produced from a fission reaction (approximately 170 MeV) and reduced to account for electronic energy losses. It is assumed that only ballistic effects are generating Frenkel pairs in this work. The electronic energy losses have been previously calculated to be 95%, thus the damage energy here is taken as 8.5 MeV. This yields approximately 14,000 defects per fission in γ U-Mo. Any bias towards interstitials or vacancies in the defect production process is neglected, assuming that an equal number of both types of defects are generated.

In classical rate theory, the GBs are constant sinks and their strength k^2 is estimated as $15/L^2$ (L is the grain size, in units of nm) for GBs with a regular pattern and is identical for both interstitials and vacancies. This assumption is utilized here as a first approximation, and, along with a grain boundary size estimate of 10 microns, completes the parametrization of the rate theory equations.

The absorption and emission coefficients are calculated by Eqns. 86 and 87 as described below

$$\beta_n = \frac{4\pi(r_1+r_n)D_v}{V_{at}} \quad (86)$$

$$\alpha_{n+1} = \beta_n \exp\left(\frac{E_b^n}{kT}\right) \quad (87)$$

where r_1 is the size of a single vacancy; r_n is the radius of a Xe cluster containing n vacancies; V_{at} is the atomic volume for body-centered cubic crystal structure; E_b^n is the binding energy of a Xe cluster containing n vacancies. E_b^n can be calculated by the following equation

$$E_b^n = E_F^{n+1} - E_F^n - E_v \quad (88)$$

here E_F^n is the formation energy of Xe cluster with n vacancies, and E_v is the vacancy formation energy. The vacancy formation energy is assumed to be 1.6 eV in the present work [118]. Utilizing the temperature-dependent recombination rate constant (K_{iv}), the temperature-dependent diffusion coefficients, the defect production rate, the Xe production rate, the assumed grain sink strength (assumed

grain size: 10 μm), binding energy, and a given FR, the coupled rate theory equations can be solved for the steady-state concentration of defects in $\gamma\text{U-10Mo}$ under irradiation.

2.6.1.3 Radiation-Enhanced Diffusion Coefficients of U, Mo, and Xe

U and Mo in $\gamma\text{U-Mo}$ can diffuse via both vacancies and interstitials [118]. However, it is assumed that Xe diffuses primarily via vacancy clustering due to its extremely slow diffusion. Radiation-enhanced diffusion of U/Mo and Xe are determined in a different way. Given a steady-state concentration of defects under irradiation, the radiation-enhanced diffusion coefficient (D_{RED}) of U and Mo can be expressed as

$$D_{RED}^{U/Mo} = D_v^{th} C_v^{irr} + D_i^{th} C_i^{irr} \quad (89)$$

where D^{th} is the thermal (intrinsic) diffusion coefficient, and C^{irr} is the equilibrium concentration of defects under irradiation. The radiation-enhanced diffusion coefficient (D_{RED}) of Xe can be described as

$$D_{RED}^{Xe} = \sum_{k=1}^n D_{Xe-nv}^{th} C_{Xe-nv}^{irr} \quad (90)$$

where D_{Xe-nv}^{th} is the thermal diffusion coefficient of Xe cluster containing n vacancies, and C_{Xe-nv}^{irr} is the equilibrium concentration of Xe cluster containing n vacancies under irradiation. Utilizing both experimental diffusional observations [119] and previous MD studies [8], the total diffusion coefficients of U, Mo, and Xe can be obtained as the summation of the intrinsic diffusion, the radiation-enhanced diffusion, and the radiation-driven diffusion, and they will be presented in this work.

2.6.2 Results

2.6.2.1 Calculation of Recombination Rate Constants

Fifty Frenkel pairs were inserted into a system of 128,000 atoms and allowed to evolve and recombine. The total number of defects, and thus the defect concentration, was tracked as a function of time. This defect evolution simulation was performed from 600 to 1200 K in increments of 100 K. Temperatures below 600 K were not explored since intrinsic diffusion on MD timescales is very limited below 600 K in $\gamma\text{U-10Mo}$. The number of defects as a function of time for a system at 1000 K is displayed in Figure 64, as an example. Note that recombination was taken into account in the evolution of defects in the system. It can be observed that the number of defects reduces as a function of time in a near-exponential fashion, with the rate of annihilation slowing as a function of time due to the decreased number of defects present. This decay can be fit to $C = C_0 / (C_0 * K_{iv} * t + 1)$, where K_{iv} is the recombination rate constant. The fit to the data is also shown in Figure 64, which provides a value of the recombination rate constant (K_{iv}) at a given temperature. The recombination rate constant was calculated from the defect concentration as a function of time at each temperature. Table 14 lists the recombination rate constant (K_{iv}) calculated in the temperature range between 600 and 1200 K.

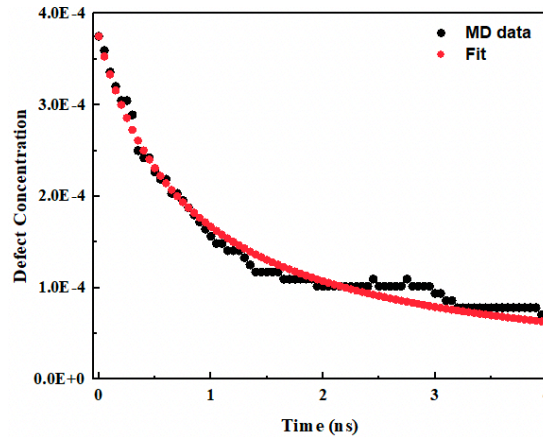


Figure 64. Evolution of defect concentration as a function of time at 1000 K.

Table 14. Recombination rate constants (K_{iv}) at different temperatures.

Temp. (K)	K_{iv} (1/ns)
600	172.1
700	429.2
800	1057.1
900	2280.9
1000	3380.3
1100	5785.7
1200	8447.4

According to kinetic theory, the recombination rate constant (K_{iv}) can be estimated as $K_{iv} = 4\pi(D_i + D_v)r_{iv}/V_{at}$, where V_{at} is the atomic volume for body-centered cubic, and r_{iv} is the recombination radius. Typical values of the recombination radius are on the order of 2–3 times the equilibrium lattice constant (a_0). By utilizing the fit values of the recombination rate constant and the known diffusion coefficients and equilibrium volume, the recombination radius can be determined. It is found that recombination radius is significantly larger than what is typically observed. For example, at 1000 K, the recombination radius is approximately $8 \cdot a_0$. As the temperature decreases, the recombination radius increases farther, such that the value of the recombination radius at 600 K is $24 \cdot a_0$. It is assumed that this is due to very long stress field interactions between interstitials and vacancies, leading to rapid recombination. This perhaps compensates for the incredibly low interstitial formation energies in γ U systems, in that the large number of defects that can be created also rapidly recombine. Such a phenomenon was hinted at in previous studies on displacement energies in γ U [120].

2.6.2.2 Calculation of Formation and Binding Energies of Xe-Vacancy Clusters

Figure 65a represents formation energies of Xe substitutional and Xe-vacancy clusters as a function of temperature. The formation energies were calculated at seven different temperatures. Xe clusters having more than four vacancies nearby are not considered in this work due to extremely low concentration. It was found that the formation energies of Xe clusters increased almost linearly with increasing temperature. Thus, the formation energies were linearly fitted, and the fitted values were obtained at temperatures from 300 to 1400 K in increments of 50 K in order to calculate the steady-state defect concentrations under irradiation. Figure 65b shows an example of binding energies of Xe clusters as a function of cluster size at 1000 K, obtained from the formation energies. The binding energies increased with increasing Xe cluster size.

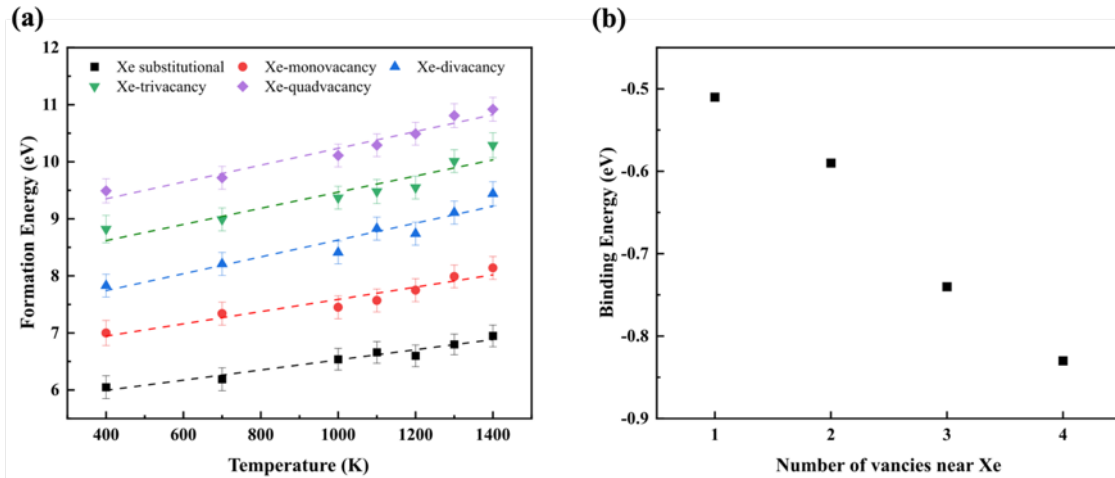


Figure 65. (a) Formation energies of Xe-vacancy clusters as a function of temperature. (b) Binding energies of Xe-vacancy clusters at 1000 K.

2.6.2.3 Evolution of Defect Concentration under Irradiation

Evolution of defect concentrations in γ U-10Mo were studied as a function of time. Figure 66 shows the result of calculating the coupled rate theory equations at the FR of 5×10^{20} fiss/m³/s at 1000 K, as an example. These calculations indicate that the equilibrium defect concentrations are approximately 1.7×10^{-8} for vacancies, 2.45×10^{-9} for interstitials, 7.35×10^{-9} for Xe-mono vacancies, 3.03×10^{-15} for Xe-divacancies, 1.43×10^{-21} for Xe-trivacancies, and 7.13×10^{-28} for Xe-quadvacancies. The steady-state concentration of Xe-vacancy clusters decreased as the cluster size increased. It took approximately 0.5 s to reach steady state for vacancies and interstitials. However, the concentration of Xe and Xe clusters kept growing slowly with respect to time since Xe was continuously produced with a yield of 0.06. The defect concentration at the time of 1 year was considered to be the steady-state defect concentration with the assumption that 1 year (3.15×10^7 s) is long enough to reach equilibrium.

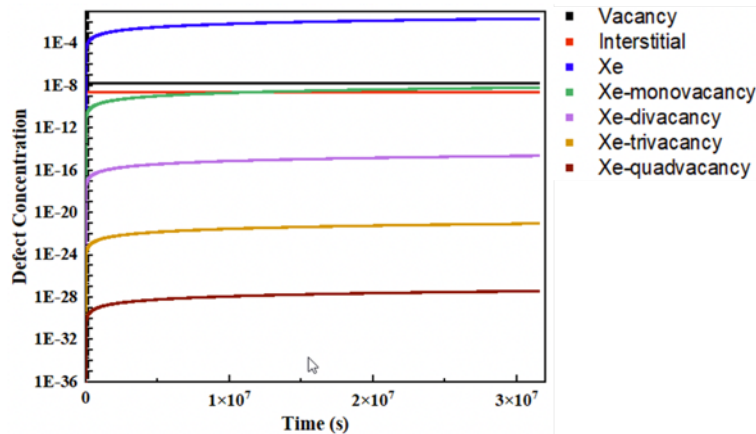


Figure 66. Rate theory calculations of defect concentration evolution as a function of time at the FR of 5×10^{20} fiss/m³/s at 1000 K.

Figure 67 shows the steady-state defect concentration as a function of inverse temperature in γ U-10Mo at three different FRs. The evaluated temperature range was from 300 to 1400 K in increments of 50 K. The concentration of vacancies and interstitials increased with an increasing FR. As the temperature decreased below 600 K, the interstitial concentration decreased, while the vacancy concentration stayed

almost the same. This is presumably due to the restricted diffusion of vacancies, which increases the amount of interstitial diffusion to GBs, instead of leading to recombination with vacancies. Above 600 K, both concentrations decrease with increasing temperature, as an increase in diffusion leads to increased recombination. It should be emphasized that the interstitial and vacancy concentrations display opposite trends as a function of temperature under irradiation below 600 K. The concentration of Xe-monovacancy cluster increased with increasing the temperature up to 950 K at the FR of 5×10^{19} fiss/m³/s and then decreased as the temperature further increased. As the FR increased, the temperature where the concentration of the Xe-monovacancy cluster is the highest increased. At the FR of 5×10^{21} fiss/m³/s, the concentration of the Xe-monovacancy clusters increased up to 1400 K. Decreased concentration of Xe-monovacancy clusters at the high temperatures (e.g., > 950 K at the FR of 5×10^{19} fiss/m³/s) was due to decreased concentration of vacancies which recombined with interstitials and diffused into GBs. This complex temperature-dependent behavior is only captured due to the temperature-dependent recombination rate coefficient.

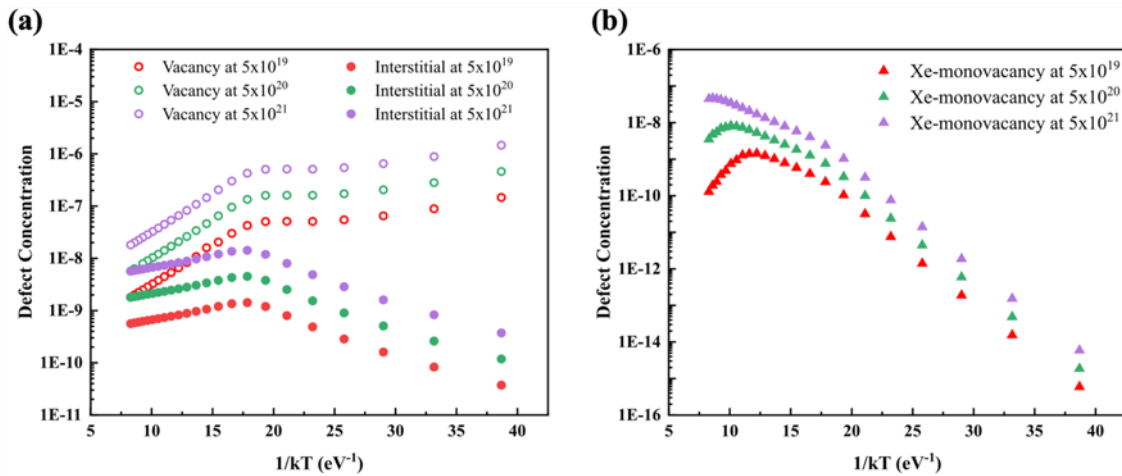


Figure 67. The steady-state defect concentration of (a) vacancies and interstitial (b) Xe-monovacancy as a function of temperature in γ U-10Mo for three different FRs: 5×10^{19} , 5×10^{20} , and 5×10^{21} fiss/m³-s.

2.6.2.4 Thermal (Intrinsic) Diffusion Coefficients of U, Mo, and Xe

The thermal diffusion coefficients of U, Mo, and Xe were calculated and fitted into the Arrhenius equation for the calculation of diffusion coefficients at lower temperatures as shown in Figure 68a. The calculation of vacancy and interstitial diffusion of U and Mo in γ U-10Mo were conducted by Park et al. [118], and additional MD calculations were conducted at 900 K, 1100K, 1300 K, and 1400 K to improve statistics. Diffusion of U and Mo through a vacancy was not investigated below 900 K due to insignificant diffusion. Diffusion via interstitials was faster than the diffusion via vacancies, indicating that the diffusion mechanism in γ U-10Mo takes place primarily through interstitials. In addition, diffusion of U was faster than diffusion Mo, which is in agreement with the experimental observations [119]. Diffusion coefficient of Xe was slower than that of U and Mo despite the fact that Xe diffuses through vacancy clustering. This proves that diffusion of Xe is extremely slow. Diffusion of Xe was negligible below 1000 K. Since the diffusion coefficients were independent of the Xe cluster size, as shown in Figure 68b, the diffusion coefficients were averaged over all cluster sizes at each temperature. In order to estimate the diffusion coefficients at lower temperatures, the diffusion coefficients were fitted to the Arrhenius equation.

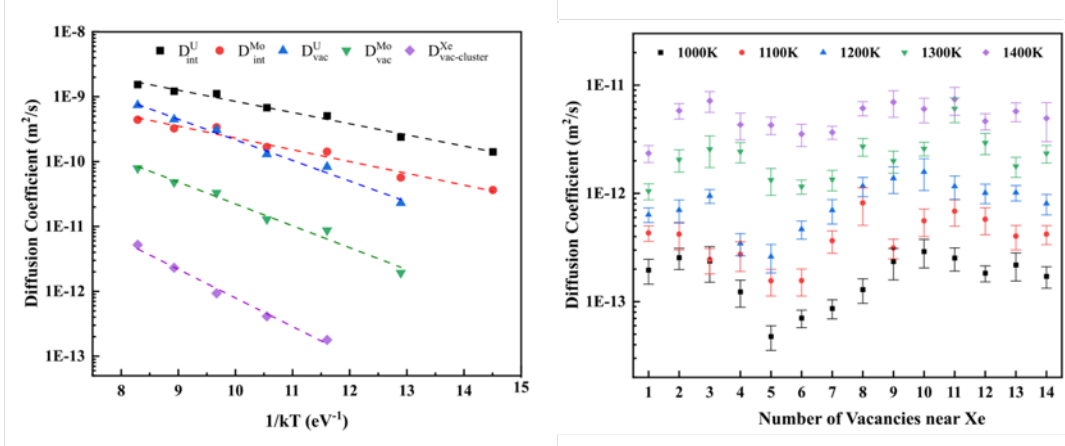


Figure 68. Diffusion coefficient of (a) U, Mo, and Xe (b) Diffusion coefficient of Xe as a function of cluster size from 1000 to 1400 K.

2.6.2.5 Radiation-Enhanced Diffusion Coefficients of U, Mo, and Xe

Based on Turnbull's model [22], diffusion under irradiation is comprised of three components: intrinsic diffusion (D_{INT}), radiation-enhanced diffusion (D_{RED}), radiation-driven diffusion (D_{RDD}). The total diffusion coefficient (D_T) under irradiation can be calculated by adding the three components

$$D_T = D_{INT} + D_{RED} + D_{RDD} \quad (91)$$

Since no experimental data exists at low temperatures, intrinsic diffusion coefficients of U and Mo at low temperatures were obtained by extrapolating the experimental data [119] into the low temperatures using the Arrhenius equation. The pre-factor and activation energy were $1.28 \times 10^{-5} \text{ m}^2/\text{s}$ and 1.76 eV for U and $1.62 \times 10^{-5} \text{ m}^2/\text{s}$ and 1.97 eV for Mo. No experimental data for intrinsic diffusion of Xe exists. Radiation-driven diffusion coefficients of U, Mo in γ U-10Mo were calculated by Beeler et. al [8]. Radiation-driven diffusion of the elements was dependent on PKA energy (per volume), the mean-squared displacements of each element, and fission fragment kinetic energy of a single fission event. The radiation-driven diffusion coefficients of U and Mo in γ U-10Mo can be described as follows

$$D_{RDD}^U = 1.97 \times 10^{-41} \times \dot{F} \quad (92)$$

$$D_{RDD}^{Mo} = 2.01 \times 10^{-41} \times \dot{F} \quad (93)$$

$$D_{RDD}^{Xe} = 5.07 \times 10^{-41} \times \dot{F} \quad (94)$$

Due to different diffusion mechanisms within the system, radiation-enhanced diffusion coefficients of U/Mo and Xe are calculated differently. First, radiation-enhanced diffusion coefficients of U and Mo, calculated using Eqn. 89, are represented in Figure 69a. Due to the variable dependence of the defect concentration on temperature, the radiation-enhanced diffusion coefficient needs to be piecewise fit with two Arrhenius equations for U and Mo. Thus, the data shown in Figure 69a is divided into four unique functions: (1) U at high T ($> 600 \text{ K}$), (2) U at low T ($\leq 600 \text{ K}$), (3) Mo at high T ($> 600 \text{ K}$), and (4) Mo at low T ($\leq 600 \text{ K}$). The effect of FR on radiation-enhanced diffusion of U and Mo was evaluated at 600 K. A square root dependence of the radiation-enhanced diffusion coefficient was observed. By dividing the total radiation-enhanced diffusion by the square root of the FR and the total radiation-enhanced diffusion, a coefficient for FR dependence can be obtained to construct a comprehensive equation for the total diffusion under irradiation. Therefore, the total diffusion coefficient of U and Mo can be described as follows

$$D_{U-highT} = 1.28 \times 10^{-5} \times \exp\left(-\frac{1.76}{kT}\right) + 1.38 \times 10^{-5} \times \exp\left(-\frac{0.73}{kT}\right) \times 5.3 \times 10^{-11} \times \sqrt{\dot{F}} + 1.97 \times 10^{-41} \times \dot{F} \quad (95)$$

$$D_{U-lowT} = 1.28 \times 10^{-5} \times \exp\left(-\frac{1.76}{kT}\right) + (1.24 \times 10^{-13}) \times \exp\left(-\frac{1.11}{kT}\right) \times 5.3 \times 10^{-11} \times \sqrt{\dot{F}} + 1.97 \times 10^{-41} \times \dot{F} \quad (96)$$

$$D_{Mo-highT} = 1.62 \times 10^{-5} \times \exp\left(-\frac{1.97}{kT}\right) + (1.65 \times 10^{-16}) \times \exp\left(-\frac{0.73}{kT}\right) \times 5.3 \times 10^{-11} \times \sqrt{\dot{F}} + 2.01 \times 10^{-41} \times \dot{F} \quad (97)$$

$$D_{Mo-lowT} = 1.62 \times 10^{-5} \times \exp\left(-\frac{1.97}{kT}\right) + (1.47 \times 10^{-14}) \times \exp\left(-\frac{1.02}{kT}\right) \times 5.3 \times 10^{-11} \times \sqrt{\dot{F}} + 2.01 \times 10^{-41} \times \dot{F} \quad (98)$$

It was found that intrinsic diffusion, radiation-enhanced diffusion, and radiation-driven diffusion were dominant at low-, intermediate-, and high-temperature regime, respectively, depending on the FR. More specifically, the temperature range that radiation-enhanced diffusion dominates increased with increasing FR. At the FR of 5×10^{19} fiss/m³/s, the radiation-enhanced diffusion was dominant between 450 and 600 K. As the FR increased to 5×10^{21} fiss/m³/s, the radiation-enhanced diffusion dominated between 550 to 650 K. Thus, it is expected that the radiation-enhanced diffusion dominates at lower temperatures at lower FRs (lower than 5×10^{19} fiss/m³/s), which is close to the operating temperatures of research reactors. Thus, radiation-enhanced diffusion of U and Mo will play an important role in the diffusion process in a low FR regime. In addition, radiation-enhanced diffusion of U and Mo will dominate in case of accidents at the FRs evaluated.

Utilizing the thermal diffusion coefficients and steady-state defect concentrations under irradiation (Eqn. 88), radiation-enhanced diffusion coefficients of Xe were also calculated as a function of inverse temperature as shown in Figure 69b. It is observed that the radiation-enhanced diffusion increased with increasing fission rates. At high temperatures, radiation-enhanced diffusion of Xe plateaued due to decreased concentration of Xe-vacancy clusters.

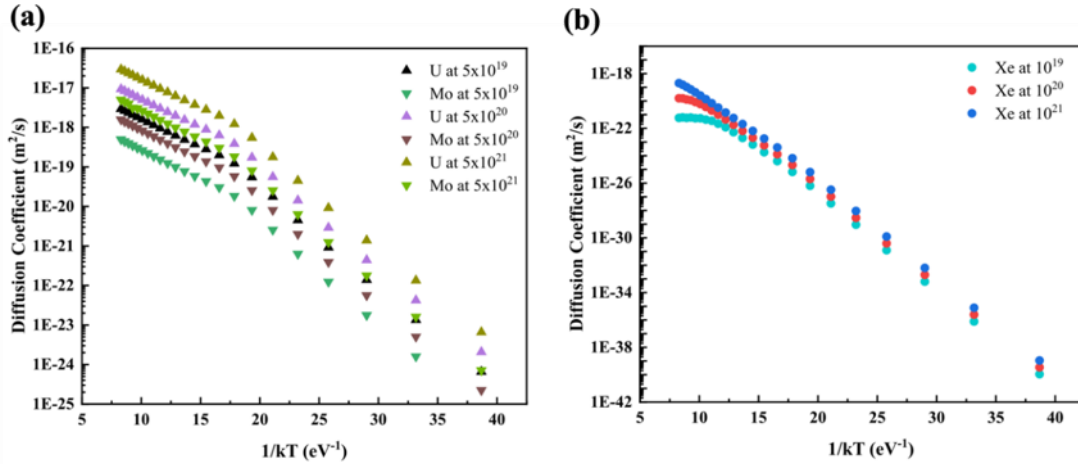


Figure 69. Radiation-enhanced diffusion of (a) U/Mo (b) Xe at three different fission rates. Units of the diffusion coefficients are fiss/m³/s.

Therefore, the total diffusion coefficients (D_T) of Xe in γ U-10Mo under irradiation can be expressed as follows

$$D_{T1}^{Xe} = 1.28 \times 10^{-9} \times \exp(-1.76/kT) + 1.97 \times 10^{-41} \times \dot{F} + \sum_{n=1}^{\infty} C_{Xe-nv}^{irr} \times 2 \times 10^{-8} \times \exp(-1.01/kT) \quad (99)$$

$$D_{T2}^{Xe} = 3.00 \times 10^{-10} \times \exp(-1.85/kT) + 1.97 \times 10^{-41} \times \dot{F} + \sum_{n=1}^{\infty} C_{Xe-nv}^{irr} \times 2 \times 10^{-8} \times \exp(-1.01/kT) \quad (100)$$

where k is the Boltzmann constant. It should be noted that in Eqns. 99 and 100, it has been assumed intrinsic diffusion of Xe is slower than the intrinsic diffusion of U by four orders of magnitude [58]. In this work, the intrinsic diffusion coefficient of Xe was calculated using the diffusion coefficient of Xe in a Xe-monovacancy cluster since diffusion of Xe is primarily facilitated by a vacancy. Three components of diffusion of U, Mo, and Xe (intrinsic diffusion, radiation-driven diffusion, and radiation-enhanced diffusion) were plotted as a function of FR in Figure 70. It was found that radiation-enhanced diffusion does not significantly affect the total diffusion of Xe under irradiation. The temperature where a transition from the intrinsic diffusion to radiation-driven diffusion occurs increased with an increasing FR. A transition was observed at 850, 900, and 1000 K at 5×10^{19} fiss/m³/s, 5×10^{20} fiss/m³/s, and 5×10^{21} fiss/m³/s, respectively. The temperature where radiation-enhanced diffusion overtakes the intrinsic diffusion increased from 350 K to 600 K as the FR increased from 5×10^{19} fiss/m³/s to 5×10^{21} fiss/m³/s. The total diffusion coefficients of U, Mo, and Xe are represented in Figure 71.

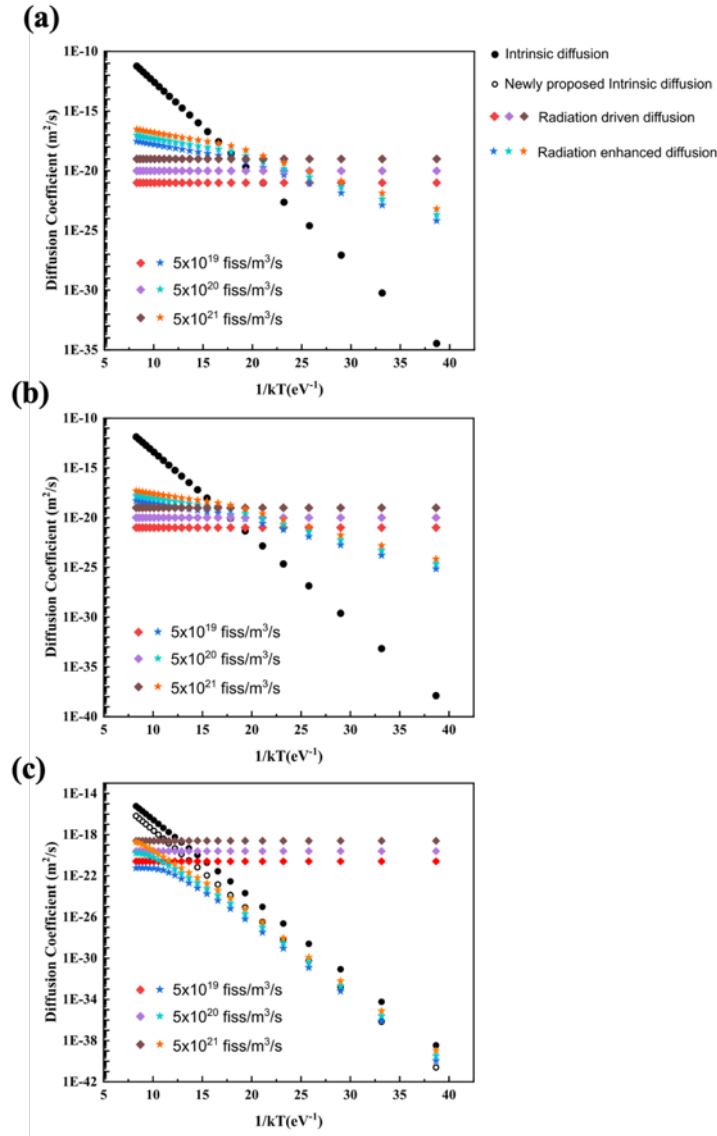


Figure 70. Intrinsic diffusion, radiation-driven diffusion, and radiation-enhanced diffusion of (a) U (b) Mo (c) Xe in γ U-10Mo at three different fission rates.

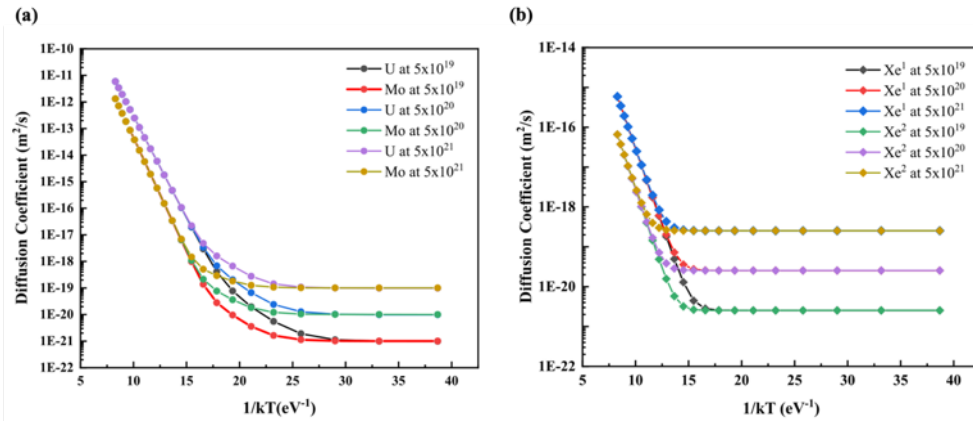


Figure 71. The total diffusion of (a) U, Mo and (b) Xe at three different fission rates in γ U-10Mo. Xe1: previously assumed intrinsic diffusion [11], Xe2: newly proposed intrinsic diffusion in this work. Units are fissions/m³/s.

2.6.3 Summary

In the present work, radiation-enhanced diffusion coefficients of U, Mo, and Xe in γ U-10Mo were calculated using rate-theory models and MD simulations. In addition, intrinsic diffusion of Xe was calculated using MD simulations. Utilizing the intrinsic diffusion, radiation-enhanced diffusion, and radiation-driven diffusion, the total diffusion of U, Mo, and Xe under irradiation was also determined in the temperature range between 300 and 1400 K. It was found that radiation-enhanced diffusion of U and Mo were dominant in the intermediate temperature range (450 to 650 K) at the evaluated fission rates, whereas the radiation-enhanced diffusion of Xe did not significantly contribute to the total diffusion of Xe under irradiation at any temperature range. The total diffusion coefficients of U, Mo, and Xe calculated in this work will be utilized as important parameters in mesoscale engineering-scale nuclear-fuel models.

2.7 Historical Characterization Data Analysis

The improvement and creation of predictive fuel microstructure modeling and simulation require accurate experimental data for computational inputs and validation. Predictions of the fuel behavior rely on the accuracy of the physics computations performed and the physical data used as inputs or for validation of said computations [27,100,121]. Therefore, data collection of the microstructure characteristics of uranium molybdenum (U-Mo) alloy fuels was undertaken to understand the available data for computational scientists and provide a starting point for creating a library or collection of this data for use by computational researchers. A list of the identified target information was collected, as seen in [59], is shown to underscore the exact data needs of various missing or unavailable microstructure data types.

The microstructure modeling data collection work performed throughout the FY included collecting MP-1 characterization data and creating a library of U-Mo, material management, and minimization (M³) focused experiments. To provide the computational process with the correct data, a tiered process of collecting the microstructure data is proposed as:

1. Collect historical data available in reports and the literature to understand gaps in the information and what is available.

This step was accomplished and included in a review journal article currently being written.

2. Quantify and understand ongoing work on U-Mo metallic fuels to find researchers and scientists whose work complements the computational needs.

- a) A team of experimental and computational scientists was proposed and connected based on the ongoing FY-20 research outline in work packages.
- 3. Create and plan targeted experiments to collect data types that are not available or currently being worked on within the USHPRR and characterization groups.
 - a) As part of this work, data from the ongoing LEU-resonant ultrasonic spectroscopy laser (RUSL) experiments will be provided to the group and briefly explained herein to show the collaboration of this proposed experiment and how it will benefit the computational data collection.

Following the above method for data collection allows for the simultaneous collection of data from past experiments and the collaboration between experimentalists and computational researchers on the needs for microstructure characterization, PIE, and how modeling and simulation may improve ongoing experimental work.

Table 15. Microstructure modeling data collection targets and details.

Microstructure Modeling (MM)	Target information	Details	Current FQ planned work
MM1	Volume fractions of different phases before and after irradiation	a. Fraction of alpha and gamma in as-fabricated condition and post-irradiation.	PLN-4886 R4 PLN-5380 R4 FY-20–FY-21 Activity (A49615)
		b. Carbide distribution before and after irradiation	FY-20 Activity (A49620) FY-21 Activity (A49645)
MM2	Features (dislocation, grain boundary, carbide, etc.) type, size, and density before and after irradiation	a. Grain boundary size and aspect ratio before and after (B&A) irradiation. In the recrystallized zone and the non-recrystallized zone.	PLN-4886 R4 PLN-5380 R4 FY-21 Activity (A49607) FY-20–FY-21 Activity (A49615)
		b. Dislocation density B&A irradiation. Emphasis decomposed regions.	FY-20 Activity (A49620) FY-21 Activity (A49645) FY-22 Activity (A49660)
MM3	Mo concentration inhomogeneity B&A irradiation	Mo concentration profiles B&A irradiation, including regions of bulk and regions of GBs, defects, precipitates, and phase decomposed areas	PLN-4886 R4 PLN-5380 R4 FY-20–FY-21 Activity (A49615) FY-20 Activity (A49620) FY-21 Activity (A49645) FY-22 Activity (A49660)
MM4	Grain boundary bubble size distribution as a function of burnup	Inside and outside recrystallization region.	PLN-4886 R4 FY-21 Activity (A49607) FY-20–FY-21 Activity (A49615) FY-20 Activity (A49620) FY-21 Activity (A49645)

Microstructure Modeling (MM)	Target information	Details	Current FQ planned work
MM5	U-10Mo recrystallized volume fraction as a function of burnup and initial grain size		FY-20–FY-21 Activity (A49615) FY-20 Activity (A49620) FY-21 Activity (A49645)
MM6	Gas density within bubbles at a given burnup	Multiple bubble sampling to determine gas pressure inside bubbles.	
MM7	Defect diffusion (self-diffusion and Xe diffusion)	a. Preferably both irradiation-enhanced and thermal	
		b. Diffusivity (U and Xe) on GBs	
		c. Effect of pressure on defect diffusivity and formation energy	
MM8	Grain boundary denuded zone width	a. Thickness of region around GBs with no FGBs	
		b. Variation with irradiation condition (flux and temperature)	
MM9	U-Mo/Zr interdiffusion region	a. Characterization of phases	PLN-4886 R4 PLN-5380 R4 FY-21 Activity (A49607) FY-20–FY-21 Activity (A49615) FY-22 Activity (A49630) FY-21 Activity (A49645)
		b. Mo concentration profile	
		c. Gas bubble density, gas bubble size, and gas bubble distribution as a function of burnup	
		d. Mechanical properties: elastic constants, yield strength	
MM10	Effect of gas bubble structures on mechanical properties (stress-strain curves)		
MM11	Elastic constants and Yield stress of U-Mo single crystal and polycrystal, B&A irradiation		
MM12	Interstitial loop stability in U-Mo matrix with gas bubble superlattice		

Microstructure Modeling (MM)	Target information	Details	Current FQ planned work
MM13	As-fabricated grain size distributions in RERTR12 archive plates.		

2.7.1 Microstructure Data Library

The data library for the M³ characteristics attached to this report shows a copious amount of data on the various MM aspects; it is difficult to compare the different experiments collected by different scientists. Due to the fact, image analysis methods are not standardized and may impact the results of the analysis as well as the differences in fuel types and fabrication techniques. Additionally, the presentation of the data varies; some studies provide a mean of the data, others present the data in a distribution, and others provide data as a range of values. Discrepancies in the presentation and collection of the data add a layer of complication when comparing experimental results and incorporating the information into a model or simulation. From past M³ experimental data collection, the data types and the data itself are explained here and in the microstructure library as a starting point for collecting the MM target requirements. For the complete information on the references, fission conditions, and other microstructure elements, it is best to see the data library, so researchers may choose and understand the type of data and from where it originated.

Several of the 13 MM essential data areas in Table 15 are regularly collected during fuel characterization and PIE work [122–125]. The data, however, is not always readily available to researchers. Collecting the information into a central location will make finding and using the data more accessible for those needing it and act as a repository for completed work to speed up the communication between experimentalists and computational scientists.

The MM target areas are broken into the following topics to simplify the data collection methods:

- Mechanical properties: MM-11 and technically all MS will relate to this
- Porosity and FGBs: MM-4, MM-6, MM-8, MM-10, and MM-12
- Grain morphology: MM-13, MM-2a, and MM-8
- Grain refinement: MM-5
- Chemical homogeneity: MM-3
- Phase decomposition: MM-1a
- Interdiffusion zones: MM-9
- Atomistic data: MM-7, MM-2b, MM-12.

Not all topics areas are included in the data library due to the non-existence of the data type or that the information available was not from M³ experiments.

2.7.2 M³ Data Collection

The data collected from the M³ experiments and literature included ATR full-size plate in center flux trap position (AFIP), RERTR, and mini-plate (MP)-1 experiments for both dispersion and monolithic fuels and as-fabricated and irradiated data. Figure 72 shows the data library breakdown into what types of fuels are in the analysis and what experiment campaigns they originate, shown in the colorful outer ring of the plot. A large portion of the data was collected from the MP-1 characterization efforts, whereas the other experiments came from various articles or reports and are collated together into the microstructure library. Additionally, the Figure 72 chart explains the amount of past data from dispersion and monolithic fuel types in the black and gray areas. Because of the differences in the fuel types, these data cannot be compared directly. However, showing the data in this manner allows for the qualification of where the information originates and illustrates the need for more monolithic data as it is currently the main focus for U-Mo fuels.

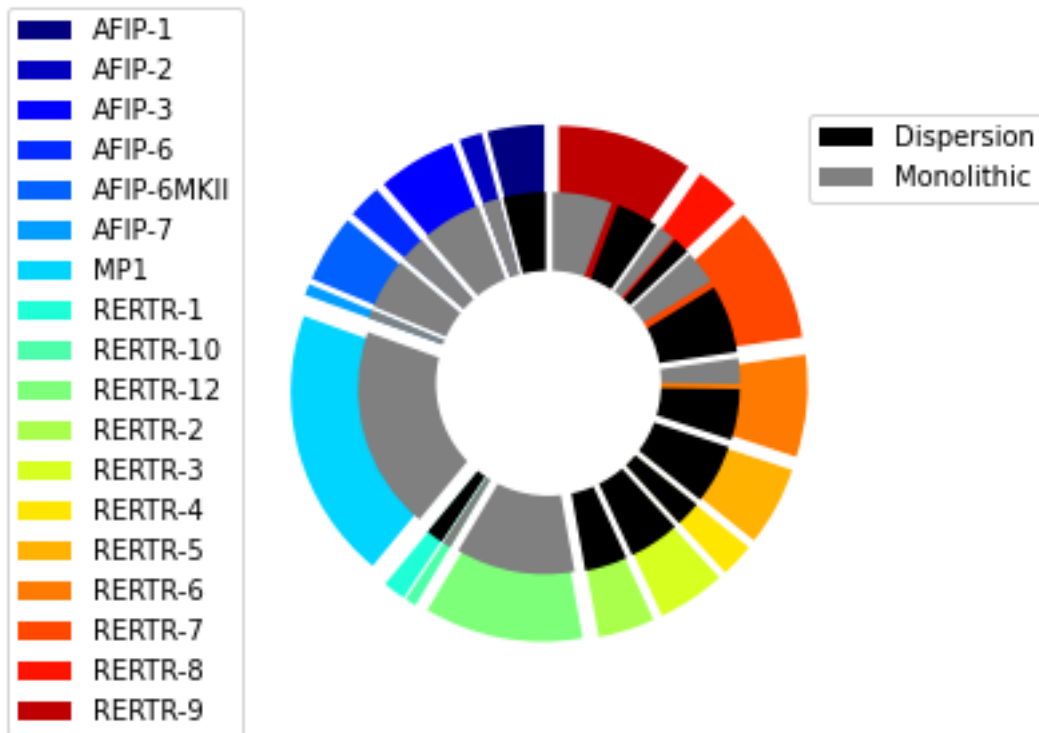


Figure 72. Data overview of all collected microstructure data, each piece corresponds to the experiment the data is from, and the black and gray areas indicate the fuel type, monolithic or dispersion.

Additionally, the form in which the data exists is vital to qualify the data for computational purposes. For example, the accuracy of the models will depend if the data is a correlation [4,126,127], a sample mean or average [4,128,129], or distribution [27,52,110]. Furthermore, validation of these models is more reliable if the data used for validation is in the form of a size distribution [27,110]. Therefore, the form of the data is also critical for computational inputs and validation methods.

The FD and FRs are plotted in the following box-and-whisker plots to further understand the differences between experiments. The importance of this is to show the fission conditions in each experiment compared against the other and the data availability differences between the experiments. An additional challenge that must be addressed in future experiments is the differences in determining each experiment sample's FD or FR. For example, in the sample "A003" from the experiment RERTR-1, the FR is reported as 3.3×10^{14} and 3.8×10^{14} fissions/cm³s, and the FD is 2.7×10^{21} and 3.0×10^{21} fissions/cm³ in different studies [27,34,37,39]. However, the discrepancies in these values are not addressed or explained in the literature. The FD and rate determination method are not given in any of the studies used here; therefore, there may be errors in these calculations affecting the overall data analysis and correlations used between the fission conditions and the microstructure. Additionally, some of the experiments do not have values for both FD and FR; some studies only presented the value. The MP-1 samples are unirradiated and therefore will not have either value as well.

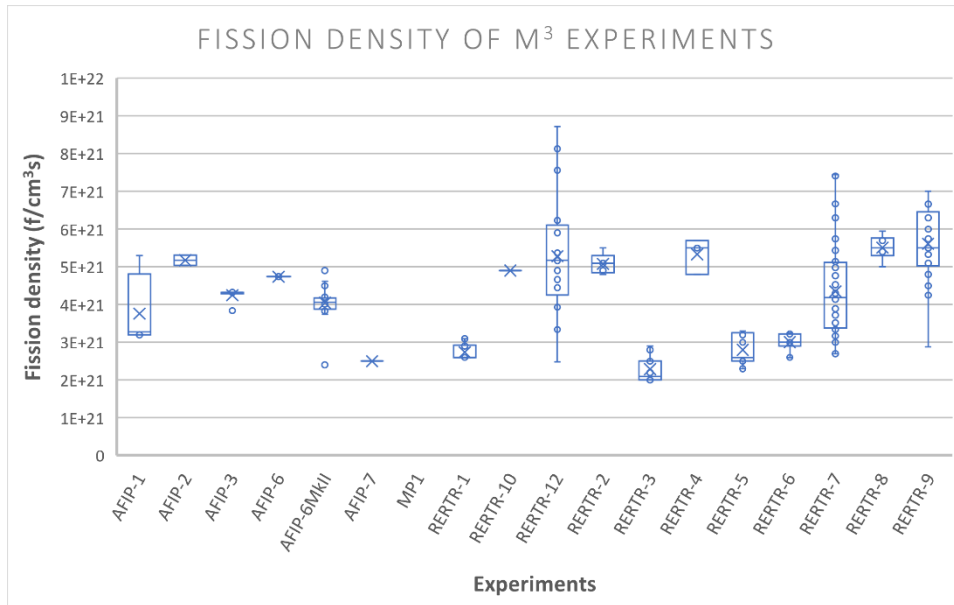


Figure 73. Box-and-whisker plot of the FD for available M³ experimental data. Some experiments had few available datum others are more readily available.

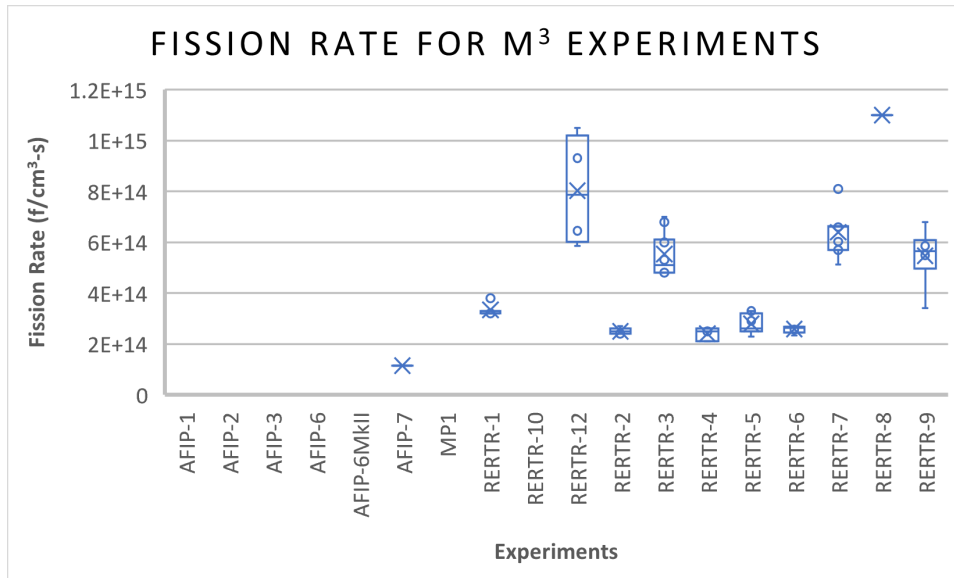


Figure 74. Box-and-whisker plot of the FR for the M³ experiments.

After observing the fission conditions and the general information of the fuel types and experiments, the microstructure data is collected. The following sections further present the data collected for the MM targets and how each meet or do not meet these requirements.

2.7.2.1 Pore or Fission-Gas Bubbles Data Collection

The MM requirements include five porosity measurements: porosity, volume fraction of the FGB, bubbles per grain size area, eccentricity, and pore size in diameter and area. The porosity data or data on FGB is the most prolific of the data collected; this is most likely due to the relationship between the FGB swelling and the overall volumetric swelling of the fuel. These gaseous fission products are not soluble in the fuel matrix and will form pores and bubbles in the fuel matrix that expand as irradiation continues and cause swelling of the fuel to increase [39,130–133]. Below 2.5×10^{21} f/cm³s fission density, the FGB will not be as prolific as at FDs between 2.5 and 3.5×10^{21} f/cm³s where FGB nucleation and growth begin [39]. Therefore, the pore size data in these FD ranges are expected to increase in size and number. After about 4×10^{21} f/cm³s, pore growth will increase further because of the collapse of the face-centered cubic superlattice that forms as intragranular pores [34,78], from all these FDs where changes to the pore behavior, we can compare the collected results and understand the recorded changes.

Figure 75 shows all five pore data types collected here and the corresponding M³ experiments. The outside of the plot shows what data types were collected, and the inner circle shows what experiments the values are presented—the most common data type in the literature is the pore size diameter followed by the porosity.

Complete fission gas pore data overview

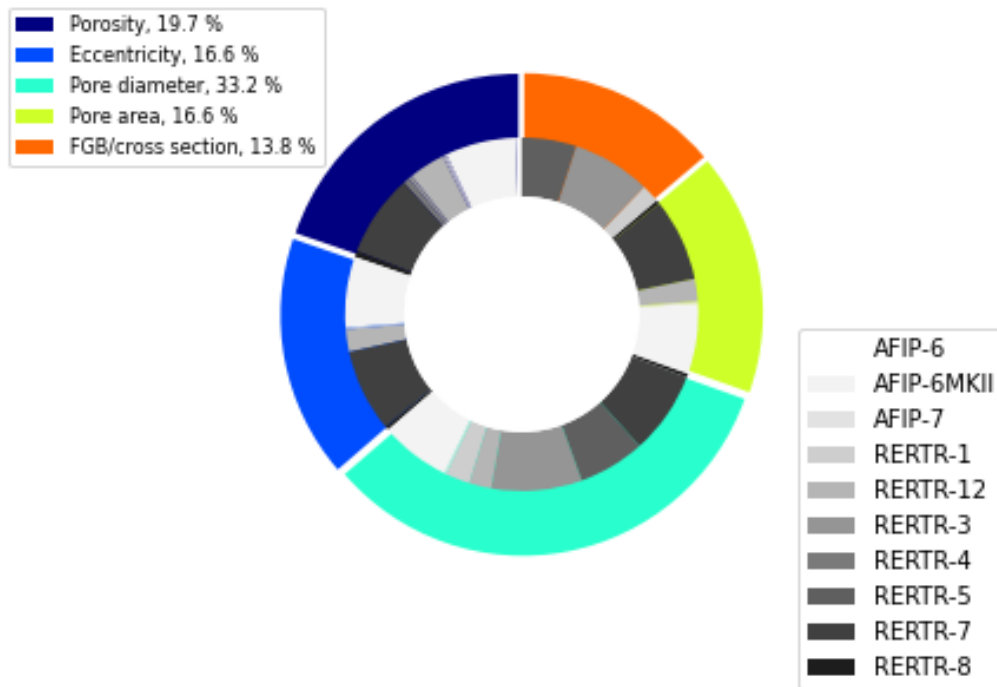


Figure 75. Pore data types, including the experiments the data is from. Most data are available as pore diameter, whereas the FGB per cross section only is reported as three RERTR, dispersion fuel experiments.

Of all the porosity data, the majority comes from RERTR-7 and AFIP6-MKII; these are from two sources: Smith et al. [23] and Verner et al. [24], as shown in Figure 76. Both use the same data collection and image analysis techniques therefore removing the inconsistencies in data collection methods that may bias or change the data. Pore size distributions may be the most useful from the data collected; however, only a few studies included the pore size distribution, which was only for RERTR-1, 3, and 5 [37]. All of which are dispersion fuels. The following sections detail more thoroughly the data collected and its interpretations.

Porosity Data

The porosity data present in the plot in Figure 76 are summarized in the following boxplot Figure 77 to show the spread of the data and the differences in the mean porosity values. Figure 77 clearly shows the spread in data for the experiments with large amounts of data from various samples. For example, in the RERTR-12 data, the lowest porosity measured is approximately 4%, and the highest is over 35% with the mean nearing 23%. Whereas samples such as RERTR-1 and -3 only include one data point from the literature. Differences in the amount of data collected and the methods by which they are collected make comparing data one to one unadvisable.

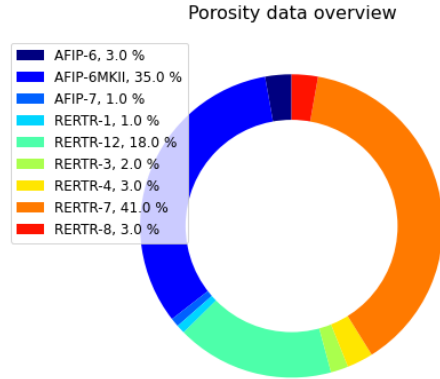


Figure 76. Porosity data collected from M3 experiments showing the most data is from AFIP6-MKII and RERTR-7 experiments.

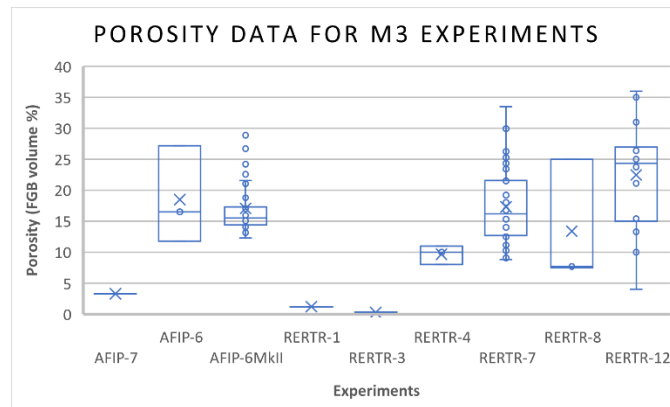


Figure 77. Boxplot of the M3 experimental porosity values in which the variation in the values is noticeable and due to FD differences and fuel types.

Eccentricity Data

The eccentricity of FGB and pores is a measure of the spherical shape of the pores and determines if it is elongated. A value of one is a perfectly spherical pore, and as the value decreases to zero, the shape becomes more elongated. Figure 78 shows that five experiments contained data on the eccentricity of the pores, with most of the data from AFIP-MkII and RERTR-7. The Figure 79 boxplots contain the data points from these studies. The boxplot shows that AFIP-7, RERTR-7, and -8 were more elongated than the other two experiments, RERTR-8 and AFIP6-MkII. However, AFIP-7 and RERTR-8 are from only one data point, and after cross-referencing these five experiments with Figure 72, both dispersion and monolithic fuels. The differences in the amount and type of data and fuel type make comparisons between the existing porosity values difficult. Eccentricity measurements were not common in the M³ collected data.

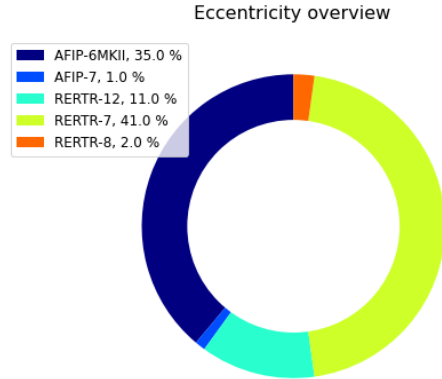


Figure 78. Eccentricity data from the experiments where five of the experimental campaign present the shape of pores in this manner.

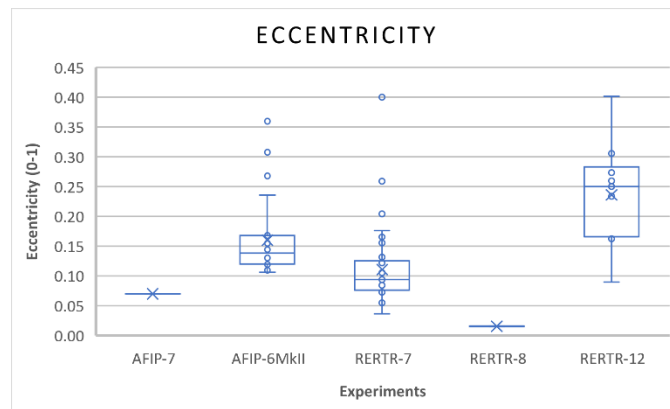


Figure 79. Boxplot of the pore eccentricity where the most elongated pores are in RERTR-7 and RERTR-8

Pore Size Diameter and Area

As stated previously, the data distributions of the pore size area are the most desirable for the validation of models. However, only two studies were found to contain this level of specificity, Kim et al. [37] and Rest et al. [27]. These studies analyze samples from RERTR-1, -3, and -5. Additionally, their work presented these data along with the FGB per unit cross section, not commonly available in other references. The pore size distributions from these sources are reproduced and plotted in Figure 80.

Fission gas bubble density and size distributions of dispersion fuels

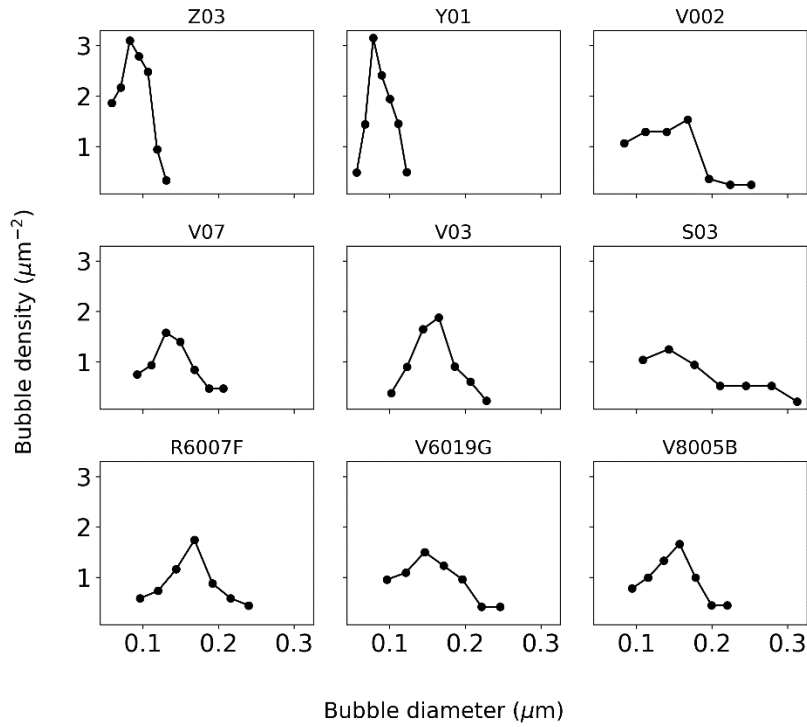


Figure 80. FGB diameter versus the bubble density per cross section of fuel for RERTR-1,-3-, and -5 dispersion fuels. Adapted from [37] and [27].

The remainder of the pore size data and the corresponding experiments are shown in Figure 81 to Figure 84. The AFIP6-MkII, RERTR-2, and -12 contain the most prominent pores of all the experiments studied. These three experiments also were exposed to the FDs above $4 \times 10^{21} \text{ f/cm}^3\text{s}$, where the recrystallization will cause the collapse of the superlattice and the increase in pore size.

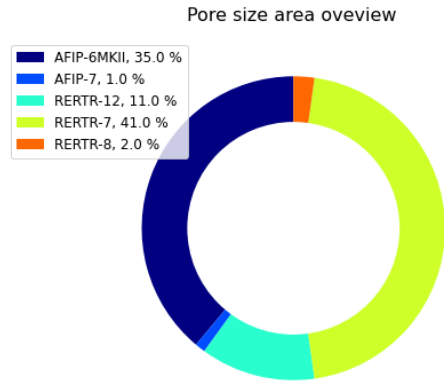


Figure 81. Pore size area experiments where the majority is from RERTR-7.

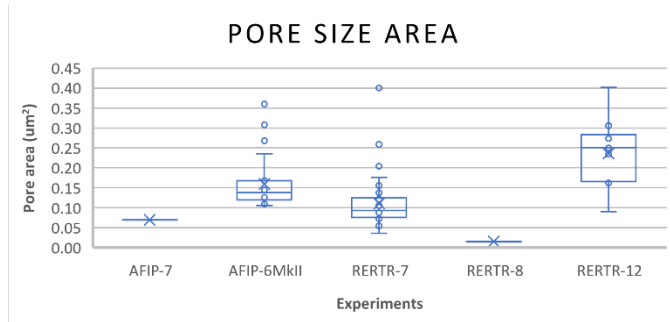


Figure 82. Pore size area boxplot of the M³ experiments. The AFIP-7 and RERTR-8 is limited compared to the other three with larger datasets.

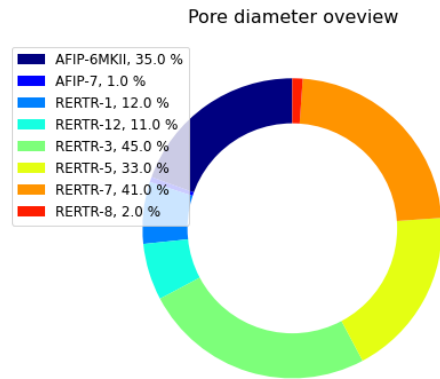


Figure 83. Pore size diameter experiments.

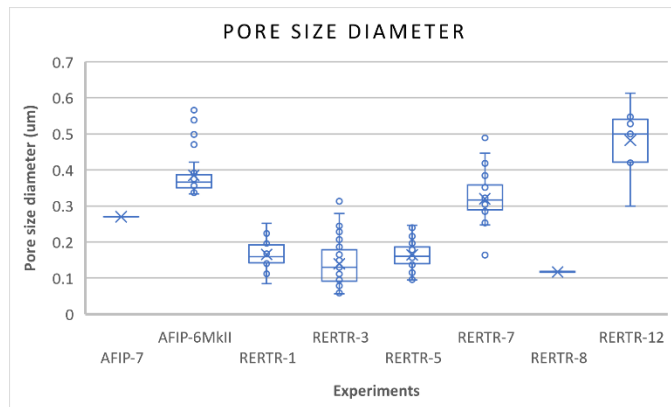


Figure 84. Boxplot of the data spread of the pore size diameter in M³ experiments where the largest diameters are from AFIP-6MkII and RERTR-12 where the FD is high enough for grain refinement to cause the large FGB to form.

2.7.2.2 Grain Size Data Types

This section includes grain morphology data presented for several MM goals. The MM-2a and MM-13 require grain size data for both as-fabricated and irradiated materials. MM-5 specifically includes the grain refinement volume fraction of the fuel. For this information involving grain morphology, there are many different ways of presenting the same information. For example, when studying grain morphology, the grain size may be given as a grain diameter, grain area, or grain number. All these measurement values were found in the literature of the M^3 experiments. Thus, there adds another layer of difficulty in comparing results between experiments and studies. Figure 85 shows the breakdown in these experiments where grain measurements and morphology were collected.

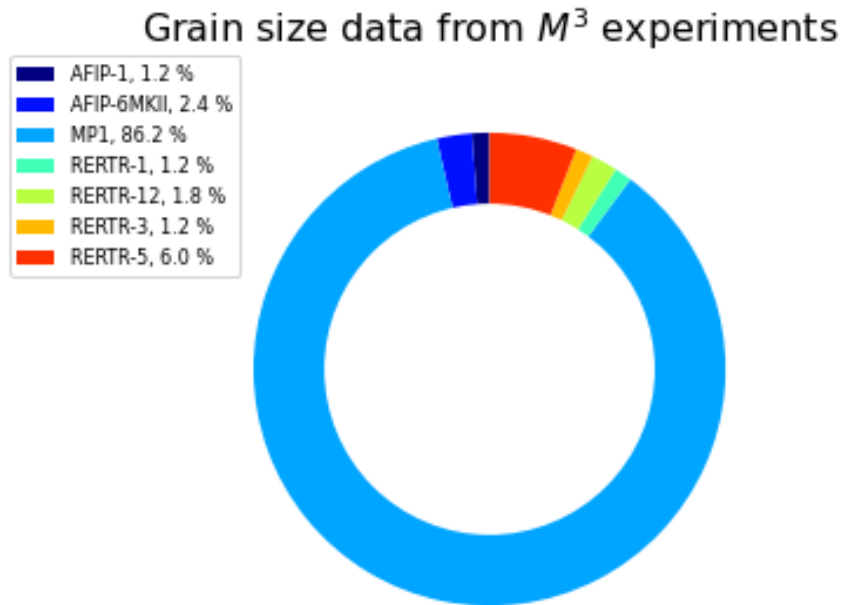


Figure 85. Grain size data breakdown shows that most grain size data come from the MP-1 as-fabricated characterization efforts. Seven other experiments contain grain morphology information.

As-Fabricated Grain Morphology

Determining the starting size of the grains in as-fabricated U-Mo is essential to predicting the post-irradiation grain size after grain refinement occurs. Therefore, M^3 data experiments of the as-fabricated grains were quantified and shown in Table 16 and the figure of the MP-1 grain numbers. In Table 16, Keiser et al. [23] determined the average grain size area for monolithic fuel plates from AFIP6-MKII and RERTR-12. Further research was performed on these samples by Di Lemma et al. [134], where electron backscatter diffraction (EBSD) determines the texture of the samples. The results determined that the grain diameter of the RERTR-12 samples was higher than those of AFIP6-MKII, but also the low grain aspect ratio indicates the grains are elongated, which will also impact the efficacy of the grain size measurements [134]. Elongated grains were measured during the characterization of these samples as high as $25\ \mu\text{m}$ [123]. These elongated grains will cause a higher standard deviation in the grain size measurements due to their nonuniform nature. Additionally, MM-2a explicitly features the need for data on the "grain boundary size and aspect ratio B&A irradiation." Di Lemma et al. [134] is the only source found that specifically included the aspect ratio for the fabricated fuels in the realm of the M^3 experiments.

Table 16. Grain size and aspect ratio of as-fabricated fuel samples.

Experiment	Sample ID	Grain diameter (μm)	Grain area (μm^2)	Aspect ratio	Source
AFIP-1	JJ-652	4			[135]
AFIP6-MKII	CB1131		68		[136]
	UM0-342-1-1	7.6 ± 4.5		0.33 ± 0.14	[134]
RERTR-12	JJ1031		54.13		[136]
	L1P757	9.3 ± 4.4		0.29 ± 0.10	[134]

The MP-1 grain size measurements are taken from the four different fabrication methods groups. The purpose of fabricating each group in varying methods is to quantify and understand fabrication technique effects on the starting microstructure of the fuel. The four fabrication methods are: as-casted where the samples are not treated past the casting phase of the production; as-casted with a zirconium diffusion barrier; cold-rolled where the samples are cast then rolled then annealed to remove the stresses added to the system during the cold-rolling steps; and the cold-rolled samples with a zirconium diffusion barrier added [137]. For the characterization of these samples, each was broken down into three transverse samples and three longitudinal samples and analyzed with SEM and OM techniques. The ASTM grain number method measured the grain size and is presented in the report "MP - 1 Intermediate Characterization Report Summary" INL/EXT-18-51367 [137]. The smallest grain sizes were produced by the cold-rolling and anneal fabrication method with the diffusion barrier. In contrast, the largest grains are in the as-casted samples with the diffusion barrier.

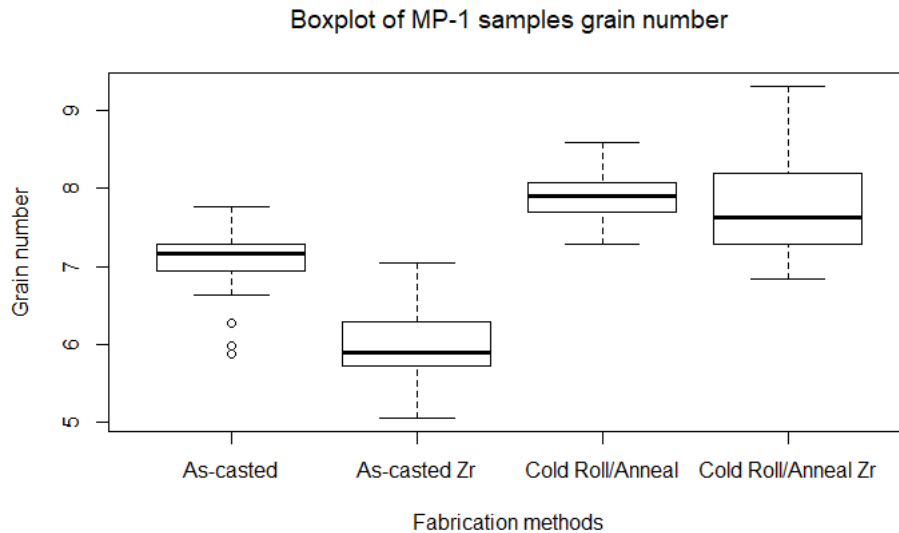


Figure 86. Boxplots of the grain number of the MP-1 characterization efforts showing the smallest fabricated grains are found in the cold-rolled and annealed Zr samples, where the largest grains are in the as-casted Zr coated samples. Adapted from Di Lemma et al. [137]

Discussion on As-Fab Grain Size

From the data collected on the grain morphology of the as-fabricated samples, it is clear that a more standardized approach to collecting and presenting this data would be helpful within the USHPRR framework. Additionally, collecting the aspect ratio of the grains along with the diameter and area would be helpful to understand the size of the grains and their shape. For example, the ideal starting grains are large, equiaxed [138]. Conversely, small grains with a low aspect ratio allow for more intergranular FGB growth and increase the swelling [128,139].

Irradiated Grain Morphology

The irradiated grain size and structure of the fuel is also important in that it shows how much grain refinement has occurred and possibly explain the amount of swelling change in the material. When comparing Table 16 of fabricated grain size measurements to the irradiation grain measurements in Table 18 illustrates the drastic change in the size of grains during irradiation of AFIP-1, AFIP6-MkII, and RERTR-12. Figure 87 shows this change graphically as well. Of the three experiments, RERTR-12 experienced the highest FD and consequently had the smallest grain size after the grain refinement occurred.

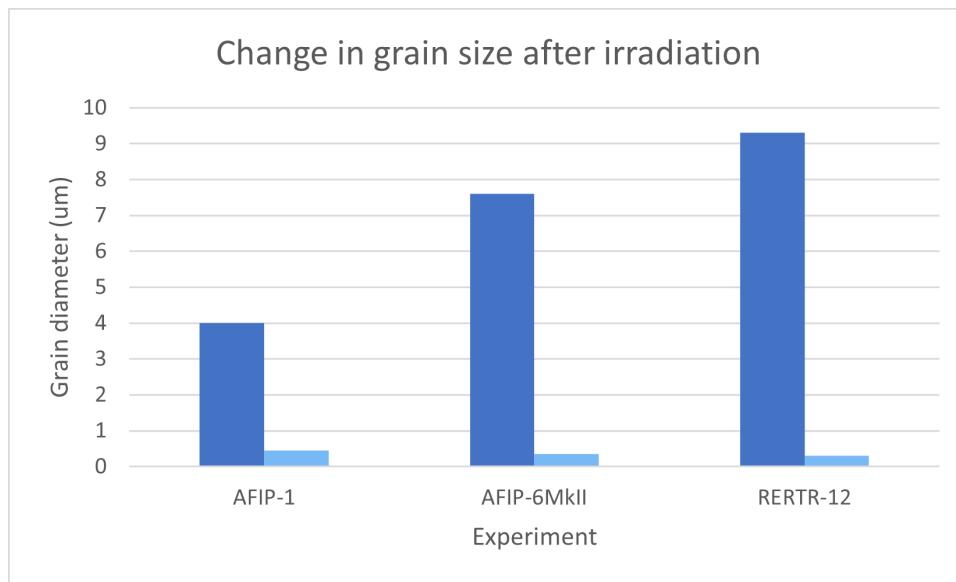


Figure 87. Grain size changes during irradiation of three available experiments. The post-irradiation grain size is significantly smaller due to the grain refinement of the material.

Additional data from dispersion fuel studies by Kim et al. [37] and Rest et al. [27] are presented in Table 17. Two methods were used to measure the grain size of these samples after irradiation. However, the as-fabricated grain size of these specific samples and experiments was not collected here to compare to the starting and ending grain microstructure. Nevertheless, one observation that can be made is the grain sizes after irradiation were not nearly as small as the previously presented irradiated samples from AFIP-1, AFIP6-MkII, and RERTR-12. Hence, this supports the hypothesis that grain refinement will not begin until after $3.5 \times 10^{21} \text{ f/cm}^3 \text{ s}$ [1,39,110] and complete near $5 \times 10^{21} \text{ f/cm}^3 \text{ s}$ [34]; these samples are similar to the beginning sizes collected in the other as-fabricated data.

Table 17. Grain size diameter of dispersion fuels using two measurement methods, four measurement average and the lineal intercept* methods.

Experiment	Sample ID	FD ($\times 10^{21} \text{ f/cm}^3$)	FR ($\times 10^{14} \text{ f/cm}^3 \text{ s}$)	Grain size (μm)	Grain size* (μm)	Source
RERTR-1	A003	2.7	3.8		2.3	[27,37]

	V002	3.1	3.8	6.3	4.9	[37]
RERTR-3	S03	2.9	7		3.6	[37]
	V03	2.6	6.3		7.3	[37]
	V07	2.1	5.1		6.5	[37]
	Y01	2	4.8		10.1	[27,37]
	Z03	2.1	5.1	24.4	23.6	[27,37]
RERTR-5	A6008H	3.3	3.3	5.3	6.2	[27,37]
	A8002L	3.2	3.2	3.9		[27,37]
	R6007F	2.6	2.6		6.2	[27,37]
	V6018G	2.3	2.3	4.9	5.2	[27,37]
	V6019G	3.3	3.3	8.5	7.6	[27,37]
	V8005B	2.5	2.5	8.1		[27,37]

Table 18. Irradiated monolithic fuels grain size data.

Experiment	Sample ID	FD ($\times 10^{21}$ f/cm ³)	Grain diameter (μ m)	Grain area (μ m ²)	Aspect ratio	Source
AFIP-1	KGT-2141	5.3	0.3			[135]
AFIP6-MkII	6II-1	2.40	0.55	0.61	0.33 \pm 0.15	[134]
	6II-1	4.90	0.35	0.1	0.49 \pm 0.12	[134]
RERTR-12	L1P755	5.20	0.45 \pm 0.25		0.46 \pm 0.12	[134]

Grain Refinement

The change in grain size that occurs during irradiation is often measured as the grain refinement and reported as a volume fraction grain refinement instead of the post-irradiation grain size. Figure 88 is a bar graph of the relationship between the mean FD and mean grain refinement for the corresponding experiments. For the experiments with FDs below the 3.5×10^{21} f/cm³s where grain refinement begins, the volume fraction of refined grains is lower. However, the higher FD samples exhibit a much higher grain refinement percentage. Thus, both observations of the data support the currently agreed-upon values for the grain refinement FDs.

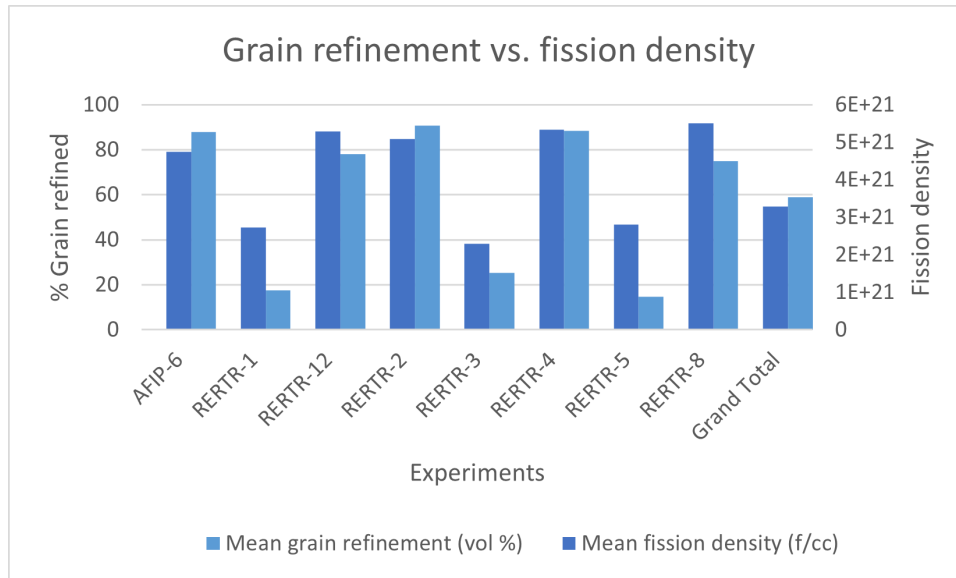


Figure 88. Compares the grain refinement and FD of various experiments showing the relationship between higher FD and the onset and completion of grain refinement.

2.7.2.3 Phase composition

MM-1 and MM-9a reference the need for data on the volume fractions of unique phases in the fuel. Phase decomposition and precipitate formation (carbides) are products of the fabrication process and impact the fuel performance during irradiation [128]. Decomposed, $\alpha + \gamma'$, phases undergo grain refinement at lower FDs than the body-centered cubic (BCC), γ , phase [1,73,120,128,140], which will increase the swelling of the fuel. On the other hand, carbides will affect the bonding of grains as they may form at the grain interface and weaken the bond [141,142]. They may also interrupt the movement of GBs and dislocations in the material [138,143]. To predict the behavior of U-Mo in the reactor environment, these factors must be characterized and understood B&A irradiation.

The only experiments with these phase volume fractions included are AFIP6-MkII, RERTR-12, and MP-1. Table 19 shows the fabricated decomposition for AFIP6-MkII and RERTR-12 archival samples. The higher decomposition in AFIP6-MkII will affect the fuel performance more significantly than in RERTR-12. In the MP-1 characterization data, the decomposition exists in almost all of the samples; however, this was reported qualitatively instead of quantitatively. The limited amount of qualitative data on the phase decomposition is a problem when trying to accurately quantify U-Mo phase decomposition and its effects on the computational predictions of the fuel performance.

Table 19. Decomposed volume fraction of as-fabricated samples.

Experiment	Sample ID	Decomposition (%)	Source
AFIP6-MkII	CB1131	14.18	[136]
	CB1131	18.0±6.1	[140]
RERTR-12	JJ1031	7.63	[140]
	JJ1031	7.4±3.6	[136]

Similarly, the carbide data is not well quantified in all of the M³ experiments. Table 20 gives the carbide volume fraction for both fabricated and irradiated samples in AFIP6-MkII and RERTR-12. There is a noticeable decrease in the volume fraction of these precipitates after irradiation in these samples. The destruction of these phases is of interest to researchers, and by using this type of data in computational models, a better understanding of what is occurring physically in the fuel may be possible.

Table 20. Carbides volume fraction in RERTR-12 and AFIP6-MkII experiments for fabricated and irradiated fuels.

Experiment	Sample ID	FD (x10 ²¹ f/cm ³ s)	Carbides vol. fraction (%)	Source
AFIP6-MkII	CB1131	Fabricated	3.95	[136]
	KGT2763	4.74	1	[140]
	96A	4.74	0.93	[140]
	97A	4.74	0.77	[140]
RERTR-12	JJ1031	Fabricated	2.44	[136]
	L1P755	5.18	0.0043	[140]
	L1P773	3.45	0.0097	[140]

MP-1 data on the carbide volume fraction is more plentiful than the phase decomposition. Carbide volume was only measured in the casted samples, cast with a Zr diffusion barrier, and the cold-rolled and annealed samples. The highest carbide fraction is in the cold-rolled samples with a maximum value of approximately 1.8% in Figure 89. Additionally, this volume of the carbide precipitates is lower than those of the fabricated RERTR-12 and AFIP6-MkII samples. The improvement in decreasing the volume of carbides then was successful in the MP-1 improved fabrication methods.

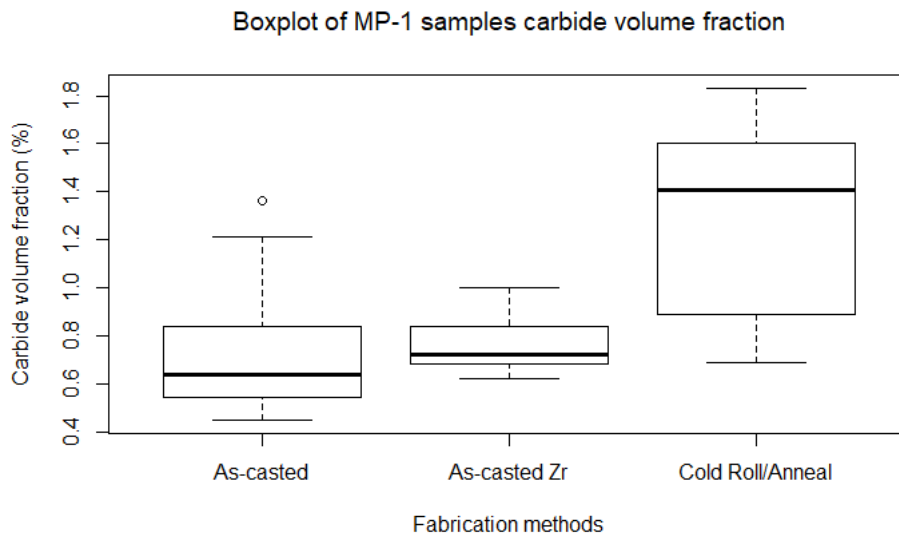


Figure 89. Carbide volume fraction of MP-1 samples showing the highest amount of carbides are in the cold-rolled fabricated foils. Adapted from Di Lemma et al. [137].

2.7.2.4 Molybdenum Concentration

The chemical composition of the fuel will have significant ramifications on the performance of the U-Mo. Inhomogeneity of the molybdenum throughout the uranium will lead to uneven grains sizes, increased swelling, and phase decomposition [70,110,144]. Quantifying the areas of high- or low-molybdenum concentration allows for better predictions of microstructure evolution in those areas and may be used in computations to perform this analysis more quickly than with physical experiments. However, physical experiments are currently needed to inform and improve the models. Existing data on the chemical composition of the fuel is presented in several ways, the chemical banding or as a range of weight percent molybdenum. Table 21 contains the chemical banding observed in RERTR-12 and AFIP6-MkII, where the banding is in 100% and 88% of the fuel, respectively [136,142]. No other data from AFIP and RERTR experiments were found containing the chemical banding data.

Table 21. Molybdenum homogeneity from RERTR-12 and AFIP6-MkII fabricated samples.

Experiment	Sample ID	Banding (%)	Light/dark phase (%)	Mo variation (wt%)	Source
RERTR-12	JJ1031	88	59/41	7-13	[136,140,142]
AFIP-6MkII	CB1131	100	60.17/39.83	8.5 -11.5	[136,140,142]

The MP-1 characterization contained the chemical variation in the as-fabricated samples where the weight percent was between 9.5 and 11 wt.% molybdenum. Figure 90 shows that the as-casted fuels had the most molybdenum variation compared to the as-casted with a diffusion barrier and the cold-rolled and annealed samples [137]. However, this data does not indicate where or how much fuel foil volume exhibited the chemical differences. Having a more precise location of the high- or low-molybdenum areas allows for comparing other microstructure characteristics in these areas to explain further how these differences in molybdenum concentration affect the grain size, swelling, or phase decomposition.

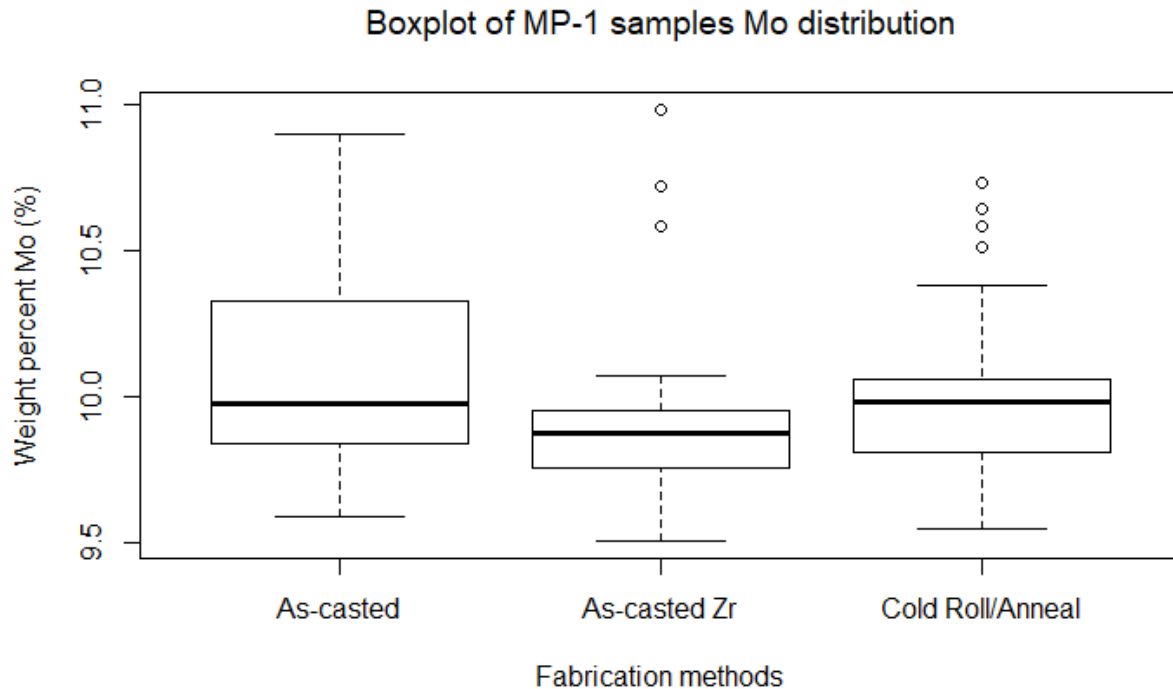


Figure 90. Boxplot comparing the molybdenum weight percent in the MP-1 fuel samples for three differing fabrication methods. Adapted from [137].

2.7.2.5 Elastic Modulus Measurements

Using the RUSL measurement technique developed at the INL for Transient Reactor Test (TREAT) facility [145,146], new data on the MP-1 samples are being collected on the elastic modulus of the samples and, consequently, the radiation-induced phase reversion of the decomposed phases. As in MM-11, data of elastic constants B&A irradiation are required, and the ongoing work with the RUSL-TREAT experiment compliments this. RUSL measures the elastic modulus of a cantilever sample during TREAT irradiation using ultrasonic lasers to excite the sample U-Mo beam and measure the light reflection off the same beam. Then the ultrasonic laser detects the sample's vibrational frequency that translates to the sample's elastic modulus.

An MP-1 sample is to be irradiated and tested with the RUSL design in late September of 2021. Three separate tests have been planned that measure the beam vibrations under three different temperature and power regimens. Figure 91 shows the planned transient tests designed for these purposes. During FY 2021, this project's design and safety analysis was performed, and the final fabrication and testing of the RUSL capsule and MP-1 samples will be completed shortly. The experiment aims to detect any microstructural changes occurring during irradiation by measuring the elastic modulus. The in-pile measurements will be provided to the computational USHPRR group to include in the previously discussed data collection efforts after the irradiation tests are complete.

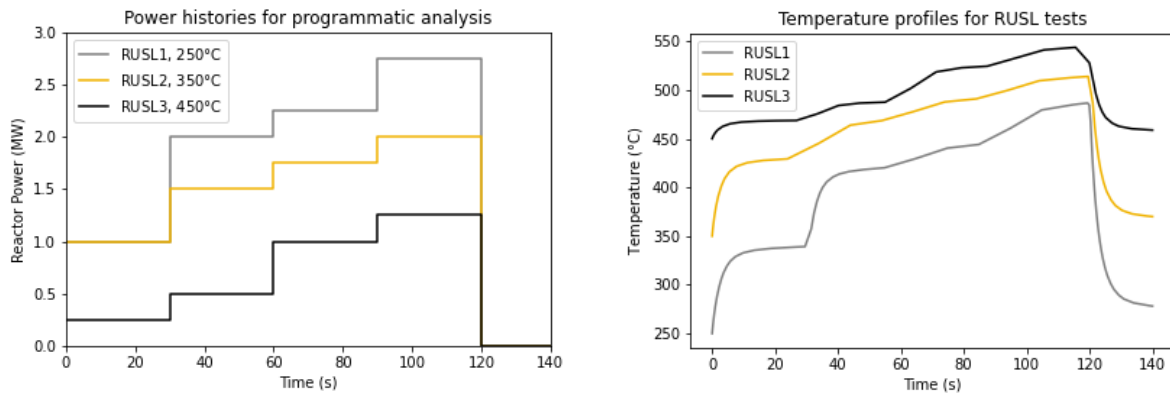


Figure 91. Power and temperature profiles for the planned RUSL transient tests to measure the elastic modulus of MP-1 samples.

2.7.3 Conclusions of the Data Collection

The takeaway from this initial microstructure data collection is the disconnect between data collection methods and data types. There are so many ways to measure the same characteristics that comparing two different samples is nearly impossible. A more standardized approach is required. Additionally, many aspects of the required MM information are missing from the available M³ experimental data. By collecting these data into one location, as was done here, computational scientists and researchers may qualify the missing areas of microstructure data. The following list highlights some significant improvements to the microstructure needed to meet the computational data requirements.

1. Standardized or explicit determination of the FD for each sample is required
2. Data on the internal pressure of FGB in MM-6 were not available and fall under the following tiers of data collection where ongoing work that provides this or brand-new tests must be performed to get the data
3. More volume fraction characterization and quantified for decomposed regions and precipitates from experiments is needed
4. As-fabricated data from all areas of the MM goals is necessary to characterize the general microstructure of the fuel prior to irradiation and connect that to the post-irradiation structure
5. Chemical homogenization data in the material and the inhomogeneity location are needed to understand the relation of other microstructure development to the chemical composition present.

As discussed previously, the next step in collecting the computational microstructure data is to find the ongoing work at the laboratory that compliments this work. Therefore, in Table 15, the ongoing FQ planned projects are highlighted to show opportunities for collaboration between computational scientists and experimentalists. The included project plans can meet some of the target information included in the same table. Collaboration between the two groups for data collection is an ongoing effort and will continue to fill in U-Mo data collection methods and use gaps.

2.8 An Integrated Fission-Gas Swelling Correlation for UMo Research Reactor Fuel

A mechanistic, microstructure-based approach has the potential to provide a more predictive fuel-performance capability than empirical fitting to limited experimental datasets. This is particularly the case when data is restricted to certain operating parameters, but the materials of interest may operate outside of that experimental phase space. By incorporating lower length scale (LLS) information (e.g., experimental microstructures), atomistic information (e.g., diffusivities), and LLS modeling information (e.g., bubble evolution), a more general model can be developed that appropriately incorporates underlying physical phenomena into macroscale predictions. This work aims to begin introducing LLS information into the fission-gas swelling models that can be implemented in the engineering-scale fuel-performance modeling simulations.

2.8.1 Fitting Procedure

Modification of the fission-gas swelling is performed to include the initial grain size, FR density, temperature, and FD. This allows for three additional levels of detail beyond the preexisting correlations, which are only function of the FD. In order to account for the additional levels of information, underlying data needs to be obtained that can be utilized to fit various descriptive functions. Thus, the DART [52] code was utilized to investigate variability of each respective quantity of interest, sufficient to gain quantitative trends. FDs at 136 increments are reported for each configuration, up to a maximum FD of approximately 7×10^{21} fiss/cm³. Three grain sizes (4.4 μm, 8.5 μm, and 17 μm) are investigated to gain a sense of variability with initial grain size. Three FR densities (3.0×10^{14} fiss/cm³-s, 5.9×10^{14} fiss/cm³-s, and 8.9×10^{14} fiss/cm³-s) were implemented to quantify the effects of FR density, assuming a constant FR density throughout the entire lifetime. Two temperatures (defined as the initial full power centerline temperature) were also studied (150°C and 115°C) to generate a temperature dependence. The nominal parameters were chosen to be 8.5 μm, 5.9×10^{14} fiss/cm³-s, and 150°C. These are reasonable parameters, although the exact conditions for each relevant research reactor will be slightly different. It should be noted that although the data sets under investigation are not wholly inclusive with respect to the potential set of conditions in research reactors of interest, the generated functions are expected to be accurate under minimal extrapolation.

The existing fuel-swelling correlations are shown below in Figure 92. Further detail on each of these individual correlations can be found in [133]. One notable, key aspect of all these models is the piecewise nature, splitting low-FD behavior from high FD. This is due to the more rapid swelling after grain refinement starts to occur. Generally, a transition occurs at a FD of 3×10^{21} fiss/cm³. A similar approach is taken here, although instead of a piecewise function, an addition of two functions is employed with an analytical Heaviside step function to effectively negative one of the functions below a certain FD. Unlike the previous correlations, the point at which the Heaviside function switches and the steepness of the transfer are fitting parameters, providing additional flexibility to accommodate the data set.

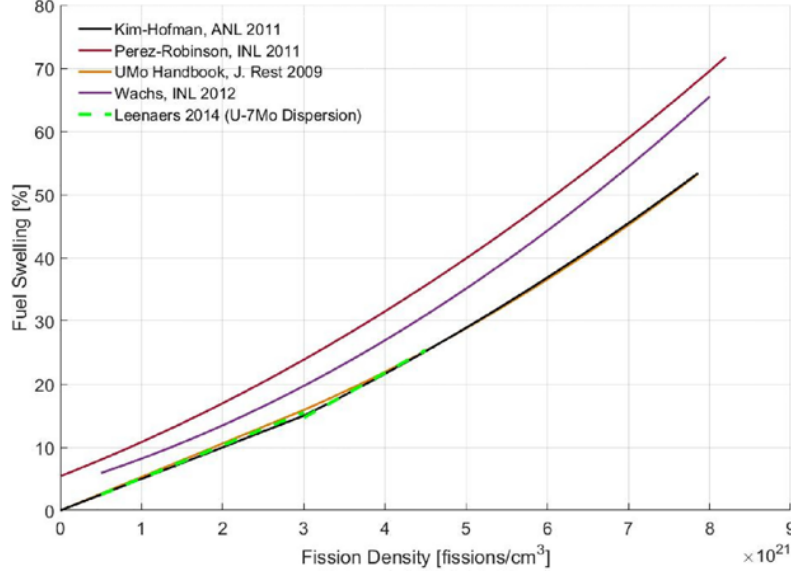


Figure 92. Fuel swelling as a function of FD. Reproduced from [133].

After initial analysis of the fission-gas swelling data from DART, the below functional forms were implemented:

$$FGS\% = [f_1(f_d, D) + f_2(f_d, D)] \times f_c(f_d) \times f_3(\dot{f}) \times f_4(T) \quad (101)$$

where f_d is the FD, D is the initial grain size, \dot{f} is the FR density, and T is the temperature.

The function f_1 , f_2 , and f_c are defined as

$$f_1 = \frac{a \times D^b}{1 + \exp(-(c \times D^d) \times (f_d - (e \times D^f)))} \quad (102)$$

$$f_2 = \frac{g \times \ln(D) + h}{1 + \exp(-(j \times D^k) \times (f_d - (l \times D^m)))} \quad (103)$$

$$f_c = \frac{1}{1 + \exp(-2 \times (f_d - 1))} \quad (104)$$

where the coefficients a through m are fitting parameters. The denominator in both f_1 and f_2 operate as the Heaviside step function. The cutoff function, f_c , enforces that as the FD approaches zero, the swelling approaches zero.

The fitting procedure is undertaken to minimize the sum of the squares of the residuals for each data point. An initially null (all zeros) guess is provided, and a random step is given to each parameter. The total error against all data points (408 data points, 136 for each grain size) is compared to the error at the previous step, and the new coefficients are saved if the error is reduced. If the error is increased due to the new coefficients, a probability function based upon the difference between the previous error and the current error is employed ($P = \exp(-10 \times \Delta err)$) to allow more flexibility in the evolution of coefficients. An R^2 value of greater than 0.99 is achieved in the fitting process, with the corresponding coefficients provided in Table 22.

Table 22. Fitting coefficients for the fission-gas swelling as a function of grain size and FD.

Coefficient	Value
a	14.55352
b	-0.13102
c	3.18009
d	-0.45099
e	3.51274
f	0.23686
g	16.1437
h	15.87839
j	3.18205
k	-0.92817
l	0.69424
m	1.17983

The FR density dependence is a second-order polynomial, given by

$$f_3 = 7.345 \times 10^{-31} \times \dot{f}^2 + 3.598 \times \dot{f} + 0.527 \quad (105)$$

where \dot{f} is provided in units of fission/cm³-s, and the temperature dependence is a linear function

$$f_4 = 0.0088 \times T - 0.3235 \quad (106)$$

where the temperature is provided in degrees Celsius.

2.8.2 Results

An example of the fission-gas swelling as a function of FD for three different grain sizes is shown in Figure 93, where the grain sizes are shown in the legend and provided in units of μm . The 8.5 μm case is considered the nominal case. As can be seen, a smaller grain size leads to more rapid swelling and a larger total swelling at the end of life. Conversely, larger grain size leads to a more gradual swelling behavior. This corresponds to previous computational PF work [59].

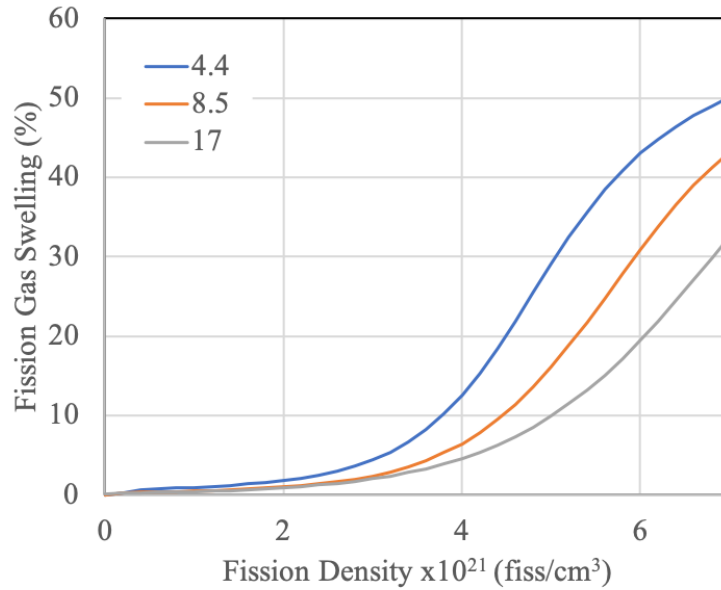


Figure 93. Fission-gas swelling as a function of FD at three unique grain sizes. Increase in the FR density, at the same FD, tends to increase the amount of swelling. The data shown is for the 4.4 μm grain size.

An example of the effect of FR density is shown in Figure 94, where the fission-gas swelling as a function of FD at three FR densities is shown. This is for the case of a grain size of 4.4 μm. As would be expected, an increase in the FR density yields a corresponding increase in the fission-gas swelling. This is believed to be largely due to the corresponding increase in the temperature that is associated with an increased FR density. Currently, there is no grain size dependence on the FR dependence, but such additional complexity will be included in the future.

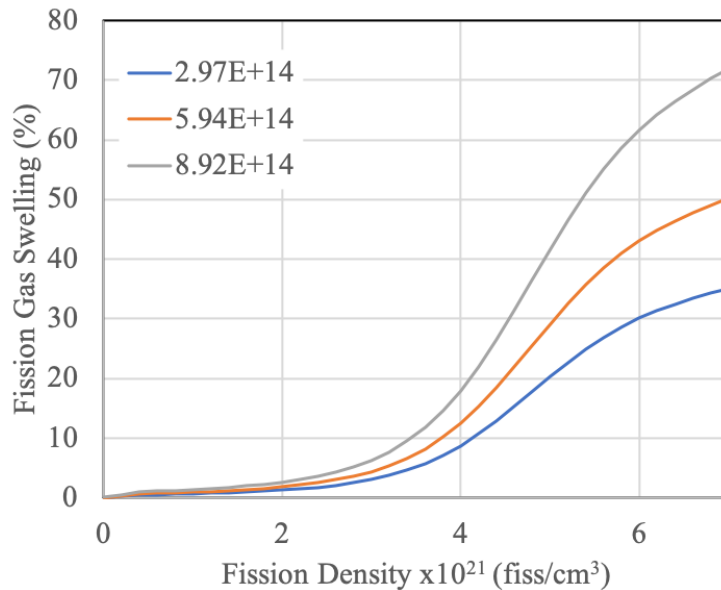


Figure 94. Fission-gas swelling as a function of FD at three unique FR densities.

The temperature dependence itself is shown in Figure 95, for a grain size of $4.4 \mu\text{m}$ and a FR density of $5.9 \times 10^{14} \text{ fiss}/\text{cm}^3\text{-s}$. Higher temperatures indeed lead to accelerated swelling behaviors. Currently, there is no grain size dependence on the temperature dependence, but such additional complexity will be included in the future.

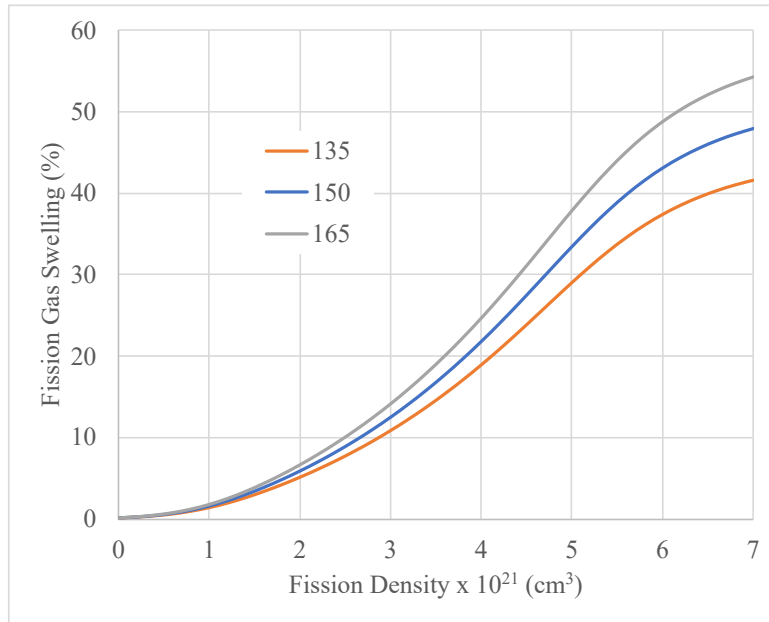


Figure 95. The fission-gas swelling as a function of FD at three unique temperatures.

2.8.3 Discussion

A comparison of the Robinson [133] swelling correlation to the fission-gas swelling predictions from the current work is shown in Figure 96. This chart assumes the nominal FR density and nominal initial centerline temperature. For the nominal grain size ($8.5 \mu\text{m}$), this work reasonably, accurately reproduces the fission-gas swelling data from Robinson. It should be emphasized that the Robinson correlation and the experimental data on which it was built were not utilized as inputs into this model, but only LLS modeling fission-gas swelling predictions from DART were utilized. Given the lack of information on nominal grain size in UMo monolithic fuel and the assumption of a nominal grain size, this is considered excellent agreement with the experimental correlations. Provided potential modifications in the fabrication process produce corresponding changes in the initial grain structures, we are showing that sufficiently large deviations from the existing nominal grain morphology can produce significant (30%) over or under predictions on the end-of-life fuel swelling. As more information on the initial grain microstructures are provided, these models can be modified to incorporate the true nominal grain size, and potentially information on grain size distributions, to describe more fully the evolution of fission-gas swelling as a function of FD. This refinement of how the nominal case is defined can also be modified for the FR density and the temperature.

Another key finding from this work that is not currently captured in the Robinson correlation is the importance of temperature. A thirty-degree difference in the initial centerline temperature can affect a 15% change in the fission-gas swelling at the end of life. Given that different research reactors possess different operating conditions, including inlet temperature which would affect fuel centerline temperature, including variability of swelling with temperature appears to be critical.

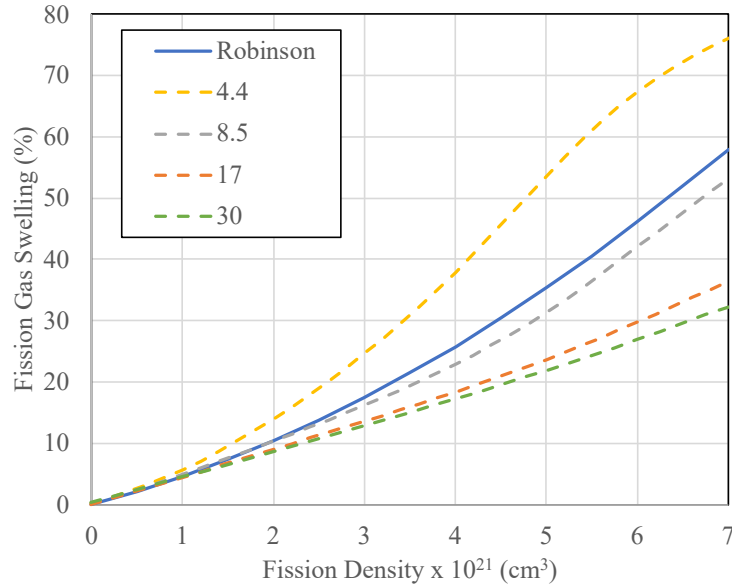


Figure 96. The fission-gas swelling as a function of FD, comparing the previous gaseous swelling correlation to four grain sizes from the present work. Legend units in μm .

2.8.4 Conclusions

An updated fission-gas swelling model was generated that incorporates grain size, temperature, FR density, and FD for UMo monolithic fuel. For the assumed nominal case, the swelling correlation presented here reasonably reproduces the experimentally based swelling correlations. This work has defined functional relationships relating the individual state variables of interest to the fission-gas swelling, allowing for exploration of operational phase spaces that are not able to be described by the existing experimental correlations. This work has highlighted the need to understand the initial microstructure of UMo monolithic fuel, as modifications in initial grain size can yield substantially different results in the fission-gas swelling behavior.

This model has been delivered to the engineering fuel-performance modeling team and is currently undergoing evaluation.

2.9 Irradiation-Enhanced Creep

In FY 21, we had three tasks: (1) complete the simulation on the effect of gas bubble structures on elastic-plastic deformation; (2) collaborate with ANL and INL for model integration; and (3) extend the PF model of non-equilibrium gas bubble evolution in polycrystalline UMo by integrating the spatial-dependent cluster-dynamics model of radiation defect evolution. In this chapter, we summarize the accomplishments in tasks 1 and 3.

2.9.1 An Integrated Model of Radiation Defect Evolution and Gas Bubble Swelling in Polycrystalline UMo

Figure 97 illustrates the flow chart of the integrated model of defect and gas bubble evolution in polycrystalline UMo by integrating the spatial-dependent cluster-dynamics model, crystal-plasticity theory, and PF model of non-equilibrium gas bubble evolution.

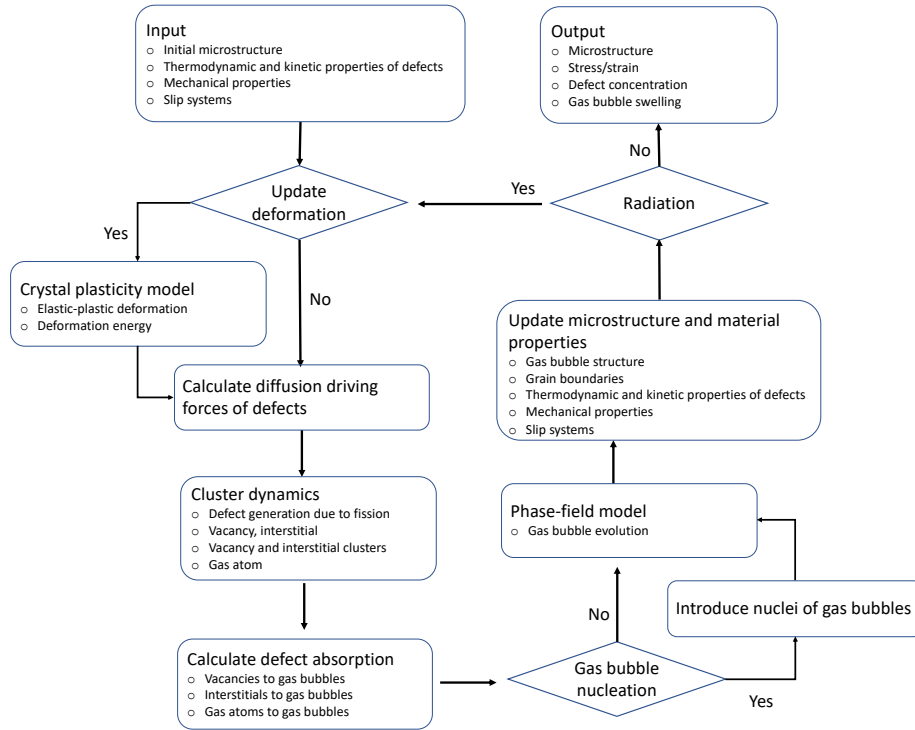


Figure 97. The flow chart of the integrated model of microstructure evolution in the UMo/Zr layer.

A PF model of grain growth and precipitation is used to generate the initial structures as shown in Figure 2. The purple layers stand for Zr diffusion barrier layers. The middle layer is the polycrystalline UMo. Light blue spheres are Xe gas bubbles, and gray regions are GBs or interfaces between UMo and Zr layers. xyz is the global coordinator while $x_\beta y_\beta z_\beta$ is the local coordinate of grain β . The simulation cell has dimensions of $128l_0 \times 32l_0 \times 128l_0$. l_0 is the characteristic length. The microstructure including different phases (Zr, UMo, and gas bubble), grain orientations, GBs, and the interface is described by order parameters. The detailed description of microstructure and inhomogeneous thermodynamic and kinetic properties are given in Sections 2.9.1.1–2.9.1.3.

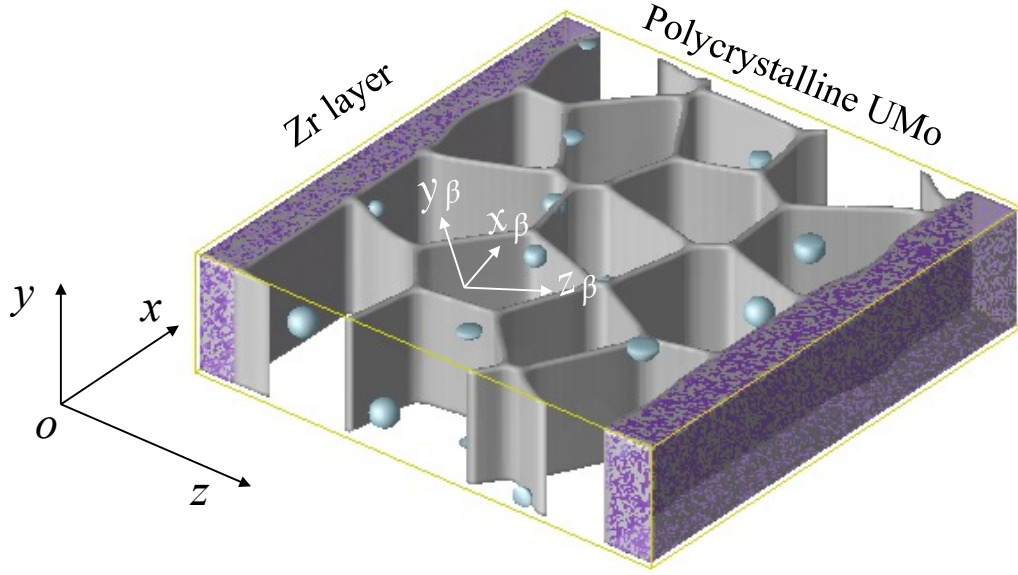


Figure 98. Simulation cell with polycrystalline UMo and Zr layer.

2.9.1.1 Microstructure-dependent Cluster Dynamics Model

In UMo fuels, ^{235}U fission generates high-energy neutrons and fission fragments that cause radiation damage. The cluster dynamics model describes the evolution of gas atoms, vacancies, interstitials, and their clusters in polycrystalline structures with distributed gas bubbles. The generation of gas atoms, vacancies, and interstitials are calculated with the fission product yields and the kinetic energy distribution of the fission products. The details of defect generation are described in the next section. GBs, gas bubbles, and dislocations are treated as sink and emission sites of defects. According to the kinetic rate theory, with the assumption that (1) only single interstitial, vacancy, and gas atoms are mobile, and (2) mobile gas atoms only interact with existing gas bubbles, the evolution of defect concentrations can be written as [147–150]:

$$\begin{aligned} \frac{dC_i(\mathbf{r}, t)}{dt} = & \nabla[D_i \nabla C_i(\mathbf{r}, t) + D_i C_i(\mathbf{r}, t) \nabla U_i / k_B T] + \dot{G}_i - \alpha C_i(\mathbf{r}, t) C_j(\mathbf{r}, t) + K_j^{li}(2) C_j(\mathbf{r}, t) C_{2i}(\mathbf{r}, t) + \\ & \sum_{m=3}^{M_I} [\gamma_i^{li}(m) - K_i^{li}(m) C_i(\mathbf{r}, t)] C_{li}(m, \mathbf{r}, t) - K_i^{li}(2) C_i(\mathbf{r}, t) C_{2i}(\mathbf{r}, t) - K_i^{li}(1) C_i^2(\mathbf{r}, t) - \\ & \sum_{m=3}^{M_V} [\gamma_j^{li}(m) - K_j^{li}(m) C_j(\mathbf{r}, t)] C_{lj}(m, \mathbf{r}, t) - K_i^{li}(2) C_i(\mathbf{r}, t) C_{2j}(\mathbf{r}, t) - \dot{S}_{i,gb}(\eta, C_i(\mathbf{r}, t)) - \\ & \dot{S}_{i,bb}(\chi, C_i(\mathbf{r}, t)) - \dot{S}_{i,dis}(\rho_{dis}, C_i(\mathbf{r}, t)) + \dot{\xi}_{i,gb}(\eta, C_i(\mathbf{r}, t), C_{i,gb}^{eq1}(\mathbf{r}, t)) + \\ & \dot{\xi}_{i,bb}(\eta, C_i(\mathbf{r}, t), C_{i,bb}^{eq1}(\mathbf{r}, t)), \quad i \neq j = I \text{ and } V \end{aligned} \quad (106)$$

$$\begin{aligned} \frac{dC_{li}(m, \mathbf{r}, t)}{dt} = & K_i^{li}(m-1) C_i(\mathbf{r}, t) C_{li}(m-1, \mathbf{r}, t) + \gamma_j^{li}(m-1) C_{li}(m-1, \mathbf{r}, t) \\ & - [K_i^{li}(m) C_i(\mathbf{r}, t) + K_j^{li}(m) C_j(\mathbf{r}, t) + \gamma_j^{li}(m)] C_{li}(m, \mathbf{r}, t) \\ & + K_j^{li}(m+1) C_j(\mathbf{r}, t) C_{li}(m+1, \mathbf{r}, t) - \dot{S}_{li,bb}(m), \quad m = 2, 3, \dots, M \\ i \neq j = I \text{ and } V, \quad m \text{ and } li \text{ stand for a cluster with } m \text{ defects } i, \quad M = M_I \text{ or } M_V \end{aligned} \quad (107)$$

where $C_i(\mathbf{r}, t)$ is the concentration of mobile single defect i , $i = V$ for a single vacancy, $i = I$ for a single interstitial; D_i is the diffusivity of defect i ; U_i is the interaction energy between the sink and defect i or chemical potential of defect on sinks; \dot{G}_i denotes generation rate of vacancy, interstitial. α is a rate constant for the recombination between single vacancies and single interstitials; K_i^{lj} is the capture coefficient of mobile defect i by defect cluster m_{lj} ; $\gamma_i^{lj}(m)$ is the emission coefficient of mobile defect i by cluster m of defect j ; $\dot{S}_{i,def}$ is the sink rate of defect i on sinks (*def*) including grain boundary (*gb*), gas bubble interface (*bb*), and dislocation network (*dis*); and $C_{i,def}^{eq1}$ is the equilibrium concentration of defect i on sinks (*def*); $\xi_{i,def}$ is the emission rate of defect i from the sink (*def*). ρ_{dis} is the dislocation density. $C_{lj}(m, \mathbf{r}, t)$ in Eqn. 107 is the concentration of defect cluster lj , which has m defects j . $\dot{S}_{li,bb}(m)$ is the sink rate of cluster li at gas bubbles. M_I and M_V are the largest allowable sizes of interstitial and vacancy clusters, respectively. The evolution of fission-gas-atom concentration (Xe is considered in this work) in UMo with distributed gas bubbles can be written as

$$\frac{dC_g(\mathbf{r}, t)}{dt} = \nabla[D_g \nabla C_g(\mathbf{r}, t) + D_g C_g(\mathbf{r}, t) \nabla U_g] + \dot{G}_g - \dot{S}_{g,bb} \quad (108)$$

where $C_g(\mathbf{r}, t)$ is the concentration of Xe atoms; D_g is the diffusivity of Xe; U_g is the interaction energy between sink and Xe or chemical potential of defect on sinks; \dot{G}_g denotes generation rate of Xe, and $\dot{S}_{g,bb}$ is the sink rate of Xe at gas bubbles.

The evolution of the dislocations is described by a model similar to the one developed by Stoller [5,6]

$$\frac{d\rho_{dis}}{dt} = 2\pi v_{li} S_{BH} - \rho_{dis} \tau_{li}^{-1} + 2\pi r_{M_I} C_{li}(M_I) \tau^{-1}(M_I), \quad i = I \quad (109)$$

The first term on the right side describes the generation of network dislocations by Bardeen-Herring source. The second term represents the annihilation of climbing dislocations. v_{li} is the climb velocity, S_{BH} the density of Bardeen-Herring sources, and τ_{lj} the mean lifetime before annihilation. The third term represents the rate at which new dislocation line length is generated by the unfauling of the largest interstitial loops (interstitial clusters M_I). r_{M_I} is the radius of an interstitial cluster of size M_I . $\tau(M_I)$ is the time needed for the incorporation of the interstitial cluster M_I into the dislocation network. The calculation of v_{li} , S_{BH} , τ_{lj} and $\tau(M_I)$ is referred to in the work [151].

Defect equilibrium concentration $C_{i,def}^{eq1}$ is calculated by $\exp(E_{i,def}^f/k_B T)$ where $E_{i,def}^f$ is the formation energy of defect i by defect *def*. The rate constant $\alpha = Z_{iv}(D_I + D_V)/a^2$ where a is the lattice constant, and Z_{iv} is the combinatorial factor of vacancy and interstitial. The rate constant $K_i^{lj}(m) = 4\pi r_{i,lj} Z_{ij}^i D_i / \Omega$ where Ω is the atom volume, $r_{i,lj}$ is the capture radius between defect i and cluster m_{lj} ; emission rate $\gamma_i^{lj}(m) = K_i^{lj}(m - 1) \exp(-E_b^i(lj)/k_B T)$ where $E_b^i(lj)$ is the binding energy between defect i and cluster m_{lj} . The capture radius $r_{i,lj}$ is estimated by $r_{i,lj} = (m_{lj})^{1/3} r_{at} + r_{at}$ and $r_{i,lj} = a\sqrt{m_{lj}/(2\pi h)}$ for vacancy and interstitial clusters, respectively. m_{lj} is the total number of vacancies/interstitials in cluster lj , and r_{at} is the atom radius. h is the magnitude of Burgers vector of an interstitial loop in units of a .

The binding energy between defect i and cluster m_{lj} is a function of cluster size $E_b^i(lj) = E_i^f + (E_{2i}^b - E_i^f) \left(\sqrt[3]{(m_{lj})^2 - 3} - \sqrt[3]{(m_{lj} - 1)^2} \right) / (\sqrt[3]{4} - 1)$. E_i^f and E_{2i}^b are the formation energy of defect i and the binding energy between defect i and $2i$, respectively [148,152]. Z_{ij}^i is the bias coefficient, which also depends on the cluster size. $\dot{S}_{li,bb}$ is the sink rate of the cluster m_{lj} at gas bubbles. The defect diffusivity D_i and the chemical potential U_i of defect i on GBs and/or gas bubbles are different from those in the matrix. The spatially dependent thermodynamic property of defect i is described as

$$\Phi_i = \Phi_{0i} + \Delta\Phi_{i,def}\theta(\eta_m, \chi) \quad (110)$$

where Φ_{0i} is the property of defect i inside the grains, and $\Delta\Phi_{i,def}\theta(\eta_m, \chi)$ is the difference of the property of defect i on the structural defect from that inside grains.

In conventional rate theory, the sink strength of defect i on a structural defect is estimated at the steady state by calculating the diffusion flux of defect i to an isolated structural defect in the matrix. For instance, the reaction-controlled sink rate of distributed gas bubbles with average radius R and density ρ_{bb} can be calculated by $4\pi R^2 D_i \rho_{bb} c_i Y_{i,bb}^s / a$ [153]. For a single gas bubble, the sink rate is written as

$$\dot{S}_{i,bb}(r, t) = Y_{i,bb}^s 4\pi R^2 D_i c_i / a \quad (111)$$

where $Y_{i,bb}^s$ is the biases of gas bubbles for interstitials or vacancies, and c_i is the average concentration of defect i at gas bubble interface. $Y_{i,bb}^s 4\pi R^2 / a$ is the sink strength of a gas bubble with a radius of R . $Y_{i,bb}^s$ depends on the type of defect i and gas bubble properties such as the defect structures at the gas bubble interface and gas pressure. An overpressure gas bubble generates a compressive stress around the gas bubble that causes an increase of $Y_{I,bb}^s$ (bias of interstitials) and a decrease of $Y_{V,bb}^s$ (bias of vacancies). For a system that has a high sink density and multiple types of sinks or has evolving sinks such as evolving voids and/or gas bubbles in nuclear fuels, the concentration c_i around the gas bubbles is not uniform, the gas bubble size varies with time, and the system may never reach steady state. This instability can be demonstrated by the observed gas bubble swelling kinetics in UMo fuels, which increase with the increase of FD [34]. Therefore, it is hard to calculate the sink rate using the rate theory Eqn. 111.

In our model, the gas bubble interface and grain boundary are implicitly described by $\theta_1(\eta_m, \chi) = \eta(\mathbf{r}, t) + 2(1 - \chi(\mathbf{r}, t))^2$. The temporal evolution of defect concentrations is obtained by solving the Eqns. 106-110 in the system with the spatial distribution and evolving sinks. The concentration near the gas bubble reflects the effect of all the coupling of the spatial dependent features of sinks mentioned above. We proposed a method to calculate the spatially dependent sink rate with the following assumptions: (1) all the defect absorption and emission take place inside the grain boundary and/or gas bubble interface zone, which is defined by $\theta_1(\eta_m, \chi)$ and (2) the sink rate inside the gas bubble interface zone can be calculated as

$$\dot{S}_{i,bb}(\mathbf{r}, t) = Z_{i,bb}^s D_i c_i, \quad \theta_1(\eta_m, \chi) > 0 \quad (112)$$

where $Z_{i,bb}^s$ is the local sink strength. The total sink strength can be calculated by integrating the local sink strength $Z_{i,bb}^s$ over the interface region ($\theta_1(\eta_m, \chi) > 0$) of the gas bubble. The local sink strength $Z_{i,bb}^s$ can be estimated with the total sink strength to be equal to $Y_{i,bb}^s 4\pi R^2 / a$ from the rate theory. If the interface thickness of a gas bubble with radius R_0 is H_0 which is defined by $\theta_1(\eta_m, \chi) > 0$, the volume of interface zone is approximately calculated by $V_0 = 4\pi R_0^2 H_0$. $Z_{i,bb}^s$ can be estimated by $Z_{i,bb}^s = Y_{i,bb}^s 4\pi R_0^2 / (aV_0) = Y_{i,bb}^s / (aH_0)$.

Our model releases the effect of coupling the spatially dependent features of sinks on the sink rate. $Z_{i,bb}^s$ measures the average sink strength in the interface zone. Given the lattice constant a and the thickness of the interface zone H_0 which is a model parameter related to the grid size in the simulation cell, $Z_{i,bb}^s$ only depends on the bias $Y_{i,bb}^s$. As discussed above, $Y_{i,bb}^s$ is a material property that depends on defect structures at the interface and the interaction between the interface and defect i and could be assessed by atomistic simulations. The defect emission rate can be defined as $S_{i,bb}^e = Z_{i,bb}^e D_i c_i$, $\theta_1(\eta_m, \chi) > 0$ at the interface zone. $Z_{i,bb}^e$ is the local emission strength which also can be described as $Z_{i,bb}^e = Y_{i,bb}^e / (aH_0)$. $Y_{i,bb}^e$ is the bias that depends on the interface energy between defect i and gas bubbles. The total emission ΔC_i of defect i from the emission zone, which is described in the previous section, is calculated with $S_{i,bb}^e$. The absorption rate can be calculated by $\dot{\xi}_{i,def} = \Delta C_i / (\Delta t N_{tot})$. In the rate theory, defect sink and emission rates at GBs have similar expressions as those at the gas bubble and/or precipitate interface [154]. The same method was used to calculate sink and emission rates at GBs.

The biases ($Y_{i,bb}^s$ and $Y_{i,bb}^e$) depend on the properties of sinks such as the misorientation angle of GBs [154–156], the coherency of the precipitate interface, and the pressure of gas bubbles. To investigate the effect of biases on gas bubble evolution, we carried out a parametric study by varying the biases.

2.9.1.2 Phase-field Model of Non-equilibrium Gas Bubble Evolution

Gas bubbles in irradiated nuclear fuels may not reach equilibrium. This means that the gas concentration inside gas bubbles may be larger or smaller than the equilibrium concentration. For example, the gas bubbles may become voids if the matrix has a high vacancy concentration. In contrast, the gas bubble might be over-pressurized if the vacancy concentration is low in the matrix. To describe the non-equilibrium gas bubbles, we assume that gas bubbles are energetically favored sinks for vacancies and gas atoms and are energetically unfavored sinks for interstitials. Once vacancies and gas atoms reach gas bubbles, they are absorbed immediately by gas bubbles while interstitials are partially absorbed or emitted by gas bubbles. Three field variables (i.e., Xe atom concentration C_{gg} , vacancy concentration C_{gV} , and order parameter χ) are used to describe the gas bubbles in the PF model of non-equilibrium gas bubble evolution. The vacancy concentration C_{gV} is different from C_V in the cluster dynamics model. Vacancies, interstitials, and their clusters sinking to gas bubbles (described by $\dot{S}_{i,bb}$ and $\dot{S}_{lj,bb}$ in the cluster dynamics model) generate a net change of vacancies inside the gas bubbles. C_{gV} accounts for the net vacancy concentration inside gas bubbles.

The Kim-Kim-Suzuki (KKS) model is used to describe the two-phase equilibrium in UMo (i.e., matrix and void). According to the KKS model [157], the total free energy density of a system with vacancies and voids can be written as

$$G = p(\chi) f^b(c_v^b) + (1 - p(\chi)) f^m(c_v^m) + wg(\chi) \quad (113)$$

where χ is the order parameter, which is zero in matrix and unity in bubbles, $p(\chi) = \chi^3(10 - 15\chi + 6\chi^2)$ is a monotonously changing function from $p(0) = 0$ to $p(1) = 1$, $g(\chi) = 30\chi^2(1 - \chi)^2$ is a double-well potential, and w is the height of the double-well potential. f^m and f^b are the bulk free energy density of the matrix and void, respectively. They are set to be $f^m = A_m(c_v^m - c_v^{eq})^2$ and $f^b = A_{bv}(c_v^b - 1)^2$ where c_v^{eq} is the equilibrium concentration of vacancy in the matrix. The total free energy $F(C_{gV}, \chi)$ of the system includes chemical free energy and interfacial energy. It is defined as

$$F(C_{gV}, \chi) = \int_{\Omega} \left[G(C_{gV}, \chi) + \frac{\kappa}{2} |\nabla \chi|^2 \right] d\Omega \quad (114)$$

where κ is a gradient coefficient. Two model parameters w and κ can be determined by the interfacial energy σ and interface thickness λ [158].

Following the KKS model, the concentration of vacancies is written as follows

$$C_{gV} = p(\chi)c_v^b + (1 - p(\chi))c_v^m \quad (115)$$

At each point in the system, local thermodynamic equilibrium is assumed

$$\frac{\partial f^b(c_v^b)}{\partial c_v^b} = \frac{\partial f^m(c_v^m)}{\partial c_v^m} \quad (116)$$

The evolution equations of gas bubbles are written as follows

$$\begin{aligned} \frac{\partial C_{gV}}{\partial t} = & \nabla \left[\frac{D_{gV}}{G_{C_{gV}C_{gV}}} \left(G_{\chi C_{gV}} \nabla \chi + G_{C_{gV}C_{gV}} \nabla C_{gV} \right) \right] + \dot{S}_{V,bb} - \dot{S}_{I,bb} \\ & + \sum_{m=2}^{M_V} m \dot{S}_{lv,bb}(m) - \sum_{m=2}^{M_I} m \dot{S}_{li,bb}(m) \end{aligned} \quad (117)$$

$$\frac{\partial \chi}{\partial t} = L \left[-\frac{\partial}{\partial \chi} \left(\frac{\kappa}{2} |\nabla \chi|^2 \right) + p'(\chi) \left(f^m(c_v^m) - f^b(c_v^b) - (c_v^m - c_v^b) \frac{\partial f^m(c_v^m)}{\partial c_v^m} \right) + w g'(\chi) \right] \quad (118)$$

where D_{gV} is the diffusivity of vacancies, and L is the interface mobility. $\dot{S}_{V,bb}$ and $\dot{S}_{I,bb}$ are sink rates of vacancy and interstitial at gas bubbles, respectively. $\dot{S}_{lv,bb}$ and $\dot{S}_{li,bb}$ are the sink rates of vacancy and interstitial clusters at the gas bubbles.

It is assumed that all gas atoms, vacancy, and vacancy and interstitial clusters are absorbed by gas bubbles when they reach the gas bubbles. The sink rate is calculated by $\dot{S}_{i,bb} = S_i m C_i \chi / \Delta t$, $i = V, I, li$, and lv . m is the number of defect clusters i . For interstitials, when their concentration on the gas bubble interface is larger than their equilibrium concentration, the interstitials are emitted as described in the cluster dynamics model.

The gas phase inside gas bubbles is treated as a solution phase. The free energy density of the gas phase is described as

$$G_1 = A_{bb} (C_{gg} - C_{gg}^{eq})^2 \quad (119)$$

where C_{gg}^{eq} is the equilibrium concentration of gas atoms which is set to 0.45 [159]. The evolution of gas-atom concentration is given as

$$\frac{\partial C_{gg}(x,t)}{\partial t} = \nabla \left[D_{gg} \nabla \frac{\partial G_1}{\partial C_{gg}} \right] + \dot{S}_{g,bb} \quad (120)$$

where D_{gg} is the diffusivity of gas atoms, and $\dot{S}_{g,g}$ is the sink rate of gas atoms calculated in the cluster dynamics model. For large gas bubbles, it is reasonable to assume that gas atoms are confined inside gas bubbles once they are absorbed by the gas bubbles. To apply this assumption in the model, D_{gg} is defined as $D_{gg} = D_{gg0} \chi^2$. D_{gg} is equal to D_{gg0} inside the gas bubble and equal to zero in the matrix. D_{gg0} is the diffusivity of gas atoms inside gas bubbles, which should be much larger than that in the matrix.

One of the merits of this work is that we developed a PF model of non-equilibrium gas bubble evolution in nuclear fuels. The Eqns. 113-118 describe two-phase equilibrium (i.e., void and matrix phases). Eqns. 119-120 describe the gas phase inside the void. Eqn. 120 only evolves inside the voids, which can be seen from the definition of the diffusivity D_{gg} . D_{gg} is zero outside voids. All gas atoms inside the voids are from the sink term in Eqn. 120, which is calculated from the cluster dynamic model. The evolution Eqn. 120 drives the gas concentration inside voids to reach a uniform value (a solution phase). So, the non-equilibrium gas bubble model can describe the transition from the overpressure gas bubble (high gas concentration) to the void-like gas bubble (low gas concentration), which completely depends on the ratio of gas atoms and vacancy inside the gas bubble.

Nucleation of Gas Bubbles

The concentration distributions of vacancies, interstitials, and their clusters are nonuniform because of inhomogeneous grain and gas bubble structures. With the increase of local net vacancy concentration (single vacancy, single interstitial, and clusters), the defects will collapse and form a void. Based on this assumption, a statistical method is used to introduce the nuclei of gas bubbles. To do so, the total vacancy concentration, $c_{tot_M}(\mathbf{r}, t)$ is calculated by summing all the defects (single vacancy, single interstitial, and their clusters) at every N_1 simulation step. The sum of vacancy concentration c_{tot} in the matrix can be calculated by integrating $c_{tot_M}(\mathbf{r}, t)$. The number of potential nucleation sites is determined by $N_2 = c_{tot}/c_{crt}$, where c_{crt} is the critical value of vacancy concentration required for the formation of a nucleus. Then, position x_i , ($i = 1, 2, \dots, N_2$) is chosen randomly; the total vacancy c_{tot_1} at x_i is determined by integrating $c_{tot_M}(\mathbf{r}, t)$ in a sphere with radius r_1 ; and a spherical nucleus with radius r_c is introduced if the total vacancy c_{tot_1} is larger than the critical value c_{crt} . Inside the nucleus, the order parameter χ is set to be 1.0; the radius r_c is calculated by $[3c_{tot_1}/(4\pi)]^{1/3}$. N_1 and c_{crt} are model parameters. Given the model parameters, r_1 is estimated by $\sqrt{D_V N_1 \Delta t}$. In the simulations, N_1 and c_{crt} are set to be 5000 and 1.0, respectively.

2.9.1.3 Elastic-plastic Deformation Under the Crystal-Plasticity Framework

With the assumption of small deformation, the deformation energy density can be calculated by

$$f_{def} = \frac{1}{2} C_{ijkl}(\mathbf{r}) \varepsilon_{ij}^e \varepsilon_{kl}^e - \sigma_{ij}^{appl} \bar{\varepsilon}_{ij} \quad (121)$$

where $C_{ijkl}(\mathbf{r})$ is the elastic constant tensor, ε_{ij}^e is the elastic strain, σ_{ij}^{appl} is the applied stress tensor, and $\bar{\varepsilon}_{kl}$ is the average strain tensor.

The elastic strain is expressed as

$$\varepsilon_{ij}^e = \varepsilon_{ij} - \varepsilon_{ij}^* \quad (122)$$

where ε_{ij} is the total strain, and ε_{ij}^* is the total eigenstrain associated with lattice mismatch between the matrix and distributed defects such as interstitial, vacancy, fission products, and dislocations. The eigenstrain is defined as

$$\varepsilon_{ij}^*(\mathbf{r}, t) = \varepsilon_0 (C_{gg}) \delta_{ij} h(\chi) + (\sum_d \varepsilon_{0d} \delta_{ij} C_d) (1 - h(\chi)) + \varepsilon_{ij}^p(\mathbf{r}, t), \quad d = I, V, Xe \quad (123)$$

where $\varepsilon_0 (C_{gg})$ is the eigenstrain of gas bubbles which can be estimated by the EOS of Xe gas phase inside the gas bubble, δ_{ij} is the Kronecker delta function, C_d is the concentration of interstitial, vacancy, and Xe atoms in the matrix, ε_{0d} is the eigenstrain associated with lattice detorsion of defect d, and $\varepsilon_{ij}^p(\mathbf{r}, t)$ is the plastic strain which is calculated from crystal-plasticity theory.

According to crystal-plasticity theory, the plastic strain rate at the point \mathbf{r} inside grain β can be generally calculated as [160,161]

$$\dot{\varepsilon}^{\beta p}(\mathbf{r}) = \sum_{s=1}^N \mathbf{m}^s(\mathbf{r}) \dot{\gamma}^s(\mathbf{r}) = \dot{\gamma}_0 \sum_{s=1}^N \mathbf{m}^s(\mathbf{r}) \left(\frac{|\mathbf{m}^s(\mathbf{r}) : \boldsymbol{\sigma}(\mathbf{r})|}{\tau_0^s(\mathbf{r})} \right)^n \text{sgn}(\mathbf{m}^s(\mathbf{r}) : \boldsymbol{\sigma}'(\mathbf{r})) \quad (124)$$

where $\dot{\gamma}^s(\mathbf{r})$, $\tau_0^s(\mathbf{r})$, and $\mathbf{m}^s(\mathbf{r})$ are the shear strain rate, the critical resolved shear stress, and the Schmid tensor, respectively. The superscript s denotes the slip system s at material point \mathbf{r} , and N is the total number of the slip systems of the crystal at material point \mathbf{r} . $\dot{\gamma}_0$ is a normalization factor, and n is the stress exponent (inverse of the rate-sensitivity exponent). $\boldsymbol{\sigma}'(\mathbf{r})$ is the deviatoric stress tensor. The Schmid tensor is a dyadic tensor and is calculated using Eqn. 125

$$\mathbf{m}^s = \frac{1}{2b} (\mathbf{b}^s \otimes \mathbf{n}^s + \mathbf{n}^s \otimes \mathbf{b}^s), \quad (125)$$

where \mathbf{b}^s and \mathbf{n}^s are the Burger's vector and the normal direction of slip system s at point \mathbf{r} inside grain β . Then, the total plastic strain rate is calculated as

$$\dot{\boldsymbol{\epsilon}}^p(\mathbf{r}) = \sum_{\beta=1, \dots, \beta_0} \dot{\boldsymbol{\epsilon}}^{\beta p}(\mathbf{r}) \eta_{\beta}(\mathbf{r}) \quad (126)$$

We use $\mathbf{A}_{\beta} = (a_{ij}^{\beta})$ denoting the rotation matrix of the local coordinate of grain β . The coordinate transfer of the second-order tensor $\boldsymbol{\epsilon}$, such as stress, strain, and diffusivity tensors, from local coordinate to global can be written as

$$\boldsymbol{\epsilon}_{global} = \mathbf{A}_{\beta} \boldsymbol{\epsilon}_{local} \mathbf{A}_{\beta}^T \quad (127)$$

where \mathbf{A}_{β}^T is the transpose of \mathbf{A}_{β} . With the Euler angles of grain β , the components of the rotation matrix are given as

$$\mathbf{A}_{\beta} = \begin{bmatrix} a_{11}^{\beta} & a_{12}^{\beta} & a_{13}^{\beta} \\ a_{21}^{\beta} & a_{22}^{\beta} & a_{23}^{\beta} \\ a_{31}^{\beta} & a_{32}^{\beta} & a_{33}^{\beta} \end{bmatrix} = \begin{bmatrix} \cos\psi_{\beta} \cos\varphi_{\beta} \cos\theta_{\beta} - \sin\varphi_{\beta} \sin\theta_{\beta} & -\cos\psi_{\beta} \cos\varphi_{\beta} \cos\theta_{\beta} - \sin\varphi_{\beta} \cos\theta_{\beta} & \sin\psi_{\beta} \cos\varphi_{\beta} \\ \cos\psi_{\beta} \cos\varphi_{\beta} \cos\theta_{\beta} + \cos\varphi_{\beta} \sin\theta_{\beta} & -\cos\psi_{\beta} \sin\varphi_{\beta} \sin\theta_{\beta} + \cos\varphi_{\beta} \cos\theta_{\beta} & \sin\psi_{\beta} \sin\varphi_{\beta} \\ -\sin\psi_{\beta} \cos\theta_{\beta} & \sin\psi_{\beta} \sin\theta_{\beta} & \cos\psi_{\beta} \end{bmatrix} \quad (128)$$

Assuming that gas bubble phase has isotropic elastic constants C_{ijkl}^b and the single crystal UMo has anisotropic elastic constant C_{ijkl}^M , the elastic constant tensor in the global coordinate, can be described as

$$C_{ijkl}(\mathbf{r}) = \sum_{\beta=1, \beta_0} C_{pqst}^M a_{ip}^{\beta} a_{jq}^{\beta} a_{ks}^{\beta} a_{lt}^{\beta} \eta_{\beta}(\mathbf{r}, t) + C_{ijkl}^b \chi(\mathbf{r}, t) \quad (129)$$

To calculate deformation energy density in Eqn. 121, we need to solve the shear strain rate $\dot{\gamma}^s(\mathbf{r})$ from Eqn. 124. In this work, a formulation based on FFTs [162] is employed to solve for the shear strain rate $\dot{\gamma}^s(\mathbf{r})$.

Here we summarize the method as follows. At time $t + \Delta t$, the total strain includes elastic strains and plastic strains at a material point \mathbf{r}

$$\boldsymbol{\epsilon}^{t+\Delta t}(\mathbf{r}) = \boldsymbol{\epsilon}^{e, t+\Delta t}(\mathbf{r}) + \boldsymbol{\epsilon}^{p, t}(\mathbf{r}) + \dot{\boldsymbol{\epsilon}}^{p, t+\Delta t}(\mathbf{r}) \Delta t \quad (130)$$

where $\boldsymbol{\epsilon}(\mathbf{r})$ represents the total strain tensor, $\boldsymbol{\epsilon}^e(\mathbf{r})$ is the elastic strain tensor, $\boldsymbol{\epsilon}^p(\mathbf{r})$ is the viscoplastic strain tensor, and $\dot{\boldsymbol{\epsilon}}^p(\mathbf{r})$ is the viscoplastic strain rate tensor. The viscoplastic strain rate $\dot{\boldsymbol{\epsilon}}^p(\mathbf{r})$ is constitutively related to the local deviatoric stress, $\boldsymbol{\sigma}'(\mathbf{r}) = \boldsymbol{\sigma}(\mathbf{r}) - p(\mathbf{r})\mathbf{I}$, where $p(\mathbf{r}) = \frac{1}{3}[\sigma_{11}(\mathbf{r}) + \sigma_{22}(\mathbf{r}) + \sigma_{33}(\mathbf{r})]$ and \mathbf{I} being the hydrostatic stresses and a unit matrix, respectively, via a sum over the N active slip systems described by Eqn. 124.

The Euler implicit time discretization scheme is used to solve the solution of the Eqn. 130. The expression, in small strains, of the stress tensor at material point \mathbf{r} at $t + \Delta t$ is given by

$$\boldsymbol{\sigma}^{t+\Delta t}(\mathbf{r}) = \mathbf{c}(\mathbf{r}) : \boldsymbol{\epsilon}^{e, t+\Delta t}(\mathbf{r}) = \mathbf{c}(\mathbf{r}) : [\boldsymbol{\epsilon}^{t+\Delta t}(\mathbf{r}) - \boldsymbol{\epsilon}^{p, t}(\mathbf{r}) - \dot{\boldsymbol{\epsilon}}^{p, t+\Delta t}(\mathbf{r}) \Delta t], \quad (131)$$

where $\boldsymbol{\sigma}(\mathbf{r})$ is the Cauchy stress tensor, and $\mathbf{c}(\mathbf{r}) = \{c_{ijkl}(\mathbf{r})\}$ is the elastic stiffness tensor. The stresses must satisfy the stress equilibrium equation

$$\sigma_{ij, j}^{t+\Delta t}(\mathbf{r}) = 0 \quad (132)$$

and associated boundary conditions.

For known plastic deformation strain $\boldsymbol{\varepsilon}^{p,t}(\mathbf{r})$ at step t , the stress $\boldsymbol{\sigma}^{t+\Delta t}(\mathbf{r})$, strain $\boldsymbol{\varepsilon}^{t+\Delta t}(\mathbf{r})$, and plastic strain rate $\dot{\boldsymbol{\varepsilon}}^{p,t+\Delta t}(\mathbf{r})$ at time step $t + \Delta t$ can be obtained by the following two steps:

Step 1. Seek solutions of $\boldsymbol{\tau}^{t+\Delta t}(\mathbf{r})$ and $\mathbf{e}^{t+\Delta t}(\mathbf{r})$ for the following equations

$$\boldsymbol{\tau}^{t+\Delta t}(\mathbf{r}) = \mathbf{c}(\mathbf{r}):[\mathbf{e}^{t+\Delta t}(\mathbf{r}) - \boldsymbol{\varepsilon}^{p,t}(\mathbf{r})], \text{ or } \boldsymbol{\tau}(\mathbf{r}) = \mathbf{c}(\mathbf{r}):[\mathbf{e}(\mathbf{r}) - \boldsymbol{\varepsilon}^{p,t}(\mathbf{r})] \quad (133)$$

by removing the superscript $t + \Delta t$ and keeping the previous timestep superscript t . The stress, $\boldsymbol{\tau}(\mathbf{r})$, satisfies the equilibrium Eqn. 132

$$\tau_{ij,j}(\mathbf{r}) = 0 \quad (134)$$

The strains, $\mathbf{e}(\mathbf{x})$, are related to the displacements, $\mathbf{u}(\mathbf{r})$, as follows

$$e_{ii} = u_{i,i}, e_{ij} = \frac{1}{2}(u_{i,j} + u_{j,i}), i \neq j \quad (135)$$

Combining Eqns. 133 and 134, we have

$$\tau_{ij}(\mathbf{r}) = c_{ijkl}(\mathbf{r}) \left(e_{kl}(\mathbf{r}) - \varepsilon_{kl}^{p,t}(\mathbf{r}) \right) = c_{ijkl}(\mathbf{r}) \left(u_{k,l}(\mathbf{r}) - \varepsilon_{kl}^{p,t}(\mathbf{r}) \right) \quad (136)$$

We use iteration and FFT to solve Eqns. 134 and 136 and let the obtained stresses and displacements satisfy the given boundary condition. The boundary condition is satisfied in the concept of average values, for example:

1. For a polycrystal under uniaxial tensile stress along the x_1 -axis with a strain rate of $\dot{\varepsilon}_{11}$, the boundary condition is given by $\bar{e}_{11} = \bar{\varepsilon}_{11}^t + \dot{\varepsilon}_{11}\Delta t$ and $\bar{\tau}_{22} = \bar{\tau}_{33} = \bar{\tau}_{23} = \bar{\tau}_{13} = \bar{\tau}_{12} = 0$ where $\bar{\varepsilon}_{11}^t$ is the average value of ε_{11}^t from the previous step t and is known for the current step.
2. For a polycrystal under a constant pressure stress σ_0 along the x_1 -axis with a shear strain rate $\dot{\varepsilon}_{12}$ and a fixed side-boundary condition to mimic billet material inside a die chamber, the boundary condition can be expressed as $\bar{\tau}_{11} = \sigma_0$, $\bar{e}_{22} = \bar{e}_{33} = \bar{e}_{23} = \bar{e}_{13} = 0$ and $\bar{e}_{12} = \bar{\varepsilon}_{12}^t + \dot{\varepsilon}_{12}\Delta t$, where $\bar{\varepsilon}_{12}^t$ is known for the current step, similar to $\bar{\varepsilon}_{11}^t$.

Stresses, $\tau_{ij}(\mathbf{r})$, and strains, $e_{ij}(\mathbf{r})$, can be obtained through an iteration procedure [163].

Step 2. To get the final solutions of $\boldsymbol{\sigma}^{t+\Delta t}(\mathbf{r})$, $\boldsymbol{\varepsilon}^{t+\Delta t}(\mathbf{r})$, and $\dot{\boldsymbol{\varepsilon}}^{p,t+\Delta t}(\mathbf{r})$, or $\boldsymbol{\sigma}(\mathbf{r})$, $\boldsymbol{\varepsilon}(\mathbf{r})$, and $\dot{\boldsymbol{\varepsilon}}^p(\mathbf{r})$ without the superscript $t+\Delta t$ for Eqns. 130-131 under given boundary conditions, a residual function $R_{ij}(\mathbf{r})$ is introduced [162]

$$R_{ij}(\mathbf{r}) = \sigma_{ij}(\mathbf{r}) - \tau_{ij}(\mathbf{r}) + c_{ijkl}^0[\varepsilon_{kl}(\mathbf{r}) - e_{kl}(\mathbf{r})] \quad (137)$$

where $\tau_{ij}(\mathbf{r})$ and $e_{ij}(\mathbf{r})$ have been obtained from Step 1, and $\sigma_{ij}(\mathbf{r})$ and $\varepsilon_{ij}(\mathbf{r})$ will be solved through nullification of $R_{ij}(\mathbf{r})$ coupled with Eqn. 124 and 131. The nullification of Eqn. 124 is solved using a Newton-Raphson (N-R) scheme, that is

$$\sigma_{ij}^{(l+1)}(\mathbf{r}) = \sigma_{ij}^{(l)}(\mathbf{r}) - \left[\left(\frac{\partial R_{ij}}{\partial \sigma_{ij}} \right)^{-1} \right]^{(l)} R_{ij}^{(l)}(\mathbf{r}) \quad (138)$$

where the superscript l denotes the l -th iteration step. The iteration is stopped when $|R_{ij}|$ is less than a predetermined value. Through this step, we can finally get $\sigma_{ij}(\mathbf{r})$, $\varepsilon_{ij}(\mathbf{r})$, and $\dot{\varepsilon}_{ij}^p(\mathbf{r})$ for the given boundary condition and time step.

For materials with strength hardening, $\tau_0^s(\mathbf{r})$ varies with $\dot{\gamma}^s(\mathbf{r})$. For example, linear strength hardening can be expressed by $\Delta\tau_0^s = H \sum_{s=1}^N \dot{\gamma}^s(\mathbf{r}) \Delta t$ with H being a constant. In such a case, $\tau_0^s(\mathbf{r})$ in Eqn. 135 is replaced by

$$\tau_0^{s,t+\Delta t}(\mathbf{r}) = \tau_0^{s,t}(\mathbf{r}) + \Delta\tau_0^s = \tau_0^{s,t}(\mathbf{r}) + H \sum_{s=1}^N \dot{\gamma}^{s,t}(\mathbf{r}) \Delta t \quad (139)$$

Through Steps 1 and 2, $\sigma_{ij}(\mathbf{r})$, $\varepsilon_{ij}(\mathbf{r})$, and $\dot{\varepsilon}_{ij}^p(\mathbf{r})$ are obtained. With a known strength hardening law such as Eqn. 139, the shear strain rate $\dot{\gamma}^s(\mathbf{r})$ can be obtained from Eqn. 124.

2.9.2 Material Properties of UMo

The thermal and mechanical properties of UMo that depend on temperature and neutron fluence [164] have been assessed by experiments [2,165–168]. The temperature dependence of Young's modulus E (GPa) is expressed as [169]

$$E(T) = 110.84 - 72.926 \times 10^{-3}T - 1.8718 \times 10^{-5}T^2, \quad 294 \leq T \leq 873K \quad (140)$$

where T is the temperature (K).

The Poisson's ratio was adapted from [34], and it is constant 0.324. The temperature dependence of yield strength σ_y is expressed as [170]

$$\sigma_y = -1.2727 \times 10^{-6}T^3 + 2.430 \times 10^{-3}T^2 - 2.4285T + 1478.6, \quad 300 \leq T \leq 866 K \quad (141)$$

Since we do not have the yield stress of single crystal UMo, the Eqn. 141 is used to estimate the critical resolved stress in the crystal-plasticity model. Formation energy and migration energy of Xe are calculated by atomistic simulations [54,171,172].

2.9.3 Model Parameters

2.9.3.1 Model Parameters in Crystal-plasticity and Phase-field Model

Both experiments and atomistic simulations show that gamma UMo has isotropic elastic properties. Thus, two of the three elastic moduli (i.e., Young's modulus, Shear modulus, and Poisson's ratio) can describe the elastic properties of UMo. In this work, the temperature is set to be 500 K, which is approximately the operation temperature of UMo fuels in high-performance research reactors [2]. From Eqns. 140 and 141, E is 70 GPa and the yield strength σ_y is 0.718 GPa at $T = 500K$. The constant H in Eqn. 139 is set to be $5.0 \times 10^6 Pa$. γ -UMo has a body-centered cubic (bcc) structure, where 24 slip systems are often activated during deformation: 12 $\{110\}\langle\bar{1}11\rangle$ and 12 $\{211\}\langle\bar{1}11\rangle$ systems. The crystal-plasticity model is general and can consider all the slip systems. For model validation, only 12 $\{110\}\langle\bar{1}11\rangle$ slip systems are considered in the simulations. Table 23 lists the model parameters of crystal plasticity and the PF model of gas bubble evolution. In Zr layers, Zr has hcp crystal structure. It is possible to assign different slip systems in different grain. For simplicity, we assume there is no plastic deformation in Zr layers because Zr has much high yield stress than UMo. In the simulations, the elastic constants and slip systems as UMo in Zr layers are set to be the same as that of UMo, but a higher yield stress 2.0 GPa is assigned in Zr layers to limit the plastic deformation.

Table 23. Model parameters of the crystal plasticity and the PF models of gas bubble evolution for U-Mo crystals [173].

Parameter	Value	Parameter	Value
T	500 K	dt	0.1 s
c_{11}^m	101.5 GPa	c_{11}^b	$90E_0$ GPa
c_{12}^m	48.7 GPa	c_{12}^b	$30E_0$ GPa
c_{44}^m	26.4 GPa	c_{44}^b	$30E_0$ GPa
σ_y	718 MPa	c_m^{eq}	1.0×10^{-6}
b	0.248 nm	c_h^{eq}	0.6
l_0	10 nm	A_{1m}	$2.02 \times 10^{12} J/m^3$
w	$1.0 J/m^2$	A_{2m}	$-8.77 \times 10^{12} J/m^3$
λ	$1.5l_0$	A_{3m}	$5.71 \times 10^{12} J/m^3$

Parameter	Value	Parameter	Value
<i>Slip systems</i>	1/2 $\langle \bar{1}11 \rangle \{110\}$	A_{1b}	$-1.18 \times 10^{10} \text{ J/m}^3$
Ω	$1.4 \times 10^{-5} \text{ m}^3/\text{mol}$	A_{2b}	$-1.91 \times 10^{12} \text{ J/m}^3$
L	$5 \times 10^{-10} \text{ m}^3/\text{Js}$	A_{3b}	$1.92 \times 10^{12} \text{ J/m}^3$
Mismatch strain ε_{b0}	0.05	f_0	40
Mismatch strain ε_{0d}	0.05, -0.03, and 0.05, d = I, V and Xe	E_0	0.01, 0.1, 0.3, 0.6

2.9.3.2 Calculation of Defect Generation During Fission

To calculate the defect generation \dot{G}_i , we need to know the fission product yields and the kinetic energy distribution of the fission products. Fission product (FP) yields depend on the fissioning nuclide and the energy of the neutron causing the fission. Here, we evaluate the model for fission from $^{235}_{92}\text{U}$ due to thermal neutrons (neutron energy=0.0253 eV), which is applicable for light-water reactors. Based on the previous work of Setyawan et al. [174], we take the independent FP yield (iFPY) from the JEFF 3.3 library to calculate the defect generation in this work. The distribution of the FPs and kinetic energies (E_{tot}) as a function of atomic number can be found in [174]. The 18 elements listed in Table 24 make up almost 100% of the distribution. Every fission creates two FPs, one light FP, and one heavy FP. The mass of the most probable isotope in each element is taken as the mass of the element. UMo fuels are currently developed for high-performance research reactors. In high-performance research reactors such as High Flux Isotope Reactor at Oak Ridge National Laboratory, the percentages of fissions caused by neutrons in the thermal, intermediate, and fast neutron ranges are 83.03% (< 0.625 eV), 15.50% (0.625 eV – 100 keV), and 1.48% (>100 keV) [175]. We calculated the FP yields for neutron energy of 40keV. The calculation shows that the sum of FP yields from 18 elements is less than 0.5% for neutron energy 0.0253 eV and 40keV.

Using E_{tot} and the mass of the most probable isotope, the SRIM simulations are performed to obtain the portion of the energy lost due to electronic stopping (E_{electron}) and the energy that effectively causes damage via displacement cascade (E_{damage}), for each FP. For SRIM simulations, the displacement threshold energy (E_d) of γU from MD cascade simulations [120] and the material density of pure γU are used. The NRT formula of $0.4 \cdot E_{\text{damage}}/E_d$ is used to estimate the Frenkel pair generation per fission [176]. The results show that one $^{235}_{92}\text{U}$ fission generates about 14,825 Frenkel pairs in γU . Table 2 summarizes the E_{tot} , E_{electron} , E_{damage} , and the number of Frenkel pairs for each FP.

Table 24. The most probable isotopes of FPs from $^{235}_{92}\text{U}$ due to thermal neutrons, the independent fission product yield (iFPY), total kinetic energy (E_{tot}), electronic loss (E_{electron}), and $E_{\text{damage}} = E_{\text{tot}} - E_{\text{electron}}$ used in SRIM simulations to estimate the number of Frenkel pairs in γU with displacement threshold energy $E_d=35.6\text{eV}$ at 800K.

Element	iFPY	E_{tot} (MeV)	E_{electron} (MeV)	E_{damage} (MeV)	Frenkel Pairs
$^{86}_{34}\text{Se}$	0.042	101.3	98.362	2.938	1376.9
$^{87}_{35}\text{Br}$	0.051	101.2	98.117	3.083	1751.6
$^{90}_{36}\text{Kr}$	0.164	101.5	98.333	3.167	5829.3
$^{93}_{37}\text{Rb}$	0.112	101.2	97.840	3.360	4216.0

Element	iFPY	$E_{tot}(\text{MeV})$	$E_{electron}(\text{MeV})$	$E_{damage}(\text{MeV})$	Frenkel Pairs
$^{94}_{38}\text{Sr}$	0.209	101.1	97.766	3.334	7816.4
$^{97}_{39}\text{Y}$	0.114	101.3	97.792	3.508	4504.4
$^{100}_{40}\text{Zr}$	0.180	101.4	97.536	3.864	7824.6
$^{102}_{41}\text{Nb}$	0.073	101.8	97.728	4.072	3319.2
$^{104}_{42}\text{Mo}$	0.041	101.2	97.172	4.028	1847.3
$^{130}_{50}\text{Sn}$	0.041	81.5	75.928	5.572	2555.1
$^{133}_{51}\text{Sb}$	0.073	78.8	73.052	5.748	4685.4
$^{134}_{52}\text{Te}$	0.180	77.5	71.641	5.859	11864.3
$^{136}_{53}\text{I}$	0.114	74.6	68.582	6.018	7726.5
$^{138}_{54}\text{Xe}$	0.209	71.9	66.289	5.611	13154.9
$^{141}_{55}\text{Cs}$	0.112	68.2	61.898	6.322	7931.9
$^{144}_{56}\text{Ba}$	0.164	64.8	58.330	6.470	11908.0
$^{146}_{57}\text{La}$	0.051	62.6	56.049	6.551	3721.8
$^{148}_{58}\text{Ce}$	0.042	60.2	53.491	6.709	3144.7
SUM		1.969			
iFPY-weighted sum of Frenkel pairs = 14825					

2.9.3.3 Thermodynamic and Kinetic Properties of Defects

Table 25 lists the model parameters used in the simulations. Very limited thermodynamic and kinetic properties of defects in U-10Mo, which are needed in cluster dynamics and PF models, are available in the literature. The defect formation energies of U vacancy and interstitials are assessed from the data of DFT and MD simulations in U and UMo alloys [177–179]. Self-diffusivity of U is from MD simulations and experiments [119,172,180,181]. Xe diffusion is adopted from the rate theory model of gas bubble swelling in UMo [34]. Capture radius, bias coefficients, and model parameters of network dislocations are adopted from the cluster dynamic and rate theory models [148,151,154,182,183].

Table 25. Model parameters in the cluster dynamics model [184].

Parameter	Value	Parameter	Value
T	453K	Z_{IV}	50
r_{at}	1.5Å	$Z_{I,dis}$	1.25
Ω	$2.1 \times 10^{-29} \text{m}^3$	$Z_{V,dis}$	1.0
a	3.48Å	M_I	30
D_V	$1.83 \times 10^{-19} \text{m}^2/\text{s}$	M_V	10
D_I	$1.42 \times 10^{-18} \text{m}^2/\text{s}$	E_i^f	0.8eV
D_g	$1.83 \times 10^{-20} \text{m}^2/\text{s}$	E_{2i}^b	0.5eV
ρ_{dis0}	$1.0 \times 10^{14} \text{m}^{-2}$	E_v^f	1.61eV
$E_{i,gb}^f$	0.7eV	E_{2v}^b	0.5eV

Parameter	Value	Parameter	Value
$E_{v,gb}^f$	0.8eV	σ	1.0 J/m ²
D_0	$1.42 \times 10^{-18} \text{m}^2/\text{s}$	l_0	12nm
\dot{f}_0	$3.29 \times 10^{22} \text{fission}/\text{s}/\text{m}^3$	λ	36nm
A_m	$10.75 k_B T$	A_{bv}	$0.91 k_B T$
A_{bb}	$0.91 k_B T$	Δt	0.101s
h	2	Z_{ij}^v	1.0
Z_{ij}^i	1.25	Z_{ij}^f	42

2.9.4 Results

2.9.4.1 Effect of Gas Bubble Structures on Mechanical Properties

In this section, we validate the crystal-plasticity model in polycrystalline UMo with distributed Xe gas bubbles. We investigate the effect of gas bubble structures on the mechanical response by solving Eqns. 132-141. The radiation and gas bubble evolution are ignored by turning off the Eqns. 106-120. The concentrations of vacancy, interstitial, and Xe in the matrix are set to zero. Figure 99 illustrates the simulation cell with dimensions of $128l_0 \times 32l_0 \times 128l_0$, cylindrical grains along the y-direction, and distributed gas bubbles. The average grain size in the xz plane is about 340 nm, which is on the order of the typical grain size observed in recrystallized grains in UMo fuels. Periodic boundary conditions are applied in the x-, y-, and z-directions, and a strain along the z-direction is applied to perform tensile or compressive deformation.

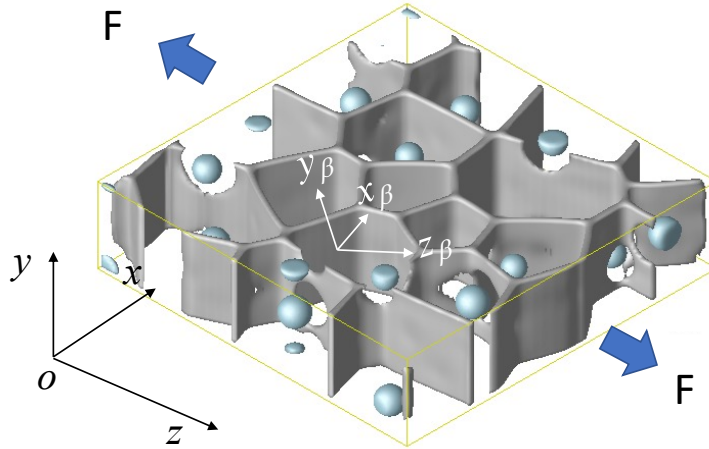


Figure 99. Simulation cell of polycrystalline UMo with distributed gas bubbles to validate crystal-plasticity model.

Effect of Gas Bubble Structures on Mechanical Properties

Three gas bubble structures with gas bubble volume fractions ($V_f = 3.5\%$, 6.7% , and 9.7%) are generated with a PF model of gas bubble evolution in polycrystalline structures. Gas bubbles, which have an average gas bubble size of 80 nm in diameter, are randomly distributed in the simulation cell. It is assumed bubbles are pressurized, and the pressure is associated with the lattice mismatch between the gas phase and the matrix UMo phase. The lattice mismatch is described by an eigenstrain tensor $\varepsilon_{ij}^{gb*} = \varepsilon_{b0} \delta_{ij} C_{gg}(\mathbf{r}, t) h(\chi)$, where $C_{gg}(\mathbf{r}, t)$ is the Xe concentration inside the gas bubble, $h(\chi)$ is the shape

function defined by Eqn. 108, δ_{ij} is the Kronecker delta function, and ε_{b0} is the mismatch strain. For the first-order approximation, if the bulk modulus, pressure, and Xe equilibrium concentration inside the gas bubble are B_{gb} , p_{gb} , and c_b^{eq} , respectively, the mismatch strain can be estimated by $\varepsilon_{b0} = \frac{p_{gb}}{B_{gb} c_b^{eq}}$. In

principle, the EOS of Xe gas phase [117,159,185] can be used to estimate the bulk modulus B_{gb} and the equilibrium Xe concentration for a given pressure, hence, the mismatch strain ε_0 . From the EOS [117], when the internal pressure is about 2GPa the bulk modulus is about 30GPa. Here, we assigned the elastic constants of the gas phase to be $c_{11}^b = 90E_0 \text{ GPa}$, $c_{12}^b = 30E_0 \text{ GPa}$, and $c_{44}^b = 30E_0 \text{ GPa}$, the bulk modulus B_{gb} is $50E_0 \text{ GPa}$, and the Poisson's ratio is 0.125, where E_0 is a parameter that depends on the pressure p_{gb} and the concentration c_b^{eq} inside the gas bubble. Pressure, equilibrium concentration, and lattice mismatch inside gas bubbles change with the local stresses and chemistry (local vacancy and Xe concentrations) in UMo fuels in service. For evolving gas bubbles, the molar volume is calculated by the Xe concentration inside the gas bubble. With the molar volume, the pressure and bulk modulus can be calculated with the EOS. To study the effect of steady-state gas bubble structures on mechanical response, we can prescribe fixed values of c_b^{eq} and ε_{b0} , which are listed in Table 23, and vary E_0 to describe the pressure inside the gas bubbles.

Stress Field Around Pressured Gas Bubbles

In the elastic-plastic deformation model, the iteration approach [163] is used to solve the mechanical equilibrium equations and the stress field in an elastic inhomogeneous material with a distribution of stress-free strains as described in Eqn. 120. The stress field around gas bubbles with an average radius of 50 nm and different internal pressures ($P_{gb} = 0.07, 0.60, 1.2 \text{ and } 2.1 \text{ GPa}$) under elastic deformation is calculated. Stress fields on the middle plane of the simulation cell in the y-direction are presented in Figure 100. The light black lines denote the grain boundary while the white circles show the interfaces between gas bubble and matrix. It is found that the pressure ($P = -(\sigma_{11} + \sigma_{22} + \sigma_{33})/3$) inside the gas bubbles is uniform which is in agreement with Eshelby's solution [186], and the shear stress (σ_{13}) around the gas bubble is larger than the yield stress of UMo (0.718GPa) when the internal pressure is larger than 1 GPa. The internal pressure inside nano-sized gas bubbles may reach a few GPa according to MD simulations [117,159,187], but with the increase of gas bubble size, the pressure decreases. In addition, a stress field associated with the cladding constraint in UMo monolithic fuels might increase the stresses in the matrix. Therefore, the internal pressure and the cladding constraint may result in plastic deformation in UMo under service.

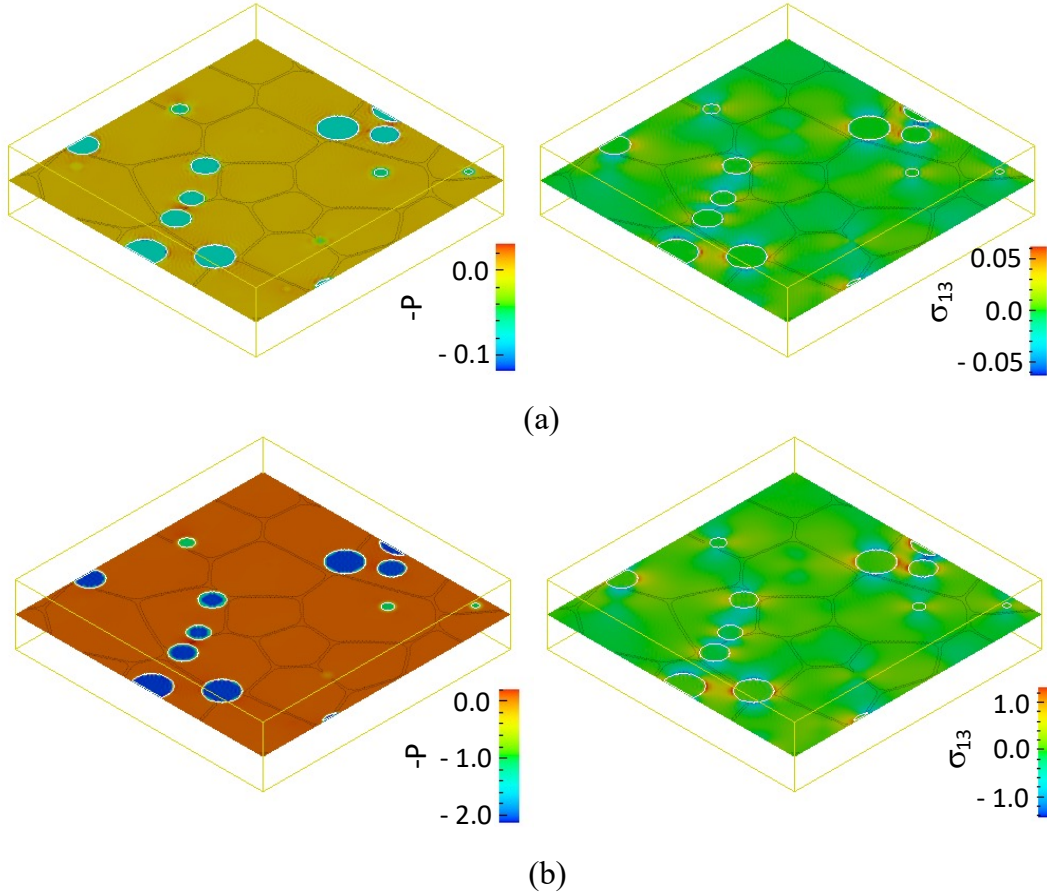


Figure 100. Pressure (P) and shear stress (σ_{13}) distributions on the plane S for gas bubbles with internal pressures of (a) 0.07 GPa and (b) 2.1 GPa. The units of pressure and stress are GPa.

Effect of Gas Bubble Structures on Stress-strain Curves

Gas bubble structures with different volume fractions ($V_f = 3.5\%$, 6.7% , and 9.7%) and different initial internal pressures ($P_{gb} = 0.07$, and 1.2 GPa) are used to study the effect of gas bubble structures on stress-strain curves under elastic-plastic deformation. In the simulations, a strain rate of $d\bar{\epsilon}_{33}/dt = 3 \times 10^{-4}$ (1/s) (the other strain components are zero, $\bar{\epsilon}_{ij} = 0$) is applied in z-direction for tensile deformation while $d\bar{\epsilon}_{33}/dt = -3 \times 10^{-4}$ (1/s) is applied for compressive deformation. Xe concentration in the matrix is set to be 5×10^{-5} , and the stress-free strain associated with Xe-induced lattice change in the matrix is set to be 0.1. Figure 101a–b presents the effect of gas bubble structures on stress-strain curves under tensile and compress deformation. The black curves are the stress-strain curves in polycrystalline structures with Xe concentration of 5×10^{-5} but without gas bubbles. The results in Figure 101a are stress-strain curves for gas bubbles with a low initial internal pressure of $P_{gb} = 0.07$ GPa, while the results in Figure 101b are for gas bubbles with a higher initial internal pressure of $P_{gb} = 1.2$ GPa. Because of the lattice mismatch associated with distributed Xe in the matrix and the internal pressure inside gas bubbles, a residual stress field is present. The residual stress, which is a compressive stress field due to a positive stress-free strain, shifts the total stress at an applied strain of zero to a negative value. The negative stress value is marked by the small circle in the stress-strain curves. It can be seen that the effect of gas bubble volume fraction on the stress shift at an applied strain of $\bar{\epsilon}_{33} = 0$ is small, especially for the case of gas bubbles with a low internal pressure $P_{gb} = 0.07$ GPa. For gas bubbles with high pressure, the stress shift increases with the increase of gas bubble volume fraction which can be

seen by zooming in on the stress-strain curves at $\bar{\epsilon}_{33} = 0$ in Figure 101b. For the simulation conditions, the residual stress is mainly determined by the distributed Xe (its concentration and stress-free strain) in the matrix. If the matrix vacancy is rich, the distributed vacancies and Xe results in the reduction of the UMo lattice constant, and the stress-free strain is negative. It is expected that the residual stress is a tensile stress field due to a negative stress-free strain, and the stress-strain curves shift to a positive value at $\bar{\epsilon}_{33} = 0$.

Comparing the results in Figure 101, we can conclude that (1) for all the cases the effective Young's modulus, which is the slope at the linear part of the stress-strain curves, decreases with the increase of gas bubble volume fraction. This is expected because the gas phase has a lower Young's modulus than that of the matrix UMo phase. (2) The Young's modulus depends on both gas bubble structure (gas bubble volume fraction and internal pressure) and applied stress (tensile or compress). (3) The yield stress decreases with the increase of gas bubble volume fraction. The yield stress has a similar dependence on gas bubble structure and applied stress as that of the Young's modulus; and (4) the hardening coefficient increases with the increase of gas bubble volume fraction, especially for gas bubbles with higher internal pressures, which is indicated by the slope of stress-strain curves in the plastic deformation stage.

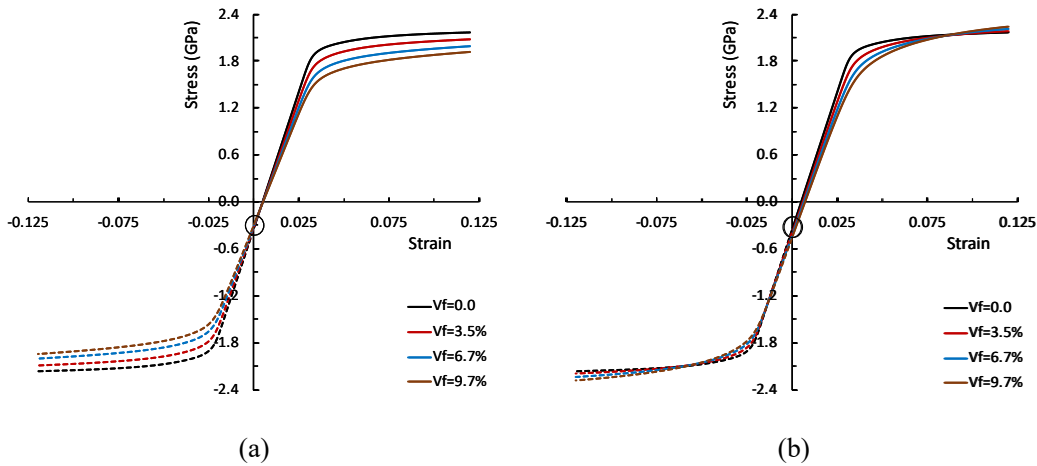


Figure 101. Effect of gas bubble volume fraction and internal pressure on stress-strain curves. Results shown are for gas bubbles with a pressure of (a) $P_{gb} = 0.07GPa$, (b) $P_{gb} = 1.2GPa$. Both tensile and compressive stresses are applied.

The strain hardening is determined by the plastic strain rate. The distributions of plastic strain ϵ_{13}^p on the center plane S in polycrystalline structures with gas bubble volume fraction 9.7% at different applied strain $\bar{\epsilon}_{33}$ are shown in Figure 102. The results in Figure 101a and Figure 102b are for gas bubbles with a pressure of $P_{gb} = 0.07GPa$ and $P_{gb} = 1.2GPa$ under tensile deformation, respectively. Before the applied strain reaches $\bar{\epsilon}_{33} = 0.02$, the deformation is elastic, and the plastic strain is zero as shown in Figure 101. It is observed that plastic deformation first takes place near the gas bubble interface, particularly at the interface region of two nearby gas bubbles as shown $\bar{\epsilon}_{33} = 0.054$, where the stress concentration is higher than that at the interface of an isolated gas bubble, as shown in Figure 100a. With the increase of applied strain, plastic strain increases. The plastic strain in regions with yellow color has a positive sign while the plastic strain in regions with green color has a negative sign. The flaky pattern of plastic strain (ϵ_{13}^p) distribution at $\bar{\epsilon}_{33} = 0.1$ indicates the formation of shear bands where shear strain has a uniform and high value of $\bar{\epsilon}_{33} = 0.1$. Figure 103 plots the distributions of the shear stress component σ_{13} on the center plane S at $\bar{\epsilon}_{33} = 0.1$. The white lines show the $\langle 101 \rangle$ directions. From the results in Figure 103, we can see that (1) most bands of shear stress σ_{13} align along the $\langle 101 \rangle$ directions while the

effect of grain orientation on shear stress σ_{13} is minor. The isotropic elastic properties of UMo, which has the Zener ratio ($2C_{44}/(C_{11} - C_{12})$) of 1, can explain the grain orientation independence of shear stresses, and (2) the alignment of gas bubbles along the $\langle 101 \rangle$ direction enhances the shear stress bands for both cases of gas bubbles (with low and high initial pressures). Compared with the shear stress, the bands of shear plastic strain (ε_{13}^p) shown in Figure 101 do not well align along the $\langle 101 \rangle$ directions. This is because dislocation sliding depends not only on the resolved shear stress but also on grain orientations. The red and blue of the color bar in Figure 102 and Figure 103 present the maximum and minimum values of shear strain (or stress) in the simulation cell during deformation for a given gas bubble structure with low (or high) pressure. Comparing the maximum values in the color bars in Figure 102 and Figure 103, we can see that both the maximum plastic strain and shear stress for gas bubbles with low pressure are larger but more localized near the gas bubbles than that for gas bubbles with high pressure. In other words, the shear stress and strain fields around gas bubbles with a low gas pressure are more inhomogeneous than those around gas bubbles with a high gas pressure. We also calculated the evolution of the total shear plastic strain in the simulation cell during the deformation. The results show that the total plastic strain for a system with low-pressure gas bubbles is higher than that for a system with high-pressure gas bubbles. Therefore, we can conclude that the more inhomogeneous a stress field is, the less strain hardening is. And the gas bubble dependence of hardening behavior showed in Figure 101 is attributed to the inhomogeneous stress-induced inhomogeneous plastic deformation.

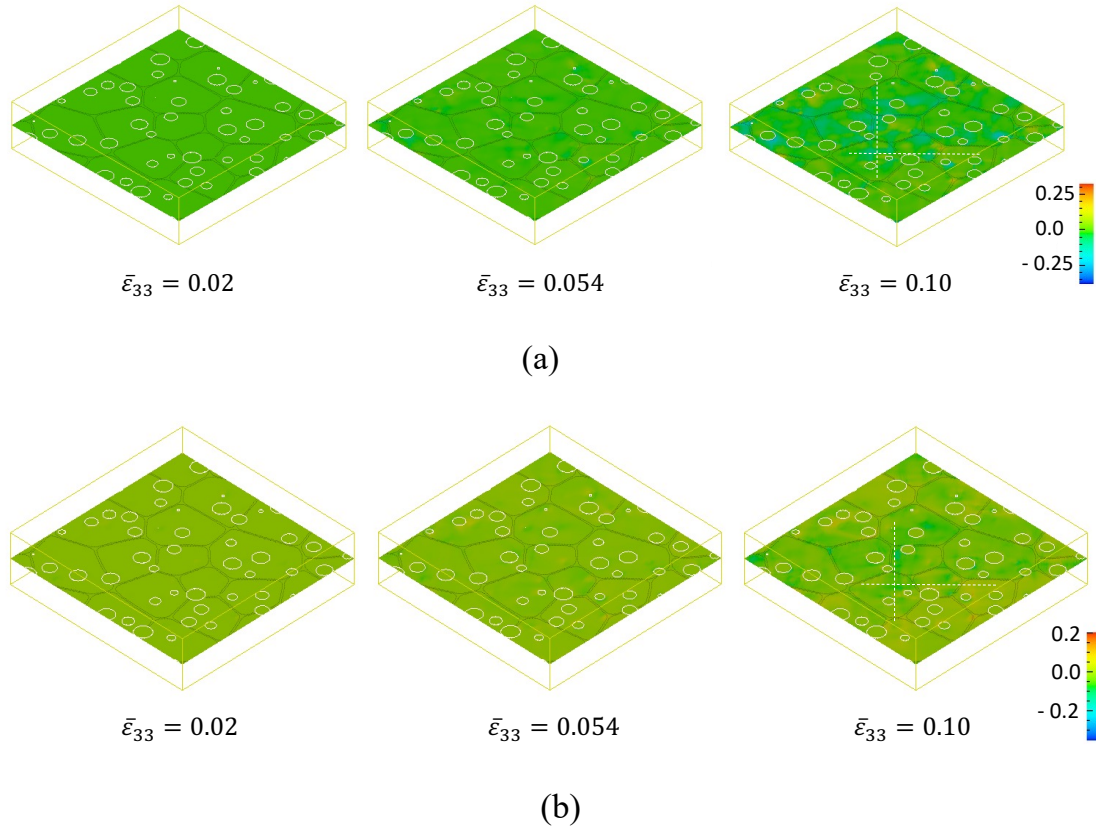


Figure 102. Distributions of plastic strain ε_{13}^p on the plane S in polycrystalline structures with gas bubble volume fraction 9.7% at different applied strains ($\bar{\varepsilon}_{33} = 0.02, 0.054, \text{ and } 0.10$). (a) gas bubbles with initial pressure $P_{gb} = 0.07GP$ and (b) gas bubbles with initial pressure $P_{gb} = 1.2GPa$.

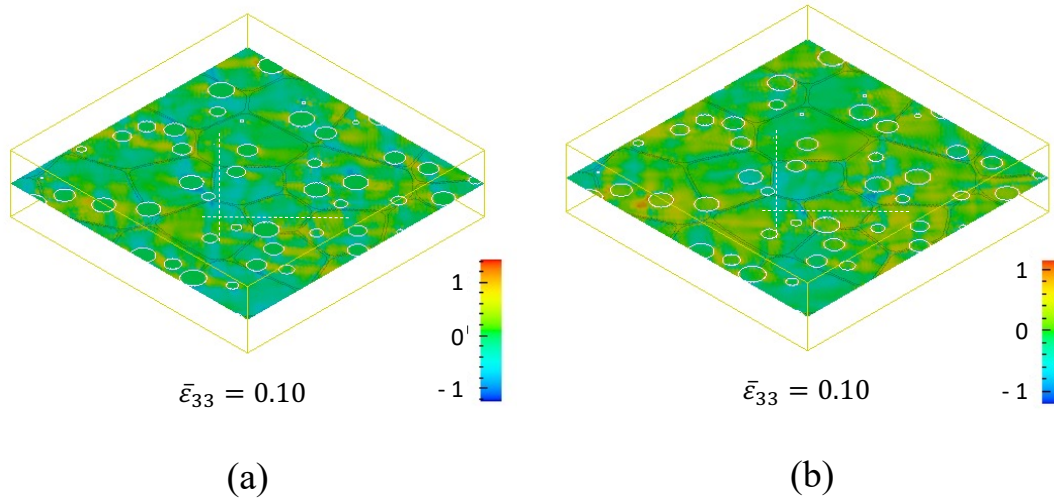


Figure 103. Distribution of shear stress σ_{13} at $\bar{\epsilon}_{33} = 0.1$. (a) gas bubble with initial internal pressure $P_{gb} = 0.07 GPa$, and (b) gas bubble with initial internal pressure $P_{gb} = 1.2 GPa$.

2.9.4.2 Dynamic Interaction Among Radiation Defects, Gas Bubble Swelling, and Elastic-plastic Deformation

In this section, we study the dynamic interaction among radiation defects, gas bubbles, and elastic-plastic deformation using the integrated model. The Eqns. 105-141 are solved in the order described in the flow chart of the integrated model. The polycrystalline structure shown in Figure 98 are used in the simulations. Most model parameters are listed in Table 23–25. Some thermodynamic and kinetic properties are unknown or have large uncertainty such as the defect generation rate, kinetic properties of defects on GBs. In Section 2.9.3.2 the generation of Frenkel pairs per ^{235}U fission in γU is estimated at 14,825. The MD method has been used to simulate the defect evolution under energetic cascades in metals [188–190]. It is found that (1) most generated Frenkel pairs annihilate during a very short period (within a few ps), and (2) the NRT formula of $0.4 \cdot E_{damage}/E_d$ overestimates the number of defects by a factor 3 ~ 4. For long-time cascade defect aging up to tens of ns, object kinetic Monte Carlo (OkMC) simulations in tungsten show that the number of defects further decreases. The amount of reduced defects depends on PKA energy and temperature [191]. The generation rate of defects can be calculated by $\dot{G}_I = \dot{G}_V = G \dot{f}_0$, where \dot{f}_0 is the FR. G is the number of survived Frenkel pairs per fission during the simulation time increment Δt . G is an unknown model parameter, based on the MD and OkMC simulations of defect evolution $G = 1000$, which means less than 20% of defects calculated by the NRT formula survive, and this should be a safe estimation. The generation rate of gas atoms is calculated by $\dot{G}_g = 0.25 \dot{f}_0$, which means four fissions generate one gas atom. GBs are sinks of vacancies and interstitials. Interstitial aggregation on GBs may lead to grain growth or interstitial emission from GBs. On other hand, vacancy aggregation on boundaries may lead to void or gas bubble formation. The sink and emission of GBs could be described by the natural properties of defects on GBs including their chemical potentials and mobility. High mobility of interstitial and vacancy on GBs increase their recombination rate and reduce their concentrations, hence, result in interstitial and vacancy fluxes (or sink) to GBs. The increase of interstitials or vacancy concentrations increase their chemical potentials which may drive interstitial or vacancy migrate back (or emit) to interior grains. Gas bubbles are also sinks of defects. Low pressure gas bubbles or voids are natural sinks. In other word, gas bubbles absorb all defects once they diffuse into the absorption zone of gas bubbles. However, high-pressure gas bubbles may absorb vacancy but partially emit interstitials and Xe atoms in gas bubble interfaces. For simplicity, we only consider the kinetic properties like the conventional rate theory by assuming uniform chemical potential of diffusive defects

(vacancy, interstitial and Xe atoms) in the polycrystalline structure. We also assume that (1) vacancy and Xe are absorbed by gas bubbles and partial interstitials are emitted from gas bubbles; and (2) vacancy and interstitial have larger mobility on GBs than that inside grains; and there is no defect emission from GBs. We will simulate the effect of these kinetic properties on defect accumulation and gas bubble evolution.

Effect of Defect Mobility at Grain Boundaries on Defect Accumulation

We first study the effect of defect mobility at GBs on defect evolution. The simulation is performed in the polycrystalline structure without gas bubbles under a FR of $\dot{f}_0 = 3.05 \times 10^{22} \text{ fission}/\text{m}^3/\text{s}$. The ratio of defect diffusivity on grain boundary and interior grain, which is denoted as $D_{ratio} = D_a|_{\text{on grain boundary}}/D_a|_{\text{inside grains}}$, $d = \text{vacancy, interstitial}$, is assumed to be 20. Figure 104 shows the evolution of vacancy and interstitial concentrations on the AA' line shown in Figure 104a. The solid lines stand for interstitial concentration, and the dashed lines for vacancy concentration. What we can see is that the interstitial concentration distribution quickly reaches steady state while the vacancy concentration keeps evolving. The interstitial concentration on GBs is lower. The vacancy concentration on GBs increases with time, implying there is a net vacancy production. In the simulation the dislocation density is set up to be $1.0 \times 10^{14}/\text{m}^2$, the bias coefficient of interstitials at dislocations $Z_{I,dis}$ is larger than that of vacancies, interstitial diffusivity is larger than that of vacancy, all these kinetic properties lead to more interstitials sinks to dislocations. The effect of defect diffusivity inhomogeneity on interstitial and vacancy concentration at $t=32\text{s}$. For $D_{ratio} = 1$, the system reaches a steady state although the dislocation density is not zero. The vacancy and interstitial concentrations are uniform. The vacancy aggregation on GBs increases with the increase of D_{ratio} . Therefore, the reason that vacancy concentration could not reach a steady state is the inhomogeneous defect diffusivity. The vacancy aggregation may cause void or gas bubble formation in the presence of fission-gas atoms which are observed in gas bubble structure in nuclear fuels.

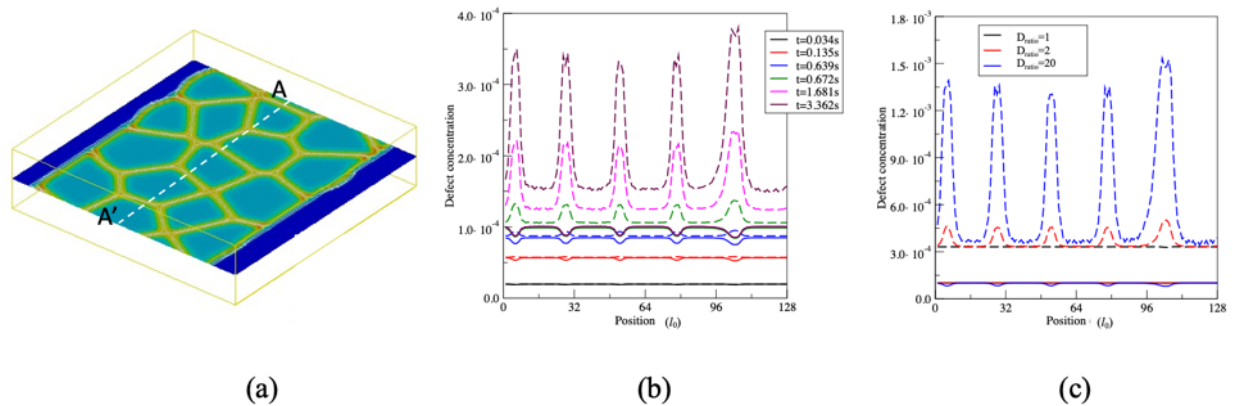


Figure 104. (a) the center plane of the simulation cell, (b) evolution of vacancy and interstitial concentrations, and (c) defect concentrations at $t=32\text{s}$ for different $D_{ratio} = 1, 2, \text{ and } 20$.

Effect of Fission Rates on Defect Accumulation

With a lower FR $\dot{f}_0 = 3.05 \times 10^{21} \text{ fission}/\text{m}^3/\text{s}$ and $D_{ratio} = 20$, the defect evolution is simulated. The results are plotted in Figure 105. The interstitial concentration reaches a steady-state distribution which is almost uniform. Compared the results in Figure 105 and Figure 104 (b), we find that (1) it takes much longer time for interstitial concentration reaching a steady state; (2) vacancy concentration on GBs at the earlier stage is lower than that inside grains, but at the later stage vacancy concentration on GBs becomes higher than that inside grains; (3) both the steady-state interstitial concentration and vacancy concentration on GBs are more than one magnitude lower than that in the case with higher FR $\dot{f}_0 =$

$3.05 \times 10^{22} \text{ fission}/\text{m}^3/\text{s}$. Therefore, FR affects defect concentrations but not the tendency of defect aggregation.

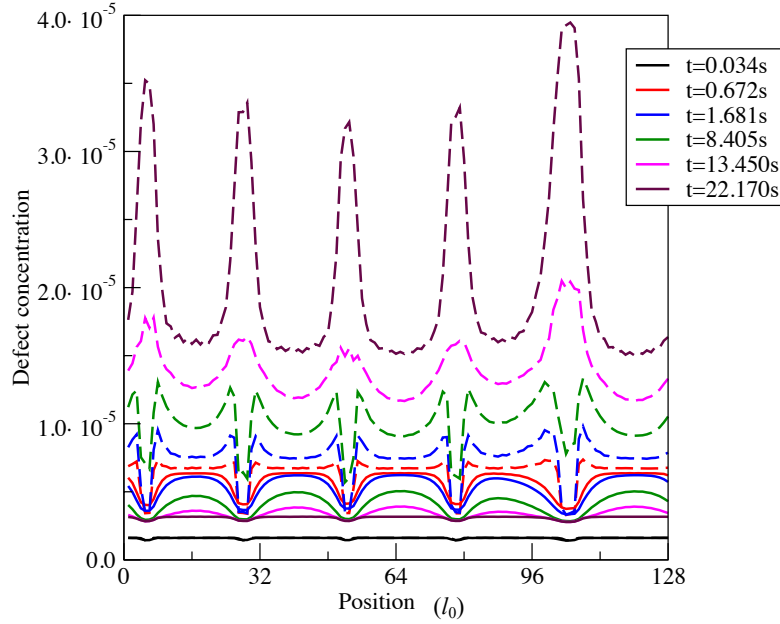


Figure 105. Evolution of vacancy and interstitial concentrations under a FR $\dot{f}_0 = 3.05 \times 10^{21} \text{ fission}/\text{m}^3/\text{s}$ and $D_{ratio} = 20$.

Effect of Gas-Bubble Structures and Stress on Defect Accumulation

Gas bubbles act as sinkers of vacancy, interstitial, and fission gas Xe. The evolution of gas bubbles affects the overall sinker strength, hence, the defect concentration in the matrix. We consider three gas-bubble structures with gas bubble volume fraction 0%, 7% and 12%, respectively. The Xe concentration inside the gas bubbles are set to be 0.5 which has an internal pressure about 2.0GPa. The simulations start with defect concentration $1. \times 10^{-6}$. A compressive strain rate $\dot{\epsilon}_{33} = -1.0 \times 10^{-2}$ is applied in the z-direction. Once the applied strain reaches $\epsilon_{33} = -0.01$ we turn on the radiation with a FR $\dot{f}_0 = 3.05 \times 10^{21} \text{ fission}/\text{m}^3/\text{s}$ and $D_{ratio} = 20$. Figure 106a shows the three gas-bubble structures. The distribution of pressure ($p = (\sigma_{11} + \sigma_{22} + \sigma_{33})/3$) on the middle plane at the applied strain $\epsilon_{33} = -0.01$ are shown in Figure 106b. Since the system has three phases (i.e., UMo matrix, Xe gas bubble with internal pressures, and Zr diffusion barrier layer), they have different mechanical properties. It can be seen that the pressure in polycrystalline structure depends on the gas-bubble structure due to the internal pressure and different mechanical properties. The pressure increases with the increase of gas-bubble volume fraction. Diffusion-controlled creep is associated with mass transport minimizing the deformation energy. Therefore, it is expected that the inhomogeneous stress affects the defect diffusion and their aggregation.

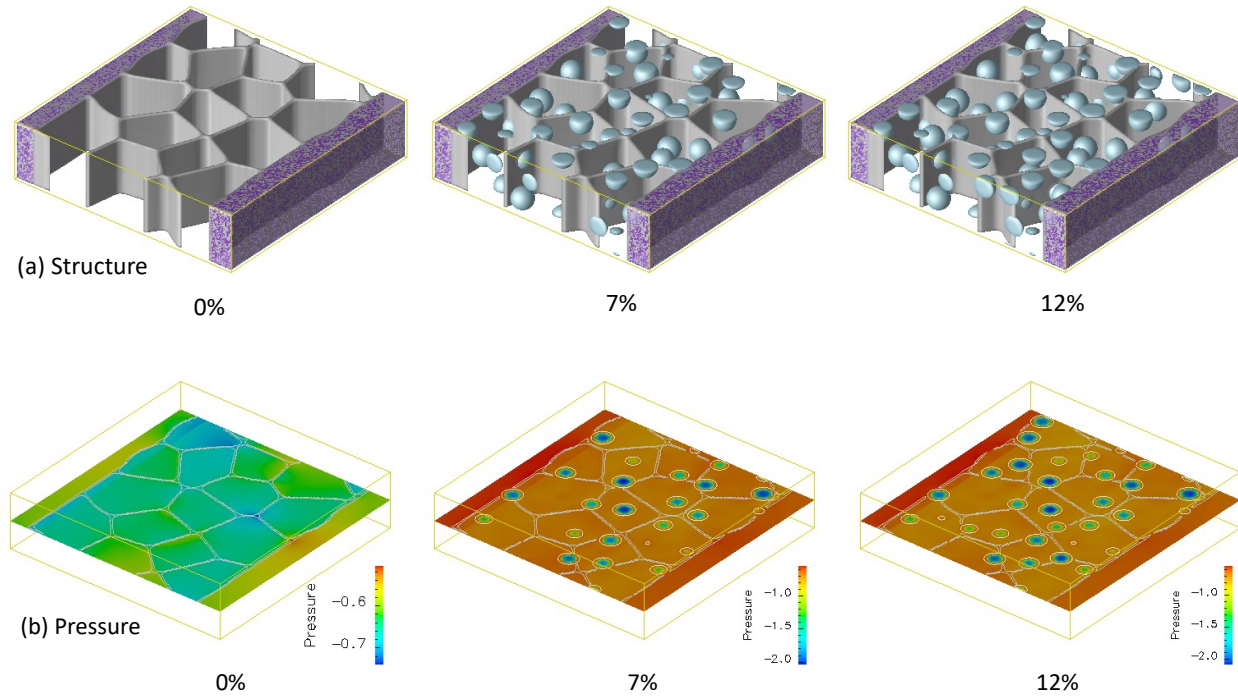


Figure 106. (a) Polycrystalline structures with different volume fraction of gas bubbles, (b) pressure distribution at applied stain $\epsilon_{33} = -0.01$.

Figure 107 shows the comparison of vacancy concentration between the case without applied strain and the case with applied strain after 30s radiation. The color bar shows the concentration. It is observed that vacancy concentration on GBs is higher than that inside grains. Comparing the color bar in horizontal figures, the vacancy concentration increases with the increase of gas-bubble volume fraction. Comparing the color bar in vertical figures, the vacancy concentration decreases with the applied compressive strain. Comparing the pressure distribution in Figure 106b and the vacancy concentration in Figure 107b, we could find certain correlations between the highest pressure (negative) and lowest vacancy concentration. However, general tendency that a compressive stress reduces the vacancy concentration exists. Interstitials have much lower concentration than vacancy. It is found that effect of pressure on interstitial aggregation is negligible.

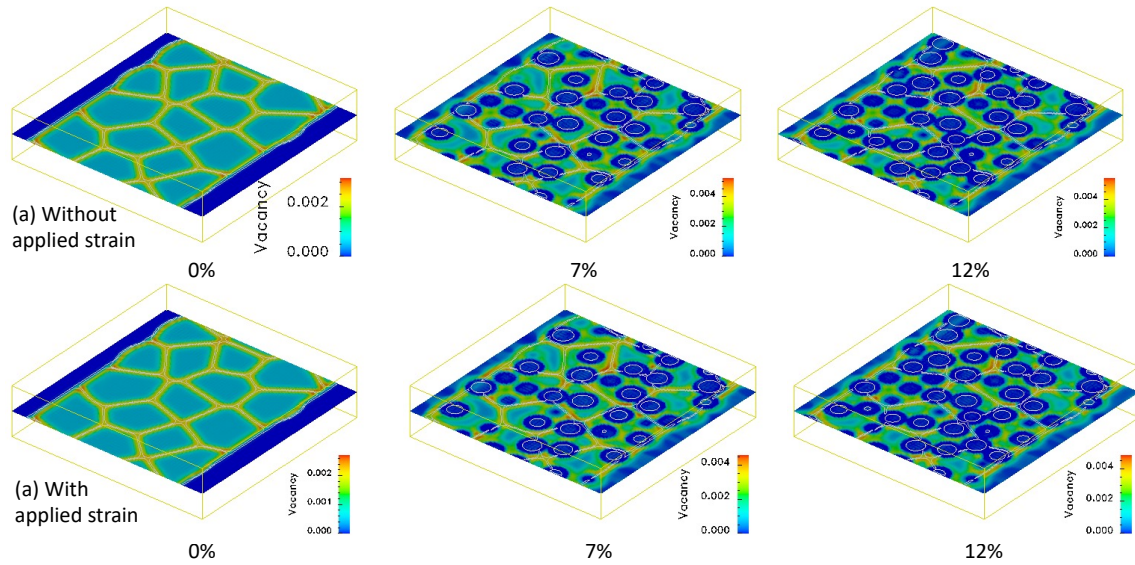


Figure 107. Vacancy concentration distribution on the middle plane of the simulation cell after 30s radiation. (a) in the case without applied strain, and (b) in the case with applied strain $\epsilon_{33} = -0.01$.

The simulations about the effect of elastic-plastic deformation on gas-bubble swelling has not been completed. In addition, the uncertain thermodynamic and kinetic properties cause a broad model parameter space which make the systematic study difficulty. With the more reliable thermodynamic and kinetic properties assessed by this research team, we will continue to quantify the model parameters and have more systematic investigation in FY-22.

2.9.5 Conclusions and Remarks

In this work, we developed a mesoscale model of gas-bubble swelling and elastic-plastic deformation in a polycrystalline UMo with a Zr layer. The model integrates (1) spatial-dependent cluster-dynamics model of radiation defect evolution; PF model of non-equilibrium gas-bubble evolution; and elastic-plastic deformation under a crystal-plasticity framework. The flow chart of the model is illustrated in Figure 97. The model has several features. For example, the radiation defects including U and Mo interstitial, U and Mo vacancy, vacancy and interstitial clusters, and fission-gas atoms Xe are considered. The lattice mismatch between the host atom (U) and a defect is described by a stress-free strain tensor. It enables one to consider stress-driven diffusion of solutes and vacancies which is one of the creep mechanisms. The Xe concentration inside gas bubbles is determined by the gas-bubble size and absorbed Xe atoms. So, the model is able to describe the transition between over-pressured gas bubbles and voids which is determined by the local flux of vacancy and Xe to gas bubbles. The thermodynamic and kinetic properties of radiation defects are described in a function of order parameters which presents different phases including UMo, gas bubble, and Zr cladding. The inhomogeneous thermodynamic and kinetics properties evolve with gas-bubble and grain-structure evolution. Plastic strain rate-based crystal plasticity is employed to describe the elastic-plastic deformation. It enables the capture of the effect of anisotropic mechanical properties such as grain orientation and individual slip system on elastic-plastic deformation and creep. In summary, this is a physics-based model with a multiphysics coupling of radiation damage, gas-bubble swelling, stress-driven diffusion creep, and elastic-plastic deformation. The model can be used to study the effect of radiation conditions, initial grain structures, and thermodynamic and kinetic properties of radiation defects on defect accumulation, gas-bubble swelling, stress-driven diffusion creep, and elastic-plastic deformation.

With the developed model, we simulated the effect of gas-bubble structures (different volume fraction and internal pressure) on stress-strain curves and the effect of local stress fields on gas-bubble evolution. The results show that (1) the effective Young's modulus decreases with the increase of gas-bubble volume fraction; (2) the yield stress decreases with the increase of gas-bubble volume fraction; and (3) the hardening coefficient increases with the increase of gas-bubble volume fraction, especially for gas bubbles with higher internal pressure. The effect of FR, defect diffusivity inhomogeneity, gas-bubble structure and stresses on defect evolution and aggregation are simulated with the integrated model. The results show that interstitial quickly reaches a steady state, but vacancy concentration does not reach a steady state. The vacancy concentration strongly depends on FR, gas-bubble structure, defect diffusivity, and stresses.

The results demonstrate that the developed model is capable of studying the dynamic interaction among radiation defect and defect cluster evolution, elastic-plastic deformation, and evolving gas bubbles, and assessing the effect of gas bubbles on the mechanical response (i.e., stress-strain curves under elastic-plastic deformation). In the simulations, the time step is determined by the grid size and the largest diffusivity of defects. The parametric studies assumed that the interstitial diffusivity is only one order magnitude higher than Xe diffusivity to speed up the simulations. However, if interstitial diffusivity or defect diffusivity on GBs are several order magnitudes higher than Xe diffusivity, we have to use a much smaller time step. So large-scale simulations are required to capture the microstructure evolution in a representative volume of monolithic fuels and to reach the FD of interest. In FY-22, we will complete the effect of thermodynamic and kinetic properties and fission conditions on elastic-plastic deformation and gas-bubble swelling with the more reliable thermodynamic and kinetic properties assessed by our research team.

2.10 Atomistic Modeling to Support Mesoscale Creep Models

Irradiation creep models rely on the fundamental behavior of point defects in a stress field. How that applied stress field affects diffusion or equilibrium concentrations of defects will in turn affect the time- and stress-dependent evolution of the material system. How point defect properties vary as a function of applied pressure is largely unknown for U-Mo systems. It has been shown in Fe [192] that application of pressure can significantly affect both the formation energy of defects and their generation under irradiation. In this work, we study how the application of hydrostatic tension and compression affects the formation energy and diffusion coefficient of interstitials and vacancies in U-Mo as a function of pressure, temperature, and composition.

2.10.1 Computational Details

MD simulations are performed utilizing the LAMMPS [53] software package and the U-Mo ADP [55]. A 14x14x14 supercell consisting of 5,488 atoms is constructed in a body-centered cubic (bcc) structure. Relaxation is performed in an NPT-ensemble, relaxing each x, y, and z component individually, with a damping parameter of 0.1. A Nose-Hoover thermostat is utilized with the damping parameter set to 0.1 ps. Systems are investigated over a range of temperatures, from 600 K up to 1,200 K, in increments of 200 K. This temperature range was chosen due to the inherent properties of the potential, in that below 600 K γ U becomes mechanically unstable and above 1,200 K the crystal structure is approaching the melting point. Systems are relaxed for 100 ps, with volumes averaged over the final 50 ps. The equilibration is performed at a given pressure, ranging from -10 kbar to +10 kbar (-1 GPa to +1 GPa) in increments of 5 kbar. This pressure range should exceed any expected stress state of the fuel and as such should present the possibilities of extreme behavior on defect evolution. Additionally, trends in behavior can be determined and explored at the pressures of interest. Eight individual compositions are investigated, including bcc U and bcc Mo, U-5Mo, U-10Mo, U-15Mo, U-30Mo, U-50Mo, and U-70Mo. All compositions are given in weight percent unless otherwise noted. This variation in composition allows for analysis for a wide range of U-Mo systems, including all relevant compositions in monolithic fuel.

Following the relaxation, the system is scaled to the averaged volume as determined from the NPT simulation. A relaxation of 50 ps is performed, the final 25 ps of which is utilized to determine average energies. A defect (vacancy or interstitial) is then inserted into the system and allowed to evolve for 50 ps, the final 25 ps of which is utilized to determine average energies. For an alloy composition, a proportional number of atoms are either removed or inserted, depending on the defect type, to closely maintain the stoichiometry of the system. For interstitials, an atom is randomly deposited into the supercell, provided that no other atom is within 1.5 Å, allowing for a random sampling of the entire supercell and all possible local configurational environments. To ensure statistical certainty of the results, 2,000 simulations for each defect type, pressure, and temperature are performed.

The formation energy is defined as

$$E_f = E_f^{def} - \frac{n \pm 1}{n} E_f^{bulk}$$

where n is the total number of atoms in the system with no defects and E_f^{bulk} or E_f^{def} is defined as

$$E_f^{def/bulk} = E^* - N_U E_U - N_{Mo} E_{Mo}$$

where E^* is the total energy of the system either with or without a defect, N_U is the number of uranium atoms in the system, E_U is the energy per atom of U, N_{Mo} is the number of molybdenum atoms in the system, and E_{Mo} is the energy per atom of Mo. The energy is defined for a given temperature and pressure, according to the system of interest.

The diffusion coefficient as a function of temperature and pressure is determined for the same sets of pressures as described above but only for temperatures at 800 K and above. This is due to the limited thermal diffusion at low temperatures on a MD time scale. The number of compositions is reduced to five (bcc U, U-5Mo, U-10Mo, U-15Mo, and bcc Mo) due to the computational cost associated with diffusion calculations. However, the primary concentration range of interest for U-Mo monolithic fuel is encompassed by this compositional range. An identical procedure is followed for the implementation of defects for investigation of diffusion as that which was followed for the investigation of defect energies. Following the defect insertion and relaxation, an additional evolution step of 10 ns was performed, over which the mean-squared displacement of the total system, and of each elemental species, was tracked. Over this 10 ns trajectory, three overlapping trajectories were obtained, each of length 6 ns, in order to subsample the trajectory and increase the statistics of the dataset. Additionally, five unique simulations are performed for each temperature, composition, and pressure to further ensure statistical significance of the results. This results in a standard error for defect energies of less than 0.05 eV.

2.10.2 Results

2.10.2.1 Point Defect Formation Energies

An example of the formation energy as a function of pressure for U-10Mo at 1200 K is shown in Figure 108. In correspondence with prior work [118] on defect energetics in U-Mo systems, the interstitial formation energy for the nominal case is less than 1 eV (0.62 eV), and the vacancy formation energy is significantly high than the interstitial formation energy (1.92 eV). Considering slight differences in methodology, this is reasonable agreement with the previous literature. From Figure 108, it can be seen that as vacancies and interstitials exhibit opposite trends as a function of applied pressure, as would be expected. As a crystal structure is compressed (positive pressure), atoms are closer together than in the equilibrium case. As such, it would be expected that a vacancy is more easily formed in the compressive state, and this is indeed observed. In the tensile state (negative pressure), atoms are farther apart than at equilibrium, and there is additional space between the atoms. In this case, it would be expected that it is comparatively easier for an interstitial to form, and this is indeed observed. There is a generally linear dependence of the formation energy on the applied pressure in the system, with vacancies exhibiting a negative slope and interstitials exhibiting a positive slope. The total magnitude change in the defect

formation energy for this case is 0.14 eV and 0.17 eV for interstitials and vacancies, respectively. This corresponds to approximately a 4-5X higher defect concentration across this pressure range.

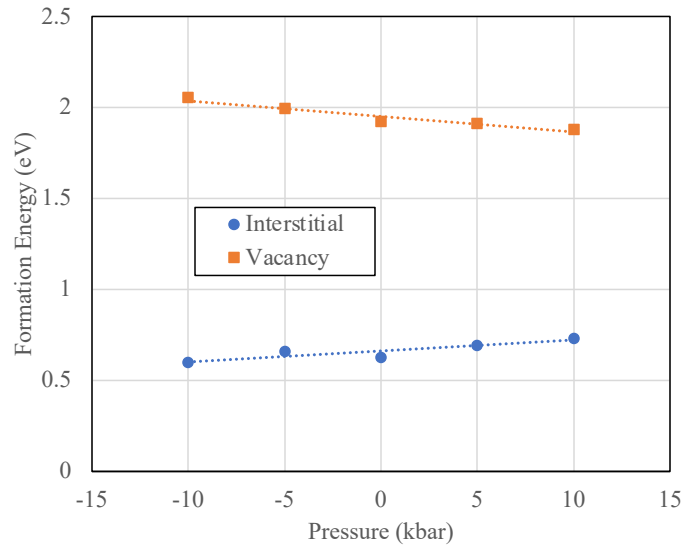


Figure 108. The interstitial and vacancy formation energy as a function of pressure for U-10Mo at 1200 K.

Generalizing to the U-Mo system, the interstitial and vacancy formation energies as a function of composition and pressure at 1200 K are shown in Figure 109 and Figure 110, respectively. The defect formation energies vary in a similar manner as a function of composition, with a minimum in the formation energy at 20–30 atomic percent. Interestingly, this is the target composition (22 atomic percent) for U-Mo monolithic fuel. Additionally, defect energies are at a maximum for the pure bcc Mo system for both interstitials and vacancies. The pressure sensitivity is not uniform for defect type and composition, in that interstitials are the most sensitive to pressure at intermediate compositions (40–60 atomic percent), while vacancies are the most sensitive to pressure in the U-rich regime. The trends of applied pressure observed in Figure 108 hold for all compositions.

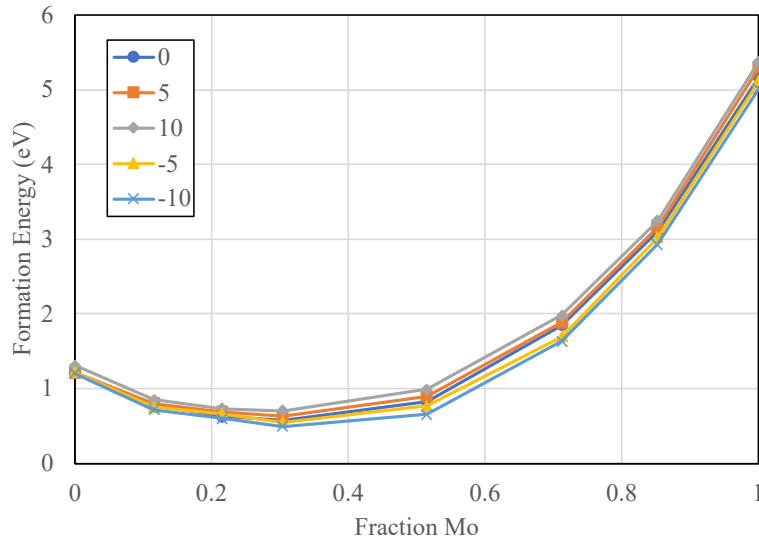


Figure 109. The interstitial formation energy as a function of composition for five applied pressures at 1,200 K.

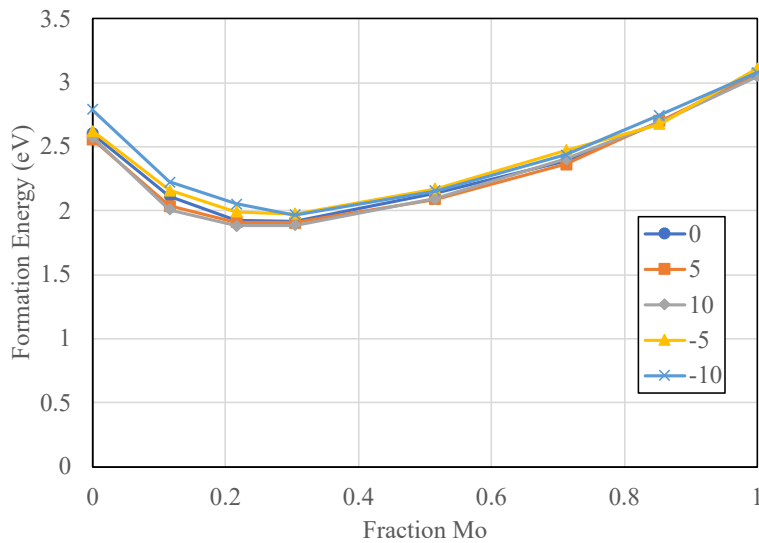


Figure 110. The vacancy formation energy as a function of composition for five applied pressures at 1,200 K.

The temperature dependence of the nominal pressure defect formation energies is shown in Figure 111. For interstitials, the temperature dependence undergoes an inflection point as a function of composition; in the U-rich regime, higher temperatures lead to higher interstitial energies, while in the Mo-rich regime higher temperatures lead to lower interstitial energies. This transition occurs at approximately 30 atomic percent or 15 weight percent Mo. For vacancies, the trend of defect energy with temperature is consistent across the compositional spectrum, in that higher temperatures lead to higher defect energies. The sensitivity of this temperature dependence varies with composition, with the most temperature-sensitive compositions in the U-rich regime. The application of pressure does affect the temperature dependence of defect formation energies nor does the temperature affect the trends of applied pressure on defect formation energies. However, it does appear that at lower temperatures, the effects of

pressure on interstitial formation energy are slightly dampened. Averaging over the entire compositional regime, an applied pressure of 10(-10) kbar at 1,200 K produces a 11(9)% increase(decrease) in the formation energy. At 600 K, an applied pressure of 10(-10) kbar produces a 6(7)% increase(decrease) in the formation energy.

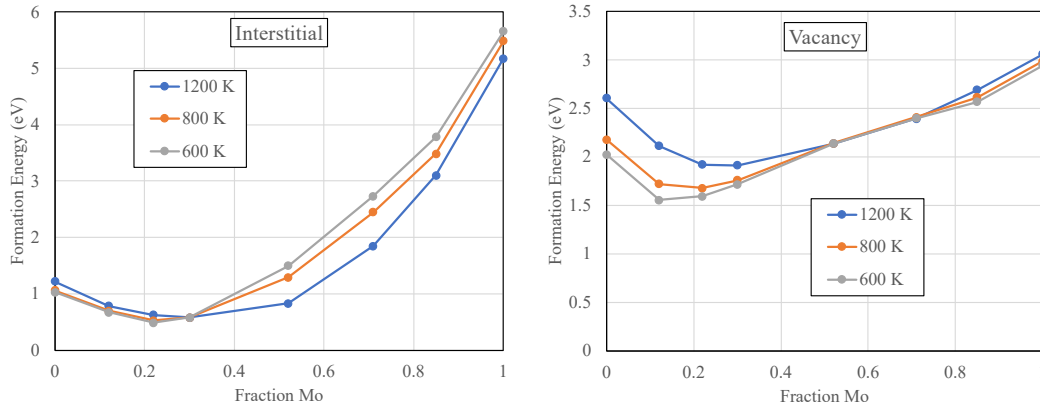


Figure 111. Temperature and compositional dependence of interstitial and vacancy formation energies in U-Mo.

It is found that generally, vacancies are much less sensitive to pressure than interstitials, and that sensitively is not significantly affected by the temperature of interest. On average, an applied pressure of 10(-10) kbar produces a 3% increase(decrease) in the vacancy formation energy. Since the magnitude of the vacancy formation energy is larger than the magnitude of the interstitial formation energy, the absolute (not relative) change in the defect formation energy with applied pressure is approximately the same for both interstitials and vacancies. Under reasonable applied bulk pressures below the yield point (<100 MPa), negligible deviations in the defect formations are observed. However, in circumstances where the pressures may be quite large (e.g., in the area surrounding a highly pressurized nanometer-sized bubble) statistically significant changes in the local defect formation energy could be observed, potentially altering FGB evolution and creep behaviors.

2.10.2.2 Point Defect Diffusion

The diffusion coefficient of interstitials and vacancies as a function of composition and temperature is shown in Figure 112. As previously observed [118], the defect diffusion coefficient varies as a function of composition, generally decreasing with an increasing content of Mo. However, there is an inflection point above U-15Mo for interstitials, as the interstitial diffusion coefficient for bcc Mo is higher than that of U-15Mo. For vacancies, there is no evident turnaround point. This is consistent with existing literature.

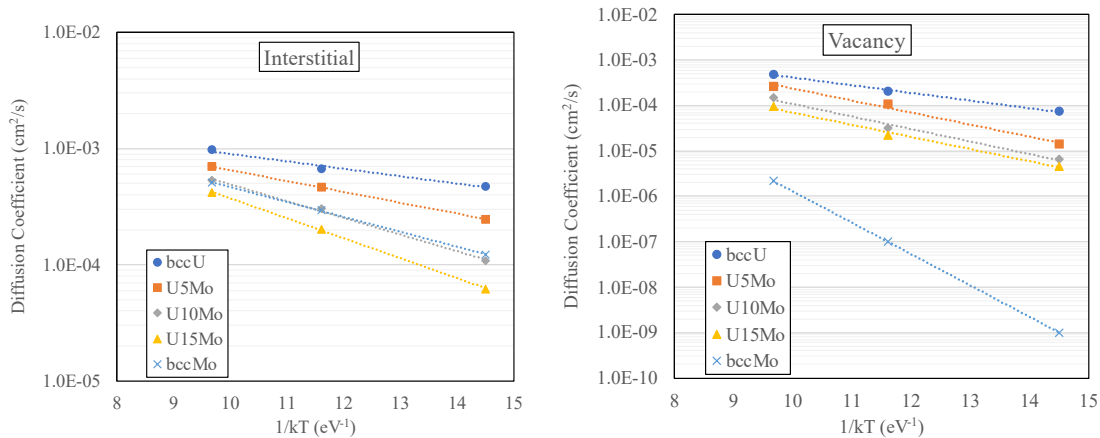


Figure 112. Diffusion coefficient of interstitials and vacancies as a function of temperature and composition.

The diffusion coefficient for vacancies and interstitials as a function of pressure in U-10Mo at three temperatures is shown in Figure 113. There is minimal variation as a function of applied pressure, but clear trends do present themselves. As the pressure increases and the system is in compression, the diffusion coefficient tends to decrease for both vacancies and interstitials. Thus, there is a clear distinction between pressure effects on the formation energy and pressure effects on the diffusion. The diffusion will consist of a series of components, including the migration barrier and the jump frequency. The migration barrier can be elucidated from the slope of the Arrhenius fit to the diffusion data. Such plots are shown in Figure 114 for U-10 Mo for all five pressures of interest.

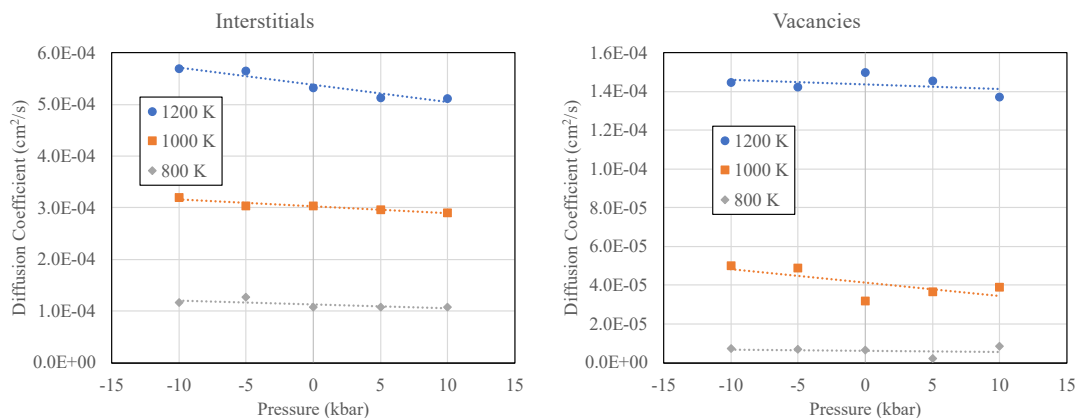


Figure 113. Diffusion coefficient of vacancies and interstitials as a function of pressure for U-10 Mo.

There is very minimal variation in the migration energy as a function of pressure. The difference between the maximum and minimum predicted migration barriers is 0.02 eV, which is less than the presumed statistical certainty. As such, it can be supposed that applied pressure produces no statistically significant change in the migration barrier. To cause a slight reduction in the diffusion coefficient, it is then assumed that a compressive state reduces the attempt frequency of both types of defects, thereby reducing the magnitude of the defect diffusion. However, such changes in the diffusion coefficient are on the order of less than 10% for 500 MPa (5 kbar). Additionally, it appears that the magnitude of the pressure dependence on interstitial diffusion decreases as the temperature decreases, taken from the slope in Figure 113. Given research reactor temperatures are below the investigated temperature range, expected pressures are significantly below the investigated range, and extrapolating the observed trends to

lower temperatures, it is presumed that effectively negligible effects on point defect diffusion from the system pressure will be observed and can thus be safely ignored.

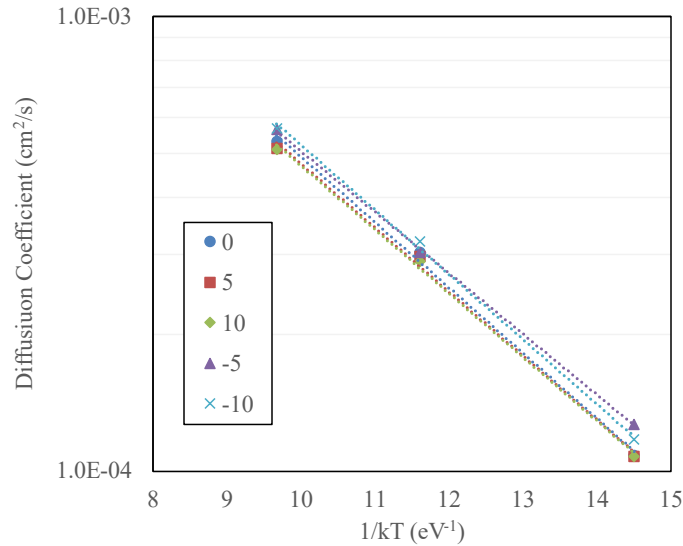


Figure 114. Arrhenius plots of the interstitial diffusion coefficient as a function of inverse temperature for U-10Mo. Pressure in the legend is in units of kbar.

2.10.3 Conclusions

This work investigated how the application of hydrostatic tension and compression affects the formation energy and diffusion coefficient of interstitials and vacancies in U-Mo as a function of pressure, temperature, and composition. On average, the maximum applied pressure of 10 kbar produces a 6% increase in the interstitial formation energy and a 3% decrease in the vacancy formation energy. Under reasonable applied bulk pressures below the yield point (<100 MPa), negligible deviations in the defect formations are observed. Also, applied pressures should yield negligible variation on point defect diffusion at relevant temperatures and pressures. There are impacts of the applied pressure on defect formation and diffusion, and clear trends can be observed, but these effects are sufficiently small, even at large pressures, that they likely can be neglected for practical purposes. However, in circumstances where the pressures may be quite large (e.g., in the area surrounding a highly pressurized nanometer-sized bubble) statistically significant changes in the local defect formation energy and diffusion coefficient could be observed, potentially altering FGB evolution and creep behaviors.

3. REVIEW AND FUTURE STUDY

3.1 Fiscal Year 2021 Review

In accordance with the microstructural modeling working group roadmap, as outlined in the FY-20 annual report, the tasks set forth for FY-21 were, with their respective laboratory and task-phenomena area:

1. INL/NCSU/Purdue – Geometric stability: gas diffusivity in different phases
2. INL/UW – Property degradation: fuel elasticity
3. INL/UW – Property degradation: degradation in fracture stress at interaction layers
4. INL – Property degradation: thermal conductivity
5. INL/Uoff – Microstructure data: historical samples characterization data assessment

6. PNNL – Geometric stability: irradiation-enhanced creep
7. ANL – Fabrication specification: effect of carbides on mechanical integrity
8. ANL – Fabrication specification: effect of variable enrichment in carbides
9. INL/ANL – Model integration: integration of microstructural work into fuel-performance modeling
10. ANL – FQ support: assessment of swelling at various fission rates and temperatures.

Task 1 was completed in FY-21, producing a complete description of diffusion including intrinsic, radiation enhanced, and radiation-driven diffusion for U, Mo, and Xe in UMo monolithic fuels. This task will be carried over to finalize publications. Task 2 demonstrated impressive success this year, generating significant information on the atomistic scale that has already been utilized within other modeling methodologies. Additionally, PF modeling has been developed which can provide the linkages of elasticity degradation to the engineering scale. Task 2 has inherent linkages to Task 3, and under Task 3, an integrated elasticity degradation model will be delivered in FY-22. Task 3 began in FY-21 and has shown significant progress within the first year. Task 4 was a tremendous success in FY-21, with a thermal conductivity degradation model delivered to the engineering-scale modeling team. This model will be refined with improved fundamental behaviors and variable microstructures in FY-22. Task 5 has led to a publication in FY-21 (to be submitted) and has generated stronger links between the characterization and modeling teams, which will continue to grow and expand in future years. Task 7 and 8 demonstrated impressive results in FY-21, generating novel information on how carbides fundamentally behave in UMo fuel, and their potential roles on fuel-performance evolution. Task 9 was a flagship task for this program, in that there is now a microstructurally informed fission-gas swelling model that has been implemented into the engineering-scale fuel-performance models. Full testing of this model will be completed in FY-22, and further refinements related to different microstructures and variables of interest will be implemented. Task 10 was completed through the DART code and generated key data that was utilized in Task 9. Task 10 allows for direct implementation of microstructural models generated in other task areas, prior to implementation in engineering-scale models.

Despite the numerous obstacles presented by the pandemic, significant progress has been made this FY by the Microstructural Modeling Working Group.

3.2 Publications

1. S.Y. Hu, B. Beeler, Gas bubble evolution in polycrystalline UMo fuels under elastic-plastic deformation: A phase-field model with crystal-plasticity, *Frontiers in Materials*, 8 (2021) doi:10.3389/fmats.2021.682667.
2. Z.G. Mei, B. Ye, A. M. Yacout, B. Beeler, “First-principles study of the interface structure, stability, and mechanical properties of γ -U/UC”, (manuscript under preparation, 2021).
3. B. Beeler, M.W.D. Cooper, Z.-G. Mei, D. Schwen, Y. Zhang, “Radiation driven diffusion in γ U-Mo,” *Journal of Nuclear Materials*, Volume 543 (2021) 152568.
4. G. Park, B. Beeler, M. Okuniewski, “An atomistic study of defect energetics and diffusion with respect to composition and temperature in γ U and γ U-Mo alloys,” *Journal of Nuclear Materials*, Volume 552 (2021) 152970.
5. S. Hu, W. Setyawan, B. Beeler, J. Gan, D. Burkes, “Defect cluster and nonequilibrium gas bubble associated growth in irradiated UMo fuels – A cluster dynamics and phase field model,” *Journal of Nuclear Materials*, Volume 542 (2020) 152441.
6. Z.-G. Mei, B. Ye, A. Yacout, B. Beeler, Y. Gao, “First-principles study of the surface properties of uranium carbides,” *Journal of Nuclear Materials*, Volume 542 (2020) 152257.

3.3 Conference Presentations

1. Hu S., and B. Beeler. 09/20/2021. "Mesoscale model of stress and radiation-driven microstructure and property evolution in UMo fuels." Abstract submitted to MiNES 2021, Pittsburgh, Pennsylvania. PNNL-SA-160935.
2. Hu S. 03/15/2021. "Effect of distributed gas bubbles on elastic-plastic deformation behavior in polycrystalline UMo." Presented by S. Hu at TMS 2021 Annual Meeting & Exhibition, Online, Washington. PNNL-SA-160394.
3. Z.G. Mei, B. Ye, A. M. Yacout, B. Beeler, "First-principles study of the interfaces between g-U and uranium carbide," Materials in Nuclear Energy Systems (MiNES) 2021 conference, Pittsburgh, Pennsylvania.
4. B. Beeler, P. Gyuchul, M. Cooper, Z.-G. Mei, D. Schwen, Y. Zhang, M. Okuniewski, "Constructing Multi-component Diffusion under Irradiation in U-Mo Alloys," TMS 2021 Annual Meeting & Exhibition, Online, Washington.

3.4 Fiscal Year 2022 Plan

The following sub-tasks are proposed to continue the ongoing efforts of the microstructural modeling working group to address the most important microstructural questions, provide practical guidance to the fabricator, and provide mechanistic inputs for the existing fuel-performance code:

1. Fabrication specification: Effects of Impurities on Fuel Performance: Si and Al (INL/PNNL)
2. Fabrication specification: Effect of U235 Enrichment in Carbides (ANL)
3. Property degradation: Degradation in Fracture Stress at Interaction Layers (INL)
4. Model integration: Integration of the Effect of U-235 Uniformity on Swelling into Fuel-Performance Model (INL)
5. Model integration: Integration of the Effect of U-235 Uniformity on Swelling (ANL)
6. Model integration: Assessment of Swelling with Different Fabrication Microstructure (PNNL)
7. Microstructure data: Comparison to Experimental Characterization Data: Uncertainty Analysis (ANL)

The following are carryover tasks from FY-21 which will be continued in FY-22.

1. Property degradation: Degradation in Fracture Stress at Interaction Layers (INL)
2. Model integration: Assessment of Swelling at Various Fission Rates (ANL)
3. Property degradation: Thermal Conductivity (INL)
4. Model integration: Integration of Microstructural Modeling (INL).

This task list is focused on providing fundamental materials and evolutionary models that describe key phenomena, implementing these models in an integrated fashion across time and length scales, as well as research locations, compared and validated against the most recent and standardized experimental data. This work will improve the basic knowledge of the fuel system and how it behaves in reactor, while also providing tangible benefits to improve the engineering-scale fuel-performance modeling.

A delayed deliverable—a reduced-order model describing elasticity degradation—will be completed in FY-22. Additional deliverables at the conclusion of FY-22 include an irradiation creep model that will be provided to both microstructural and fuel-performance modelers. The model for fission-gas swelling that was implemented into the engineering-scale fuel-performance simulations will be refined based upon further experimental and computational data. Finally, the thermal conductivity model will be refined to improve upon fundamental materials models and incorporate variable underlying microstructures.

In FY-23 and beyond this work will be continued, exploring additional effects such as the inclusion of other impurities, such as silicon. Additional microstructural support for FQ is anticipated for yet-to-be-determined phenomena, dependent upon the information from the MP-1 experiments and the requirements from engineering-scale fuel-performance models. FY-22–24 will also include the evaluation and validation of existing models comparing to MP-1, MP-2, and MP-ATR PIE information.

For reference, the updated microstructural modeling working group roadmap is provided in Figure 115.

Task	FY18	FY19	FY20	FY21	FY22	FY23	FY24
Geometric stability: Dimensional Change	Effect of gas bubble internal pressure on swelling during coarsening						
	Effect of secondary phases, interfaces and recrystallization on swelling kinetics						
	Effect of fission rate and fission density on swelling						
		Gas diffusivity in different phases					
		Irradiation enhanced creep					
Fabrication Specification: U235/Mo homogeneity and impurities; phase decomposition and recrystallization	U235 Uniformity: Variability and scoping studies						
	Mo uniformity: Phase decomposition and reversal and their effects on recrystallization and swelling						
			Effect of carbides on fuel integrity		Effect of U235 enrichment in carbides		
					Effect of other impurities: Al, Si, Cr		
Property Degradation			Elasticity				
			Thermal Conductivity				
				Fracture Stress			
Model integration and calibration			Integration of microstructural work into fuel performance modeling				
					Fuel qualification support		
					Comparison to Experimental Characterization Data		
			Summary Report				
Processing, Microstructure and Performance Data			Historical Samples Data Assessment				
			Summary Report				

Figure 115. Microstructural modeling working group roadmap.

4. CONCLUSIONS

This report summarized the microstructural-level fuel-performance modeling of U-Mo monolithic fuel under the USHPRR Program FQ pillar. The DART fuel-performance code has been updated to simulate U-10Mo monolithic fuel-swelling behavior during irradiation, further illustrating the importance of initial grain size and temperature of fuel-swelling behavior. A thermal conductivity degradation model was developed that incorporates the effects of point defects (vacancy and fission products), GBs, intergranular gas bubbles, and intragranular gas bubbles on heat transport. The degradation of elastic properties was investigated, with MD calculations informing the elastic constants of U-10Mo and AEH methods incorporating realistic microstructures to predict mechanical properties as a function of burnup. The degradation in fracture toughness in the interdiffusion interaction zone was investigated, illustrating the strongly plastic behavior of UMo and providing the basis for future development of a microstructure-dependent fracture degradation correlation. The research on the effect of carbides on mechanical properties and swelling showed that carbides have a minimal impact on the Young's modulus of the fuel, and that the FR effects from variable enrichments in carbides are minor but can accelerate gas-bubble swelling. The radiation-enhanced diffusion coefficients in UMo were calculated, illustrating that radiation-driven diffusion is likely the primary form of diffusion for Xe in UMo fuels. Historical characterization data was analyzed, illustrating variances in data collection methods and data types collected, and emphasized the need for standardization and increased communication and cooperation between the microstructural modeling and characterization teams. A microstructure-informed fission-gas swelling model was developed and implemented into the engineering-scale fuel-performance simulations, allowing for exploration of fuel behavior in off-normal conditions or outside of the existing parameter space. The irradiation creep model was refined to study the effect of gas-bubble structures on deformation, including point defect behavior, allowing for the development of an integrated irradiation creep model in the future. Finally, the behavior of point defects under applied strain was investigated to support the irradiation creep model, indicating that only in highly pressurized conditions will the energetics or kinetics of point defects in UMo be significantly affected.

This work has been conducted as a coordinated effort involving a team of modeling experts across ANL, INL, PNNL, University of Purdue, University of Wisconsin-Madison, and North Carolina State University. The multiscale modeling and simulation effort is generating knowledge and data that enhance the fundamental understanding of fuel behavior and ultimately reduce risks and fuel cost by maximizing achievable burnup and potentially relaxing fabrication specifications.

5. REFERENCES

- [1] M.K. Meyer, J. Gan, J.F. Jue, D.D. Keiser, E. Perez, A. Robinson, D.M. Wachs, N. Woolstenhulme, G.L. Hofman, Y.S. Kim, IRRADIATION PERFORMANCE OF U-Mo MONOLITHIC FUEL, *Nucl. Eng. Technol.* 46 (2014) 169–182. <https://doi.org/10.5516/NET.07.2014.706>.
- [2] M. Meyer, B. Rabin, J. Cole, I. Glagolenko, W. Jones, J.F. Jue, D.D. Keiser, C. Miller, G. Moore, H. Ozaltun, F. Rice, A. Robinson, D. Wachs, W. Williams, N. Woolstenhulme, Research and Development Report for U-Mo Monolithic Fuel, 2017.
- [3] J. Rest, The DART dispersion analysis research tool: a mechanistic model for predicting fission-product-induced swelling of aluminum dispersion fuels, 1995.
- [4] B. Ye, J. Rest, Y.S.S. Kim, G. Hofman, B. Dionne, DART Analysis of Irradiation Behavior of U-Mo/Al Dispersion Fuels, *Nucl. Technol.* 191 (2015) 27–40. <https://doi.org/10.13182/NT14-56>.
- [5] B. Ye, G.L. Hofman, A. Leenaers, A. Bergeron, V. Kuzminov, S. den Berghe, Y.S. Kim, H. Wallin, A modelling study of the inter-diffusion layer formation in U-Mo/Al dispersion fuel plates at high power, *J. Nucl. Mater.* 499 (2018) 191–203. <https://doi.org/10.1016/j.jnucmat.2017.11.035>.
- [6] S. Hu, V. Joshi, C.A. Lavender, A Rate-Theory–Phase-Field Model of Irradiation-Induced Recrystallization in UMo Nuclear Fuels, Springer, 2017. <https://doi.org/10.1007/S11837-017->

- 2611-4.
- [7] Z.G. Mei, L. Liang, A.M. Yacout, First-principles study of the surface properties of U-Mo system, *Comput. Mater. Sci.* 142 (2018) 355–360. <https://doi.org/10.1016/J.COMMATSCI.2017.10.033>.
- [8] B. Beeler, M.W.D. Cooper, Z.G. Mei, D. Schwen, Y. Zhang, Radiation driven diffusion in γ U-Mo, *J. Nucl. Mater.* 543 (2021) 152568. <https://doi.org/10.1016/J.JNUCMAT.2020.152568>.
- [9] H. Ozaltun, P.G. Medvedev, B.H. Rabin, Assessment of Failure Modes of Monolithic Fuel Plates, in: American Society of Mechanical Engineers Digital Collection, 2018. <https://doi.org/10.1115/ICONE26-82437>.
- [10] H. Ozaltun, B.H. Rabin, Thermo-Mechanical Performance Assessment of Selected Plates From MP-1 Low Power Experiments, in: American Society of Mechanical Engineers Digital Collection, 2019. <https://doi.org/10.1115/IMECE2018-86010>.
- [11] J. Rest, GRASS-SST: A comprehensive, mechanistic model for the prediction of fission-gas behavior in UO₂-base fuels during steady-state and transient conditions, 1978.
- [12] Y.S. Kim, G.L. Hofman, J.S. Cheon, Recrystallization and fission-gas-bubble swelling of U-Mo fuel, *J. Nucl. Mater.* 436 (2013) 14. <https://doi.org/10.1016/j.jnucmat.2013.01.291>.
- [13] A. Leenaers, W. Van Renterghem, S. Van Den Berghe, High burn-up structure of U(Mo) dispersion fuel, *J. Nucl. Mater.* 476 (2016) 218–230. <https://doi.org/10.1016/J.JNUCMAT.2016.04.035>.
- [14] D. Edwards, C. Henager, R. Ermi, D. Burkes, A. Scheme-Kohm, D. Senior, N. Overman, Characterization of U-Mo Foils for AFIP-7, n.d.
- [15] J.F. Jue, D. Keiser, J. Madden, T. Trombridge, A. Winston, Characterization summary report on grain size and Mo distribution in monolithic U-Mo fuels, 2018.
- [16] D.R. Olander, D. Wongsawaeng, Re-resolution of fission gas – A review: Part I. Intragranular bubbles, *J. Nucl. Mater.* 354 (2006) 94–109. <https://doi.org/10.1016/j.jnucmat.2006.03.010>.
- [17] D.R. Olander, P. Van Uffelen, On the role of grain boundary diffusion in fission gas release, *J. Nucl. Mater.* 288 (2001) 137–147. [https://doi.org/10.1016/S0022-3115\(00\)00725-X](https://doi.org/10.1016/S0022-3115(00)00725-X).
- [18] J. Rest, The effect of irradiation-induced gas-atom re-resolution on grain-boundary bubble growth, *J. Nucl. Mater.* 321 (2003) 305–312. [https://doi.org/10.1016/S0022-3115\(03\)00303-9](https://doi.org/10.1016/S0022-3115(03)00303-9).
- [19] R.S. Nelson, The stability of gas bubbles in an irradiation environment, *J. Nucl. Mater.* 31 (1969) 153–161. [https://doi.org/10.1016/0022-3115\(69\)90189-5](https://doi.org/10.1016/0022-3115(69)90189-5).
- [20] K. Govers, C.L. Bishop, D.C. Parfitt, S.E. Lemehov, M. Verwerft, R.W. Grimes, Molecular dynamics study of Xe bubble re-resolution in UO₂, *J. Nucl. Mater.* 420 (2012) 282–290. <https://doi.org/10.1016/J.JNUCMAT.2011.10.010>.
- [21] J.A. Turnbull, The distribution of intragranular fission gas bubbles in UO₂ during irradiation, *J. Nucl. Mater.* 38 (1971) 203–212. [https://doi.org/10.1016/0022-3115\(71\)90044-4](https://doi.org/10.1016/0022-3115(71)90044-4).
- [22] J.A. Turnbull, C.A. Friskney, J.R. Findlay, F.A. Johnson, A.J. Walter, The diffusion coefficients of gaseous and volatile species during the irradiation of uranium dioxide, *J. Nucl. Mater.* 107 (1982) 168–184. [https://doi.org/10.1016/0022-3115\(82\)90419-6](https://doi.org/10.1016/0022-3115(82)90419-6).
- [23] K. Govers, S. Lemehov, M. Verwerft, In-pile Xe diffusion coefficient in UO₂ determined from the modeling of intragranular bubble growth and destruction under irradiation, *J. Nucl. Mater.* 374 (2008) 461–472. <https://doi.org/10.1016/j.jnucmat.2007.10.005>.
- [24] M.L. Bleiberg, L.J. Jones, B. Lustman, Phase Changes in Pile-Irradiated Uranium-Base Alloys, *J. Appl. Phys.* 27 (1956) 1270–1283. <https://doi.org/10.1063/1.1722250>.
- [25] J.F. Ziegler, SRIM-2003, *Nucl. Instruments Methods Phys. Res. Sect. B Beam Interact. with Mater. Atoms.* 219–220 (2004) 1027–1036. <https://doi.org/10.1016/j.nimb.2004.01.208>.
- [26] D. Olander, Fundamental aspects of nuclear reactor fuel elements, 1976.
- [27] J. Rest, G.L. Hofman, Y.S. Kim, Analysis of intergranular fission-gas bubble-size distributions in irradiated uranium–molybdenum alloy fuel, *J. Nucl. Mater.* 385 (2009) 563–571. <https://doi.org/10.1016/j.jnucmat.2009.01.001>.
- [28] J. Rest, An analytical study of gas-bubble nucleation mechanisms in uranium-alloy nuclear fuel at high temperature, *J. Nucl. Mater.* 402 (2010) 179–185.

- <https://doi.org/10.1016/j.jnucmat.2010.05.022>.
- [29] E.E. Gruber, Calculated Size Distributions for Gas Bubble Migration and Coalescence in Solids, *J. Appl. Phys.* 38 (1967) 243–250. <https://doi.org/10.1063/1.1708962>.
- [30] C. Ronchi, Extrapolated equation of state for rare gases at high temperatures and densities, *J. Nucl. Mater.* 96 (1981) 314–328. [https://doi.org/10.1016/0022-3115\(81\)90575-4](https://doi.org/10.1016/0022-3115(81)90575-4).
- [31] M. Speight, A Calculation on the Migration of Fission Gas in Material Exhibiting Precipitation and Re-solution of Gas Atoms Under Irradiation, *Nucl. Sci. Eng.* 37 (1969) 180–185. <https://doi.org/10.13182/NSE69-A20676>.
- [32] J.C. Fisher, Calculation of Diffusion Penetration Curves for Surface and Grain Boundary Diffusion, *J. Appl. Phys.* 22 (1951) 74–77. <https://doi.org/10.1063/1.1699825>.
- [33] K. Maschke, H. Overhof, P. Thomas, A Note on Percolation Probabilities, *Phys. Status Solidi.* 60 (1973) 563–566. <https://doi.org/10.1002/pssb.2220600211>.
- [34] Y.S.Y.S. Kim, G.L.L. Hofman, J.S.S. Cheon, Recrystallization and fission-gas-bubble swelling of U–Mo fuel, *J. Nucl. Mater.* 436 (2013) 14–22. <https://doi.org/10.1016/j.jnucmat.2013.01.291>.
- [35] J. Rest, T. Allen, R. Stoller, S. Yamanaka, R. Konings, *Comprehensive Nuclear Materials*, Elsevier Science, 2011.
- [36] A.B. Robinson, W.J. Williams, W.A. Hanson, B.H. Rabin, N.J. Lybeck, M.K. Meyer, Robinson, A., Williams, W., Hanson, W., Rabin, B., Lybeck, N., Meyer, M., Swelling of U-Mo Monolithic Fuel: Developing a Predictive Swelling Correlation under Research Reactor Conditions, *J. Nucl. Mater.* 544 (2021) 152703. <https://doi.org/10.1016/j.jnucmat.2020.152703>.
- [37] Y.S. Kim, G.L. Hofman, J. Rest, Characterization of Intergranular Fission Gas Bubbles in U-MO Fuel, Argonne National Laboratory, 2008. <https://doi.org/10.2172/929261>.
- [38] L. Santaló, *Integral Geometry and Geometric Probability*, (Encyclopedia of Mathematics and Its Applications), Addison-Wesley Publishing Company, 1976.
- [39] Y.S. Kim, G.L. Hofman, Fission product induced swelling of U–Mo alloy fuel, *J. Nucl. Mater.* 419 (2011) 291–301. <https://doi.org/10.1016/j.jnucmat.2011.08.018>.
- [40] D. Perez, M. Lillo, G. Chang, N. Woolstenhulme, RERTR-12 Insertion 1 Irradiation Summary Report, 2012.
- [41] D. Perez, G. Chang, D. Wachs, G. Roth, RERTR-12 Insertion 2 Irradiation Summary Report, 2012.
- [42] S. Zhou, R. Jacobs, Y. Zhang, C. Jiang, D. Morgan, Combined ab-initio and empirical model for irradiated metal alloys with a focus on uranium alloy fuel thermal conductivity, *J. Nucl. Mater.* 549 (2021) 152891. <https://doi.org/10.1016/j.jnucmat.2021.152891>.
- [43] Y. Jiang, Y. Xin, W. Liu, Z. Sun, P. Chen, D. Sun, M. Zhou, X. Liu, D. Yun, Phase-field simulation of radiation-induced bubble evolution in recrystallized U–Mo alloy, *Nucl. Eng. Technol.* (2021).
- [44] P.G. Lucuta, H. Matzke, I.J. Hastings, A pragmatic approach to modelling thermal conductivity of irradiated UO₂ fuel: Review and recommendations, *J. Nucl. Mater.* 232 (1996) 166–180. [https://doi.org/10.1016/S0022-3115\(96\)00404-7](https://doi.org/10.1016/S0022-3115(96)00404-7).
- [45] S. Van den Berghe, W. Van Renterghem, A. Leenaers, Transmission electron microscopy investigation of irradiated U–7 wt%Mo dispersion fuel, *J. Nucl. Mater.* 375 (2008) 340–346. <https://doi.org/10.1016/J.JNUCMAT.2007.12.006>.
- [46] J. Maxwell, *A treatise on electricity and magnetism*, Oxford, Clarendon press, 1873.
- [47] J.K. Carson, S.J. Lovatt, D.J. Tanner, A.C. Cleland, Thermal conductivity bounds for isotropic, porous materials, *Int. J. Heat Mass Transf.* 48 (2005) 2150–2158. <https://doi.org/10.1016/J.IJHEATMASSTRANSFER.2004.12.032>.
- [48] M.E. Cunningham, K.L. Peddicord, Heat conduction in spheres packed in an infinite regular cubical array, *Int. J. Heat Mass Transf.* 24 (1981) 1081–1088. [https://doi.org/10.1016/0017-9310\(81\)90157-5](https://doi.org/10.1016/0017-9310(81)90157-5).
- [49] T.H. Bauer, A general analytical approach toward the thermal conductivity of porous media, *Int. J. Heat Mass Transf.* 36 (1993) 4181–4191. [https://doi.org/10.1016/0017-9310\(93\)90080-P](https://doi.org/10.1016/0017-9310(93)90080-P).

- [50] M.R. Tonks, X.-Y.Y. Liu, D. Andersson, D. Perez, A. Chernatynskiy, G. Pastore, C.R. Stanek, R. Williamson, Development of a multiscale thermal conductivity model for fission gas in UO₂, *J. Nucl. Mater.* 469 (2016) 89–98. <https://doi.org/10.1016/j.jnucmat.2015.11.042>.
- [51] J.A. Horak, T.H. Blewitt, Fast neutron irradiation induced resistivity in metals, *Phys. Status Solidi.* 9 (1972) 721–730. <https://doi.org/10.1002/pssa.2210090238>.
- [52] B. Ye, J. Rest, Y.S. Kim, A Description of the Mechanistic DART-THERMAL Dispersion Fuel Performance Code and Application to Irradiation Behavior Analysis of U-Mo/Al, Argonne, IL (United States), 2013. www.anl.gov.
- [53] S. Plimpton, Fast Parallel Algorithms for Short-Range Molecular Dynamics, *J. Comput. Phys.* 117 (1995) 1–19. <https://doi.org/10.1006/JCPH.1995.1039>.
- [54] D.E. Smirnova, A.Y. Kuksin, S. V Starikov, V. V Stegailov, Z. Insepov, J. Rest, A.M. Yacout, A ternary EAM interatomic potential for U–Mo alloys with xenon, *Model. Simul. Mater. Sci. Eng.* 21 (2013) 035011. <https://doi.org/10.1088/0965-0393/21/3/035011>.
- [55] S. V. Starikov, L.N. Kolotova, A.Y. Kuksin, D.E. Smirnova, V.I. Tseplyaev, Atomistic simulation of cubic and tetragonal phases of U-Mo alloy: Structure and thermodynamic properties, *J. Nucl. Mater.* 499 (2018) 451–463. <https://doi.org/10.1016/J.JNUCMAT.2017.11.047>.
- [56] B. Beeler, Private Communications, (2021).
- [57] Y. Zhang, A. Manzoor, C. Jiang, D. Aidhy, D. Schwen, A statistical approach for atomistic calculations of vacancy formation energy and chemical potentials in concentrated solid-solution alloys, *Comput. Mater. Sci.* 190 (2021) 110308. <https://doi.org/10.1016/j.commatsci.2021.110308>.
- [58] S. Hu, D.E. Burkes, C.A. Lavender, D.J. Senior, W. Setyawan, Z. Xu, Formation mechanism of gas bubble superlattice in UMo metal fuels: Phase-field modeling investigation, *J. Nucl. Mater.* 479 (2016) 202–215. <https://doi.org/10.1016/J.JNUCMAT.2016.07.012>.
- [59] B. Beeler, J. Cole, W. Frazier, Y. Gao, I. Glagolenko, G. Hofman, S. Hu, V. Joshi, C. Lavender, N. Lombardo, S. Masengale, Z.-G. Mei, A. Oaks, M. Okuniewski, G. Park, K. Verner, A. Yacout, B. Ye, Y. Zhang, Microstructural-Level Fuel Performance Modeling of U-Mo Monolithic Fuel, 2020.
- [60] P.W. Chung, K.K. Tamma, R.R. Namburu, Homogenization of Temperature-Dependent Thermal Conductivity in Composite Materials, *J. Thermophys. Heat Transf.* 15 (2001) 10–17. <https://doi.org/10.2514/2.6590>.
- [61] X.-M. Bai, M.R. Tonks, Y. Zhang, J.D. Hales, Multiscale modeling of thermal conductivity of high burnup structures in UO₂ fuels, *J. Nucl. Mater.* 470 (2016) 208–215. <https://doi.org/10.1016/j.jnucmat.2015.12.028>.
- [62] J. Pinho-da-Cruz, J.A. Oliveira, F. Teixeira-Dias, Asymptotic homogenisation in linear elasticity. Part I: Mathematical formulation and finite element modelling, *Comput. Mater. Sci.* 45 (2009) 1073–1080. <https://doi.org/10.1016/J.COMMATSCI.2009.02.025>.
- [63] J.A. Oliveira, J. Pinho-da-Cruz, F. Teixeira-Dias, Asymptotic homogenisation in linear elasticity. Part II: Finite element procedures and multiscale applications, *Comput. Mater. Sci.* 45 (2009) 1081–1096. <https://doi.org/10.1016/J.COMMATSCI.2009.01.027>.
- [64] J.D. Hales, M.R. Tonks, K. Chockalingam, D.M. Perez, S.R. Novascone, B.W. Spencer, R.L. Williamson, Asymptotic expansion homogenization for multiscale nuclear fuel analysis, *Comput. Mater. Sci.* 99 (2015) 290–297. <https://doi.org/10.1016/j.commatsci.2014.12.039>.
- [65] N. Moelans, B. Blanpain, P. Wollants, Quantitative Phase-Field Approach for Simulating Grain Growth in Anisotropic Systems with Arbitrary Inclination and Misorientation Dependence, *Phys. Rev. Lett.* 101 (2008) 25502. <https://doi.org/10.1103/PhysRevLett.101.025502>.
- [66] L.K. Aagesen, D. Schwen, M.R. Tonks, Y. Zhang, Phase-field modeling of fission gas bubble growth on grain boundaries and triple junctions in UO₂ nuclear fuel, *Comput. Mater. Sci.* 161 (2019) 35–45. <https://doi.org/10.1016/j.commatsci.2019.01.019>.
- [67] L.K. Aagesen, D. Andersson, B.W. Beeler, M.W.D. Cooper, K.A. Gamble, Y. Miao, G. Pastore, M.R. Tonks, Phase-field simulations of intergranular fission gas bubble behavior in U₃Si₂ nuclear fuel, *J. Nucl. Mater.* 541 (2020). <https://doi.org/10.1016/j.jnucmat.2020.152415>.

- [68] L. Liang, Z.-G. Mei, Y. Soo Kim, M. Anitescu, A.M. Yacout, Three-dimensional phase-field simulations of intragranular gas bubble evolution in irradiated {U}-Mo fuel, *Comput. Mater. Sci.* 145 (2018) 86–95. <https://doi.org/10.1016/j.commatsci.2017.12.061>.
- [69] L.K. Aagesen, Y. Gao, D. Schwen, K. Ahmed, Grand-potential-based phase-field model for multiple phases, grains, and chemical components, *Phys. Rev. E*. 98 (2018) 23309. <https://doi.org/10.1103/PhysRevE.98.023309>.
- [70] B. Beeler, Y. Zhang, Y. Gao, An atomistic study of grain boundaries and surfaces in γ U-Mo, *J. Nucl. Mater.* 507 (2018) 248–257. <https://doi.org/10.1016/j.jnucmat.2018.05.007>.
- [71] Z. Xiao, Y. Wang, S. Hu, Y. Li, S.-Q. Shi, A quantitative phase-field model of gas bubble evolution in UO₂, *Comput. Mater. Sci.* 184 (2020) 109867. <https://doi.org/10.1016/j.commatsci.2020.109867>.
- [72] Y. Wang, Z. Xiao, S. Hu, Y. Li, S.Q. Shi, A phase field study of the thermal migration of gas bubbles in UO₂ nuclear fuel under temperature gradient, *Comput. Mater. Sci.* 183 (2020) 109817. <https://doi.org/10.1016/J.COMMATSCI.2020.109817>.
- [73] S. Hu, A.M. Casella, C.A. Lavender, D.J. Senor, D.E. Burkes, Assessment of effective thermal conductivity in U–Mo metallic fuels with distributed gas bubbles, *J. Nucl. Mater.* 462 (2015) 64–76. <https://doi.org/10.1016/j.jnucmat.2015.03.039>.
- [74] L.K. Aagesen, D. Schwen, K. Ahmed, M.R. Tonks, Quantifying elastic energy effects on interfacial energy in the Kim-Kim-Suzuki phase-field model with different interpolation schemes, *Comput. Mater. Sci.* 140 (2017) 10–21. <https://doi.org/10.1016/j.commatsci.2017.08.005>.
- [75] V.I. Levitas, M. Javanbakht, Phase-field approach to martensitic phase transformations: Effect of martensite–martensite interface energy, *Int. J. Mater. Res.* 102 (2011) 652–665. <https://doi.org/10.3139/146.110529>.
- [76] R. Bullough, GROWTH, STABILITY, AND INTERACTIONS OF VOIDS AND GAS BUBBLES IN SOLIDS., Pp 233-51 *Radiat. Damage React. Mater.* Vol. II. Vienna Int. At. Energy Agency (1969). (1969).
- [77] R. Schiedung, I. Steinbach, F. Varnik, Multi-phase-field method for surface tension induced elasticity, *Phys. Rev. B*. 97 (2018) 035410. <https://doi.org/10.1103/PhysRevB.97.035410>.
- [78] Y. Park, J. Yoo, K. Huang, D.D. Keiser, J.F. Jue, B. Rabin, G. Moore, Y.H. Sohn, Growth kinetics and microstructural evolution during hot isostatic pressing of U-10 wt.% Mo monolithic fuel plate in AA6061 cladding with Zr diffusion barrier, *J. Nucl. Mater.* 447 (2014) 215–224. <https://doi.org/10.1016/j.jnucmat.2014.01.018>.
- [79] C. Miehe, F. Welschinger, M. Hofacker, Thermodynamically consistent phase-field models of fracture: Variational principles and multi-field FE implementations, *Int. J. Numer. Methods Eng.* 83 (2010) 1273–1311. <https://doi.org/10.1002/nme.2861>.
- [80] C. Miehe, M. Hofacker, F. Welschinger, A phase field model for rate-independent crack propagation: Robust algorithmic implementation based on operator splits, *Comput. Methods Appl. Mech. Eng.* 199 (2010) 2765–2778. <https://doi.org/10.1016/j.cma.2010.04.011>.
- [81] C.J. Permann, D.R. Gaston, D. Andrš, R.W. Carlsen, F. Kong, A.D. Lindsay, J.M. Miller, J.W. Peterson, A.E. Slaughter, R.H. Stogner, R.C. Martineau, MOOSE: Enabling massively parallel multiphysics simulation, *SoftwareX*. 11 (2020) 100430. <https://doi.org/10.1016/j.softx.2020.100430>.
- [82] A. Stukowski, Visualization and analysis of atomistic simulation data with OVITO—the Open Visualization Tool, *Model. Simul. Mater. Sci. Eng.* 18 (2009) 15012. <https://doi.org/10.1088/0965-0393/18/1/015012>.
- [83] Y. Zhang, P.C. Millett, M. Tonks, S.B. Biner, Deformation twins in nanocrystalline body-centered cubic Mo as predicted by molecular dynamics simulations, *Acta Mater.* 60 (2012) 6421–6428. <https://doi.org/10.1016/j.actamat.2012.08.029>.
- [84] J.-F.F. Jue, D.D. Keiser, B.D. Miller, J.W. Madden, A.B. Robinson, B.H. Rabin, Effects of irradiation on the interface between U-Mo and zirconium diffusion barrier, *J. Nucl. Mater.* 499 (2018) 567–581. <https://doi.org/10.1016/j.jnucmat.2017.10.072>.

- [85] E.J. Kautz, S. Shahrezaei, M. Athon, M. Frank, A. Schemer-Kohrn, A. Souлами, C. Lavender, V. V. Joshi, A. Devaraj, Evaluating the microstructure and origin of nonmetallic inclusions in as-cast U-10Mo fuel, *J. Nucl. Mater.* 554 (2021) 152949. <https://doi.org/10.1016/J.JNUCMAT.2021.152949>.
- [86] E. Kautz, D. Burkes, V. Joshi, C. Lavender, A. Devaraj, Nanoscale Spatially Resolved Mapping of Uranium Enrichment, *Sci. Reports* 2019 91. 9 (2019) 1–10. <https://doi.org/10.1038/s41598-019-48479-5>.
- [87] A. Leenaers, Y. Parthoens, G. Cornelis, V. Kuzminov, E. Koonen, S. den Berghe, B. Ye, G.L. Hofman, J. Schulthess, S. Van den Berghe, B. Ye, G.L. Hofman, J. Schulthess, Effect of fission rate on the microstructure of coated UMo dispersion fuel, *J. Nucl. Mater.* 494 (2017) 10–19. <https://doi.org/10.1016/j.jnucmat.2017.06.036>.
- [88] T. Ajantiwalay, C. Smith, D.D. Keiser, A. Aitkaliyeva, A critical review of the microstructure of U–Mo fuels, *J. Nucl. Mater.* 540 (2020) 152386. <https://doi.org/10.1016/j.jnucmat.2020.152386>.
- [89] E.A. Nyberg, D.M. Paxton, V. V Joshi, D.E. Burkes, C.A. Lavender, D.M. Paxton, D.E. Burkes, C.A. Lavender, *The Influence of Casting Conditions on the Microstructure of As-Cast U-10Mo Alloys: Characterization of the Casting Process Baseline*, 2013.
- [90] A. Devaraj, L. Kovarik, E. Kautz, B. Arey, S. Jana, C. Lavender, V. Joshi, Grain boundary engineering to control the discontinuous precipitation in multicomponent U-10Mo alloy, *Acta Mater.* 151 (2018) 181–190. <https://doi.org/10.1016/j.actamat.2018.03.039>.
- [91] V. V Joshi, C. Lavender, D. Paxton, D. Burkes, *The Effect of Rolling As-Cast and Homogenized U-10Mo Samples on the Microstructure Development and Recovery Curves*, 2016.
- [92] J. Sauvola, M. Pietikäinen, Adaptive document image binarization, *Pattern Recognit.* 33 (2000) 225–236. [https://doi.org/10.1016/S0031-3203\(99\)00055-2](https://doi.org/10.1016/S0031-3203(99)00055-2).
- [93] N. Phansalkar, S. More, A. Sabale, M. Joshi, Adaptive local thresholding for detection of nuclei in diversity stained cytology images, *ICCSP 2011 - 2011 Int. Conf. Commun. Signal Process.* (2011) 218–220. <https://doi.org/10.1109/ICCSP.2011.5739305>.
- [94] C.A. Schneider, W.S. Rasband, K.W. Eliceiri, NIH Image to ImageJ: 25 years of image analysis, *Nat. Methods* 2012 97. 9 (2012) 671–675. <https://doi.org/10.1038/nmeth.2089>.
- [95] D. Gross, T. Seelig, *Fracture Mechanics - With an Introduction to Micromechanics* | Dietmar Gross | Springer, (2011). <http://www.springer.com/gb/book/9783642192395> (accessed September 8, 2021).
- [96] Z. Hashin, S. Shtrikman, A variational approach to the theory of the elastic behaviour of multiphase materials, *J. Mech. Phys. Solids.* 11 (1963) 127–140. [https://doi.org/10.1016/0022-5096\(63\)90060-7](https://doi.org/10.1016/0022-5096(63)90060-7).
- [97] A. Devaraj, R. Prabhakaran, E. McGarrah, V. Joshi, S. Hu, C. Lavender, *Theoretical Model for Volume Fraction of UC, 235U Enrichment, and Effective Density of Final U-10Mo Alloy*, 2016.
- [98] M. Tokar, A. Nutt, J. Leary, *Mechanical Properties of Carbide and Nitride Reactor Fuels*, 1970.
- [99] H. Ozaltun, H. Shen, P. Medvedev, Numerical Simulation for Mechanical Behavior of U-10Mo Monolithic Miniplates for Research and Test Reactors, in: *ASME 2011 Int. Mech. Eng. Congr. Expo. IMECE 2011*, American Society of Mechanical Engineers Digital Collection, 2012: pp. 311–325. <https://doi.org/10.1115/IMECE2011-62114>.
- [100] Z.G. Mei, L. Liang, Y.S. Kim, T. Wiencek, E. O’Hare, A.M. Yacout, G. Hofman, M. Anitescu, Grain growth in U–7Mo alloy: A combined first-principles and phase field study, *J. Nucl. Mater.* 473 (2016) 300–308. <https://doi.org/10.1016/J.JNUCMAT.2016.01.027>.
- [101] G. Kresse, D. Joubert, From ultrasoft pseudopotentials to the projector augmented-wave method, *Phys. Rev. B.* 59 (1999) 1758–1775. <https://doi.org/10.1103/PhysRevB.59.1758>.
- [102] G. Kresse, J. Furthmüller, Efficient iterative schemes for ab initio total-energy calculations using a plane-wave basis set, *Phys. Rev. B.* 54 (1996) 11169–11186. <https://doi.org/10.1103/PhysRevB.54.11169>.
- [103] P.E. Blöchl, Projector augmented-wave method, *Phys. Rev. B.* 50 (1994) 17953–17979. <https://doi.org/10.1103/PhysRevB.50.17953>.

- [104] J.P. Perdew, K. Burke, M. Ernzerhof, Generalized Gradient Approximation Made Simple, *Phys. Rev. Lett.* 77 (1996) 3865–3868. <https://doi.org/10.1103/PhysRevLett.77.3865>.
- [105] S.L. Dudarev, G.A. Botton, S.Y. Savrasov, C.J. Humphreys, A.P. Sutton, Electron-energy-loss spectra and the structural stability of nickel oxide: An LSDA+U study, *Phys. Rev. B.* 57 (1998) 1505–1509. <https://doi.org/10.1103/PhysRevB.57.1505>.
- [106] A. Van De Walle, P. Tiwary, M. De Jong, D.L. Olmsted, M. Asta, A. Dick, D. Shin, Y. Wang, L.Q. Chen, Z.K. Liu, Efficient stochastic generation of special quasirandom structures, 42 (2013) 13–18. <https://doi.org/10.1016/J.CALPHAD.2013.06.006>.
- [107] L. Liang, Z.-G.G. Mei, Y.S. Kim, B. Ye, G. Hofman, M. Anitescu, A.M. Yacout, Mesoscale model for fission-induced recrystallization in U-7Mo alloy, *Comput. Mater. Sci.* 124 (2016) 228–237. <https://doi.org/10.1016/j.commatsci.2016.07.033>.
- [108] L. Liang, Z.-G.G. Mei, A.M. Yacout, Fission-induced recrystallization effect on intergranular bubble-driven swelling in U-Mo fuel, *Comput. Mater. Sci.* 138 (2017) 16–26. <https://doi.org/10.1016/J.COMMATSCI.2017.06.013>.
- [109] I. Steinbach, Phase-Field Model for Microstructure Evolution at the Mesoscopic Scale, *Annu. Rev. Mater. Res.* 43 (2013) 89–107. <https://doi.org/10.1146/annurev-matsci-071312-121703>.
- [110] J. Rest, Evolution of fission-gas-bubble-size distribution in recrystallized U–10Mo nuclear fuel, *J. Nucl. Mater.* 407 (2010) 55–58. <https://doi.org/10.1016/j.jnucmat.2010.07.009>.
- [111] J.P. Simmons, C. Shen, Y. Wang, Phase field modeling of simultaneous nucleation and growth by explicitly incorporating nucleation events, *Scr. Mater.* 43 (2000) 935–942. [https://doi.org/10.1016/S1359-6462\(00\)00517-0](https://doi.org/10.1016/S1359-6462(00)00517-0).
- [112] L.Q. Chen, J. Shen, Applications of semi-implicit Fourier-spectral method to phase field equations, *Comput. Phys. Commun.* 108 (1998) 147–158. [https://doi.org/10.1016/S0010-4655\(97\)00115-X](https://doi.org/10.1016/S0010-4655(97)00115-X).
- [113] J. Rest, Derivation of analytical expressions for the network dislocation density, change in lattice parameter, and for the recrystallized grain size in nuclear fuels, *J. Nucl. Mater.* 349 (2006) 150–159. <https://doi.org/10.1016/J.JNUCMAT.2005.10.007>.
- [114] J. Rest, A model for the influence of microstructure, precipitate pinning and fission gas behavior on irradiation-induced recrystallization of nuclear fuels, *J. Nucl. Mater.* 326 (2004) 175–184. <https://doi.org/10.1016/j.jnucmat.2004.01.009>.
- [115] M.S. Daw, M.I. Baskes, Embedded-atom method: Derivation and application to impurities, surfaces, and other defects in metals, *Phys. Rev. B.* 29 (1984) 6443. <https://doi.org/10.1103/PhysRevB.29.6443>.
- [116] M.S. Daw, M.I. Baskes, Semiempirical, Quantum Mechanical Calculation of Hydrogen Embrittlement in Metals, *Phys. Rev. Lett.* 50 (1983) 1285. <https://doi.org/10.1103/PhysRevLett.50.1285>.
- [117] B. Beeler, S. Hu, Y. Zhang, Y. Gao, A improved equation of state for Xe gas bubbles in γ U-Mo fuels, *J. Nucl. Mater.* 530 (2020) 151961. <https://doi.org/10.1016/J.JNUCMAT.2019.151961>.
- [118] G. Park, B. Beeler, M.A. Okuniewski, An atomistic study of defect energetics and diffusion with respect to composition and temperature in γ U and γ U-Mo alloys, *J. Nucl. Mater.* 552 (2021) 152970. <https://doi.org/10.1016/J.JNUCMAT.2021.152970>.
- [119] K.E. Huang, D.D. Keiser, Y. Sohn U-Mo, Interdiffusion, Intrinsic Diffusion, Atomic Mobility, and Vacancy Wind Effect in gamma(bcc) Uranium-Molybdenum Alloy, (n.d.). <https://doi.org/10.1007/s11661-012-1425-9>.
- [120] B. Beeler, Y. Zhang, M. Okuniewski, C. Deo, Calculation of the displacement energy of α and γ uranium, *J. Nucl. Mater.* 508 (2018) 181–194. <https://doi.org/10.1016/J.JNUCMAT.2018.05.039>.
- [121] M.R. Tonks, D. Andersson, S.R. Phillpot, Y. Zhang, R. Williamson, C.R. Stanek, B.P. Uberuaga, S.L. Hayes, Mechanistic materials modeling for nuclear fuel performance, *Ann. Nucl. Energy.* 105 (2017) 11–24.
- [122] J. Jue, D. Keiser, C. Breckenridge, B. Rabin, G. Moore, A. Robinson, F.J. Rice, M. Meyer, RERTR – 12 Characterization Summary Report, Idaho Falls, ID, 2013.

- [123] J.-F. Jue, T. Breckenridge, T. Trowbridge, T. Holleran, D. Keiser, AFIP – 6 MKII Characterization Summary Report, 2014.
- [124] W. Williams, F.J. Rice, A.B. Robinson, M. Meyer, B. Rabin, AFIP-6 MKII Post-irradiation Examination Summary Report, Idaho Falls, ID (United States), 2015.
- [125] F.J. Rice, W. Williams, A. Robinson, J. Harp, M. Meyer, B. Rabin, RERTR-12 Post-irradiation Examination Summary Report, Idaho Falls, ID (United States), 2015. <https://doi.org/INL/LTD-14-33066>.
- [126] S.L. Hayes, G.L. Hofman, M.K. Meyer, J. Rest, J.L. Snelgrove, MODELING OF HIGH-DENSITY U-MO DISPERSION FUEL PLATE PERFORMANCE, in: Int. Meet. Reduc. Enrich. Res. Test React., San Carlos de Bariloche, Argentina, 2002: pp. 1–10.
- [127] M. Stan, J.C. Ramirez, P. Cristea, S.Y. Hu, C. Deo, B.P. Uberuaga, S. Srivilliputhur, S.P. Rudin, J.M. Wills, Models and simulations of nuclear fuel materials properties, *J. Alloys Compd.* 444–445 (2007) 415–423. <https://doi.org/10.1016/j.jallcom.2007.01.102>.
- [128] D.B.C.L.V.J. SY Hu, Effect of grain morphology on gas bubble swelling in UMo fuels – A 3D microstructure dependent Booth model, *J. Nucl. Mater.* 480 (2016) 323. <https://doi.org/10.1016/j.jnucmat.2016.08.038>.
- [129] W.E. Frazier, S. Hu, D.E. Burkes, B.W. Beeler, A Monte Carlo model of irradiation-induced recrystallization in polycrystalline UMo fuels, *J. Nucl. Mater.* 524 (2019). <https://doi.org/10.1016/j.jnucmat.2019.07.004>.
- [130] S. Van den Berghe, W. Van Renterghem, A. Leenaers, Transmission electron microscopy investigation of irradiated U–7wt%Mo dispersion fuel, *J. Nucl. Mater.* 375 (2008) 340–346. <https://doi.org/10.1016/j.jnucmat.2007.12.006>.
- [131] J. Gan, D.D. Keiser, D.M. Wachs, A.B. Robinson, B.D. Miller, T.R. Allen, Transmission electron microscopy characterization of irradiated U–7Mo/Al–2Si dispersion fuel, *J. Nucl. Mater.* 396 (2010) 234–239. <https://doi.org/10.1016/j.jnucmat.2009.11.015>.
- [132] J. Gan, D.D. Keiser, B.D. Miller, A.B. Robinson, J.-F. Jue, P. Medvedev, D.M. Wachs, TEM characterization of U–7Mo/Al–2Si dispersion fuel irradiated to intermediate and high fission densities, *J. Nucl. Mater.* 424 (2012) 43–50. <https://doi.org/10.1016/j.jnucmat.2012.02.001>.
- [133] A.B. Robinson, W.J. Williams, W.A. Hanson, B.H. Rabin, N.J. Lybeck, M.K. Meyer, Swelling of U-Mo Monolithic Fuel: Developing a Predictive Swelling Correlation under Research Reactor Conditions, *J. Nucl. Mater.* 544 (2021) 152703. <https://doi.org/10.1016/j.jnucmat.2020.152703>.
- [134] F.G. Di Lemma, J. Burns, J.W. Madden, A.J. Winston, A.B. Robinson, J.-F. Jue, D.D. Keiser, J.I. Cole, Texture analyses and microstructural evolution in monolithic U-Mo nuclear fuel, *J. Nucl. Mater.* 544 (2021) 152677. <https://doi.org/10.1016/j.jnucmat.2020.152677>.
- [135] D. Jadernas, J. Gan, D. Keiser, J. Madden, M. Bachhav, J.-F. Jue, A. Robinson, Microstructural characterization of as-fabricated and irradiated U-Mo fuel using SEM/EBSD, *J. Nucl. Mater.* 509 (2018) 1–8. <https://doi.org/10.1016/j.jnucmat.2018.06.007>.
- [136] D.D. Keiser, J.-F. Jue, K. Verner, T. Trowbridge, C.A. Smith, A. Aitkaliyeva, A.B. Robinson, B. Miller, Quantitative Image Analysis of AFIP6-MkII and RERTR-12 Fresh Fuel and Irradiated Fuel Fission Gas Bubble and Recrystallized Fraction, Idaho Falls, Idaho, 2018. <https://doi.org/INL/LTD-18-51296>.
- [137] F.G. Di Lemma, T. Trowbridge, C. Brizzee, J.-F. Jue, MP - 1 Intermediate Characterization Report Summary, Idaho Falls, ID, 2018.
- [138] W.E. Frazier, S. Hu, N. Overman, C. Lavender, V. V. Joshi, Short communication on Kinetics of grain growth and particle pinning in U-10 wt.% Mo, *J. Nucl. Mater.* 498 (2018) 254–258. <https://doi.org/10.1016/j.jnucmat.2017.10.041>.
- [139] J. Gan, D.D. Keiser, B.D. Miller, J.-F. Jue, A.B. Robinson, J. Madden, TEM characterization of irradiated U-7Mo/Mg dispersion fuel, *J. Nucl. Mater.* 494 (2017) 380–397. <https://doi.org/10.1016/j.jnucmat.2017.07.030>.
- [140] A. Robinson, W. Williams, B. Rabin, J.-F. Jue, D. Keiser, N. Lybeck, Follow on Investigation of U-Mo Monolithic Fuel Swelling in the AFIP-6 MkII Experiment, Idaho Falls, ID, 2018.

- <https://doi.org/INL/LTD-18-50149>.
- [141] M.K. Meyer, G.A. Moore, J.-F. Jue, D.D. Keiser, I.Y. Glagolenko, D.M. Wachs, P.E. Murray, A.B. Robinson, F.J. Rice, H. Ozaltun, S.J. Miller, M.A. Okuniewski, B.H. Rabin, H.W. Glunz, N.J. Lybeck, Investigation of the Cause of Low Blister Threshold Temperatures in the RERTR-12 and AFIP-4 Experiments, Idaho Falls, ID, 2012.
- [142] J.-F. Jue, D.D. Keiser, C.R. Breckenridge, G.A. Moore, M.K. Meyer, Microstructural characteristics of HIP-bonded monolithic nuclear fuels with a diffusion barrier, *J. Nucl. Mater.* 448 (2014) 250–258. <https://doi.org/10.1016/j.jnucmat.2014.02.004>.
- [143] V. V. Joshi, E.A. Nyberg, C.A. Lavender, D. Paxton, D.E. Burkes, Thermomechanical process optimization of U-10wt% Mo – Part 2: The effect of homogenization on the mechanical properties and microstructure, *J. Nucl. Mater.* 465 (2015) 710–718. <https://doi.org/10.1016/j.jnucmat.2015.07.005>.
- [144] M. K. Meyer, G. L. Hofman, S. L. Hayes, C. R. Clark, T. C. Wiencek, J. L. Snelgrove, R. V. Strain, K.H.H. Kim, Low-temperature irradiation behavior of uranium–molybdenum alloy dispersion fuel, *J. Nucl. Mater.* 304 (2002) 221–236. [https://doi.org/10.1016/S0022-3115\(02\)00850-4](https://doi.org/10.1016/S0022-3115(02)00850-4).
- [145] R. Schley, L.K. Aagesen, Z. Hua, D. Hurley, Detailed Analysis of RUS Insertion Experiment and Scoping Studies for Performing Next Experiment using an Enriched Fuel Sample, Idaho Falls, ID, 2019.
- [146] R.S. Schley, D.H. Hurley, Z.A. Hua, Optical fiber technique for in-reactor mechanical properties measurement, in: *AIP Conf. Proc.*, American Institute of Physics AIP, 2013: pp. 1701–1708. <https://doi.org/10.1063/1.4789246>.
- [147] L.K. Mansur, Theory and experimental background on dimensional changes in irradiated alloys, *J. Nucl. Mater.* 216 (1994) 97–123. [https://doi.org/10.1016/0022-3115\(94\)90009-4](https://doi.org/10.1016/0022-3115(94)90009-4).
- [148] D. Brimbal, L. Fournier, A. Barbu, Cluster dynamics modeling of the effect of high dose irradiation and helium on the microstructure of austenitic stainless steels, *J. Nucl. Mater.* 468 (2016) 124–139. <https://doi.org/10.1016/J.JNUCMAT.2015.11.007>.
- [149] A.A. Kohnert, B.D. Wirth, Cluster dynamics models of irradiation damage accumulation in ferritic iron. I. Trap mediated interstitial cluster diffusion, *J. Appl. Phys.* 117 (2015) 154305. <https://doi.org/10.1063/1.4918315>.
- [150] A.A. Kohnert, B.D. Wirth, Cluster dynamics models of irradiation damage accumulation in ferritic iron. II. Effects of reaction dimensionality, *J. Appl. Phys.* 117 (2015) 154306. <https://doi.org/10.1063/1.4918316>.
- [151] R.E. Stoller, Modeling Dislocation Evolution in Irradiated Alloys, (n.d.).
- [152] A. Hardouin Duparc, C. Moingeon, N. Smetniansky-De-Grande, A. Barbu, Microstructure modelling of ferritic alloys under high flux 1 MeV electron irradiations, *J. Nucl. Mater.* 302 (2002) 143–155. [https://doi.org/10.1016/S0022-3115\(02\)00776-6](https://doi.org/10.1016/S0022-3115(02)00776-6).
- [153] A.D. Brailsford, R. Bullough, The rate theory of swelling due to void growth in irradiated metals, *J. Nucl. Mater.* 44 (1972) 121–135. [https://doi.org/10.1016/0022-3115\(72\)90091-8](https://doi.org/10.1016/0022-3115(72)90091-8).
- [154] G. Was, *Fundamentals of Radiation Materials Science*, Springer-Verlag Berlin Heidelberg, 2007.
- [155] T.S. Duh, J.J. Kai, F.R. Chen, L.H. Wang, Numerical simulation modeling on the effects of grain boundary misorientation on radiation-induced solute segregation in 304 austenitic stainless steels, *J. Nucl. Mater.* 294 (2001) 267–273. [https://doi.org/10.1016/S0022-3115\(01\)00493-7](https://doi.org/10.1016/S0022-3115(01)00493-7).
- [156] L.D. Xia, Y.Z. Ji, W.B. Liu, H. Chen, Z.G. Yang, C. Zhang, L.Q. Chen, Radiation induced grain boundary segregation in ferritic/martensitic steels, *Nucl. Eng. Technol.* 52 (2020) 148–154. <https://doi.org/10.1016/J.NET.2019.07.009>.
- [157] S.G. Kim, W.T. Kim, T. Suzuki, Phase-field model for binary alloys, *Phys. Rev. E.* 60 (1999) 7186. <https://doi.org/10.1103/PhysRevE.60.7186>.

- [158] Y. Li, S. Hu, X. Sun, M. Stan, A review: applications of the phase field method in predicting microstructure and property evolution of irradiated nuclear materials, *Comput. Mater.* 3 (2017) 1–17. <https://doi.org/10.1038/s41524-017-0018-y>.
- [159] S. Hu, W. Setyawan, V. V. Joshi, C.A. Lavender, Atomistic simulations of thermodynamic properties of Xe gas bubbles in U-10Mo fuels, *J. Nucl. Mater.* 490 (2017) 49–58. <https://doi.org/10.1016/J.JNUCMAT.2017.04.016>.
- [160] A. Ma, F. Roters, D. Raabe, A dislocation density based constitutive model for crystal plasticity FEM including geometrically necessary dislocations, *Acta Mater.* 54 (2006) 2169–2179. <https://doi.org/10.1016/J.ACTAMAT.2006.01.005>.
- [161] A. Ma, F. Roters, A constitutive model for fcc single crystals based on dislocation densities and its application to uniaxial compression of aluminium single crystals, *Acta Mater.* 52 (2004) 3603–3612. <https://doi.org/10.1016/J.ACTAMAT.2004.04.012>.
- [162] R.A. Lebensohn, A.K. Kanjarla, P. Eisenlohr, An elasto-viscoplastic formulation based on fast Fourier transforms for the prediction of micromechanical fields in polycrystalline materials, *Int. J. Plast.* 32–33 (2012) 59–69. <https://doi.org/10.1016/J.IJPLAS.2011.12.005>.
- [163] S.Y. Hu, L.Q. Chen, A phase-field model for evolving microstructures with strong elastic inhomogeneity, *Acta Mater.* 49 (2001) 1879–1890. [https://doi.org/10.1016/S1359-6454\(01\)00118-5](https://doi.org/10.1016/S1359-6454(01)00118-5).
- [164] P.G. Medvedev, H. Ozaltun, A.B. Robinson, B.H. Rabin, Shutdown-induced tensile stress in monolithic miniplates as a possible cause of plate pillowing at very high burnup, *Nucl. Eng. Des.* 328 (2018) 161–165. <https://doi.org/10.1016/J.NUCENGDES.2018.01.004>.
- [165] S. Polkinghorne, J. Lacy, Thermo-physical and mechanical properties of ATR core materials, EG&G Inc. Technical Report, 1991.
- [166] J.G. (John G. Kaufman, Properties of aluminum alloys : tensile, creep, and fatigue data at high and low temperatures, (1999) 305.
- [167] K. Farrell, R. King, Tensile Properties of Neutron-Irradiated 6061 Aluminum Alloy in Annealed and Precipitation-Hardened Conditions, *ASTM Spec. Tech. Publ.* (1979) 440–449. <https://doi.org/10.1520/STP38180S>.
- [168] K. Farrell, Assessment of aluminum structural materials for service within the ANS reflector vessel, (1995). http://inis.iaea.org/Search/search.aspx?orig_q=RN:27048252 (accessed September 14, 2021).
- [169] G. Beghi, GAMMA PHASE URANIUM-MOLYBDENUM FUEL ALLOYS, (n.d.).
- [170] J. Klein, Uranium and Its Alloys, in: A. Kaufman (Ed.), *Nucl. React. Fuel Elem.*, Wiley, 1962.
- [171] D.E. Smirnova, S. V. Starikov, V. V. Stegailov, New interatomic potential for computation of mechanical and thermodynamic properties of uranium in a wide range of pressures and temperatures, *Phys. Met. Metallogr.* 2012 1132. 113 (2012) 107–116. <https://doi.org/10.1134/S0031918X12020147>.
- [172] D.E. Smirnova, A.Y. Kuksin, S. V. Starikov, V. V. Stegailov, Atomistic modeling of the self-diffusion in γ -U and γ -U-Mo, *Phys. Met. Metallogr.* 2015 1165. 116 (2015) 445–455. <https://doi.org/10.1134/S0031918X1503014X>.
- [173] S. Hu, B. Beeler, Gas Bubble Evolution in Polycrystalline UMo Fuels Under Elastic-Plastic Deformation: A Phase-Field Model With Crystal-Plasticity, *Front. Mater.* 8 (2021) 173. <https://doi.org/10.3389/FMATS.2021.682667>.
- [174] W. Setyawan, M.W.D. Cooper, K.J. Roche, R.J. Kurtz, B.P. Uberuaga, D.A. Andersson, B.D. Wirth, Atomistic model of xenon gas bubble re-resolution rate due to thermal spike in uranium oxide, *J. Appl. Phys.* 124 (2018) 075107. <https://doi.org/10.1063/1.5042770>.
- [175] C. Xoubi, R. Primm, Modeling of the High Flux Isotope Reactor Cycle 400, 1996.
- [176] M.J. Norgett, M.T. Robinson, I.M. Torrens, A proposed method of calculating displacement dose rates, *Nucl. Eng. Des.* 33 (1975) 50–54. [https://doi.org/10.1016/0029-5493\(75\)90035-7](https://doi.org/10.1016/0029-5493(75)90035-7).
- [177] B. Beeler, B. Good, S. Rashkeev, C. Deo, M. Baskes, M. Okuniewski, First principles calculations

- for defects in U, *J. Phys. Condens. Matter.* 22 (2010) 505703. <https://doi.org/10.1088/0953-8984/22/50/505703>.
- [178] B. Beeler, C. Deo, M. Baskes, M. Okuniewski, First principles calculations of the structure and elastic constants of α , β and γ uranium, *J. Nucl. Mater.* 433 (2013) 143–151. <https://doi.org/10.1016/J.JNUCMAT.2012.09.019>.
- [179] K.R. Lund, K.G. Lynn, M.H. Weber, M.A. Okuniewski, Vacancy Formation Enthalpy in Polycrystalline Depleted Uranium, *J. Phys. Conf. Ser.* 443 (2013) 012021. <https://doi.org/10.1088/1742-6596/443/1/012021>.
- [180] S.J. Rothman, L.T. Lloyd, R. Weil, A.L. Harkness, SELF-DIFFUSION IN GAMMA URANIUM, *Trans. Am. Inst. Min. Metall. Eng.* 218 (1959) 605–607. <https://doi.org/10.2172/4220599>.
- [181] Y. Adda, A. Kirianenko, Etude de l'autodiffusion de l'uranium en phase α , *J. Nucl. Mater.* 6 (1962) 130–134. [https://doi.org/10.1016/0022-3115\(62\)90224-6](https://doi.org/10.1016/0022-3115(62)90224-6).
- [182] A.A. Kohnert, B.D. Wirth, L. Capolungo, Modeling microstructural evolution in irradiated materials with cluster dynamics methods: A review, *Comput. Mater. Sci.* 149 (2018) 442–459. <https://doi.org/10.1016/J.COMMATSCI.2018.02.049>.
- [183] J.H. Ke, H. Ke, G.R. Odette, D. Morgan, Cluster dynamics modeling of Mn-Ni-Si precipitates in ferritic-martensitic steel under irradiation, *J. Nucl. Mater.* 498 (2018) 83–88. <https://doi.org/10.1016/J.JNUCMAT.2017.10.008>.
- [184] S. Hu, W. Setyawan, B.W. Beeler, J. Gan, D.E. Burkes, Defect cluster and nonequilibrium gas bubble associated growth in irradiated UMo fuels – A cluster dynamics and phase field model, *J. Nucl. Mater.* 542 (2020) 152441. <https://doi.org/10.1016/J.JNUCMAT.2020.152441>.
- [185] J.W. Harrison, An extrapolated equation of state for xenon for use in fuel swelling calculations, *J. Nucl. Mater.* 31 (1969) 99–106. [https://doi.org/10.1016/0022-3115\(69\)90047-6](https://doi.org/10.1016/0022-3115(69)90047-6).
- [186] J. Eshelby, The determination of the elastic field of an ellipsoidal inclusion, and related problems, *Proc. R. Soc. London. Ser. A. Math. Phys. Sci.* 241 (1957) 376–396. <https://doi.org/10.1098/rspa.1957.0133>.
- [187] H.-X. Xiao, 肖红星, C.-S. Long, 龙冲生, A modified equation of state for Xe at high pressures by molecular dynamics simulation, *Chinese Phys. B.* 23 (2013) 020502. <https://doi.org/10.1088/1674-1056/23/2/020502>.
- [188] K. Nordlund, S.J. Zinkle, A.E. Sand, F. Granberg, R.S. Averback, R. Stoller, T. Suzudo, L. Malerba, F. Banhart, W.J. Weber, F. Willaime, S.L. Dudarev, D. Simeone, Improving atomic displacement and replacement calculations with physically realistic damage models, *Nat. Commun.* 2018 91. 9 (2018) 1–8. <https://doi.org/10.1038/s41467-018-03415-5>.
- [189] C. Björkas, K. Nordlund, Comparative study of cascade damage in Fe simulated with recent potentials, *Nucl. Instruments Methods Phys. Res. Sect. B Beam Interact. with Mater. Atoms.* 259 (2007) 853–860. <https://doi.org/10.1016/J.NIMB.2007.03.076>.
- [190] C. Björkas, K. Nordlund, S. Dudarev, Modelling radiation effects using the ab-initio based tungsten and vanadium potentials, *Nucl. Instruments Methods Phys. Res. Sect. B Beam Interact. with Mater. Atoms.* 267 (2009) 3204–3208. <https://doi.org/10.1016/J.NIMB.2009.06.123>.
- [191] G. Nandipati, W. Setyawan, H.L. Heinisch, K.J. Roche, R.J. Kurtz, B.D. Wirth, Displacement cascades and defect annealing in tungsten, Part II: Object kinetic Monte Carlo simulation of tungsten cascade aging, *J. Nucl. Mater.* 462 (2015) 338–344. <https://doi.org/10.1016/J.JNUCMAT.2014.09.067>.
- [192] B. Beeler, M. Asta, P. Hosemann, N. Grønbech-Jensen, Effects of applied strain on radiation damage generation in body-centered cubic iron, *J. Nucl. Mater.* 459 (2015) 159–165. <https://doi.org/10.1016/J.JNUCMAT.2014.12.111>.